UNIVERSIDADE Ð COIMBRA

Simone Pereira Rodrigues

DEVELOPMENT OF HYBRID SURFACE TREATMENTS FOR CONTROLLING WETTABILITY AND IMPROVING TRIBOLOGICAL PERFORMANCE

Doctoral Thesis of the Doctoral Program on Advanced Materials and Processing, supervised by Professor Doctor Albano Augusto Cavaleiro Rodrigues de Carvalho and by Professor Doctor Sandra Maria Fernandes Carvalho, submitted to the Department of Mechanical Engineering, Faculty of Sciences and Technology of the University of Coimbra.

August 2019

University of Coimbra

DEVELOPMENT OF HYBRID SURFACE TREATMENTS FOR CONTROLLING WETTABILITY AND IMPROVING TRIBOLOGICAL PERFORMANCE

Simone Pereira Rodrigues

Doctoral Thesis of the Doctoral Program on Advanced Materials and Processing (AdvaMTech), supervised by Professor Doctor Albano Augusto Cavaleiro Rodrigues de Carvalho and Professor Doctor Sandra Maria Fernandes Carvalho, submitted to the Department of Mechanical Engineering, Faculty of Sciences and Technology of the University of Coimbra.

August 2019

1 2 9 0

UNIVERSIDADE Ð
COIMBRA

PhD scholarship (PD/BD/112079/2015) financed by:

Aos meus Avós pelos Valores transmitidos.

Que eu continue a ser abençoada pela vossa Luz no meu caminho.

Como me ensinastes "Pulso firme, dos fracos não reza a história".

"Maior que a tristeza de não haver vencido é a vergonha de não ter lutado"

Rui Barbosa

GRATA

Agradecimentos

Este foi sem dúvida o período mais difícil da minha vida até hoje, no entanto, quero agradecer a todas a pessoas que estiveram presentes e que me acompanharam ao longo desta etapa de cinco anos. Primeiramente aos meus pais pela compreensão, auxílio e confiança que me transmitiram, mesmo em momentos familiares tão difíceis, são os meus heróis e a vossa ajuda será inesquecível, vou recordar sempre a minha mãe a minha espera para comer uma sopa às onze da noite quando eu chegava de uma viagem de Guimarães. Ao meu irmão Vitor e cunhada Paula, que ao jeito deles me espicaçaram e incentivaram a terminar esta tese de uma vez por todas. E obrigada pela alegria do Afonso!

Ainda assim, quando quis realmente desistir, em boa hora encontrei o grande Líder Adelino Cunha que acreditou mais em mim do que eu própria, e agradeço a ele e a toda a equipa Solfut - I HAVE THE POWER pelo tanto que me fizeram evoluir e crescer como pessoa e profissional. Tenho sem dúvida uma excelente bagagem para um futuro de sucesso, obrigada! Estão no meu coração para sempre!

Um agradecimento ao meu orientador, o Prof. Albano Cavaleiro, por ter aceitado que eu fosse sua aluna de doutoramento, mesmo sem ele saber muito bem em que é que se estava a meter, obrigada pela confiança e orientação, que em conjunto com a Prof. Sandra Carvalho amparou o processo até este momento. Guardo também comigo pessoas especiais, que foram um reforço de amizade tremendo ao longo destes anos, e desejo-lhes muito sucesso pelas pessoas que são. Um grande "obrigada" aos Doutores Cristiana Alves, Isabel Carvalho e Ricardo Serra. Gratidão também a minha colega Luísa Fialho que me fez sentir mais perto da Engenharia Biomédica durante parte deste percurso. Agradecimento também ao Doutor Manuel Evaristo pelo suporte dado.

Foi também importante toda a comunidade do refeitório da UM, que mesmo às vezes uns minutos depois da hora ainda me abriam a porta e me serviam o jantar com toda a amabilidade, depois de tantas horas a anodizar no Departamento de Física e de atravessar sozinha a avenida escura, gelada e por vezes também molhada, em pleno inverno do Norte. Da mesma forma agradeço a todos os seguranças que me fizeram companhia durante a noite no laboratório e me escoltavam de madrugada até ao carro nas traseiras da UM, quando ainda não havia luz! À "família" acolhedora de Guimarães, Maria José, Augusto e Catarina que me ofereceram "condições de rainha", obrigada pelo hambúrguer à meia-noite, que tão bem me sabia, pois já estava outra vez cheia de fome. Obrigada por me ouvirem também!

Apesar de muitos momentos a querer deitar a "toalha ao chão", quero dar um especial agradecimento também aos colaboradores do LED&MAT do IPN (Eng.º João Paulo, António Fonseca, Carlos Patacas, João Costa e Bruno Martins e Rui Azevedo), por todo o suporte e ensinamento que me deram e pela disponibilidade prestada para sessões de SEM e manutenção da

câmara de deposição. Ainda hoje me lembro da frase do João Costa "tu consegues, toda a gente consegue, o segredo é não desistir". Obrigada!

Ao Prof. Tomas Polcar da Universidade Técnica de Praga (CTU) que permitiu que eu conhecesse outra realidade de trabalho e disponibilizou os seus laboratórios para efetuar os últimos testes tribológicos da minha tese. Agradecimento especial ao Doutor Kosta Simonovic e ao Doutor Emilio Frutos pelo suporte e conhecimento científico prestados.

A toda a comunidade científica nacional do programa doutoral e também internacional que contribuiu para o sucesso deste projeto. Especial agradecimento para a Prof. Ana Paula Piedade pela ajuda nos processos burocráticos, tão difíceis na fase inicial. À Maria João por ser sempre impecável a ajudar em tudo o que era preciso, obrigada por seres tão doce em me ouvires e me fazeres ver a razoabilidade das situações também. Agradeço também grandemente a todas as pessoas que tive oportunidade de conhecer nas conferências onde estive presente, essas pessoas fizeram-me acreditar ainda mais de que o fim seria possível de atingir. Estou muito grata à Fundação para a Ciência e Tecnologia (FCT) pela bolsa de doutoramento concedida no âmbito do programa doutoral AdvaMTech, assim como à Fundação Luso-Americana (FLAD) e comissões científicas das conferências ICMCTF 2018 e SVC 2019 pelo financiamento que me cederam para que fosse possível estar presente em tão célebres eventos científicos com os melhores do mundo na área. Não tem preço o valor que guardo comigo dessas experiências!

Um reconhecimento também ao Prof. Rui Silva da Universidade de Aveiro por me ter dado a oportunidade de aprender tanto e assim contribuir para que o meu percurso científico tivesse dado início ao doutoramento. Abraço forte às amigas que nunca me deixaram fraquejar, fazendo-me ver que tudo passa, obrigada por tantos momentos divertidos. Abraço forte minhas queridas Ermelinda Salgueiredo, Flávia Almeida, Patrícia Neves, Isa Branco, Filipa Neves, Susana Lavoura, Ana Sofia e Elsa Guerra.

E agradeço a Deus e Anjos da Guarda por me terem sempre guiado com tanta Luz e dado forças para manter a auto-motivação para continuar nesta etapa, que foi sem dúvida uma missão não só de trabalho mas também de muita Fé. Tive realmente a perceção da célebre frase bíblica "pede e receberás". Fui brindada com momentos de "coincidência" maravilhosos. Um abraço forte também ao grande Sr. Carlos Valente da AELP-Aveiro por me permitir desenvolver, aprender e ajudar tantas pessoas. Ao Dr. Diogo Amorim do IMI-Coimbra pelos excelentes tratamentos de acupuntura que me permitiram ter mais saúde e serenidade, chegando até aqui sem antidepressivos. Imensa gratidão!

OBRIGADA MESMO!
Que Deus vos abençoe Grandemente!

Resumo

A produção de resíduos poluentes ou nocivos, assim como o consumo exagerado de plásticos, são nos dias de hoje grandes problemas que em muito comprometem a sustentabilidade ambiental. A este respeito, materiais com funcionalidades especiais que possam durar mais tempo são as grandes exigências da indústria atual. Em particular, o controlo da molhabilidade da superfície dos materiais, bem como o seu comportamento tribológico, têm recebido grande atenção devido às suas potenciais aplicações em sistemas auto-lubrificantes, resistentes à corrosão, em sistemas auto-limpantes, anti-embaciamento ou anti-incrustantes. Nesse sentido, a abordagem usada para controlar a molhabilidade da superfície dos materiais a um determinado líquido geralmente depende da alteração da sua rugosidade e/ou química superficial usando métodos de texturização/estruturação de superfície, que podem ser usados isoladamente, ou combinados com a deposição de revestimentos.

Neste trabalho, a alteração da rugosidade da superfície foi induzida em substratos de uma liga de alumínio (Al6016-T4) através do processo de anodização, e posteriormente as superfícies texturadas/estruturadas foram quimicamente modificadas através da deposição de revestimentos de base WS_2-C dopados com flúor (F), por pulverização catódica reativa (Ar/CF_4).

A anodização de Al realizada em configuração a um passo levou à formação de uma superfície em forma de concavidades com um diâmetro pequeno (SD) de cerca de 31 nm (quando se usa H_2SO_4 como eletrólito), e com um diâmetro maior (LD) de cerca de 223 nm (quando se usa H_3PO_4 como eletrólito). A superfície LD foi a que demonstrou ter maior hidrofobicidade. A anodização a dois passos permitiu obter camadas de óxido de Al poroso mais espesso, com diferentes diâmetros de poro (~30 e ~250 nm), contudo todas apresentaram um comportamento de superfície superhidrofílico e superoleofílico. Os revestimentos WS-CF para promover a modificação química das superfícies anodizadas foram primeiramente desenvolvidos e caracterizados em substratos de aço polido. Observou-se que, até um determinado fluxo de CF_4, o F foi incorporado nos revestimentos (máximo de 9,5 at. %) e contribuiu tanto para o aumento da dureza como para o aumento da energia de superfície (SFE) e hidrofilicidade dos revestimentos. A redução do coeficiente de atrito encontrada (coeficiente de atrito de 0,016 quando testado a 200 °C sem lubrificação) foi atribuída ao aumento da distância interplanar provocada pela inserção de F na estrutura do WS_2.

Posteriormente, a espessura dos revestimentos WS-CF foi ajustada de modo a que quando depositados sobre as superfícies anodizadas com forma de concavidades pudessem replicar a sua rugosidade. E assim, revestimentos com cerca de 200 nm foram também previamente caracterizados sobre substratos de aço, e confirmaram em grande parte o desempenho que já tinha sido verificado para os respetivos filmes espessos. No entanto, a análise estrutural mostrou os planos basais como sendo a orientação preferencial, facto este devido às características de crescimento inicial típico deste tipo de filmes; e os revestimentos dopados com F mostraram um ligeiro aumento do ângulo de contacto relativamente ao óleo, facto este não observado nos revestimentos espessos.

No final, as estruturas híbridas (designadas como LD+WS2 e LD+WS-CF5) obtidas pela deposição dos revestimentos finos (200 nm) WS-CF sobre as superfícies de Al anodizadas em forma de concavidade (de tamanho maior) foram avaliadas em termos do comportamento de atrito e de grau de molhabilidade. Os testes tribológicos realizados à temperatura ambiente sem lubrificação indicaram que as superfícies rugosas revestidas apresentaram valores de coeficiente de atrito mais baixos; enquanto, nos ensaios realizados em condições lubrificadas com PAO-8, os valores foram mais elevados que nas superfícies anodizadas não revestidas. Estas diferenças estão relacionadas com a rugosidade e com as propriedades mecânicas das superfícies em contacto, bem como com a sua energia de superfície na fase inicial do contacto. Relativamente ao comportamento de molhabilidade das superfícies híbridas, verificou-se que, em geral, tanto a química como a rugosidade do revestimento contribuíram para esse comportamento. Sendo assim, o comportamento hidrofóbico/oleofílico da superfície LD+WS2 pode ser útil para sistemas auto-limpantes ou processos de separação água-óleo, enquanto, o comportamento hidrofílico/oleofílico (LD+WS-CF5) pode ter um papel importante em processos de impressão ou aplicações em microfluídica.

PALAVRAS-CHAVE: ligas de alumínio, molhabilidade da superfície, processo de anodização, revestimentos WS_2, dopagem com flúor, pulverização catódica, tribologia.

Abstract

Nowadays, the production of pollutant or harmful residues and plastic consumption are big issues compromising environmental sustainability. In this regard, materials with special functionality that can withstand longer lifetimes are more demanding over the current industrial entities. Namely, the surface wettability control of materials as well as their friction performance has received special research attention due to their potential applications on self-lubricating, corrosion resistance, and self-cleaning, anti-fogging or anti-fouling purposes. According to this, the approach used to control the wettability of materials' surface to a particular liquid usually relies on the surface roughness and chemistry modification by surface texturing/structuring methods, which can be used isolated or further combined with the deposition of coatings.

 In this study, the surface roughness modification was induced on aluminum alloy (Al6016-T4) substrates through anodization and those textured/structured surfaces were thereafter chemically changed by deposition with F-alloyed WS_2-C based coatings by reactive (Ar/CF_4) magnetron sputtering method.

The Al anodization carried out in one-step configuration led to dimple-shaped surfaces with a small diameter (SD) of around 31 nm (when using H_2SO_4 electrolyte), and with larger diameters (LD) of around 223 nm (when using H_3PO_4 electrolyte). LD surface made it possible to reach the more hydrophobic surface. Despite this, the two-step anodization allowed thicker porous Al oxide layers to be achieved, with different pore sizes (~30 nm or ~250 nm), but all showing a superhydrophilic and superoleophilic surface behaviour. WS-CF coatings to promote the chemical modification of the bottom anodized surfaces were firstly developed and characterized on polished steel substrates. It was possible to observe that, until a certain CF_4 flow rate, F was incorporated in the coatings (maximum of 9.5 at. %) and contributed to the increase of their hardness as well as their surface energy (SFE) and hydrophilicity. The encountered friction decrease at room temperature (friction coefficient of 0.016 when tested at 200 °C without lubrication) was attributed to the higher interplanar distance due to F insertion in the WS_2 structure.

Thereafter, the thicknesses of WS-CF coatings were adjusted in order to be deposited over the dimple-shaped anodized surfaces and replicate their bottom roughness. Coatings of around 200 nm were also previously characterized over steel substrates, and fairly confirmed the performance reached for the respective thick coatings. However, the structural analysis showed the basal planes as preferential orientation due

to initial growth features typical for these based-coatings; and the F-doped coatings showed a slight oil contact angle increase, which was not observed for thick coatings.

In the end, hybrid structures (named as LD+WS2 and LD+WS-CF5) created by depositing thin (200 nm) WS-CF coatings over dimple-shaped anodized Al surfaces were evaluated in terms of friction performance and wettability behaviour. Tribological tests performed at room conditions without lubrication indicated that coated roughened surfaces had lower friction values, while for tests conducted in lubricated conditions with PAO-8 oil, the coated anodized surfaces had higher friction values than the non-coated ones. This feature was related with the roughness and mechanical properties of the contacting surfaces, being the surface free energy also important in the initial contact. In regard to the wettability behaviour of the hybrid surfaces, it was verified overall, that both the coating chemistry and surface roughness have effect on it. And further, the hydrophobic/oleophilic behaviour of LD+WS2 surface can have also potential for self-cleaning or oil-water separation purposes, whereas the hydrophilic/oleophilic behaviour of LD+WS-CF5 surface can have potential role on printing or microfluidic applications.

KEYWORDS: aluminum alloys, surface wettability, anodization process, WS_2 coatings, fluorine doping, magnetron sputtering, tribology.

LIST OF PUBLICATIONS

The work of this thesis resulted on 5 published/submitted papers listed below.

Published Papers:

The wettability and tribological behaviour of thin F-doped WS$_2$ films deposited by magnetron sputtering
<u>S. P. Rodrigues</u>, T. Polcar, S. Carvalho and A. Cavaleiro
Surface and Coatings Technology
https://doi.org/10.1016/j.surfcoat.2019.125033

Fluorine-carbon doping of WS-based coatings deposited by reactive magnetron sputtering for low friction purposes
<u>S. P. Rodrigues</u>, M. Evaristo, S. Carvalho and A. Cavaleiro
Applied Surface Science 445 (**2018**) 575-585

Water and oil wettability of anodized 6016 aluminum alloy surface
<u>S. P. Rodrigues</u>, C. F. Almeida Alves, A. Cavaleiro and S. Carvalho
Applied Surface Science 422 (**2017**) 430-442

Other publications in which the author has contributed with her thesis' work:

Nanoporous thin films obtained by oblique angle deposition of aluminum on porous surfaces
R. J. Santos, A. Chuvilin, E. Modin, <u>S. P. Rodrigues</u>, S. Carvalho and M. T. Vieira
Surface and Coatings Technology 347 (**2018**) 350-357

Submitted Paper:

Tribological performance of hybrid surfaces: dimple-shaped anodized Al alloy surfaces coated with WS-CF sputtered thin films
<u>S. P. Rodrigues</u>, S. Carvalho and A. Cavaleiro
International Journal of Advanced Manufacturing Technology

List of symbols and abbreviations

γ_{LV} – Liquid-Vapour surface tension

γ_{SL} – Solid-Liquid surface tension

γ_{SV} – Solid-Vapour surface tension

θ_W – Wenzel contact angle

AA – Aluminum Alloy

AAO – Anodic Aluminum Oxide

AFM – Atomic Force Microscopy

ASTM – American Society for Testing and Materials

CAH – Contact Angle Hysteresis

CEMMPRE – Centre for Mechanical Engineering, Materials and Processes

CFUM/UP – Centre of Physics of the Universities of Minho and Porto

COF – Coefficient of Friction

CTU – Czech Technical University

CVD – Chemical Vapour Deposition

DC – Direct Current

DLC – Diamond-Like Carbon

E – Young Modulus

EDS – Energy Dispersive X-ray Spectroscopy

EHDA – Electrohydrodynamic atomization

FAS – Fluoroalkylsilane

FET – Field-Effect Transistor

FIB – Focused Ion Beam

FWHM – Full Width at Half Maximum

H – Hardness

ICDD – International Centre for Diffraction Data

IPN – Instituto Pedro Nunes

LbL – "Layer-by-Layer"

L_c – Critical Load

LD – Large Dimple

LED&MAT – Laboratory for Wear, Testing and Materials

LT – Laser Technology

LUB – Lubrication

NA – Not Anodized

NPs – Nanoparticles

NT – Not Treated

OCA – Oil Contact Angle

OWRK – Owens-Wendt-Rabel-Kaelble

PECVD – Plasma Enhanced Chemical Vapour Deposition

PEG – Polyethylene Glycol

PFTE – Polytetrafluoroethylene

PLD – Physical Laser Deposition

PVD – Physical Vapour Deposition

PVDF – Polyvinylidene Fluoride

R_a – Average surface roughness

rf – radiofrequency

RH – Relative Humidity

RIE – Reactive Ion Etching

RT – Room Temperature

SD – Small Dimple

SE – Secondary Electrons

SEM – Scanning Electron Microscopy

SFE – Surface Free Energy

SP – Spreading Parameter

TMD – Transition Metal Dichalcogenide

WCA – Water Contact Angle

WD – Working Distance

WDS – Wavelength Dispersive Spectroscopy

XPS – X-ray Photoelectron Spectroscopy

XRD – X-ray Diffraction

Table of Contents

List of Figures

List of Tables

INTRODUCTION

The current technological and industrial development is more and more demanding for materials with outstanding properties that can yield better performance, sometimes with multifunctional abilities. In this sense, materials and surface engineering work together to achieve the best solutions for high performance components, focusing on cost-effective and eco-friendly production processes without losing the end product durability and functionality.

Tailoring the materials or their surface properties (e.g. electrical, mechanical, chemical, tribological, wetting, optical, etc) is the issue for any application. Particularly, the control of surface wettability, from superhydrophilic to superhydrophobic surfaces potentiates: 1) self-cleaning properties for windshields of automobiles, optical devices, medical devices (sterility by detaching the bacteria from the instrument surface), window glasses and solar panels; 2) anti-icing properties (e. g. protection of aerofoils, power transmission lines, pipes of air conditioners and refrigerators, radar or telecommunication antennas); 3) anti-corrosion; 4) hydrodynamic drag reduction; 5) anti-fogging and paintings; 6) liquid-repellent textiles; 7) anti-fouling and oil-water separation purposes for maritime and oil industries.

Particularly, the mechanical components' assemblage in the automobile industry requires constant devices' lubrication. The lubricant must be applied efficiently in order to avoid not only breakdown production on the assembly line due to maintenance and cleaning operations, but also to avoid the lubricant waste since it is hazardous to the environment and human health. So, the development of lubricative tools with self-cleaning characteristics addressing the homogeneous lubricant distribution would be welcome. Although, the surface must keep suitable mechanical resistance in order to reduce friction, and thus, the resultant wear due to the repetitive lubrication actions. Another important field is the production of grids/meshes or membranes for oil-water separation in the maritime industry when oil spills happen, or for water desalination or ionic separation in biological processes. These are applications where special surface wettability has to be tuned.

The surface wettability of metals generally encompasses the previous surface texturing/structuring (roughening) created by laser technology or anodization processes. Subsequently, these surfaces can be modified with polymeric low-energy coating application, which are commonly dotted with fluoralkilsilane radicals. Although, those

coatings often involve complex chemical reactions on their production and does not encourage its use when the application requires high mechanical solicitation.

Work Motivation

The use of metallic components has a huge impact in the world economy, particularly in the automotive and oil industries. For example, a big amount of mechanical components have to be previously lubricated daily before the final assemblage. In spite of the metallic lubricative tools with different shapes and in constant sliding movement, alternative solutions are needed to tune the surface wettability and friction in order to reduce or avoid the permanent grease lubrication. Another issue is the development of metallic meshes for oil-water separation processes as mentioned before. Thus, there is an urgent need to control water or oil surface repellence that can lead to reduced use of environmentally harmful lubricants. Simultaneously, it is desired to improve the mechanical performance of the metallic surfaces, decreasing the friction and the wear when in sliding contact.

The current surface modification methods mostly used to modify the surface properties of metals are the deposition of CVD or PVD coatings, laser texturing and anodization. The purpose of this study was to combine two methods addressing surfaces with different water or oil wettability, ensuring good mechanical and tribological performance.

Main Objectives

The overall aim of the present study is to combine different processing methods to modify Al alloy surfaces in order to get different wettability behaviour in regard to water and/or oils (hydro-oleo/philic-phobic character), which can be used in different applications. The methodology followed the existing expertise in the two host Institutions involved, the Universities of Minho and Coimbra. In the first, a surface treatment consisting on structuring/texturing by the anodization method was developed whereas, in the latter, the deposition of thin solid coatings/films produced by reactive magnetron sputtering technique allowed for the optimization of the intrinsic surface properties of an Al alloy surface (Al6016-T4). The partial objectives of the investigation were, therefore:

1- To understand the effect of the anodization parameters, such as the electrolyte and its concentration, the potential, the temperature and running time, on the pore size, geometry and its distribution over the anodic layer;

2- To correlate the achieved morphology/topography with the Al alloy surface wettability, namely on the hydro-oleo/philic-phobic behaviour;

3- To deposit WS_2-C based coatings with fluorine incorporation, in order to control the hydro-oleo/phobic-phillic characteristics, without compromising the mechanical resistance and self-lubricant properties of WS_2-C;

4- To understand the fluorine doping effect on the chemical composition, morphology, structure and tribological performance of the WS_2-C based coatings as a function of the sputtering deposition conditions;

5- To gather the best results achieved in both the physico-chemical surface treatments under anodization and the optimized fluorine-doped WS_2-C based coatings and combine them to optimize the final performance regarding the hydro-oleo/phobic-phillic surface behaviours and the tribological performance (hybrid system);

Thesis Outline

Apart from this introduction, this thesis is mainly based on a compilation of four scientific papers, three of them published in relevant journals of this research area and another that has only been submitted. Before their presentation, a state of the art in regard to: a) the surface wettability control and physico-chemical structured surfaces found in Nature and applications of hydro/oleo – phobic/phillic surface properties; b) the most used techniques to mimic/develop the structures presented in Nature, particularly, the anodization process as a micro/nano structuring method to control the surface roughness in Al-alloys and c) the low energy coatings deposited by magnetron sputtering technique with particular emphasis on the transition metal dichalcogenides materials and on the fluorine doping, is addressed in Chapter 1. Chapter 2 also describes the parameters controlled on the processing methods, anodization and magnetron sputtering, as well as the characterization techniques used for the surface and coatings' analysis. Chapter 3 presents the results on the anodization of the Al alloy surfaces. The development of the fluorine-doped WS_2-C by reactive magnetron sputtering is focused in Chapter 4, as well as their thickness optimization. The combination of the dimple-shaped anodized Al

surfaces with thin WS-CF films created hybrid-like structures which were evaluated in terms of wettability behaviour as well as in terms of tribological performance in dry and lubricated conditions, is depicted in Chapter 5. And the main conclusions of the whole work, and some future perspectives are presented in Chapter 6, before the Appendix section.

CHAPTER I
State of the Art

In this part of the thesis it is described an overview about the processing methods to reach different surface wettability behaviours in regard to water and oil. Furthermore, a summary about the Al anodization process to create different topographies in regard to surface wettability was followed. And in the end, there is the state of the art in relation to magnetron sputtered coatings deposited for increasing mechanical resistance and manage the surface wettability, with emphasis on the fluorine-doping of TMD-based materials.

1.1 Wettability

Wettability is a surface property that characterizes the degree of a liquid interaction with a solid surface. And, the level of liquid adhesion (affinity) to the surface is dependent on the surface roughness/topography and chemical composition [1-3].

Wettability in natural systems

The engineered methodologies used to modify the roughness and chemistry of surfaces, in order to control wettability, usually get inspiration from textures, structures and morphologies of particular plants and animals found in Nature [4-7]. For example, superhydrophobicity is found in the surface of the well-known *Lotus* leaves (*Nelumbo nucifera specie*) [8], which present water contact angles above 150°, ultra-low adhesion and remarkable self-cleaning properties; then, for achieving this behaviour, their unique dual micro-nano scale structure will be required in order to allow the rainfall to remove dust and particles easily, as shown in Figure 1.1 (a). Regarding superoleophobicity, the sharks' skin is superhydrophilic presenting an underwater oleophobic character (Figure 1.1 (b)).
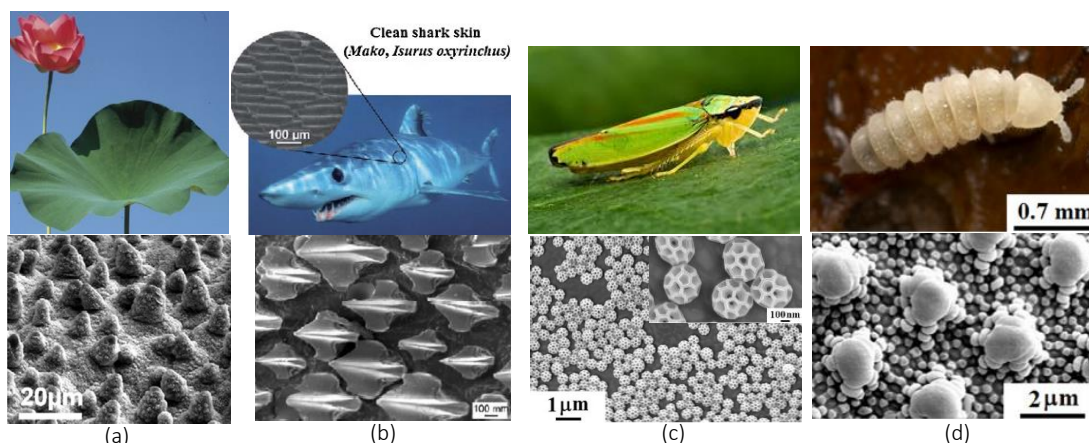
Figure 1.1 Structures of natural systems: (a) superhydrophobicity of *Lotus* Leaf [6]; (b) superoleophobicity in shark's skin [14]; (c) in spherical bronchosomes on Leafhoppers [9], (d) and on (d) springtails [11].

Leafhoppers are also reported as natural systems presenting superoleophobic properties (Figure 1.1 (c)) [9]. These insects have structured spherical particles covered with a hollow core (200-700 nm in diameter) in a honeycomb shape which presented re-entrant curvatures containing polar proteins on their composition responsible for the superoleophobicity. Despite the superoleophobicity, those structures are also able to repel water. Springtails (*Collembola specie*) have also been studied due their micro-nano

structures on the cuticle that showed superoleophobic and superhydrophobic behaviour (Figure 1.1 (d)) [10-13]. Their cuticle has a binary structure composed of three different layers, one inner layer made of a lamellar chitin skeleton with numerous pore channels, an epicuticular layer made of structural proteins such glycine, tyrosine and serine and, the topmost envelope, composed of lipids such as hydrocarbon acids and esters, steroids and terpenes.

Liquid interaction with solid surfaces

A simple qualitative method used to define the relative surface wettability relies on contact angle (CA) measurements. These measurements depend on the liquid surface tension, solid surface energy and their interaction. Figure 1.2 (a)-(c) schematically represents the three proposed wettability models that explain the liquid interaction with a solid substrate. According to the Young's wettability model [14], when a solid surface is perfectly smooth and chemically homogeneous, the measured contact angle (CA) (θ) of a liquid on a surface depends on the solid-vapour, solid-liquid and liquid-vapour surface tensions (see Figure 1.3), respectively represented as γ_{SV}, γ_{SL} and γ_{LV} in the equation below, known as Young's equation:

$$\cos\theta = \frac{(\gamma_{SV} - \gamma_{SL})}{\gamma_{LV}}. \hspace{3cm} \text{(Equation 1.1)}$$
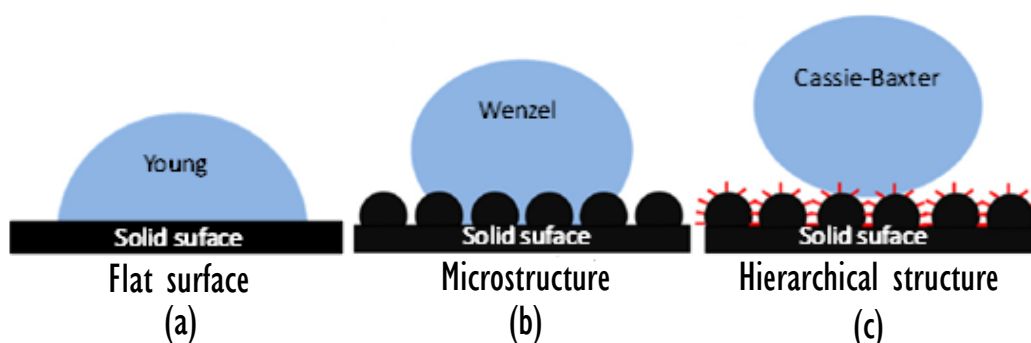
Figure 1.2 Schematic diagrams of the different wetting models: (a) Young's model; (b) Wenzel model and (c) Cassie-Baxter model. (*Adapted from* [15])
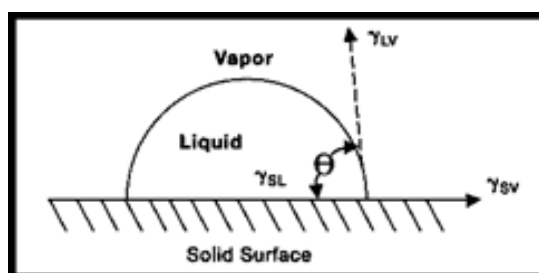
Figure 1.3 Representation of the physical interaction of a liquid droplet with a solid surface according to the Young model.

Thus, if the contact angle is below 90°, the solid surface is referred to as hydrophilic surface and if it is higher than 90° the surface becomes hydrophobic. In terms of surface energy, in a hydrophilic domain, the forces associated with the interaction of water with the surface (adhesive forces) are greater than the cohesive forces associated with the bulk liquid water. In a hydrophobic state, the cohesive forces between water molecules are larger than the adhesive forces to the surface. In the hydrophilic domain, when the CA is lower than 30°, the forces of interaction between water and the surface nearly equal the cohesive forces of bulk water and water does not cleanly drain from the surface. In the same way, when the CA is below 10°, the water spreads over the surface and the surface is often designed as superhydrophilic. For a hydrophobic behaviour, the water forms droplets on the surface and, if the contact angle is higher than 150°, the surface is termed as superhydrophobic. Regarding to superhydrophobic surfaces, the water adhesion level on the surface is often determined by dynamic contact angle measurements. In this methodology, a water droplet is made to roll down over a tilted surface and the angle formed at the front end of droplet motion is known as advancing angle and its back angle is known as the receding angle [16]. The difference between these two angles gives the contact angle hysteresis (CAH) value under the sliding angle.

When a surface is rough and chemically heterogeneous, the contact angle measurement is more complex. According to this, there are two models which explain the contact angle measurements, the Wenzel model [17, 18] and the Cassie-Baxter model [19], represented as (b) and (c), respectively, in Figure 1.2 above. In the Wenzel state, the water droplet can fill the rough surface structure and, as the roughness of a hydrophobic surface is increased turns it hydrophobic and the roughness increase on an hydrophilic surface still turns it with a hydrophilic character. So, the contact angle (θ_w) appears changed according to the equation:

$$\cos\theta_w = r\cos\theta, \hspace{4cm} \text{(Equation 1.2)}$$

where θ_w is the Wenzel contact angle, θ is the apparent contact angle when considering an ideal smooth surface and r is the surface roughness factor. The roughness factor (r) is dimensionless and is defined as the ratio of the real/actual solid surface area to the apparent projected area of a rough surface [20]. Above a certain roughness factor, the Wenzel state transits to the Cassie-Baxter model. Indeed, when dealing with dual scale (micro-nano) surface structure, the thermodynamically stable Wenzel model is not

satisfactory. The Cassie-Baxter, as metastable model, proposed that the liquid droplet sits on the top asperities. Due to that dual scale surface structure the air is supposed to be trapped in the rough structure underneath the liquid. As a result, the liquid and solid interface area is minimized and the water and air interface is maximized which gives a high water contact angle.

Surface free energy (SFE)

For complete understanding of both the physical interaction and adhesion properties of liquids with surfaces, contact angle measurements are thus important values for the determination of their surface free energy. It is commonly defined as the excess of energy at the surface of a material free to interact with the exterior, comparatively to the bulk surface. And, it is a result of intermolecular interactions at the interface which include non-polar (e.g van der Waals forces, London dispersive forces, Debye inductive forces) and polar contributions (e.g hydrogen bonding, dipole-dipole interactions). Then, taking into account the thermodynamic balance at the three phase contact of solid-liquid-vapour, Young described it in Equation 1.1 above, considering an ideal smooth surface. The SFE of a solid surface is described by using the contact angle (Θ), the liquid surface tension (γ_{LV}) and the interfacial tension between solid-liquid (γ_{SL}). Θ and γ_{LV} can be easily obtained but γ_{SL} cannot be measured directly which makes the SFE determination tricky. In order to solve the equation, many methods were developed to determine the SFE, having on their basis the equation of the work of adhesion from the thermodynamic equilibrium between interfaces ($W_{SL} = \gamma_{LV} + \gamma_{SV} - \gamma_{SL}$) and the Young equation. Then, all SFE formulations have on their basis the known Young-Dupré equation achieved for the work of adhesion [21-23]:

$$W_{SL} = \gamma_{LV}(1 + \cos\Theta). \hspace{4cm} \text{(Equation 1.3)}$$

All methods use different assumptions in relation to the relationship of the interfacial phase interactions and on the way of calculation [23].

The SFE calculation by the Van Oss-Chaudhury-Good method [24] considers the γ_{SV} divided into two components. One includes long-range interactions (called Lifshitz-van der Waals component - γ^{LW}), and other includes the acid-base interactions, defined as Lewis interactions (γ^{AB}) and based on electron-donor ($^+$) and electron-acceptor ($^-$) interactions or other polar interactions. And, they got the following relationship:

$$(\gamma_{SV}^{LW} \gamma_{LV}^{LW})^{0.5} + \left(\gamma_{SV}^{+} \gamma_{LV}^{-}\right)^{0.5} + \left(\gamma_{SV}^{-} \gamma_{LV}^{+}\right)^{0.5} = 0.5\gamma_{LV}(1 + cos\theta). \qquad \text{(Equation 1.4)}$$

This equation arrives at a system with three independent linear equations for calculation of three unknown surface tension entities (γ_{SV}^{LW}, γ_{SV}^{+} and γ_{SV}^{-}). That determination is achieved by measuring the contact angles formed with the solid surface using at least three different liquids with known properties (one polar and two non-polar). Notice that some values of the coefficients appearing in the equation system are tabled for several liquids [25]. This method has been widely used to determine the SFE of polymeric materials, enabling to give good information about the surface properties and better understanding on the interfacial acid-base interactions. However, it commonly brings many controversies due to its sensitivity to very small variations in the CA values or in the liquid properties, which can distort the solution or lead to inconsistences and wrong interpretation, being this method sometimes not appropriate for unequivocally analysis.

Furthermore, there are other approaches for determination of the SFE of a solid surface through CA measurements when using only two testing liquids. OWRK, Wu and Owens-Wendt are three methods that take similar assumptions using the Fowkes principle [26-28], differing among them only in the way of calculation of SFE of a solid surface [23, 29, 30]. The Fowkes formulation considers that the SFE of a solid (and the liquid surface tension) is a sum of independent components associated with the specific polar (P) and non-polar (D) interactions. But later on, Owens and Wendt developed a new definition about the polar component firstly defined by Fowkes and combining with the Young equation it reached to the known OWRK equation written as:

$$\sqrt{\gamma_{SV}^{D} \gamma_{LV}^{D}} + \sqrt{\gamma_{SV}^{P} \gamma_{LV}^{P}} = 0.5\gamma_{LV}(1 + cos\theta), \qquad \text{(Equation 1.5)}$$

where there are two unknowns, γ_{SV}^{D} and γ_{SV}^{P}, that can be easily obtained with the known non-polar and polar components of two testing liquids (e.g water, glycerol or formamide as polar ones and diiodomethane or α-bromonaphthalene as non-polar ones). This is the most frequently used model in the literature for SFE calculation, once it is mentioned as a suitable method for broad range of different materials. Despite that, a less accurate but more appropriate for surfaces with low surface energy, the Wu method also accepted the Owens-Wendt definition for the polar component of SFE, but instead of using a geometric mean, his method used the harmonic one, which combined with the Young equation led to the following relationship:

$$\left[\frac{\gamma_{SV}^{D}\gamma_{LV}^{D}}{\gamma_{SV}^{D}+\gamma_{LV}^{D}} + \frac{\gamma_{SV}^{P}\gamma_{LV}^{P}}{\gamma_{SV}^{P}+\gamma_{LV}^{P}}\right] = \frac{\gamma_{LV}(1+cos\theta)}{4}. \tag{Equation 1.6}$$

Besides all this, Zisman method determines the called critical SFE without taking into account the polar and non-polar components of the solid surface. It though considers the critical SFE as the liquid surface tension being in contact with the solid for which the contact angle is zero. In practice, it relies on the plotting of the cosine of contact angle (y axis) in function of the liquid surface tension (x axis), and the critical SFE corresponds to the x value where the line equation crosses y axis in cos(Θ) = 1. For better accuracy, more than two testing liquids are required, although this method is cited as not being commonly applied, giving incorrect or negative values, mainly because of insufficient theoretical justification and time-consuming investigation procedures.

1.2 Surface wettability control: processes

Metallic surfaces (e.g. steels, Al alloys, Ti) are intensively used in tooling, oil/maritime, automotive, aerospace and biomedical industries, reason why their surface treatment has attracted intense research to avoid waxes, oils, foulants, bacteria or other organic adhesion or corrosion effects. So, industrial community is often widely seeking for surface functionalities such as self-cleaning, anti-fouling, anti-fogging, anti-icing, self-lubricating, etc. The production of these multifunctional materials usually embraces the development of textures and/or coatings, which can address omniphobic (hydrophobic and oleophobic), hydrophobic/oleophilic or hydrophilic/oleophobic and hydrophilic-oleophilic behaviours [31, 32]. Therefore, either the creation of textured surfaces with controlled roughness at micro and/or nano scales or/and the deposition of coatings with intrinsic surface wettability characteristics suitable for water or oil contact have been studied [33-36]. It is also important that the processing methods ensure the surface robustness, which means that the surface must withstand high pressures contributing for a long term wetting and mechanical stability. In the next subsections, an overview on the reported studies about the manufacturing processes used for different surface wettability behaviours will be presented.

1.2.1 Hydrophobic and oleophobic (omniphobic) surfaces

A broad research on hydrophobic and/or oleophobic treatments encompasses the production of polymeric-based coatings which could be applicable on diverse substrates

(mostly glass or silicon), for self-cleaning, anti-icing, or anti-fouling for medical and transport applications. Oleophobic character is also necessary for anti-smudge applications for example on mobiles and touchscreens where it is desired to avoid the fingerprints. Some of these coatings were composed by cellulosic fibres, deposited by electrospinning, which could be later incorporated with SiO_2 or TiO_2 nanoparticles (NPs), which in turn were modified by fluoroalkylsilane (FAS) coatings [37-39]. This multistep approach allowed to produce a flexible coating. Sol-gel technique was also used to produce omniphobic organic-inorganic hybrid coating materials through complex chemical reactions with fluorine-based polymers, e.g. bifunctionalizing SiO_2 micro and nanospheres when polymerizing fluorine content polymers [40]. Electrospinning technique was used to deposit rice-shaped TiO_2 nano/mesostructures well-adhered on glass substrates and a post-processing salinization procedure promoted the omniphobicity of the surface [41]. However, these deposition methods were rarely applied on bulk metallic substrates. Moreover, the effectiveness and performance of these coatings under a tribological assay was understandably not demonstrated and they have poor mechanical durability.

Dip-coating processes have been applied to fabrics to produce oleophobic surfaces [42, 43]. Normally, the surfaces are coated with polymeric materials containing fluorine radicals which with posterior thermal annealing allow to tune the solid surface energy of the coated surface. The re-entrant textures of the initial fabrics were also revealed to be important to the switchable oleophobicity. Silicon substrates with silane treatments are also reported as showing superoleophobicity behaviour. Conducting polymers have also been electrodeposited with monomers having two fluorine radicals in order to achieve superoleophobicity [44]. A spray casting process was applied to a nanoparticle-polymer suspension in which the ZnO nanoparticles were functionalized with perfluoracrylic polymer emulsion and superoleophobic coatings were applied to different substrates without additional surface treatment.

Regarding metallic substrates, combination of chemical treatments consisting of anodization and fluorination was applied to aluminum plate substrates to create micro- and nano-scale structures [45]. Omniphobic behaviour was achieved if specific morphological features were produced. The good adhesion and suitable hardness of the modified layer proved the good mechanical endurance of the surface.

Laser technology was also widely used for texturing or structuring of metallic surfaces, not only for wettability control but also for enhancing the tribological behaviour.

By creating dimples or grooves, lubricant reservoirs are produced, helping to keep friction at low values for longer times [46-48]. Femtosecond or nanosecond laser technology has been applied on silicon and brass substrates [49]; platinum and titanium [50]; stainless steel [51, 52] and aluminum [53]; where micro-nanostructures were successfully created allowing to achieve a superhydrophobic behaviour. A different approach, using laser texturing added to FAS modification, was applied to CoCrMo alloys to increase their hydrophobicity and improve the biotribological performance [54].

Superoleophobic behaviour of titanium surfaces were also created using a combination of anodization with laser technology [55]. The laser technology promoted the micro-texturing on the Ti surfaces while the anodization rendered a TiO_2 nanotube array formation. After this first step, the hydrophobic surface was post-processed under UV radiation and thermal annealing allowing a switchable oil wettability. Two-step anodization of Ti foils also allowed to fabricate omniphobic surfaces, by controlling the morphology of the TiO_2 nanotube surface [56]. Anodized Al alloy surfaces were modified with lauric acid to reach a superhydrophobic surface [57].

1.2.2 Hydrophilic-oleophobic vs. hydrophobic-oleophilic surfaces

The surface tension of oils and organic compounds is much lower than that of water and so, this is the reason why oil contact angles (OCA) are always lower than the water ones (WCA) for the same solid surface [58]. So, the creation of a superoleophobic surface relies on the creation of a solid surface with a surface energy lower than that of the oil surface tension [59]. Therefore, hydrophilic-oleophobic surfaces should not be expected. However, a few recent studies already showed surprising results of this hydrophilic-oleophobic peculiar dual behaviour, in the preparation of membranes for oil-water separation at oil and maritime industries [60]. Indeed, it was verified an improvement of the separation efficiency of those membranes (once oleophilic separators or absorbent materials can quickly become fouled by oil needing cleaning or replacement). Under this application, polymeric substrates were coated with a monolayer of cationic amphiphilic fluoropolymers and, significantly higher hexadecane contact angle than WCA was found [61]. In another study, a nanometer-thick perfluorinated amphiphilic polymer with a polyethylene glycol (PEG) headgroup was covalently bonded to an isocyanate-modified silica surface and, again, the hexadecane CA was significantly higher than the water contact angle (WCA) [62]. Both these studies proposed that the amphiphilic

polymer molecule takes a conformation obliging that the perfluorinated segments stay on the very top of the monolayer surface repelling hexadecane, which results in a higher CA. They also speculated that water molecules, attracted to the subsurface with high surface tension, penetrate the perfluorinated layer, resulting in a lower WCA. Other authors developed a nanometer-thick amphiphilic perfluorpolyether polymer with two different endgroups (polar hydroxyl and nonpolar CF_3 endgroups) that was dip-coated on Si wafers, being more wettable to water than to oil, although it demonstrated that the hexadecane CA significantly decreases (from 54° to 20°) after 3 days [63].

The hydrophilic-oleophobic behaviour already developed for oil-water membrane preparation normally englobes a metallic mesh as a substrate that, in turn, can be coated with for example, zeolite films [64] or nanoparticle suspensions, containing fluorinated groups in their surface [65]. Switchable superhydrophobicity-superhydrophilicity and underwater superoleophobicity was obtained in stainless steel mesh films coated with ZnO nanorod array, which exhibited highly controlled separation efficiency for oil-water mixtures [66]. Copper mesh films modified with fluorinated radicals were also prepared [67]. More works are reported taking into account the hydrophilicity and underwater oleophobicity [68, 69]. The more recent work reported on this dual hydrophilic-oleophobic character for oil-water separation was produced in a single step, using a stainless steel mesh (0.16 mm wire diameter, 0.20 mm square holes), that was dip-coated with a copolymer fluorosurfactant complex solution [60]. In three different types of maleic anhydride copolymers aligned fluorinated alkyl chains were induced toward the air-solid interface, which retrieve a low surface energy characteristic and cause hydrophilicity in the near-surface region. Maximum OCA achieved was 80°. Similar study on this opposite surface concept was conducted using PVDF (polyvinylidene fluoride) as a matrix polymer to produce a hydrophilic-oleophobic membrane to resist to various organic and biofouling for potential water and wastewater treatment applications or reduce the microorganism attachment [70, 71].

The particular hydrophilic-oleophobic behaviour is usually achieved through the use of a fluorosurfactant [32]. As shown in Figure 1.4, it contains an inner high surface tension polar head group (**A**) and an outer low surface tension tail group (repels oils) (**B**) using electrostatic interactions with surface. Hydrophobic-oleophilic surfaces were developed on aluminum plates using fluoropolymer-based treatments for anti-icing goals

when a water non-sticking behaviour is desired such as in severe winters of certain geographical regions [72].
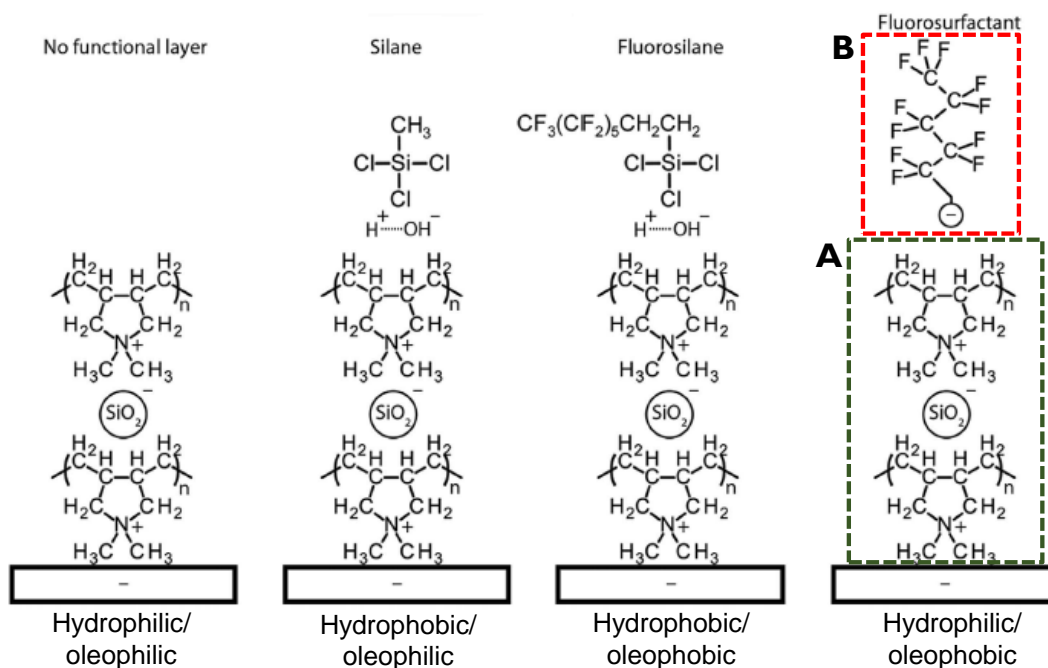
Figure 1.4 A representation of the "layer-by-layer" (LbL) composite coating (4 layers - fluorosurfactant) developed to achieve different water and oil surface repellence over a cationic polymer substrate [20] (*Adapted from*).

1.2.3 Hydrophilic-oleophilic surfaces

In the hydrophilic domain, the forces associated to the interaction of water with the surface (adhesive forces) are greater than the cohesive forces of the bulk liquid water. An anodized aluminum sheet alloy (AA1001) initially hydrophilic, turned into hydrophobic with time at air exposure. Afterwards, that surface was laser textured for printing applications to achieve a superhydrophilic behaviour presenting water contact angle below 10°, although it became again hydrophobic after 4-5 h time exposure to air [73].

Other authors [74], simply irradiated TiO_2-coated surfaces with UV light promoting photocatalytic oxidation and the surface became more hydrophilic. This type of wettability can be used in self-cleaning surfaces in outdoors exposed to rainfall, exterior tiles or other building materials like glasses and aluminum structures. Further, the photo-induced highly hydrophilic state can have anti-fogging function on eyeglasses or side-view mirrors in cars (as observed in Figure 1.5), since a thin layer of water is formed on the surface preventing fogging as water droplets.

Superhydrophilic surfaces were also developed for microfluidics application [75], using silica nanoparticles onto a patterned microchannels prepared by a LbL method which can contribute for blood plasma separation.
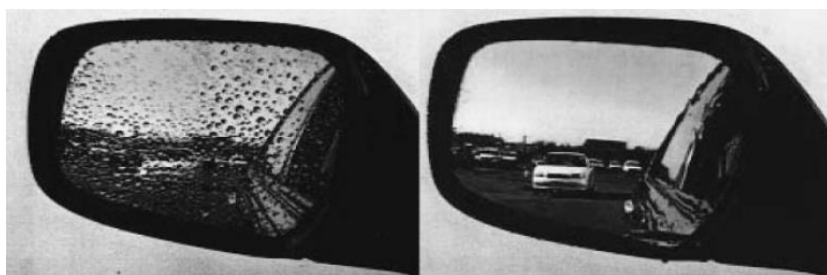
Figure 1.5 The representation of anti-fogging effect (right image) on car side-view mirror TiO_2 coated. (*From* [74])

1.3 Anodization process of Al surfaces

Due to simplicity, reliability, high controllability and low operation cost, anodization is an old powerful method for large-scale production [76]. Anodization process commonly uses a chemical attack to alter the surface of metallic materials which occurs by applying an electric current through two electrodes immersed in an electrolyte bath (typically acid or alkaline solution). The positive electrode (anode) holds the working sample to be treated that is intentionally distanced from the negative electrode (the cathode), this negative one usually made of platinum, graphite or stainless steel. The result of this electrochemical process is the creation of a protective anodic oxide layer, compact or porous, over the metallic surface (Al, Ti, Si, Ta, steels, etc).

Aluminum anodization allows the formation of aluminum oxide layers, also called "alumite". In the process, hydrogen evolves from the cathode whereas the alumina growth-dissolution occurs in the anode, both electrodes immersed in an electrolytic solution. The chemical attack can be performed in acid, neutral or alkaline solutions, although the last two are referred as creating a flat, non-porous, insulating compact aluminum oxide film. Only one study [77] reports on the comparison of phosphoric acid (H_3PO_4) to sodium hydroxide (NaOH) to create nanoporous Al_2O_3. Regarding NaOH performance, the disordered nanopores increased in size with pH, although alkaline solution revealed to be less effective than the acid in breaking down the oxide film; this is the reason why small pores were created. Indeed, acid solutions are widely reported to create porous anodic Al oxides with particular electronic, magnetic, optical and mechanical properties. Particularly, nanoporous anodic aluminum oxides (AAO) produced by anodization have found a huge range of industrial applications [78-80], such as catalysis

[81, 82], drug delivery [83], biosensing [84], template synthesis [78, 85], molecular and ion separation [86], corrosion resistance [87], surface colouring [88], tribological [89] and so forth.

In the literature, not only pure aluminum foils or sheets are anodized but also its alloys (e.g. AA1050, AA2024, AA5083, AA5754, AA6011, AA6061 and AA7075) have also been studied. For the latter, the process is trickier [90, 91]. In Al alloy anodization, the presence of alloying elements in either solid solution or second phases (precipitates, intermetallic compounds of various shapes, sizes and compositions) cause modifications in the anodic porous film growth. In fact, there exists a non-uniform flow of ionic current through the barrier film due to the different ionic resistivity of the different metal ions and the intermetallics such as Si, Mg, etc [92, 93].

The combination of surface chemistry and different topographies of the Al anodic layers has started to have special interest, not only from the mechanical resistance' point of view but also for surface wettability control of the final surface, despite their intrinsic hydrophilicity. The study of wetting properties of aluminum anodic oxide (AAO) surfaces is limited and most of the research is focused on their surface chemistry modification by using low surface energy materials (fluorine-silane treatments) [94]. However, the control of pore dimension itself can retrieve special wettability behaviour. On porous AAO, the contact angle is known to increase monotonically with pore diameter [95], at least up to a threshold value of porosity [57]. The anodization parameters such as temperature, applied voltage, electrolyte (acid) and its concentration have an important effect on the pore diameter and on the interpore distance. The most used acid solutions to create porous AAO are sulphuric acid (H_2SO_4), oxalic acid ($H_2C_2O_4$) and phosphoric acid (H_3PO_4) [96-98]. Usually, the pore ordering is enhanced by using a two-step anodization approach, in which the first anodization creates the pore template for the second anodization, after removing the anodic oxide layer formed in the first anodization. The anodic voltage has a major effect on both pore diameter and interpore distance [99]. The increase on the temperature can improve the anodic layer growth rate although creating disordered porous anodic alumina [100]. The current efficiency decreases with increasing temperatures due to the higher dissolution in the pore wall. Furthermore, the increase on the electrolyte concentration promotes a pore size increase.

Self-ordered pores with diameter below 100 nm are attainable with H_2SO_4 operating at range voltages 10-30 V or with $H_2C_2O_4$ operating at 40-60 V. If the potentials

are increased, no ordered pores are formed. Then, H_3PO_4 electrolyte permits anodizing at higher voltages (120-195 V) without excessive current flow and heat evolution [101], and further, as said before, higher potentials lead to the formation of porous anodic films with a large pore diameter near 500 nm [102-104]. Even if the pore size obtained with H_3PO_4 is larger than with $H_2C_2O_4$, its growth rate is reported to be slower [105]. Regarding to interpore distance, it increases linearly with H_3PO_4 voltage, reaching a possible maximum of 420 nm in 10 wt.% of H_3PO_4 at 160 V. Some authors [57] used a H_3PO_4 solution at 0 °C temperature with 10 wt.%, 5 wt.% and 1 wt.% acid concentration at 160, 175 and 195 V, respectively, to anodize an aluminum surface alloy (1050 foil) and have created some hydrophobic surfaces. In their two-step anodization method, structurally disordered AAO layers were produced with an average pore diameter of 140-190 nm and an interpore distance of 405 nm. After the pore widening process, pore size around 300 nm was achieved with a maximum WCA of 128°; for higher pore size the WCA starts decreasing. Furthermore, up to 6 µm of oxide layer thickness, the structure goes from slightly hydrophilic to moderately hydrophobic; for higher thickness, the WCA drops from 110° to 70°. A silane post-treatment was also applied and a WCA of 146° was reached (superhydrophobicity).

1.4 PVD coatings and wettability

As already mentioned above, the state of the art about wettability control mostly relies on using low energy coatings which involve functionalized fluoroalkyl modification (FAS) or silanization of NP oxides, such as TiO_2 and SiO_2, over a solid surface by complex chemical methods. This kind of coatings is not mechanically resistant and can hardly cover the surface uniformly to reduce the surface energy. So, even hybrid patterns with macro- micro- nano- porosity can be created onto metallic materials for wettability control; sometimes those structures are not suitable for a particular application requiring a good tribological performance. Then, the methodology would pass through the use of high strength films, which could tailor both the mechanical resistance and the surface energy, deposited by PVD or CVD processes [106, 107]. For example, associated with low surface energy, excellent mechanical properties were also achieved with Cr_2O_3 coating deposited by magnetron sputtering at high temperatures, but no oleophobic characteristics were observed [108].

1.4.1 Fluorine doping of PVD coatings

Regarding PVD techniques, magnetron sputtering is one of the most used to grow films industrially, with low substrate temperature, over large areas, with high deposition rates and without the need of post-deposition treatments. Although fluorine (F) doping has been quite used to enhance the optical, electrical and mechanical properties of materials, F-doped coatings deposited by PVD processing methods and their respective surface wettability behaviour has rarely been examined so far.

Metallic surfaces are often coated with diamond-like carbon (DLC) coatings due to their outstanding properties such as high hardness, high wear resistance, inertness, smoothness, corrosion resistance, low friction and intrinsic hydrophobic character. DLCs can then be doped with different elements, such as oxygen (O) or nitrogen (N), when a hydrophilic behaviour is required; or with fluorine (F) or silicon (Si) when a more hydrophobic surface is envisaged [109-113]. For example, when DLCs are modified with F, surface energies as low as 21 mJ/m^2 can be reached. Moreover, the friction coefficient of DLC coatings decreased with increasing WCA, i.e. when they become hydrophobic, even at very high sliding speed [114]. DLCs-F were also deposited on silicon substrates (film thicknesses ~0.3-1.9 μm) from a graphite target with a CH_4/CF_4 gas mixture by rf reactive sputtering [115]. The mechanical properties of these DLC-F films, such as hardness (H) and elastic modulus (E), did not change much when the CF_4 concentration was varied from 0 up to 50/60 vol. %, when using lower total pressures.

DC reactive magnetron sputtering was used to deposit F-doped tin oxide films on glass and quartz substrates with a Sn target under $Ar-O_2/CF_4$ gas mixture [116]. A maximum fluorine content of 8 at. % was reached; for low F concentrations (up to 3.4 at. %) both the charge carrier concentration and the mobility increased. ZnO films doped with F (FZO films) were rf sputtered deposited on glass substrates using a Ar/CF_4 gas mixture and a ZnO target to study the optical and electrical properties [117]. The increase of the CF_4 flow rate increased the F content in the ZnO films but the growth deposition rate decreased. For the same CF_4 flow rate (0.8 vol. %), the fluorine content was lower (1.72 at. %) in the films produced at 150 °C than at room temperature (7.36 at. %).

Fluorine doping has also been tried by reactive high power impulse magnetron sputtering (HiPIMS) using a pure graphite target. CF_x films were deposited on silicon substrates at 110 °C under an Ar/CF_4 gas mixture with CF_4 partial pressure varying from 0 up to 110 mPa [118]. HiPIMS has the advantage to increase the ion flux/atom ionization

in the plasma that increases the film density [119]. The increase of CF_4 partial pressure led to higher F contents in the CF_x film reaching a maximum value of 35 at. % at 80 mPa CF_4 partial pressure. Figure 1.6 presents the influence of the fluorine content on the mechanical properties (a) and on the deposition rate (b) as the CF_4 partial pressure is increased. Fluorine contents below 23 at. % give rise to amorphous films, while above 26 at. % the films have a polymeric-like structure based on C-F bonds.

CF_x films have also been deposited by HiPIMS on silicon substrates with different reactive atmospheres (Ar/CF_4 or Ar/C_4F_8) using a graphite target [120]. Generally, the increase of the fluorine content decreased the hardness of the films. In the Ar/CF_4 mixture, CF^{3+} and F^+ radicals are formed in the plasma which revealed to be useful to control the film surface wettability, especially when it is sputtered at high temperatures. Then, superhydrophobic CF_x films deposited on silicon surfaces with substrate temperature (Ts) of 430 °C and high CF_4 partial pressure, reached a WCA above 150°. When the F content exceeds 29 at. %, the CF_x films superhydrophobicity could be achieved but with a polymeric structure with hardness values below 1 GPa.
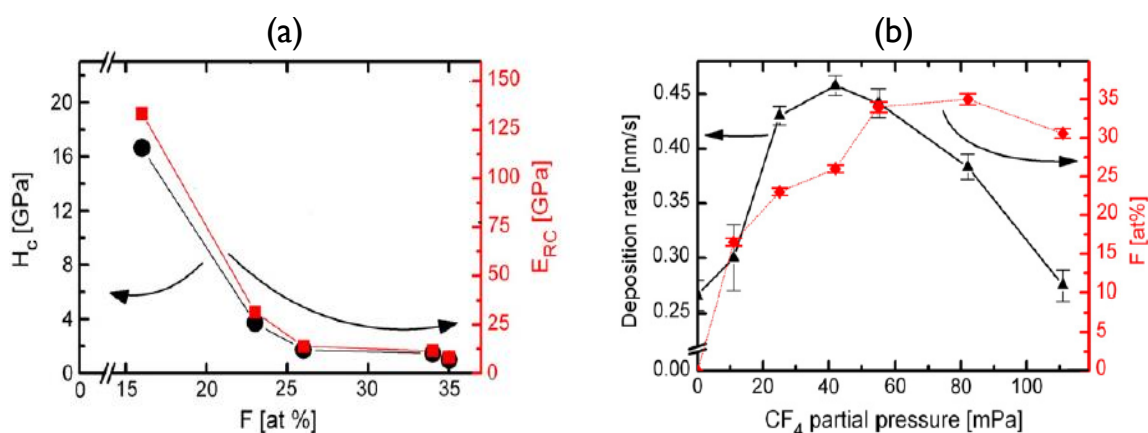
Figure 1.6 Mechanical properties, hardness and elastic modulus (a) and deposition rate (b) of CF_x films as a function of fluorine content. (*From* [101])

The fluorine insertion has been used to increase the friction properties of a-C films deposited by PECVD method [121]. The C-F bonds in a-C films form negatively charged surfaces which caused an electrostatic repulsion between sliding surfaces creating low adhesion and very low friction. The F-doping has been also used to control the refractive index of MgF_2 for photovoltaic applications and the fluorine depletion and magnesium oxidation allows a strong optical absorption [122]. In another study, CdS-F films were deposited by magnetron sputtering and the presence of F reduced the coating growth rate, increased the bandgap and reduced the refraction [123]. Apart from increased optical transparency, fluorine doped tin oxide (FTO) coatings deposited on glass

substrates by pulsed DC magnetron sputtering [124] in an environmentally friend way (no fluorine gas was used), showed an optimum F content of 5.3 at. % for highly decreasing the electrical resistivity.

Finally, F-DLC coatings deposited in a PECVD system showed that the fluorine doping resulted in greater suppression of platelet adhesion and activation, avoiding blood coagulation in medical devices [125]. Also, fluorinated films were obtained by magnetron sputtering using a PTFE target and hydrophobic surfaces were created [126]. The production of hydrophobic surfaces are widely required not only in biomedicine to reduce bacterial adhesion to implants, reduce clotting and fouling on cardiac stents, improve wound healing, but also in fabrics for advanced clothes, anti-sticking paints for buildings, in piping and boat bulls, self-cleaning windows, microfluidics and sensors, as referred before.

1.4.2 TMDs and wettability purposes

Pure TMDs consist of vertically stacked layers held together by relatively weak van der Waals forces and each layer is formed by covalently bonded transition metal (M) (e.g. W, Mo or Nb) to dichalcogenide atoms (S) (e.g. S, Se or Te) arranged in a hexagonal lattice [127], as Figure 1.7 represents. TMDs have trigged intensive research interest since they combine excellent electronic, optical, mechanical and magnetic properties, which make these materials potential candidates for a variety of applications [128, 129]. Although the considerable progress on the understanding of these properties of TMDs, the understanding of their wettability is very limited. In particular, when TMD-based surfaces are in contact with other materials, their behaviour strongly relies on their wettability and surface energy.

It is well-known that layered materials like TMDs preferably start their growth with the basal planes aligned parallel to the substrate surface, and further layers added up will form the horizontal stacked structure that contributes to surface energy minimization [130]. Although some studies have revealed that both MoS_2 and WS_2 layers are intrinsically mildly hydrophilic with WCA values of 70-80° [131], they face an aging effect due to spontaneous contamination by ambient hydrocarbons which turn them into hydrophobic. Indeed, some works reported a WCA value of 85° for sputtered MoS_2 [132], value in good agreement to that found for bulk MoS_2 [130]. The water wettability was studied for mono and few-layered WS_2 and MoS_2 films deposited on Si/SiO_2 substrates by a CVD

method [133]. The water contact angle increased as the number of layers increased from one to three reaching a stable WCA of 90°. For a hydrophilic WS$_2$ sheet (WCA = 70°),
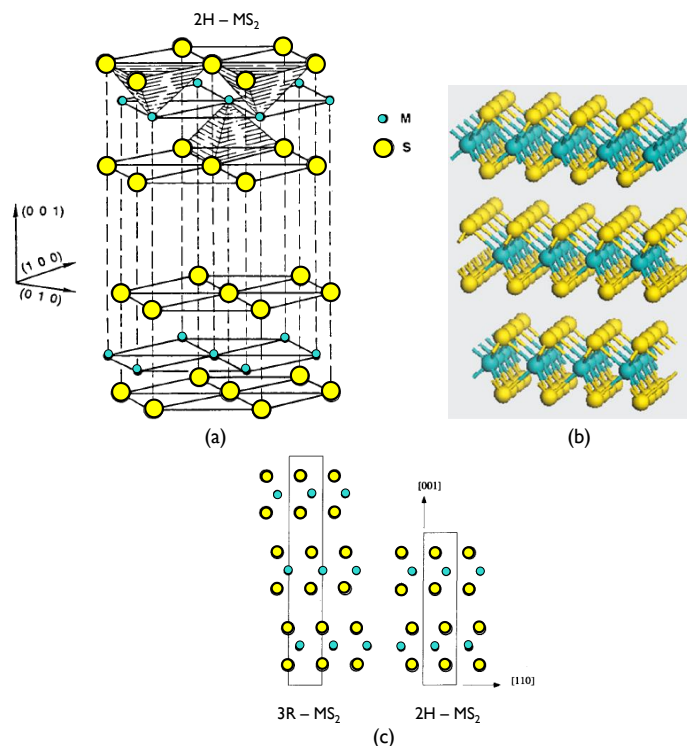
Figure 1.7 Representation of the crystalline structure of a MS$_2$: (a) molecular bonding (*Adapted from* [134]), (b) the stratification lamellar structure (*From* [135]) and (c) two possible crystalline structures (3R and 2H) (*Adapted from* [136].

after 7 days of aging, the WCA evolve for 83°. Likewise, MoS$_2$ films were synthesized at increasing temperatures, where WCA values of 24° for 500 °C and 92° for 900 °C were reached [130]. The temperature allows the diffusion of sulphur atoms through the film creating a well-ordered structure and, that way, no high energy edge binding sites exist for water interaction which would contribute to a hydrophobic character.

Usually, TMDs properties are tuned through the elemental chemical doping or by substitution of either the transition metal (M) or the chalcogenide (S). Then, structural defects are created [137] that can contribute to optimize the surface free energy, important property for many applications, particularly for improving the tribological performance of contacting surfaces.

Chloride (Cl) doping of WS$_2$ and MoS$_2$ has been studied to decrease the contact electrical resistance for high performance field-effect transistors (FETs) [138], whereas Pt nanoparticles were added to MoS$_2$ for photovoltaic applications [139]. MoS$_2$ coatings deposited at low temperature can be useful for microfluidic applications [130]. The sulphur substitution by oxygen in WS$_2$ or MoS$_2$ structure can be engineered to reach well-

controlled hydrophobic-hydrophilic patterns for water drop condensation [133]. Hydrophobic MoS_2 surfaces have been studied as biosensors for detection of biomolecules (e.g. PSA-prostate specific antigen) in order to diagnose prostate cancer [140]. The electrical properties of MoS_2 have also been used for environmental applications for Hg detection for monitoring mercury levels in drinking water [141]. In [142], the authors developed hierarchical MoS_2 wrinkled structures which created more hydrophilic surfaces inducing faster hydrogen gas detachment.

In relation to WS_2 and MoS_2, they have also been used as oil additives or as solid lubricants in dry air or vacuum due to their excellent self-lubricant characteristics. Magnetron sputtering is considered as one of the most effective methods for depositing TMD-based films for tribological applications. Pure sputtered TMDs exhibit low adhesion on standard substrate materials and high porosity. Therefore, their columnar morphology and porous structure strongly limit their ability to act as a self-lubricant coating in humid air or in presence of oxygen [143, 144], having the friction and wear rates increased [145]. Typically, pure TMDs have hardness below 1 GPa and a successful approach reported to improve the mechanical performance of these based coatings is to deposit a composite material combining self-lubricant materials with high strength materials, which can be reached alloying them with Cr [146] or Ti [147]. However, even though these metal-doped TMDs presented higher hardness, they continued to show high friction in humid environments. Then, when desiring good adhesion to the substrates, combining low friction with high-load bearing capacity, a new concept of coatings has been introduced based on the alloying of TMDs with carbon (C). The idea was to gather the excellent frictional behaviour of TMDs in vacuum and dry air with the tribological properties of the carbon matrix [148, 149].

The research group in the host institution of this thesis has developed a pioneering work on depositing WS_2-C films on silicon and steels (100Cr6 and M2 steels) by magnetron sputtering method using a carbon target with WS_2 pellets [150-152]. Films with hardness values around 8 GPa were deposited, presenting friction coefficient (COF) in humid air of about 0.07 (load ranging 5-48 N) against 100Cr6 steel balls as partners, although no studies were followed in regard to wettability behaviour. Furthermore, when the testing load and temperature increased, COF below 0.05 could be achieved. These excellent tribological properties and the low friction was attributed to the formation of a thin well-oriented tribolayer on the top of the wear track and on the counterpart surface,

responsible for decreasing the friction. Thanks to their thickness and parallel orientation, they are more resistant to the environmental attacks; the carbon in the sliding process is only secondary being its main role the increase of the coating mechanical strength and, thus, its wear resistance [153, 154]. Besides WS_2-C films, the teamwork further studied other TMD films alloyed with carbon, such as $MoSe_2$-C and MoS_2-C, synthesized on Si wafers [144, 155, 156]. Moreover, a tribological comparative study of WS_2-C and $MoSe_2$-C has been conducted and showed that $MoSe_2$-C coatings depicted lower COF than WS_2-C coatings in humid atmospheres, while WS_2-C presented higher hardness withstanding tribological tests at 1000 N load without premature failure [157]. A very recent work developed by the group engaged the production of WS_2 doped with N (WS_2-N) [158]. Tribological tests were performed under humid air (10% RH) and dry nitrogen (<1% RH) and the results revealed the achievement of an ultra-low friction coatings 2.3 µm thick, with hardness of 7.7 GPa, showing COF values below 0.003 when tested in dry nitrogen. Unfortunately, the coatings failed prematurely when tested in room conditions. Anyway, any of these last works studied the film surface wettability concerning to water or oil, which may be other world to explore.

1.4.3 Fluorine-doped TMDs

Fluorine (F) doping of pure TMDs has scarcely been explored, although F can have a role in the wettability control by reducing the surface energy of the materials. Therefore, only a couple of TMD-F studies were carried out until now. For example, the fluorine insertion has been used to decrease the friction of WS_2:CF coatings [159]. The tribological evaluation revealed that F-doped coatings deposited by PLD showed less sensitivity to moisture than pure WS_2, at least until 50-60% of RH, depicting ultralow friction in dry air (COF ≤ 0.01) against stainless steel balls. The F insertion in the WS_2 lattice was responsible for the interplanar basal distance increase with the consequent bonding energy decrease which, in turn, resulted in lower friction. However, no results were available concerning water or oil wettability behaviour. Likewise, WS_2 layers were deposited over a thick fluorine mica (FM) substrate for optoelectronic applications working as a high-performance saturable absorber for a fiber laser to operate in stable regime [160]. Another interesting work was the fluorine and nitrogen co-doping of MoS_2 nanosheets prepared via a hydrothermal method for hydrogen evolution reaction (HER) applications

[161]. The inert MoS_2 basal plane was activated through N and F co-doping which quite enhanced the HER activity compared to pure MoS_2 and N-doped MoS_2.

1.5 Partial Conclusions

In this chapter, it was shown that the current wettability control mainly relies on the development of low energy polymeric-based materials with fluorine or silane functionalized radicals or nanoparticles that can be deposited over surfaces for a wide range of applications. The production routes of these coatings often involve many steps and complex chemical reactions, requiring specialized reagents and equipment, usually unsuitable for many large-scale industrial applications. Furthermore, although different surface wettability behaviours can be reached (omniphobic, hydrophilic-oleophobic or hydrophobic-oleophilic), the polymeric-based nature of the coatings leads to poor mechanical resistance, which makes them less efficient for long-term mechanical contact or/and under high contact pressures.

Another important way to control the surface wettability is through the development of special roughness patterns on the surfaces. Anodization and laser technology (LT) have been reported as two powerful methods for texturing or structuring metallic surfaces, having some impact in both surface wettability and tribological performance. However, LT could be an expensive, time-consuming process over large areas and textures being able to only treat one component at a time. Then, even if it is not chemically clean, anodization is a simple, reproducible, inexpensive and scalable method for industrial application, which can be used for micro-nanostructuring of surfaces. Especially, Al anodization has already been used in combination with polymeric low energy coatings to create hydrophobic surfaces. However, the wettability evaluation of structures produced by anodization of Al alloys without an additional coating still does not exist, and no studies about the oil wettability has been followed so far. So, the water and oil wettability evaluation of anodized Al alloy surfaces is a challenge that makes part of the present thesis.

The aforementioned information highlighted the self-lubricating properties, good load-bearing capacity and aged hydrophobic nature of TMD-based materials. Although many methods have been used to deposit WS_2 or MoS_2 coatings to control the surface energy, the wettability of F-doped TMDs has never been studied, by our knowledge, especially when deposited by an environmental friendly magnetron sputtering method. Then, the study of F-doping TMD coatings for tribological application is worthy, as well

as their wettability behaviour since it can have a role in their tribological performance in lubricated conditions. Important to note that fluorine and/or silane dopings has been crucial to reach oleophobicity character on bulk metallic surfaces.

Hence, F-doped TMD coatings produced by magnetron sputtering is a field of research to be pursued; these coatings are good candidates to increase the mechanical resistance of roughened anodized Al alloy surfaces. This was this thesis' challenge: to create a hybrid system with tailored wettability with potential for a broad range of applications.

CHAPTER 2
Processing and Characterization Methods

This section provides complementar information and description in regard to the experimental details about the production processes used in this thesis: the anodization and magnetron sputtering. Additionally, a short description about each characterization technique and about the analysis procedure followed for the surface characterization of materials are also adressed. Detailed information in regard to SEM-EDS/WDS, XRD, XPS, AFM, contact angle measurements, 2D and 3D profilometry, Raman spectroscopy, pin-on-disc testing, *scratch* testing and nanoindentation characterization techniques will be described.

2.1 Processing Methods

Two different processing methods were combined in order to manage the surface wettability and friction performance of Al alloy surfaces. Although the anodization promotes changes on the surface chemistry, it was performed with the main purpose to get different surface topographies and roughness. Further, the magnetron sputtering was used to deposit self-lubricating WS_2-based coatings doped with fluorine and carbon in order to tune the final performance of the developed hybrid surfaces. Figure 2.1 clearly represents the proposed work methodology.
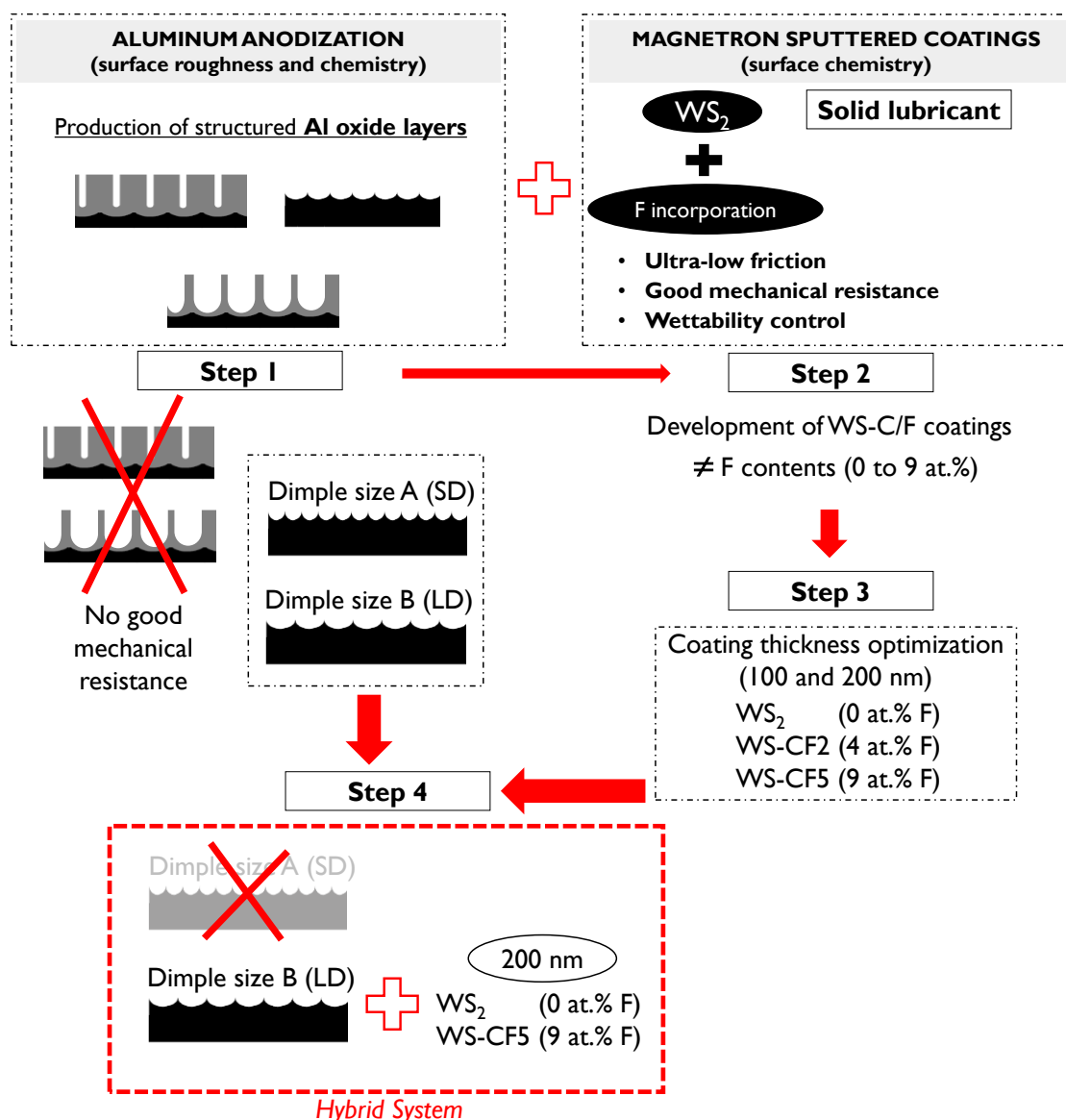
Figure 2.1 Illustration of the processing methods used in combination for optimization of surfaces with controlled surface wettability and friction performance.

2.1.1 Anodization

Anodization is an electrochemically activated process of metallic surfaces in a liquid solution. The oxide layer being thicker than the native oxide layer, can provide higher corrosion resistance of the metallic surfaces, for instances, against seawater environments [78]. Particularly, aluminum anodization is a widely spread process in industry and, depending on the anodizing conditions (mainly the electrolyte nature), a compact or porous-type oxide layer can be formed. According to this, acid electrolytes allow to reach porous-type topographies of anodic oxides on pure Al or Al alloy surfaces, with different surface properties (e.g. hardness, adhesion, electrical resistivity, etc) [162], quite interesting for several applications [80]. As mentioned before, the anodic oxide layer's properties are controlled by other parameters, such as the electrolyte concentration, the applied voltage, the duration and the temperature. The electrolyte must enable the ions (O^{2-} and OH^-) migration to the metallic surface (anode) to form the anodic oxide layer, which is potentiated by the electric field. The oxide layer thickness directly increases with the anodization time. Likewise, if the applied voltage is increased, promoting an increase on the current density (ionic species at the electrolyte/oxide and oxide/metal interfaces increases), it will also increase the anodization rate and interpore distance. Besides that, the temperature of the electrolyte is a parameter with impact in the pore diameter of porous oxide structures. For example, the increase of H_2SO_4 temperature from negative values (-8 to -1 °C) to 10 °C had increased the pore diameter of ordered Al oxide pores [163], although the increase was not that significant. The same behaviour was obtained for H_3PO_4 as anodizing electrolyte [164], although higher voltages have to be applied due to different electrical properties of H_3PO_4 in relation to H_2SO_4.

Commonly, the formation of well-ordered nanoporous anodic aluminum oxide (AAO) structures is made through a two-step anodization process at low temperature in acid solutions (such as sulphuric, phosphoric, oxalic, etc) [57, 165]. This means that there is a first anodization that creates a disordered porous oxide layer, which it will be submitted to a chemical etching for oxide removal. Then, a dimple-shaped Al surface is remained underneath and works as a template for the oxide growth in the second anodization where the pores will grow parallel and aligned. An extra etching can be performed if pore widening is desired. Figure 2.2 shows the pores formation through the dissolution mechanism assisted by electrical field of the anodization process in a two-step configuration.

Native oxide layer

Al

1st Anodization   Chemical Etching   2nd Anodization

① $Al_2O_3 + 6H^+_{(aq)} \rightarrow 2Al^{3+}_{(aq)} + 3H_2O$

② $Al \rightarrow Al^{3+}_{(ox)} + 3e^-$

③ $2Al^{3+}_{(ox)} + 3O^{2-}_{(ox)} \rightarrow Al_2O_3$

Al_2O_3

O^{2-}

$\vec{E}$

③ Al^{3+}

②

Al
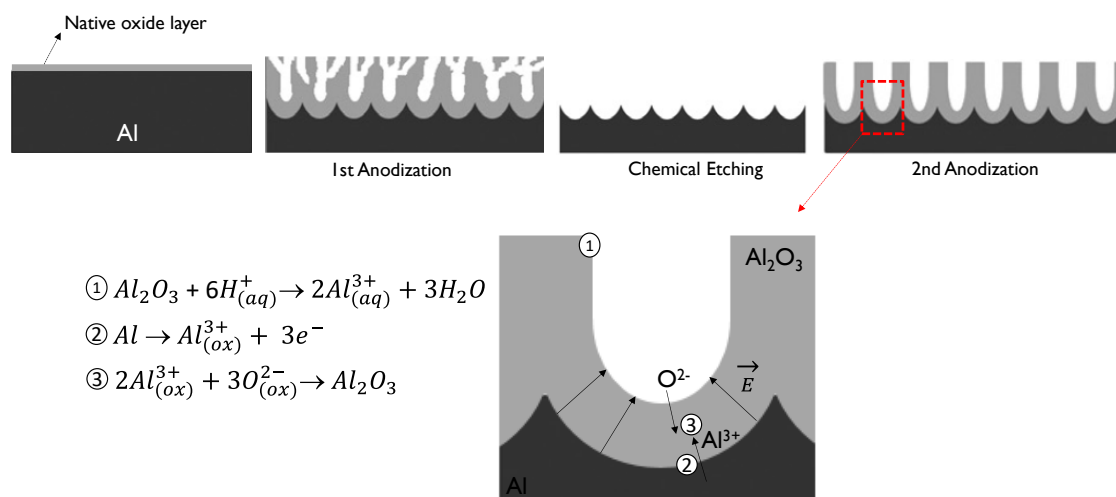
Figure 2.2 Schematic diagrams illustrating the changes of an Al substrate (anode) in two-step anodization under dissolution assisted by electrical field (E) mechanism. (*Adapted from* [80]) (Note: The radial behaviour of the electrical field justifies the circled shape of bottom dimples)

In this thesis, it was anodized a Mg-Si alloyed Al material (Al6016-T4) [166], which was previously polished (Polishing 1 and Polishing 2 in Figure 2.3) to remove the native oxide layer and after cleaned in three different chemical solutions. Afterwards, they were separately used two different acid electrolytes at different potentials (H_2SO_4: 15 V and H_3PO_4: 100 V) to anodize the Al alloy surface in one-step and two-step configurations. Figure 2.3 resumes the three phases of this stage for anodizing conditons optimization. The purpose was to get a set of different Al surface topographies with different surface roughness, which would have impact on the surface wettability. In a first approach, and considering only the optimization process, one Al sample was anodized using a *unisample anodizing system*. The system was assembled through a power supply and multimeter, and coupled to a computer for acquisition of current density over time. More details about the experimental procedure as well as about the discussion of the obtained results can be found in the next Chapter 3 of the thesis.

It should be pointed out that they were the wettability measurements with the SEM images that guided all the anodization optimization process, allowing to choose two surfaces to be coated with WS-CF coatings for the final hybrid structures. The study and characterization of those hybrid surfaces is appended in Chapter 5. In that section, there is also information about the new anodizing cell system for scale-up sample production, which allowed to anodize a maximum of 3 Al pieces at once.

PHASE 1

Mechanical Grinding

Al

Al – Polishing 1

Al – Polishing 2

Washed in Acetone and Ethanol
+
Chemical Etching in Acid solution with temperature

PHASE 2

Anodization – H_2SO_4

Potential: 15 V
Electrolyte concentration: 0.3 M and 1 M
Temperature: 15-18 °C

Configuration

ONE-STEP
ONE-STEP + ETCHING
TWO-STEP
TWO-STEP + ETCHING

PHASE 3

Anodization – H_3PO_4

Potential: 100 V
Electrolyte concentration: 0.5 M
Temperature: ~0 °C

Configuration

ONE-STEP + ETCHING
TWO-STEP
TWO-STEP + ETCHING

Figure 2.3 Resume of the three phases of Al alloy surface anodization for wettability optimization.

2.1.2 Magnetron Sputtering

Magnetron sputtering as a PVD method is widely used in industry and is based on the application of a magnetic field normal to an electric field between the cathode (target) and the anode (substrate holder) in an inert and high vacuum environment. In the generated plasma, electrons and non-reactive charged species (e.g. Ar^+, Ne^+ or He^+) are accelerated, being energetic enough to hit or bombard the target. Those collisions and momentum transference to the target promote the ejection or sputtering of atoms from it, which in turn will travel through the created plasma and will condense in the substrate. Then, the atoms undergo nucleation and coalescence phenomenon's leading to the coating growth.

A semi-industrial DC closed field unbalanced magnetron sputtering machine (TEER Coating Ltd.) provided with four cathodes water-cooled was used for the deposition and optimization of fluorine-carbon doped WS_2 coatings (see Figure 2.4). The cylindrical deposition chamber (~275 dm^3 volume capacity) made of stainless steel can hold four

targets (380x175x10 mm^3 size each) vertically aligned and oppositely pair-paralleled with a substrate holder placed in the centre at 30 cm facing the rectangular targets and put under rotation (20 rpm) (see Chapter 4 for details about the interior of PVD chamber). In this work, two WS$_2$ targets, one Cr target (when adhesion interlayer was added), were used with DC power supplies. Furthermore, there is a rotating shutter that allows the independent cleaning steps of the targets and substrates, avoiding contamination events. Important to notice that, as the substrate holder is not water-cooled; even without *bias* application during the deposition, the substrate bombardment by secondary electrons and other particles can cause re-sputtering events leading to substrate temperature increase, reaching ~120-130 °C.

Figure 2.4 Magnetron sputtering equipment used in this work for deposition of WS-CF coatings.

The vacuum system consists in two vacuum pumps, one rotatory pump (EDWARDS E2M80, 80 m^3/h) that ensures the primary vacuum, and one diffusion pump (EDWARDS DiffStak 160/200, 1500 l/s) responsible for the high vacuum. In the initial stage, the rotatory pump allows to reach a primary vacuum in the range of 10^{-1} Pa, which is enough to ensure the assistance to the diffusion pump in the deposition process itself. The diffusion pump allows to reach a base vacuum pressure in the range of 10^{-4} Pa. The

vacuum level is controlled inside the vacuum chamber through the use of two different pressure sensors. It is used a Barocel pressure sensor from Edwards to measure when pressure ranges from 0.01 to 100 Pa, while a wide range gauge (WRG-S-NW25 from Edwards) was used for low pressure recording (until 10^{-8} Pa). The substrate polarization was ensured by a DC Pinnacle Plus power supply and the cathodes were activated by a six exit MDX Pinnacle power supply which enables a maximum of 6000 W each.

Deposition procedure in a reactive mode

The development of the WS-CF coatings by magnetron sputtering relied on the use of two WS_2 targets, using an Ar/CF_4 gas mixture, in which some remarks should be taken into account in regard to the extremely reactive CF_4 gas. In this sense, it was of great importance to get very good level of base vacuum pressure and ensure the vacuum chamber has been properly thermally degassed. Because, F species can easily react with the adsorbed oxygen in the sputtering chamber, forming volatile species that are evacuated, and so, F is no longer available to be deposited in the coating. Moreover, F species can even be able to etch the metallic chamber walls, leading to possible oxygen detachment which will also be free to be bonded in the growing coating. WS_2 targets present high porosity which their proper sputter cleaning in an Ar discharge (with 35 mL/min of flow rate) prior to deposition is highly mandatory, in order to get rid of oxygen contaminations. Table 1 resumes some parameters about the etching steps before deposition.

Table 1 Parameters used for etching before the sputtering deposition using an Ar flow rate of 35 sccm.

	Power (W)	Pressure (Pa)	Substrate Bias (V)	Duration (min)
WS_2 – Target 1 and 2	1000 (each)		-600	10
Cr Target	2000	3.7×10^{-1}	-600	10
Substrate	-		-600	10

Before the coatings deposition, it was evaluated the voltage target evolution with the reactive gas (CF_4) partial pressure. Taking into account that the working pressure was kept constant, the Ar flow rate was decreased as the CF_4 flow rate was increased. It was verified that above 20 sccm of CF_4 flow rate, the vacuum system started to become very instable and the total pressure starts to increase.

Two sets of WS-CF coatings were deposited by reactive magnetron sputtering. The first set of thicker WS-CF coatings were deposited according to the depositing

conditions presented on Table 2. A second set of coatings (WS2, WS-CF2 and WS-CF5), based on the results achieved on the first set were deposited with lower thickness (~200 nm) on steel substrates (Chapter 4). Likewise, two thin coatings (WS2 and WS-CF5) demonstrated to be suitable to be deposited on the optimized textured Al alloy surfaces produced by anodization (Chapter 5).

Table 2 Thick WS-CF coatings deposited for 1h at a constant pressure of 4×10^{-1} Pa.

Coating Designation	Ar		CF_4	
	Flow rate (sccm)	Partial pressure (Pa)	Flow rate (sccm)	Partial pressure (Pa)
WS2	50	4×10^{-1}	-	
WS-CF2	50	3.80×10^{-1}	2	2.0×10^{-2}
WS-CF5	50	3.70×10^{-1}	5	3.0×10^{-2}
WS-CF7.5	48	3.65×10^{-1}	7.5	3.5×10^{-2}
WS-CF10	46	3.55×10^{-1}	10	4.5×10^{-2}
WS-CF15	40	3.45×10^{-1}	15	5.5×10^{-2}

2.2 Characterization tools

The anodized Al surfaces, the thick and thin WS-CF deposited coatings and, the combination of dimple-shaped anodized surfaces with the thin WS-CF coatings in hybrid structures, were analysed at different level through some surface characterization techniques. Table 3 summarizes the evaluated properties and the used correspondent

Table 3 Characterization techniques used for surface properties' evaluation.

Surface property	Characterization tool
Top-view Morphology Cross-section Morphology	Scanning Electron Microscopy (SEM)
Chemical Composition Chemical Bonding	Energy dispersive spectroscopy (EDS) Wavelength dispersive spectroscopy (WDS) X-ray photoelectron spectroscopy (XPS)
Structure and phase composition	X-ray diffraction (XRD) Raman spectroscopy
Surface Topography	Atomic force microscopy (AFM)
Surface wettability	Sessile drop method - Contact angle (CA)
Surface Roughness	2D profilometry
Hardness and Elastic Modulus	Nanoindentation
Adhesion	*Scratch* testing Optical Microscopy
Friction Tribological performance	Pin-on-disc testing Optical microscopy 2D and 3D profilometry

techniques. The chapter will focus on the base working principle of the technique and on informative experimental details.

2.2.1 Scanning Electron Microscopy

This characterization technique is widely used in surface engineering applications both in industry and academia. An electron beam generated by a heated metallic filament (e.g W), will pass through an electromagnetic lens system in the vertical column of the microscope. The electron beam is focused and aligned toward the sample surface (see Figure 2.5). The incidence of the electron beam over the surface will cause interactions such as elastic interactions with the atomic electrons and elastic collisions with the atomic nucleus. The result can be the ejection of secondary electrons (SE) from the sample, meaning that the elastic interaction with the electrons in the material promotes electronic transitions from higher energy levels, with consequent X-ray emission. If electrons are from deeper energy levels, the SE emission is weak and the collected signal fairly comes from the top surface layer giving only information about both morphology and topography. Likewise, the elastic collisions of the electron beam with the atomic nucleus contributes to the emission of backscattered electrons, which is influenced by the atomic number (Z) of the material in analysis. This latter emission can be important to get deep information about the atomic contrast.
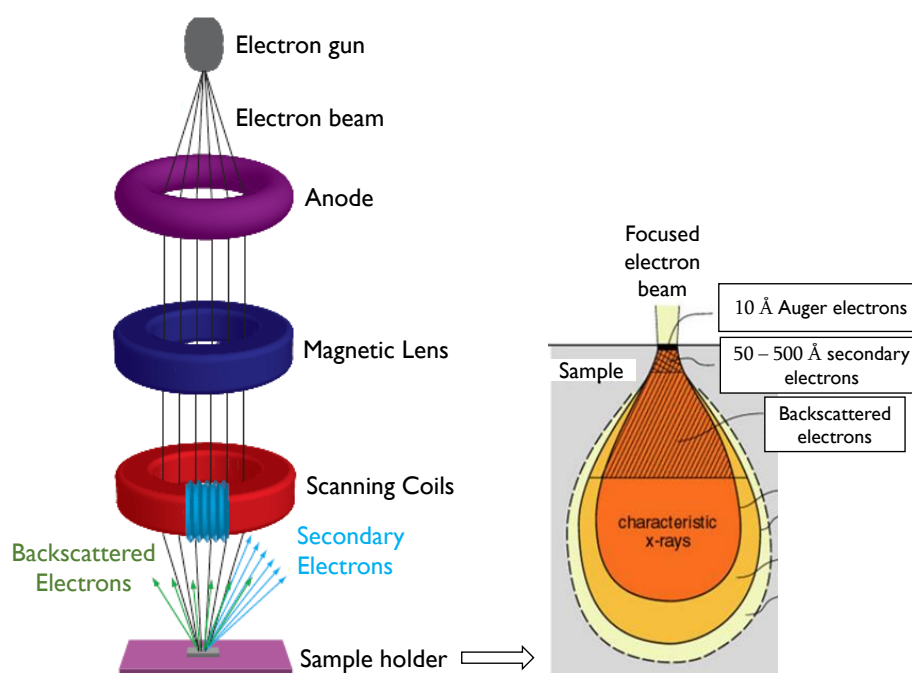
Figure 2.5 Schematic draw of the alignment and collimation processes of the electron beam through the vertical column in a SEM apparatus, until reaching the sample surface. (From [167])

SEM observation was extensively carried out in regard to anodic surface layer analysis. Before observation, the anodized Al surfaces were sputtered coated with a thin layer (5 nm) of Au-Pd (80/20) to improve sample conductivity and avoid charging effects. The anodic surface layer was characterized by a field emission SEM system (FEI Nova 200/Pegasus X4M) operating at 5 kV of acceleration voltage in SE mode, where top-view images of 200K and 100K magnification were recorded. Furthermore, the anodized Al samples were manually bended in order to expose their cross-section to get information about the oxide growth morphology and oxide thickness. Magnifications of 15K, 20K or 50K were recorded at 5 kV and with ~5 mm working distance (WD).

Both thick and thin WS-CF coatings were deposited on Si substrates for top-view and cross-section morphology assessment with a different SEM equipment (ZEISS Merlin – Field Emission Gun, High Resolution with Charge Compensation). The film thickness was also recorded by direct measurement of each SEM image obtained. Cross-sections images of 20K magnification were obtained with 2 kV while top-view images of 50K magnification were obtained at 4 kV. Moreover, after the tribological testing, the wear tracks of the thick WS-CF coatings deposited on M2 steel were also observed by SEM using 10 kV at low magnifications.

A first trial on the cross-section morphology analysis of thick WS-CF coatings deposited on porous anodized Al surfaces has also been done using a dual beam focused ion beam (FIB)-SEM system (Zeiss Auriga CrossBeam Workstation) operating at 30 kV/100pA for 30 min of sample milling.

Energy dispersive X-ray spectroscopy

Usually, the SEM equipment is able to identity the elemental composition from the sample through X-ray photons emitted from the surface after interaction with the electron beam. Characteristic X-rays are emitted whenever outer-shell electrons fill a vacancy in the inner shell of an atom, releasing X-rays in a pattern that is "characteristic" to each element. Qualitative analysis involves the identification of the lines in the spectrum. The relative intensity of an X-ray line is approximately proportional to the mass concentration of the element concerned. X-ray intensities are measured by an EDS detector.

This EDS method has been used to confirm the chemical composition of the anodized Al surfaces (using 5 keV) as well as to analyse the chemical composition of the

wear tracks (using 10 keV) after the tribological testing of thick WS-CF coatings. Figure 2.6 shows two EDS spectra obtained for a polished Al alloy surface (a) and for a porous Al oxide obtained by anodization (b), this latter showing evidence of electrolyte ions (SO_4^{2-}) incorporation in the grown oxide [168].
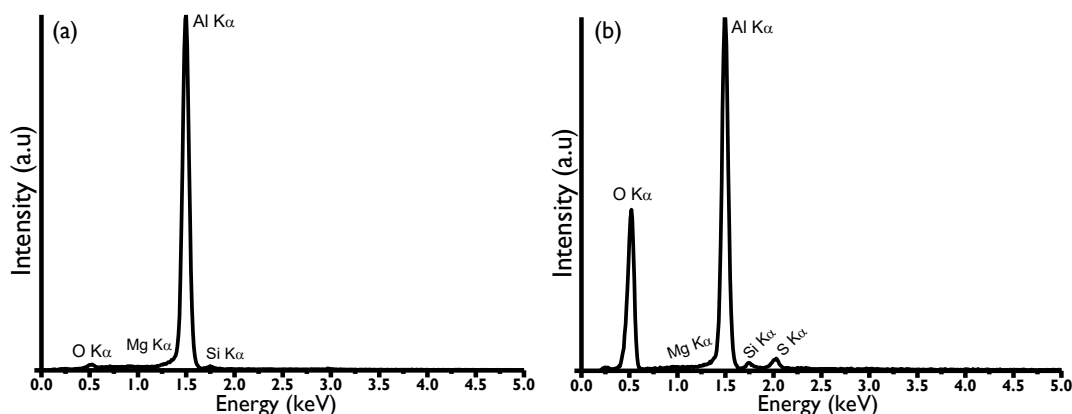
Figure 2.6 Example of an EDS spectrum obtained for: (a) a mirror-polished Al alloy and (b) a porous Al oxide obtained by a two-step anodization using H_2SO_4 as electrolyte.

Wavelength dispersive X-ray spectroscopy

Unlike EDS, the WDS can give a quantitative elemental analysis by sorting the X-rays based on each single wavelength at a time, and not producing a simultaneous spectrum of all energies or wavelengths. This means that this technique can be more time-consuming, but due to the higher spectral resolution and enhanced quantitative potential of the spectrometers, the problems of peak overlap, common for EDS, will be fewer. The WDS quantification usually requires standard reference materials, preferentially in concentrations similar to the materials to evaluate. And, the composition of the unknown sample is determined by comparing the intensities obtained for that sample with those from the standard. A special feature of WDS is also related with the much better performance that can be obtained for the analysis of light elements (e.g Be, B, C, N, O and F).

WDS methodology has then been used to get the elemental composition of the developed thick WS-CF coatings deposited on Si substrates, which has also been used later as well to confirm that quantification in the thin coatings deposited without interlayer. A WDS system (Oxford Instruments) coupled in the SEM equipment (Zeiss Merlin) was used at 10 kV acceleration voltage at 5 mm WD and 35° take off angle. The standard reference materials used for quantification were Cr K_α for Cr, FeS_2 K_α for S, W M_α for W, BaF_2 K_α for F, SiO_2 K_α for O and C K_α for C.

2.2.2 X-ray photoelectron spectroscopy

This surface characterization method is commonly used for identification of chemical elements (quantification too) and estimation of its chemical bonding state in a studied specimen. As Figure 2.7 illustrates, the incidence of monoenergetic X-rays on a surface in vacuum induces the electron excitation with consequent ejection of photoelectrons from the surface, which in turn, their kinetic energy will be collected and analysed (through the energy analyser). Then, the detector will measure the balance between the specific kinetic energy (E_k) of those emitted electrons with the energy of the X-ray source ($h\nu$). This relation is described in terms of the binding energy (E_B) of the atomic orbital from where the electrons were generated, and in terms of the work function (ϕ) of the analysed surface, as expressed in the Equation 2.1:

$$E_k = h\nu - E_B - \phi.$$
<div align="right">(Equation 2.1)</div>

The electrons on a specific orbital in a specific atom have their characteristic binding energy (E_B), and it is the evaluation of the energy of the photoelectrons that allows the identification of specific atoms in a material, as well as their chemical and bonding state. However, XPS analysis is unfortunately limited to 10 nm thickness below the surface, since due to collisions there are high energy losses of the photoelectrons coming from deeper layers.
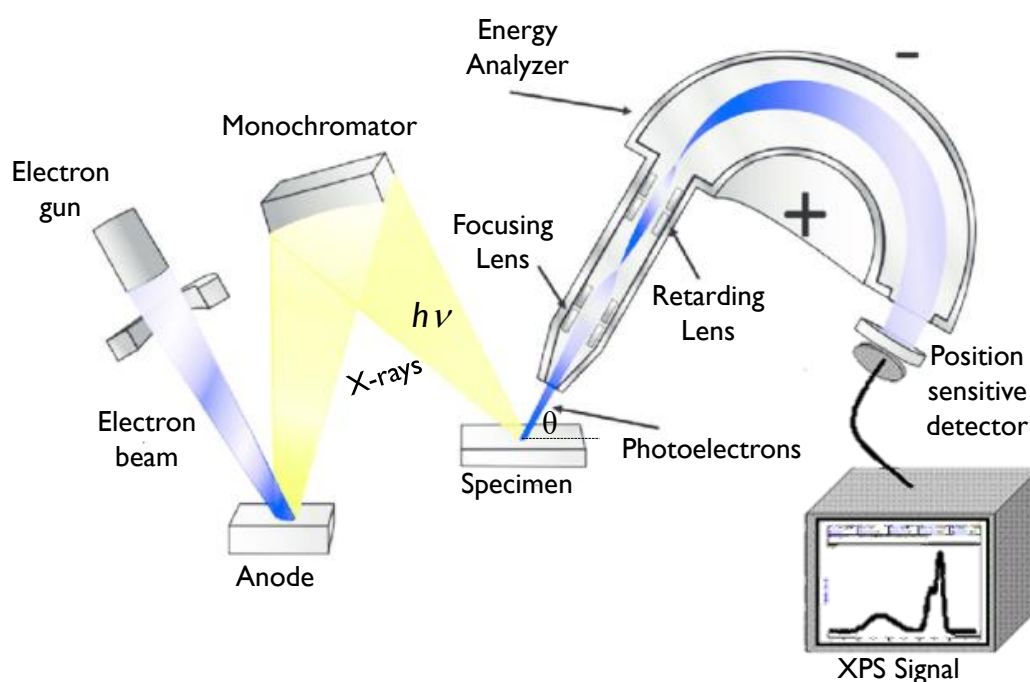
Figure 2.7 Schematic representation of the XPS signal acquisition. (*Adapted from* [169])

The chemical bonding of W, S and F elements in the thick WS-CF coatings was depicted by XPS analysis. It was used a Kratos AXIS Ultra HAS with a VISION software for data acquisition with vacuum base pressure 10^{-7} Pa. The analysis was carried out with a monochromatic Al K_α X-ray radiation source ($h\nu$ = 1486.7 eV), operating at 15 kV (90 W), in FAT mode (Fixed Analyzer Transmission), with a pass energy of 40 eV for regions ROI and 80 eV for survey. And, the photoelectrons were collected with a take-off angle of 45° from the horizontal plane of sample surface. Data acquisition has been followed with a pressure lower than 10^{-6} Pa using a charge neutralisation system.

Additionally, an Ar^+ ion etching step of 20 min duration (3 x 3 mm^2 area, 2.2 kV acceleration tension, 70 nA of emission current) was performed to remove the top layer surface contamination. These conditions took into consideration the literature information in regard to etching of WS-based coatings [170, 171]. This erosion step was not followed for pure WS_2 coating (WS2) due to possible huge vacuum chamber contamination.

The curve fitting of the XPS data was carried out with the *CasaXPS* software, considering the respective atomic relative sensitive factors and using a common Shirley background. However, the electrical charge effect was corrected by the reference of the oxygen peak at 531.0 eV [172], once our coatings have carbon on their composition.

2.2.3 X-ray diffraction

The crystalline nature of materials is often evaluated through the X-ray diffraction (XRD). When an energetic monochromatic X-ray beam bombards a crystalline materia (the atoms in a crystal are arranged in a periodic array with long-range order) with a certain angle of incidence (θ), a diffracted beam propagates only along constructive interference directions at specific angles - diffraction. Indeed, the constructive interference of the emitted beam occurs if the path difference (2d sin θ), which is dependent of the distance (d) between crystal planes, is a multiple (n) of the X-ray beam wavelength (λ), as Figure 2.8 represents. The data about the collected energy are then drawn in a diffractogramm (example in Figure 2.9) which plots the X-ray intensity on the y-axis versus the angle 2θ on the x-axis.
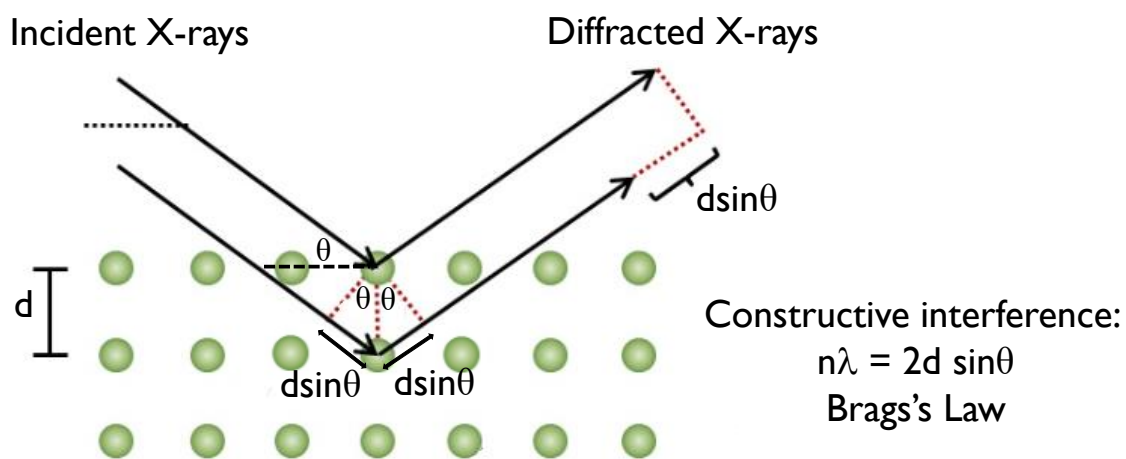
Figure 2.8 Schematic representation of the diffraction of a crystalline material. (From [173])

It was studied the crystal structure of the thick porous Al oxides produced by anodization using a XRD system Bruker D8 Discover, operating at 40 kV and 40 mA with a Cu radiation ($\lambda K_{\alpha 1}$= 0.1540600 nm) and ($\lambda K_{\alpha 2}$=0.1544339 nm) equipped with a collimator. The acquisition was performed in glancing angle configuration (5°) with step size 0.02° and 1s per step.

Likewise, the crystallographic nature of thick and thin WS-CF coatings deposited on glass by magnetron sputtering were also assessed. The XRD measurements were carried out on a PANalytical X'PERT Pro MPD system that also used a Cu Kα radiation (λ= 1.54 Å) (45 kV and 40 mA) in grazing angle (5° for thick coatings and 2° for thin coatings) in 10-80° 2θ range.
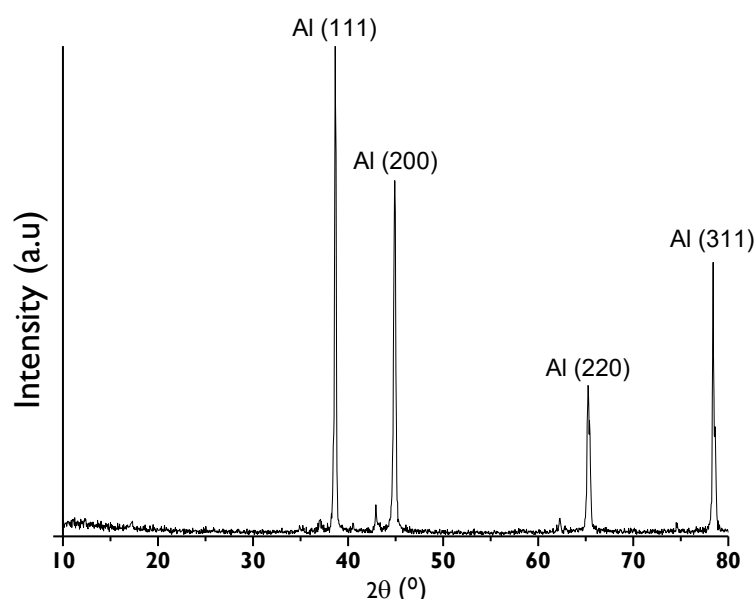
Figure 2.9 Diffractogramm obtained for a mechanical grinded Al alloy surface (until sandpaper grit size 1000) using 1° of glancing angle. Peak fitting was followed as well as the peak indexation with help of the ICCD database.

Lastly, the XRD evaluation (using 2° of glancing angle) of the hybrid surfaces (WS2 coating on a dimple anodized Al alloy surface) was also performed to verify if the coating structure was affected by the anodized surface underneath.

2.2.4 Raman spectroscopy

Raman spectroscopy is a fast and ideally non-destructive technique widely used to characterize the structural and electronic properties of nanomaterials through the identification of vibrational, rotational or even low frequency modes present in the molecules. This tool has been successfully used to characterize carbon materials such as diamond or graphene, with a recent impact on characterizing layered materials like TMDs. Raman spectroscopy is based on the inelastic scattering of a monochromatic light from a Raman-active sample.

When a monochromatic light interacts with a molecule, scattering mechanisms will be promoted. If the energy and frequency of the scattered photons are the same as those of the incident photons, the vibrational state of the molecule is unchanged and it is recognized as an elastic collision (Rayleigh scattering). Oppositely, if there is energy differences between the incident and the scattered photons, the collision is called inelastic. As a consequence, the vibrational energy of the molecule is changed and the molecule will be in an excited state for a short time before the photon scatters inelastically. Afterwards, the photon can be scattered with higher (Stokes lines) or lower (anti-Stokes lines) energy than the incident photon. Then, in order to be Raman-active, the molecule must get a change in polarization during interaction with the incident photons that has changed its vibrational state.

Raman spectroscopy is usually provided with a standard optical microscope, an excitation laser and monochromator, and a sensitive detector. The light beam hits the sample and the scattered light from the sample is collected. The elastic scattered radiation is immediately filtered out and the rest of the light collected is driven onto the detector. The Raman spectrum is a plot of the scattering intensity as a function of the frequency shifts (cm^{-1}), such as the one presented in Figure 2.10 for a WS$_2$ monolayer.

WS$_2$ is Raman-active and is characterized by three first-order modes, namely LA(M) localized at 176.0 cm^{-1}; E_{2g}^1 localized at 356.0 cm^{-1}, and A_{1g} localized at 417.5 cm^{-1}. However, for higher excitation wavelengths, it is remarkable the higher intensity of the second-order Raman peak (2LA(M)) mode localized at 352 cm^{-1}.
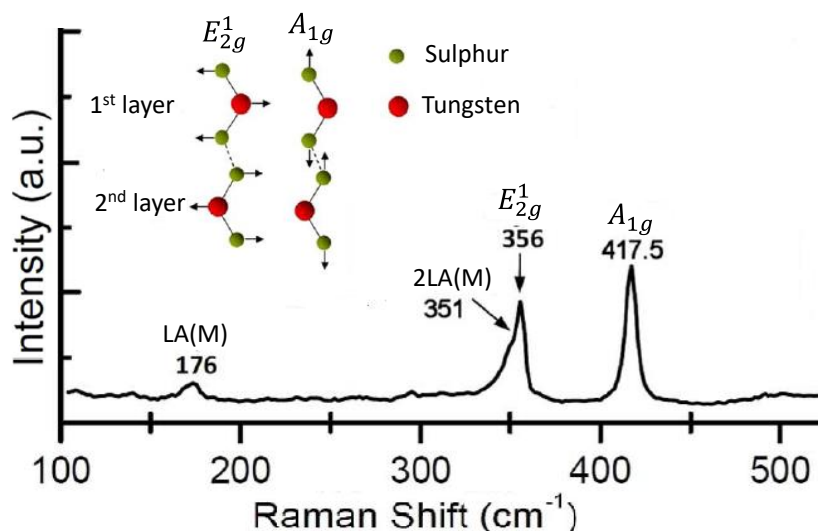
Figure 2.10 Raman spectra from a single WS_2 monolayer and representation of its vibrational modes when using a 488 nm laser excitation. (*Adapted from* [174])

Raman spectroscopy was mainly used in this work to verify the formation, or not, of the well-ordered TMD phase (WS_2) in the wear tracks after the tribological tests, comparing its intensity in relation to the as-deposited coatings. This study was conducted for the thick as well as for thin WS-CF coatings deposited on steel substrates. It was used a Horiba Raman System governed by a LabSpec software to get the Raman spectra when a green laser (λ = 532 nm) was used with 99 % laser power filtering for 20 min of spectrum acquisition time. Since, higher laser powers (or short laser wavelengths) have been reported to increase the probability to modify the structure and chemistry of these type of materials [175, 176], laser power was kept low to avoid build-up of carbon in the spot (sample burning) or even sample recrystallization or oxidation.

2.2.5 Atomic force microscopy

AFM is a powerful surface characterization technique that can analyse conductive and non-conductive surfaces in air, humid environments or liquids at a cost-effective way. Having very good vertical resolution (atomic resolution level), AFM gives information about the height and depth of the sample which mapping is commonly named as topography [177]. The measurement principle is based on the displacement of a cantilever-tip as it scans the roughness pattern of a solid surface. The distance between the surface and the tip generates attraction or repulsive forces resulting in deformation of the cantilever which is in turn measured by a photodetector (see Figure 2.11).
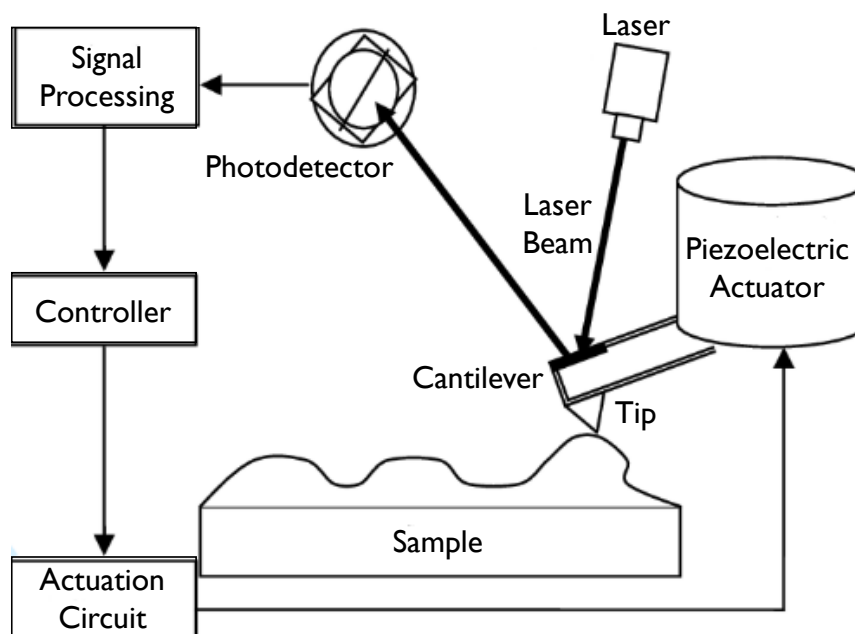
Figure 2.11 The working principle of an AFM equipment. (From [178])

Depending on the distance between the surface and the cantilever-tip, the AFM instrument can scan the surface in either contact mode or in tapping mode. In contact mode, the tip is in constant contact with the surface by application of a constant force, and this mode is more recommended to topographical analysis of smooth surfaces. Instead, in tapping mode the tip is oscillated at a known frequency at a certain distance from the surface and the cantilever deflection strongly depends on the attractive/repulsive forces. In this case, this is the appropriate mode to evaluate materials with high roughness once deformation on the asperities will be reduced. There is also the possibility of operating in non-contact mode but this mode has low resolution and the information can be highly influenced by surface contaminants (e.g. water droplets) which will mask the real topography.

The surface topographies of selected anodized Al samples, as well as of the thin WS-CF coatings deposited on glass and of the hybrid surfaces were collected. It was used an AFM system (Bruker Innova) mounted in a table damping platform placed in a controlled room environment. A silicon tip with nominal radius below 8 nm was used in tapping mode in case of anodized surfaces. However, for the thin coatings roughness measurements was used a contact mode scan. They were acquired scans of 2 x 2 μm^2 size in at least two different areas of the surfaces, with a scanning rate of 1 Hz. Afterwards, for depth profiles, an additional simple image processing was followed using the *Gwyddion* software.

2.2.6 Sessile drop method

Contact angle (CA) measurements are typically performed to qualitatively measure the wetting ability of surfaces. In case of static measurements, it is often followed the sessile drop analysis. In fact, when a liquid droplet is placed on top of a solid surface through a syringe, a camera will capture the image of the drop profile, as Figure 2.12 (a) shows. Then, an image analysis software uses the analysis of the solid/liquid/vapour interfaces of a sessile drop as Figure 2.12 (b) represents.
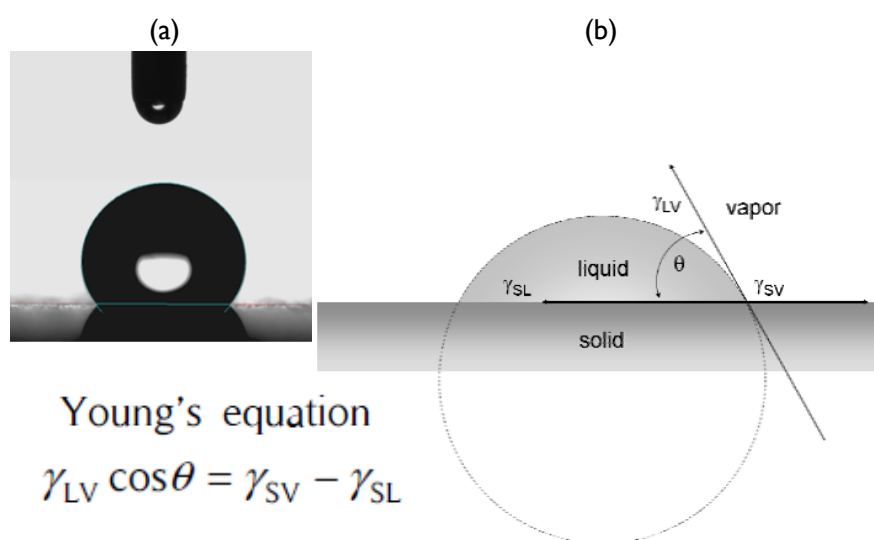
Figure 2.12 Representation of the contact angle measurement through the sessile drop analysis: (a) drop profile captured by a camera and (b) the involved solid/liquid/vapour interfacial quantities. (From [120])

Taking the information of the contact angle measurements, they help on the surface free energy (SFE) determination for complete surface wettability evaluation.

In this work, static CA measurements using the sessile drop method were widely conducted, as well as the surface free energy determination, once they easily give a first screen about the surface wettability. The CAs were obtained through a DataPhysics OCA Analysis system at a controlled room temperature (20 °C), applying a drop volume of 2 µL; at least 10 drops for statistical reliability, which were measured 2 sec after drop deposition. In case of anodized Al surfaces, they were carried out CA measurements with 3 different liquids (ultrapure water, α-bromonaphthalene and formamide) in order to determine the SFE using the Van Oss approach [23, 179-181].

Afterwards, the wettability of the thick and thin WS-CF coatings deposited on glass substrates were also evaluated. However, a third different test liquid was used (glycerol) for SFE determination, due to new laboratory regulations which forbidden

formamide usage because of its harmful potential. Then, due to superficial characteristics, the application of Van Oss approach for SFE determination was not valid, limiting a correct interpretation and the SFE was then determined using the simple OWRK/Fowkes model [29, 182, 183]. This method is often cited in the literature as giving intermediate quantitative results when compared to van Oss and Wu approaches, but qualitative results of all these methods are essentially the same. OWRK model was also followed for the wettability evaluation of the hybrid surfaces that resulted from the selected anodized Al surfaces with optimized thin WS-CF films.

2.2.7 Scratch Testing

The adhesion of the thick WS-CF coatings deposited on steel substrates was evaluated through the scratch testing (CSEM Revetest equipment), using a Rockwell indentor with a sphero-conical diamond stylus with tip radius of 0.2 mm (system shown in Figure 2.13). According to the ISO EN-1071-3, the stylus was slipped at a constant speed of 10 mm/min, loading rate of 100 N/min at a progressive load, until a maximum of 50 N.

The scratch test enables to determine failures on the coating itself (cohesive) as well as failures at interface coating-substrate (adhesive failure). The smallest load at which this failure appears is defined as the adhesive critical load (L_c), used to quantify the adhesive properties of coatings. An optical microscope (Leica DM4000 M LED microscope) was used to analyse and zoom the failures presented in the scratch track, for critical load determination through an *ImageJ* software.
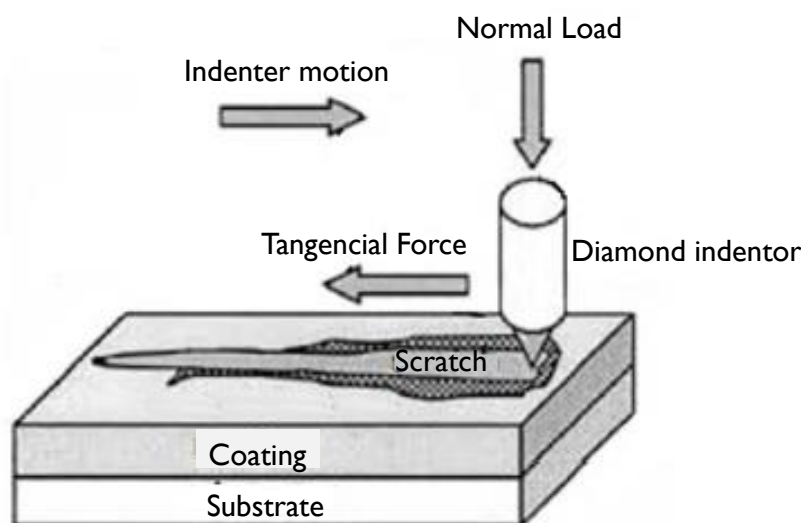
Figure 2.13 Illustration of a *scratch* testing performed under progressive load. (*Adapted from* [184])

2.2.8 Nanoindentation

Similarly to the adhesion testing, the determination of the hardness (H) and elastic modulus (E) was carried out on the thick WS-CF coatings. It was used a depth-sensing indentation equipment (MicroMaterialsNano Tester) using a Berkovich diamond pyramidal indentor. Nanoindentation allows to measure the hardness of a coating at a very shallow depth (ideally lower than 10-15% of film thickness), minimizing the substrate influence [185]. In order to fulfil this condition, preliminary essays were conducted with two different loads of indentation (3 mN and 5 mN) in order to evaluate the maximum depth indentation. Table 4 confirmed 3 mN as the most suitable load for hardness measurements. Furthermore, the indentation tester was leaning on a vibration damping table, and each experiment was carried out at room temperature (23 °C) using an loading/unloading rate of 0.17 mN/s, with a holding time at the maximum load of 30 seconds, and the results are an average from 16 measurements.

Then, the hardness (H) (resistance of a material to plastic deformation) evaluation relies on the recording of the penetration depth of the indentor (h) in function of the applied load (F). The data analysis was automatically made by the software program of the equipment, which already makes the corrections for the thermal drift, for the penetration depth at initial load and the DAF correction (diamond area function). The same program also allows to calculate the elastic modulus of each coating as well.

Table 4 The maximum depth penetration reached with 3 mN and 5 mN of indentation load applied on the coating surfaces.

Coating Designation	Coating Thickness (µm)	Indentation Load			
		3 mN		5 mN	
		Max Depth Penetration (nm)	% Thickness	Max Depth Penetration (nm)	% Thickness
WS2	1.88	691	35.8	1123	59.7
WS-CF2	1.50	135	9.0	247	15.5
WS-CF5	1.58	137	8.6	254	15.1
WS-CF7.5	1.47	126	8.6	225	15.3
WS-CF10	1.67	176	10.5	297	17.8
WS-CF15	1.32	173	13.1	589	44.6

2.2.9 Ball-on-disc testing

Tribology is a science that studies the friction and wear between two interacting surfaces in relative motion. Different tribological tests were conducted making use of two different rotational ball-on-disc tribometers (one homemade developed by the research group and the other was a CSM Instruments, both shown in Figure 2.14). Table 5 summarizes the conditions used for all the performed tribological tests.
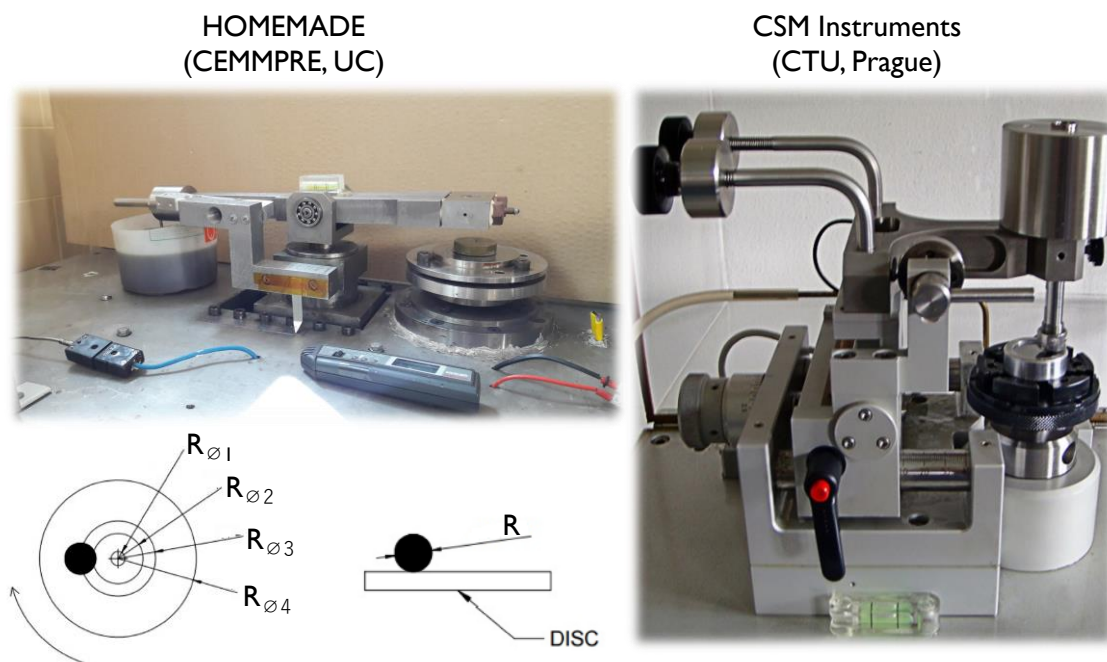
Figure 2.14 Configuration of the two ball-on-disc equipments used to perform the tribological behaviour of the coatings.

In relation to the thick WS-CF coatings deposited on disc-shaped M2 steel substrates (Set 1 in Table 5), the tribological tests were performed in air at room temperature (RT) (23°C) and at elevated temperature (200 °C), under a relative humidity (RH) of 35-40 %. Each sample was hold on a rotating disc (sliding radius of 7.5 mm) that was sliding with a constant speed (v = 0.1 m/s) against a stationary 100Cr6 steel ball of 10 mm of diameter used as counterpart loaded with 20 N for 10 000 cycles (distance of 500 m). The contact pressure was determined according to the method developed by Hertz, [186, 187] and was equal to ~700 MPa. The data acquisition system recorded the friction coefficient (COF) and the reported COF was the average value of the whole test. Furthermore, the samples and the balls were carefully cleaned in alcohol and dried before each tribological test.

Table 5 Experimental conditions used for ball-on-disc tests to evaluate the tribological behaviour in the three cases of contact. (Note: LD is the anodized Al surface textured with large dimple)

			Load (N)	v (m/s)	Distance (m)	Environment
Set 1 (Chapter 4.1)	THICK Coatings	WS2	20		500	Dry: RT Dry: 200 °C
		WS-CF2				
		WS-CF5				
Set 2 (Chapter 4.3)	THIN Coatings	WS2_200	5	0.1	50	Dry: RT Lubricated: RT
		WS-CF5_200				
Set 3 (Chapter 5)	HYBRID Surfaces	WS2_200 + LD	5		15	Dry: RT Lubricated: RT
		WS-CF5_200 + LD				

The tribological tests of Set 2 (subchapter 4.3) and Set 3 (Chapter 5) were followed in dry and lubricated conditions, using the tribometer from CSM Instruments, and under the same RH as before. The lubricant used was a synthetic oil polyalphaolefin, the PAO-Grade 8 (ρ = 0.8 g/cm^3, kinematic viscosities calculated according to ASTM D 445: ν (40 °C) = 48.5 mm^2/s and ν (100 °C) = 7.9 mm^2/s).

All tribological tests followed for Set 2 and Set 3 used a 100Cr6 steel ball with 6 mm diameter as sliding counterpart loaded with 5 N (~700 MPa Hertzian contact pressure). The coated mirror-polished steel substrates and the coated anodized Al surfaces (LD) (coatings of ~200 nm thickness) were tested at a linear speed of 0.1 m/s, whereas the number of laps carried out for Set 2 and Set 3 were equivalent to 50 m and 15 m of sliding distance, respectively. It is known that the friction coefficient is the ratio between the friction force and the normal force (μ = F/L) [188], and the COF values reported here were the average value of each sliding test in the steady-state regime.

After the tribological tests, the wear tracks obtained for the thick WS-CF coatings (Set 1) as well as their respective worn ball scars were observed by SEM, and their chemical composition was also obtained by EDS analysis. In order to calculate the wear volume of the balls, images of the worn scars were obtained in an optical microscope. Afterwards, *ImageJ* software was used to get many measurements of the diameters (*d*) and calculate the average value. And, considering the worn ball representation in Figure 2.15, the *d* average value could give the worn spherical cap height (*h*) (Equation A in Figure 2.15), that contributed to the wear volume (V_{ball}) calculation (Equation B in Figure 2.15) according to the ASTM standards [187, 189].

Equation A: $h = R_{ball} - (R_{ball}^2 - \dfrac{d^2}{4})^{1/2}$

Equation B: $V_{ball} = \dfrac{\pi h}{6}(\dfrac{3}{4}d^2 + h^2)$
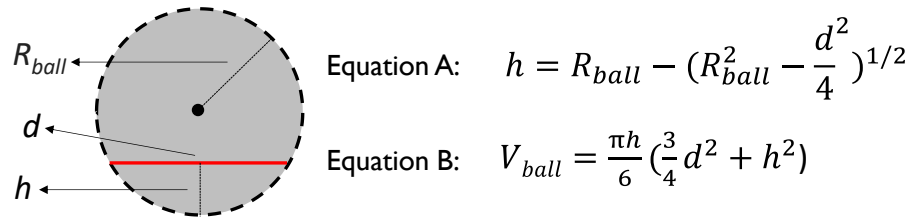
Figure 2.15 Schematic representation of a worn ball scar.

Thereafter, the specific wear rate (k_{ball}) was easily obtained by the following expression 2.3:

$$k_{ball} = \frac{V_{ball}}{S \, x \, L}\left(\frac{m^3}{N}.m\right), \qquad\qquad \text{(Equation 2.3)}$$

where S is the total running distance of the ball over the disc (equal to $2\pi R n$, with R the sliding radius and n the number of laps), and L the applied load.

Similarly, a 2D optical profilometer (Mahr Perthometer S4P) was used to get the depth profile of the wear tracks for Set 1, for at least three different zones of the wear tracks. Then, accurate average values of the sectional areas (A) of each wear track was obtained using the help of *AxioVision* software. And, the coating wear volume (V_{disc}) resulted by multiplying the average sectional area (A) of the track by the perimeter of the wear track ($2\pi R$). Finally, the specific wear rate for the coating (k_{disc}) is again easily obtained by the expression 2.4 below:

$$k_{disc} = \frac{A \, x \, 2\pi R}{S \, x \, L} = \frac{V_{disc}}{S \, x \, L}\left(\frac{m^3}{N}.m\right). \qquad\qquad \text{(Equation 2.4)}$$

The same procedure was performed for the acquisition of the profiles of wear tracks in case of coatings of Set 2 and Set 3, although a 3D profilometer (ZYGO) was used instead. Those 3D profiles were treated in a *MetroPro* software and, in case the ball hasn't reached the substrate, it was calculated the sectional areas from 2D profiles through *AxioVision* for specific wear rate calculations further on.

An important remark and challenge was to understand the friction behaviour in lubricated regime. However, it has been reported that friction behaviour is better correlated with a spreading parameter (*SP*) [182, 183, 190], at least in high lubricated systems. This parameter takes into account the polar and non-polar components of the surface free energy of both the solid and liquid. And, its value can be determined through the following formula in Equation 2.5:

$$SP = 2\left[\sqrt{\gamma_S^D \gamma_L^D} + \sqrt{\gamma_S^P \gamma_L^P} - \gamma_L\right], \qquad \text{(Equation 2.5)}$$

where, γ_S^D is the dispersive component of surface energy, γ_L^D is the dispersive component of liquid surface tension, γ_L is the total liquid surface tension, γ_S^P is the polar component of surface energy and γ_L^P is the polar component of liquid surface tension.

The *SP* can tell about the affinity degree of the lubricant oils with a solid surface, what means the possibility of the oil to create, or not, strong bonding with the surface. If so, that feature will hinder the oil spreading over the surface with consequent impact in the friction performance. Then, low *SP* values mean the oil has low affinity for the surface and it will form a constant contact angle immediately after reaching a surface due to adhesion-wetting behaviour, contributing to good lubrication degree inside the contact and so, to the friction reduction. This knowledge was suggested and taken into account to discuss the results obtained in lubricated regime in this thesis.

CHAPTER 3
Surface Texturing by Anodization

This chapter is focused on the roughness modification of an aluminum alloy surface through the use of an anodization process in order to reach different water/oil wettability behaviour. Firstly, details about the substrate pre-treatment and the anodizing conditions will be provided. Then, the results regarding the morphology, chemical composition, structure and wettability behaviour of the modified structures wil be presented and discussed. This work has been conducted in the University of Minho in the Centre of Physics of the Universities of Minho and Porto (CFUM/UP).
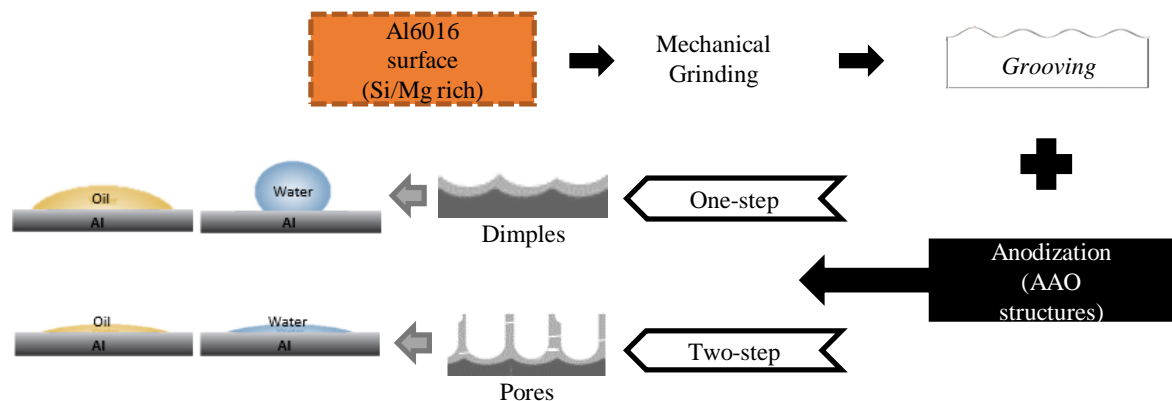
Chapter overview

The first objective in this thesis was to texture the Al surface with different surface roughness and study its impact on the water/oil surface wettability. As a starting point, it was mainly verified over the literature that the Al anodization allowed to reach porous oxide structures with different pore sizes, interpore distance and oxide thicknesses. Besides the very rare reported works on the wettability evaluation of those oxide structures, it was found that the pore diameter influenced the water surface wettability. Likewise, just a couple of recent works have reported on wettability measurements concerning the oil affinity of anodized Al surfaces. However, most of them focused on pure Al surfaces and/or undergone additional fluorination treatments. Despite this, it was possible to build up a set of anodizing conditions as well as complementary information about surface pre-treatments that was the starting point for the developed study. The focus would be always to reach different textures or different pore diameters in order to reach completely different water/oil surface wettability: hydrophilic-oleophobic, hydrophobic-oleophilic, hydrophobic-oleophobic, hydrophilic-oleophilic.

Based on the collected information, two electrolytes were selected to get ordered porous oxide growth; the H_2SO_4 for pores of lower size and H_3PO_4 for pores with higher size. During the experimental development some adjustments were considered since the reported conditions were applied to pure or low-alloyed Al surfaces. In fact, this work deals with a high-alloyed Al surface (Al6016-T4). SEM morphological characterization of surfaces was highly used to optimize the anodizing conditions. Furthermore, it was studied the oxide removal after the first anodization, using different etching times until reaching a dimple-shaped anodized Al surfaces, which were also used for comparison. This study results in 5 different aluminum oxide surface topographies which conducted to different wettability behaviours against water and oil. Two of them were dimple-shaped with different diameters (~30 and ~220 nm), and the other 3 were porous Al oxides with different pore diameter (~30, ~200 and ~250 nm).

This part of the work including sample preparation, anodizing steps, contact angle measurements, and the analysis and interpretation of the surface characterization results were drawn in a scientific article which is already published in Applied Surface Science journal (IF = 4.3).

3.1 Introduction

Aluminum (Al) and its alloys are important industrial materials because of their low weight, good corrosion resistance and machinability which make this material very versatile in the automotive and aerospace industries [166, 191]. Moreover, when high strength aluminum is required, 6000 series aluminum alloys (rich in Si and Mg) are the most commonly used because they are easily heat treated reaching a suitable intermetallic precipitates distribution allowing to achieve the desired mechanical properties. The creation of special wettability behaviours on aluminum surfaces would significantly widen their range of applications to fields such as tribology, biosensing, filtration or corrosion, addressing particular functionalities such as anti-wear, self-cleaning, anti-fouling, anti-icing, anti-greasing, etc [31, 192, 193].

Wettability is a surface property that characterizes the degree of liquid interaction with a solid surface. In practice, the control of surface wettability is inspired in features found in natural surfaces such as *lotus* leaves, cicada wings or water strider legs [6]. Indeed, the production of artificial surfaces repellent to water (hydrophobic) or oils (oleophobic) relies on various fabrication processes which are able to modify not only the surface roughness or topography (creating micro-nano or hierarchical scales) but can also change its surface chemistry (lowering the surface energy) as well as create re-entrant and overhang structures [2, 3, 194-196].

Considering the roughness factor with an homogeneous surface chemistry, the wettability of a flat solid surface was firstly described by Young's model [14] as a surface property represented by the liquid contact angle (CA) at the point of intersection between the three phases of solid-liquid-vapour. That contact point is dependent on the liquid surface tension, the surface free energy of the solid surface and their interaction. According to this, the liquid dispensed on a flat surface will spread over the surface minimizing the surface energy until thermodynamic equilibrium is reached.

In the other hand, when roughness is added to the flat surface the wetting properties are amplified and that factor is described by Wenzel and Cassie-Baxter models. In Wenzel model [17], the liquid invades the rough structures and comes fully into contact with the solid's surface. And, if the liquid CA on the respective flat surface is < 90°, the roughening of that surface will enhance liquid spreading while for liquid CA > 90° that roughness enhances surface repellence towards the liquid, both multiplied by the magnitude of surface roughness. In the model described by Cassie-Baxter [19], a more

complex rough solid surface is considered where air pockets could exist trapped between the gaps. Then, the wettability is a function of the liquid CA on that respective flat surface and of the solid's fraction area in contact with the liquid on its top. In this model, if the liquid CA of the respective flat surface is < 90°, the introduction of this complex roughness would increase the liquid CA on that surface. The transition from Wenzel to Cassie-Baxter occurs when the liquid CA on flat surface becomes > 90°.

The oil wets solid surfaces coated even with the lowest known surface energy materials, showing CA < 90° while the same surface can show hydrophobic behaviour. Indeed, oils or low surface tension liquids (< 50 mN/m) have weak cohesion forces and they are easily overcome by the adhesion forces at the liquid-solid interface and then often presenting CA < 90° on flat surfaces, this is the reason why it is a major challenge to obtain oleophobic surfaces.

On this regard, surface modification gained special attention over the recent decades due to their potential to manipulate the interaction between the liquid and the surface in order to improve materials' functionality. Laser technology is among the fabrication processes used to create superhydrophobic or/and superoleophobic metallic surfaces through micro/nanostructuring by creation of periodic dimples or grooves [50, 197, 198]. However, this methodology is costly, time-consuming, allowing to texture only one sample at a time which makes difficult this technique for industrial implementation. Anodization arises as an alternative method available which enables the growth (bottom-up process) of structured metallic oxide layers (ceramic behaviour) on surfaces allowing the modification of metallic surface wettability. In the meanwhile it can provide metallic surfaces with high corrosion and mechanical resistances [78, 89, 199]. Furthermore, anodization is a widely attractive electrochemical process once it is highly reproducible, cost-effective and reliable with easy industrial scalability [200] and, further, with a highly well-developed line of effluent treatments.

In case of aluminum anodization, there is the formation of an anodic aluminum oxide (AAO) (Al_2O_3) in which the structural morphology depends on the chemical nature of the electrolyte used in the electrochemical bath [201, 202]. Then, in neutral electrolytes, such as borates or oxalates, compact or dense aluminum oxides are formed besides the porous-type oxide formed when acidic electrolytes, such as sulphuric, oxalic, phosphoric, citric, tartaric, etc, are used [77, 203]. Note that, porous aluminum oxides have also been grown under alkaline solutions (pH = 9, 11 or 13), such as NaOH, although

more anodizing time is required due to low rate of oxide dissolution [77]. Conventionally, the production of highly ordered porous AAO is mostly performed in a two-step anodizing configuration [168], where the voltage, temperature, duration, electrolyte nature and concentration are the parameters to be controlled. In the first anodization, the grown oxide yields disordered pores and a wet chemical etching (usually a phosphoric and chromic acid solution [204, 205]) is applied for oxide removal which generates a periodic concave pattern on the aluminum surface. This pattern is a template ready for the second anodization that is typically conducted with the same conditions as the first one, leading to the growth of parallel ordered pores which in turn are aligned normal to the oxide surface plane.

Over the literature, there is a huge amount of works mainly reporting on AAO produced by anodization for improved corrosion resistance. However, even though the anodization produces oxides that makes the original surface intrinsically hydrophilic-like, the number of reported studies englobing the surface wettability having AAO structures in its composition is very limited. Depending on the conditions used, the anodization process allows to obtain different porous surface arrangements of aluminum oxides, often denominated as surface micro-nanostructuring, having an important role on tuning surface wettability properties. As known, the applied voltage is an anodizing parameter that controls the pore size diameter being its range dependent on electrolyte conductivity. Typically, in aluminum mild anodization, sulphuric acid (H_2SO_4) is used at 10-25 V voltage range allowing to achieve pore size diameters of 10-80 nm, while oxalic acid ($H_2C_2O_4$) is used at 30-60 V to get 80-150 nm pore sizes and phosphoric acid (H_3PO_4) is used at 160-195 V for getting pore sizes greater than 150 nm [206]. However, the wettability of anodized Al surfaces were mainly studied regarding to water, with just few reports referring to wettability in relation to other liquids such as oils. Al surfaces were anodized using H_3PO_4 electrolyte at different potentials and a pore widening process was used for reaching intrinsic hydrophobic porous AAO with water contact angles (WCA) of 128°, which turns into superhydrophobic (WCA >150°) by surface modification with a silane low energy coating [57]. Hierarchical aluminum surface roughness was achieved by using a chemical etching-anodization-pore widening process which, with further fluoralkyl coating to reduce surface energy, demonstrated to be superoleophobic [207-209]. In regard to water repellence, superhydrophobic Al surfaces have been engineered by combining a pillar-on-pore hybrid nanostructure, produced under a simple one-step

anodization process, with a hydrophobic perfluorsilane monolayer coating [94]. Other authors showed that porous AAO changed from hydrophilic to hydrophobic by increasing the pore diameter (260 nm) keeping the interpore distance and pore depth constant [95].

Resuming, the studies of water and oil wettability of AAO surface structures were mostly focused on the development of superhydrophobic or/and superoleophobic surface behaviours enhanced by the deposition of low energy coatings. However, those coatings are polymeric-based commonly produced by complex chemical reaction routes and their mechanical resistance under high loads will be hindered. Moreover, all the wettability studies were performed on porous anodic aluminum oxides grown only from pure or low-alloyed aluminum surfaces. Any wettability study regarding porous AAO obtained by anodization of 6000 series Al alloy surfaces has never been conducted. Thus, taking into account specific mechanical applications, such as lubrication procedures, a wear resistant metallic surface, combined with a specific non-common wettability behaviour like hydrophilic-oleophobic, is sometimes required which can simultaneously promote a self-cleaning and anti-greasy behaviour. It is now challenging in this work to provide a further insight on the water and oil wettability performance of porous aluminum oxide structures obtained only by the anodization of a Si-Mg-rich Al alloy surface.

The aim of this work was to use the anodization process combined with a prior polishing step in order to get different surface morphologies on a 6016-T4 Al alloy surface which in turn could give different surface wettability behaviours. Taking this into account and gathering all the information in the recent literature, tests were performed with two of the most used electrolytes to produce porous aluminum oxide surfaces, H_2SO_4 and H_3PO_4. Two different approaches were conducted, one using H_2SO_4 electrolyte, which is known to create porous structures at low voltages giving smaller pore size (10-50 nm range), and the other using H_3PO_4 electrolyte which allows to operate at higher voltages without excessive current flow and heat evolution, giving larger pore size (100-300 nm range).

3.2 Experimental

The substrate material used was a commercial 6016 Al alloy with elemental composition of Al–98.0 wt. %, Si–1.1 wt. %, Mg–0.9 wt. % determined by energy dispersive spectroscopy (EDS) analysis performed at 5 kV. This alloy underwent a T4 heat treatment (solution heat treated and naturally aged to a substantially stable condition). The Al-alloy

sheet was 0.2 cm thick and it was cut into small pieces of 2 x 2 cm^2. In order to control the surface wettability, this work combined surface micro-texturing followed by anodization processes.

3.2.1 Surface micro-texturing and pre-treatment

The micro-texturing of Al alloy surface was promoted by mechanical grinding conducted in a polishing machine (RotorPol 21 model by Struers with 25 cm plate diameter) with SiC sandpapers, with increasing grit size, and diamond paste. This previous step allowed to prepare three types of surface finishing: not polished (NP), grinding till grit size 1000 (P1) and further mirror polishing on a cloth with diamond paste of 3 µm size (MP). As a cleaning step prior to the anodization process, the samples were firstly degreased in acetone (15 min) and in ethanol (15min) in ultrasonic bath (US) being rinsed in distilled water between intermediate washing reagents. Subsequently, a chemical etching in an 8 wt. % H_3PO_4 + 4 wt. % CrO_3 acid solution was carried out for 20 min in ultrasonic bath, this working as a surface pre-treatment responsible for the surface's passive oxide and impurities removal [205]. In the end, samples were always cleaned in distilled water for 10 min in US bath too.

3.2.2 Anodization step as surface nanostructuring

Regarding the anodization process, a simple cylindrical polypropylene box was used as electrochemical cell and the aluminum alloy samples were placed in a two-electrode parallel arrangement exposing a circled area of around 2 cm^2, using a graphite rod as cathode, as illustrated in Figure 3.1. All the experiments were conducted in potentiostatic mode using a DC power supply (Agilent Technologies, N5751A model, max. 300 V-2.5 A) at constant voltage with an anode-cathode distance of 3 cm under magnetic stirring.

One-step and two-step anodizing configurations were conducted using H_2SO_4 and H_3PO_4 as electrolytes. Several anodizing parameters were varied as the electrolyte concentration (in case of H_2SO_4), the anodizing time (1st and 2nd), and the durations of intermediate (Etching 1) and final etchings.

In case of H_2SO_4 electrolyte, all the anodizations were performed at 15 V and the electrolyte was kept at room temperature (between 15 and 18 °C). Two different electrolyte concentrations were studied, 0.3 M and 1 M. For H_3PO_4 electrolyte, only the 0.5 M concentration was used at 100 V with initial electrolyte temperature of around 0

°C, which was kept with ice in the outside contact with the anodizing cell. In both cases (with H_2SO_4 or H_3PO_4), after the first anodization the grown alumina layer was removed (Etching 1) using a 8 wt. % H_3PO_4 + 4 wt.% CrO_3 acid solution in a thermal bath at 60 °C. The influence of Etching 1 duration was evaluated. After this etching, the samples were washed again in US bath with distilled water for 10 min. Then, the ordered concave pattern on the Al alloy surface followed the second anodization step, with the same conditions as the first one, to produce a more ordered porous AAO structure. Finally, a chemical etching (Final Etching), using a 0.5 M phosphoric acid solution kept at 30 °C in a thermal bath, was performed in some samples to enhance pore size diameter. In the end, the samples were washed in distilled water for 10 min in US bath again.
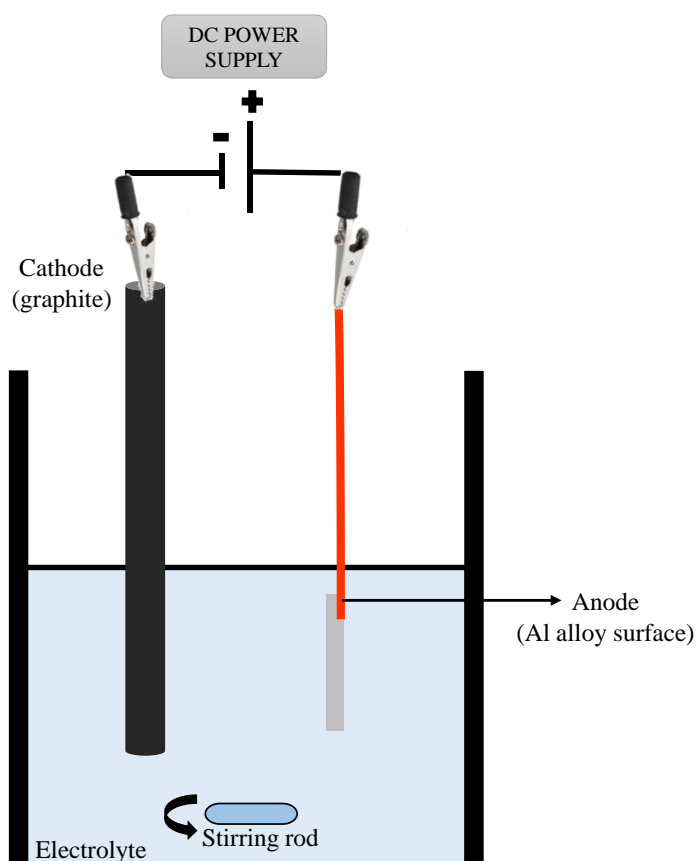
Figure 3.1 Schema of the electrochemical anodizing cell used for the experiments with a cathode-anode spacing of 3 cm.

Table 6 summarizes the conditions selected for each anodization which allowed to produce 13 different structured Al alloy surfaces. The sample designation when using H_2SO_4 electrolyte in the anodization was determined according to the following nomenclature [electrolyte nature (S)/electrolyte concentration (0.3 or 1 M)/anodization steps (ONE or TWO)/time of Etching 1 (Et1-duration)/time of Final Etching (Et2-

duration)]. When using 0.5 M H_3PO_4 electrolyte it was determined according to [electrolyte nature (P)/ anodization steps (ONE or TWO)/ time of Etching I (Et1-duration)/time of Final Etching (Et2-duration)].

Table 6 Anodizing conditions using sulphuric acid or phosphoric acid as electrolytes and respective duration of all steps.

Electrolyte	Sample	[Electrolyte]	Potential	1st anodization	Etching I	2nd anodization	Final Etching
H_2SO_4	S/0.3/ONE/Et0	0.3 M	15 V	90 min	-	-	-
	S/0.3/ONE/Et1-15			90 min	15 min	-	-
	S/0.3/ONE/Et1-90			90 min	90 min	-	-
	S/0.3/TWO/Et1-90/Et2-90			90 min	90 min	90 min	90 min (30°C)
	S/1/ONE/Et1-90	1 M		90 min	90 min	-	-
	S/1/TWO/Et1-90			90 min	90 min	90 min	-
H_3PO_4	P/ONE/Et1-0	0.5 M	100 V	60 min	-	-	-
	P/ONE/Et1-10			60 min	10 min	-	-
	P/ONE/Et1-20			60 min	20 min	-	-
	P/ONE/Et1-30			60 min	30 min	-	-
	P/TWO/Et1-30/Et2-0			60 min	30 min	60 min	-
	P/TWO/Et1-30/Et2-15			60 min	30 min	60 min	15 min (30°C)
	P/TWO/Et1-30/Et2-30			60 min	30 min	60 min	30 min (30°C)

3.2.3 Surface characterization procedure

The top-view morphology and chemical composition of the surfaces produced by combination of microtexturing and anodization steps were characterized by a field emission scanning electron microscope and energy-dispersive X-ray spectroscopy analysis (SEM/EDS) (FEI Nova 200/Pegasus X4M) operating at 5 kV in secondary electron mode. Samples were mounted on a holder with double sided conductive carbon tape and sputtered coated (Cressington Sputter coater 208 HR) with a 5 nm thin layer of Au-Pd (80/20). Moreover, the morphology and chemical composition of the polished surfaces before anodization were also characterized (NP, P1 and MP). SEM micrographs were used to analyse the diameter distribution of the surface features (dimple or pore) using *ImageJ* software. In order to visualize the pore channel growth created by anodization, selected patterned samples were manually bended and their cross-sections analysed by SEM. The surface microroughness was measured by a 2D profilometer (Perthometer S4P, Perthen). Regarding the surface wettability behaviour, static contact angles (CA) using the sessile drop method were determined using a DataPhysics OCA Analysis system applying liquid droplets of about 2 μL at room temperature. The liquids used for wettability assessment were ultrapure water and α-bromonaphthalene (non-polar liquid acting as oil) with surface tensions (γ_{LV}) of 72.8 and 44.5 mN/m, respectively.

Further, additional contact angle measurements were conducted with formamide (γ_{LV} of 58.2 mN/m) for the five optimized different structured surfaces in order to determine the surface free energy using the van Oss approach based on the Young-Dupré equation [180, 181].

3.3 Results and Discussion

3.3.1 The effect of mechanical grinding on wettability

It is well-known that bare metallic surfaces exposed to the humid air environment are subjected to fast oxidation leading to a natural oxide formation and further dust particle and greasy contaminants' accumulation. Mechanical grinding helps not only to remove the natural oxide and cleaning of the surface but also for the creation of a microtextured pattern or grooving on the aluminum alloy surface, which can influence the wetting properties. Two Al alloy surface finishing (P1 – sandpaper till grit size 1000 and MP – mirror-like polished) were compared with the non-polished sample (NP). Figure 3.2 a), b) and c) show the respective SEM micrographs of the polished and non-polished Al samples. The EDS analysis of the Al alloy material studied is also depicted in Figure 3.2 d) as well as the graph depicting the results for the static contact angles for water (WCA) and α-bromonaphthalene (OCA) of the three tested sample surfaces in Figure 3.2 e).

The SEM micrographs show that the NP Al alloy sample presents irregular microroughness and black blurs, resulting from the oxidation mechanism, which was confirmed by the oxygen presence in the Al alloy surface by the EDS analysis. P1 Al alloy sample shows aligned grooves promoted by the abrasive SiC sandpaper while the MP Al alloy has, as expected, a smooth surface with only a few remaining scratches. This is in accordance with the roughness measurements obtained by 2D optical profilometry which allowed to obtain Ra average values of about 2, 0.9 and 0.1 μm for NP, P1 and MP Al alloy surfaces, respectively.

Regarding the wettability behaviour, the graph in Figure 3.2 e) compares the water and oil (α-bromonaphthalene as the lower surface tension liquid) static CAs. The NP Al alloy surface is slightly hydrophobic (WCA = 94 ± 4°) and oleophilic (OCA = 33 ± 1°) as the P1 surface (WCA = 91 ± 4° and OCA = 32 ± 6°). However, the smoother surface of the MP Al alloy surface is more hydrophilic (WCA = 71 ± 4°) keeping a similar oleophilic-like (OCA = 27 ± 2°) behaviour. Taking into account that solid flat alumina surface has
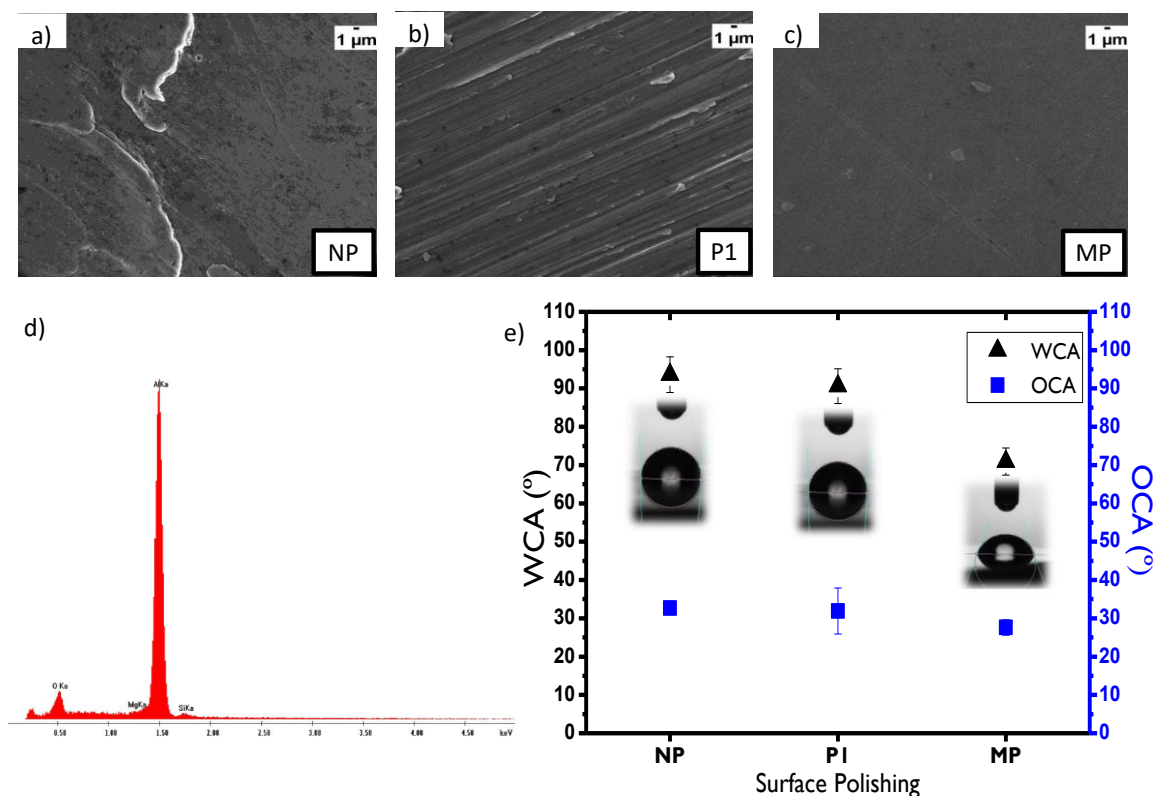
Figure 3.2 SEM micrographs of the three different Al topographies studied a) NP, b) P1 and c) MP; c) the EDS analysis of the Al6016T4 alloy and d) the graphic representation of respective static water and oil contact angles obtained.

typical water contact angle of about 85 ± 3° [95], the WCA values of 94°, 91° and 71°, respectively obtained for NP, P1 and MP surfaces, are not significantly different. This allows to conclude that the Al alloy surface has a native oxide surface layer, which is rapidly produced even after polishing treatment. In the literature, surface finishing P1 has already demonstrated to achieve superhydrophobicity and superoleophobicity (CA > 150°) but only if a prior acid etching and an additional fluorine-based coating are added [210]. In this part of the study it was noticed that the Al flat surface must be surely hydrophilic (example of MP) and the increase of the roughness by microtexturing (example of P1) led to hydrophobic surface behaviour (WCA > 90°). This surface wettability to water means a transition between Wenzel and Cassie-Baxter states. Regarding to oil repellence, the OCA slightly increased with roughness, although oleophobicity level was not reached in P1 and then that transition was not so evident, keeping a Wenzel wettability state.

Due to the wettability result presented by P1 surfaces, which showed not to be greatly influenced by the microtexturing and to be more homogeneous than NP ones, the next surface structuring studies by anodization process were only performed on P1

surface treated Al alloy surfaces. It is intended to decrease the WCA by oxide formation and increase the OCA by creation of re-entrant surface morphologies or overhang-like structures which have already been mentioned to be important on reaching oleophobicity.

3.3.2 Surface structures produced by Al anodization

The anodization process is a bottom-up process that enables to alter not only the surface chemistry of Al surfaces by producing aluminum oxides (Al_2O_3), but also alter the surface roughness by producing dimple-shaped or porous structures. According to the previous section, the polished surface P1 showed aligned abrasive grooves and good water repellence. Furthermore, three of the five anodization conditions optimized were studied on the three surface finishing (NP, P1 and MP), showing that P1 treatment can provide different wettability behaviour (see Figure A.1 in the Appendix). Figure 3.3 shows the SEM images of the oxide structures using 0.3 M concentration of H_2SO_4 during 90 min of anodization at 15 V in one-step configuration. From the top-view image (Figure 3.3 a)), it can be observed that the pore size is very narrow comparatively to the oxide wall thickness. The respective cross section view (Figure 3.3 b) and c)) shows the roughly ordered porous AAO layer of around 12 μm thickness created, with an average growth rate of about 8 μm/h (see Figure A.2 a) and b) in the Appendix).

In an attempt to create a periodic concave pattern on the Al alloy surface, the effect of chemical etching followed by the first anodization was studied. Figure 3.4 a) and b) present the SEM images of Al anodized samples with 0.3 M concentration of H_2SO_4 after removing the disordered oxide layer by a chemical etching (Etching 1) of 15 min and 90 min, respectively. As expected, an apparent concave-patterned surface with relatively small size of concavities (around 31 ± 7 nm diameter) was achieved as a result of the periodic bottom pore shape. SEM cross-section view did not allow to clearly separate the oxide layer confirming its very thin thickness. Besides, it seems that the 15 min of etching did not allow to completely remove the disordered oxide layer comparatively to 90 min etching case. Likewise, 1 M H_2SO_4 was used foreseeing an increase of the concave pattern left after 90 min etching, although no significant difference on the surface patterning in regard to 0.3 M was observed as visualized in Figure 3.4 c). In both cases, concave-shaped surface with the same average size diameter was achieved.
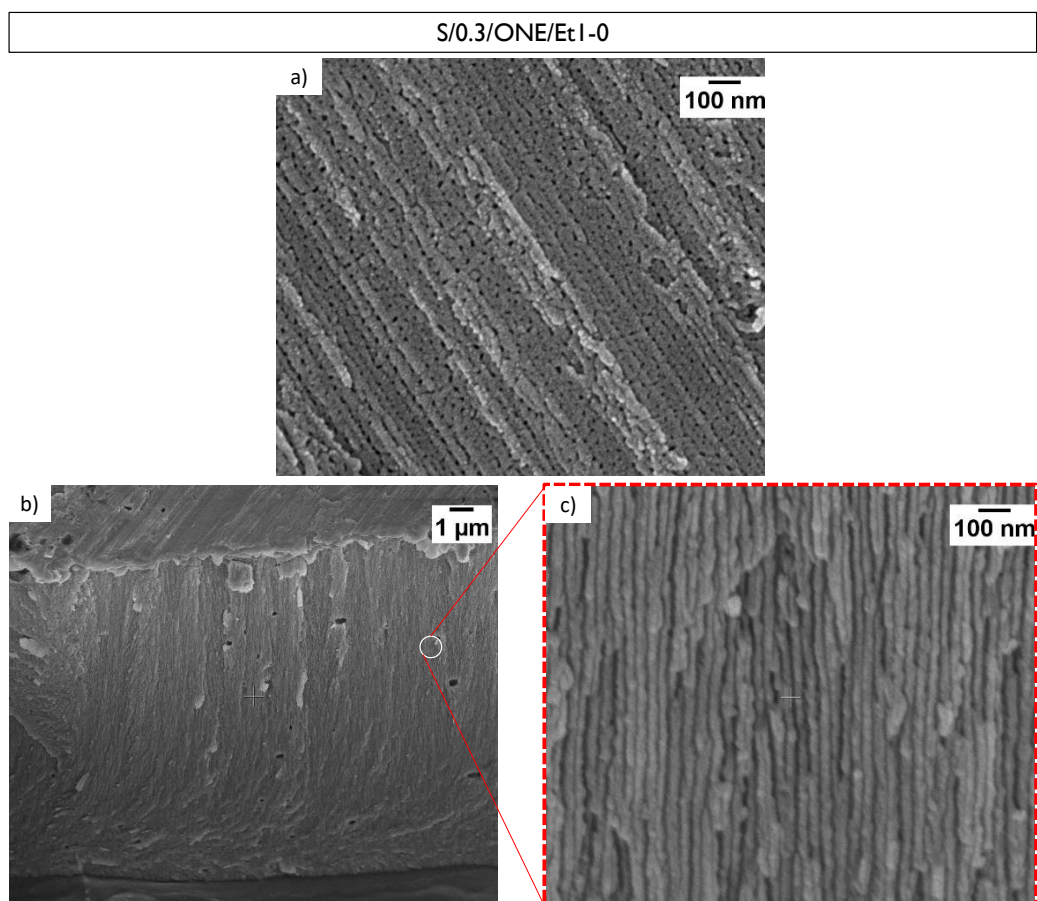
Figure 3.3 SEM morphological characterization of Al alloy surfaces anodized at 15 V with 0.3 M H_2SO_4 as electrolyte in 1-step configuration: a) top view; b) and c) cross-sections.

Using the same conditions, a second anodization with 0.3 M H_2SO_4, followed by an additional final etching carried out at 30 °C, was performed over this dimple structure (sample S/0.3/ONE/Et1-90) in order to both promote pore formation and pore widening, as shown in Figure 3.5 a). The duration of the etching led to an excessive pore widening leaving some oxide walls cracked, interconnecting surrounding pores. In this context, a second anodization using 1 M H_2SO_4 was performed without conducting final etching (sample S/1/TWO/Et1-90/Et2-0); an ordered porous structure of Al_2O_3 was obtained, as Figure 3.5 b) shows, with an average pore size diameter of around 29 ± 6 nm. From this first part of the study with sulphuric acid, the main conclusion was that the increase of electrolyte concentration in the first anodization from 0.3 M to 1 M followed by Etching 1 did not influence the size of the concavities as expected from literature for this anodizing conditions [211, 212].
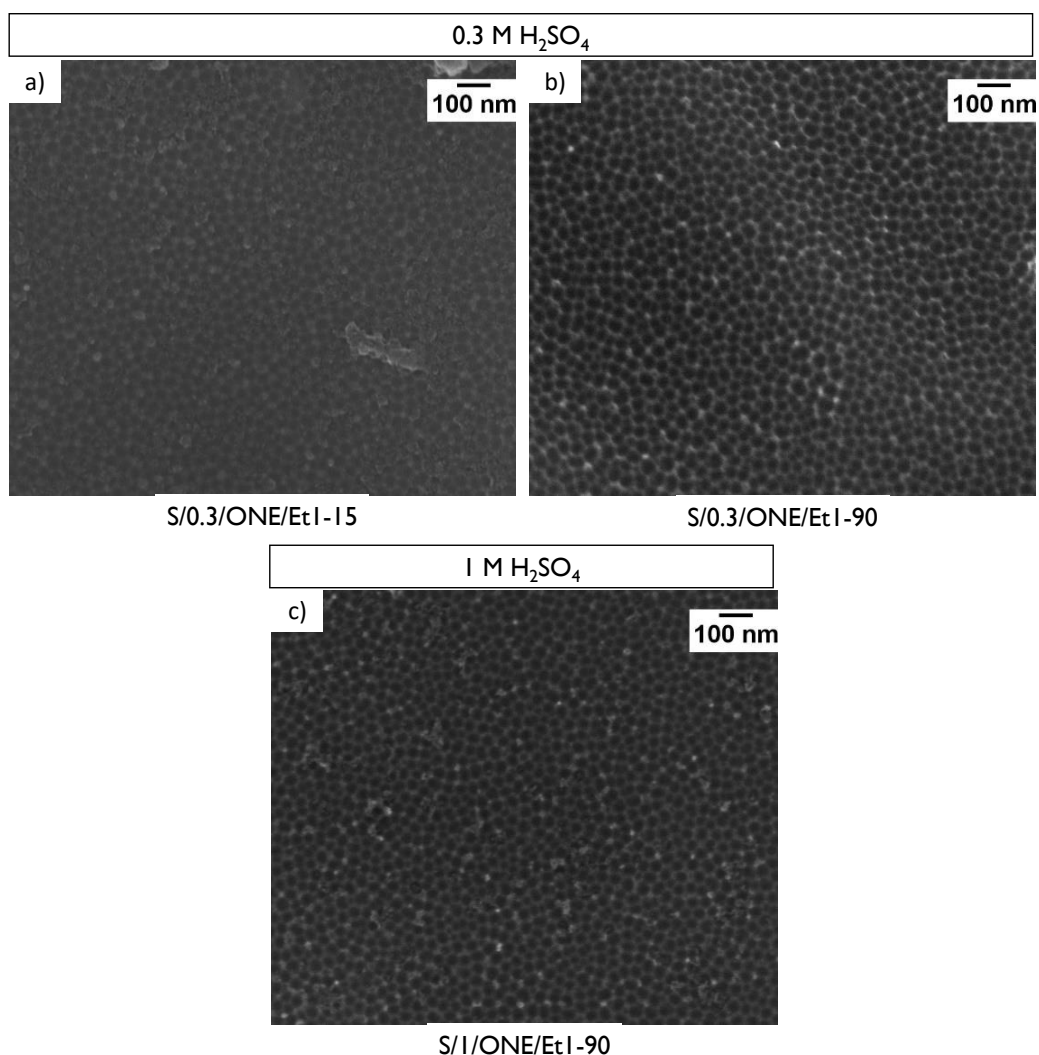
Figure 3.4 SEM morphology of Al surfaces anodized at 15 V with 0.3 M H_2SO_4 in 1-step configuration followed by chemical etching in H_3PO_4/CrO_3 solution at 60 °C for a) 15 min and b) 90 min and the same procedure but anodized with 1 M H_2SO_4 with 90 min etching c).

Then, pointing out that surface wettability is largely dependent on surface porosity [57], a different electrolyte which allows to work at higher potentials was selected in order to increase the average pore size diameter. Al alloy surfaces were anodized in 0.5 M H_3PO_4 electrolyte under 100 V at low temperature (0 °C). Figure 3.6 shows the main SEM micrographs of sample anodized during 60 min with H_3PO_4 electrolyte in one-step configuration (P/ONE/Et1-0). The top-view morphology of Figure 3.6 a) shows high porosity with a relatively broad distribution of surface pore openings. Indeed, a higher working voltage increases the radial electric field distribution leading to enhanced radial oxide dissolution which results in an increase of pore size. Furthermore, comparing this high magnification SEM micrograph with the lower magnification SEM image presented in Figure 3.6 b), it is possible to conclude that the anodization process follows the aligned

features promoted by the polishing step, with the pores occurring preferentially inside the grooves.
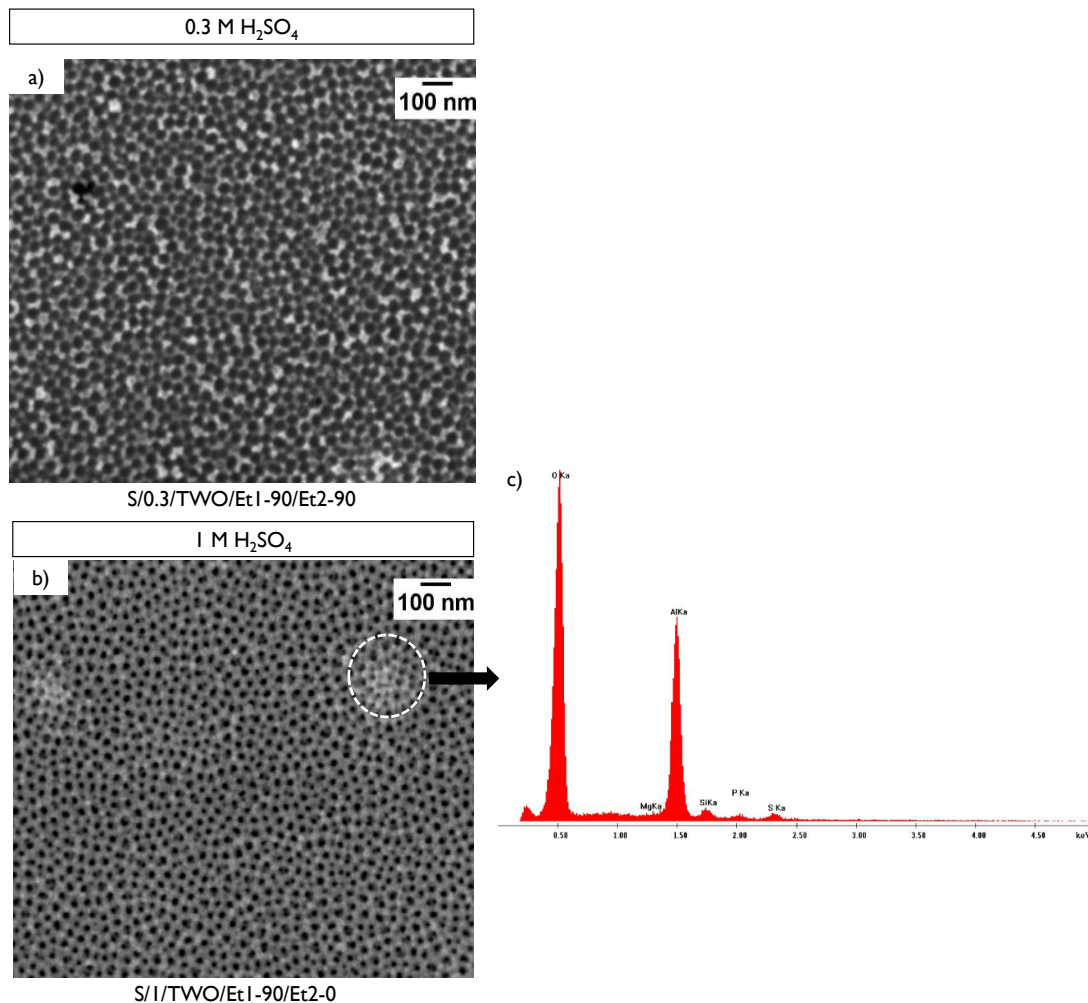
Figure 3.5 SEM morphology of Al surfaces anodized at 15 V with H_2SO_4 in 2-step config. with a) 0.3 M H_2SO_4/90 min final etching in 0.5 M H_3PO_4/30 °C and with b) 1 M H_2SO_4 without final etching. In c) there is the EDS analysis on protrusion feature.
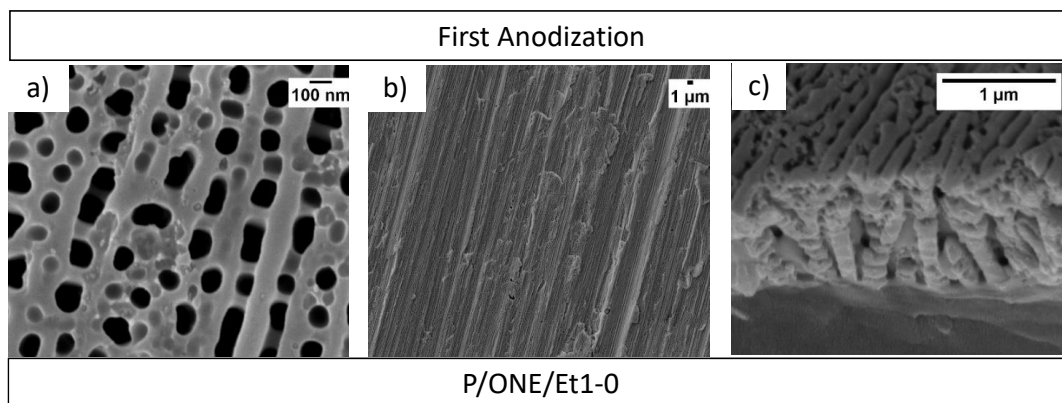
Figure 3.6 SEM morphological characterization of Al alloy surfaces anodized at 100 V with 0.5 M H_3PO_4 in 1-step configuration for 60 min. In a) it is showed the top view of anodized sample; b) obtained at low magnification and, in c) a sectional view of that anodize

This fact had also been noticed when anodizing with H_2SO_4 electrolyte. In Figure 3.6 c), the cross-section analysis showed that the pore channels are not vertically aligned. This is a consequence of an unsteady-state anodization in which the oxide dissolution reaction is promoted instead of the formation; then, the anodization process does not occur and branched pores are generated from the primary aligned pores [164, 213].

In case of H_2SO_4 anodization, the chemical etching had influence in the surface topography; so, its effect and duration on the bottom surface topography were studied again when using H_3PO_4 electrolyte.

After etching for 10 min, 20 min and 30 min in H_3PO_4/CrO_3 solution at 60°C (Figure 3.7 a), b) and c), respectively), once again the top view of the etched samples reveals very shallow pores approaching a dimple-like structure. Despite the broad size distribution, the remaining thin oxide layer, after the chemical etching, formed large concavities of about 223 ± 46 nm average size diameter. With increasing etching time, the remaining oxide layer apparently gives to P/ONE/Et1-30 sample a more mechanical consistent aspect (compare Figure 3.7 d) and e)).

Additionally, a two-step anodization procedure was performed on sample surface P/ONE/Et1-30 (Figure 3.8 a)) during 60 min. The poor ordered structure observed after the second anodization (P/TWO/Et1-30/Et2-0) still showed large pore openings (Figure 3.8 b)) with non-circular geometry and broad size distribution (205 ± 55 nm) with global dimensions of oxide wall thicknesses in the range of 130-180 nm. Note that the Al alloy of the 6000 series (rich in Si and Mg elements) can have intermetallic precipitates in its constitution which make these surfaces remarkably interesting to be studied from the electrochemical point of view [214]. Then, comparatively to the commonly self-ordered porous structures obtained with pure Al surfaces, a much more irregular structure arrangement, with branched or meshed pore structures, can be achieved and double or triple sub-channels can be formed underneath [80]. Moreover, the microroughness enhancement of the Al6016-T4 alloy surface, created by the mechanical grinding, can also contribute to this non-ordered aluminum oxide structure.

Figure 3.8 e) presents the sectional view of the grown anodic oxide layer without chemical etching of P/TWO/Et1-30/Et2-0 sample. Vertical aligned pores, typical of second anodization ordering, can be observed even if the cross-section preparation method broke many oxide walls. Transversal to the large pores perpendicular to the surface, small pores can also be detected across the oxide walls which can be attributed to different
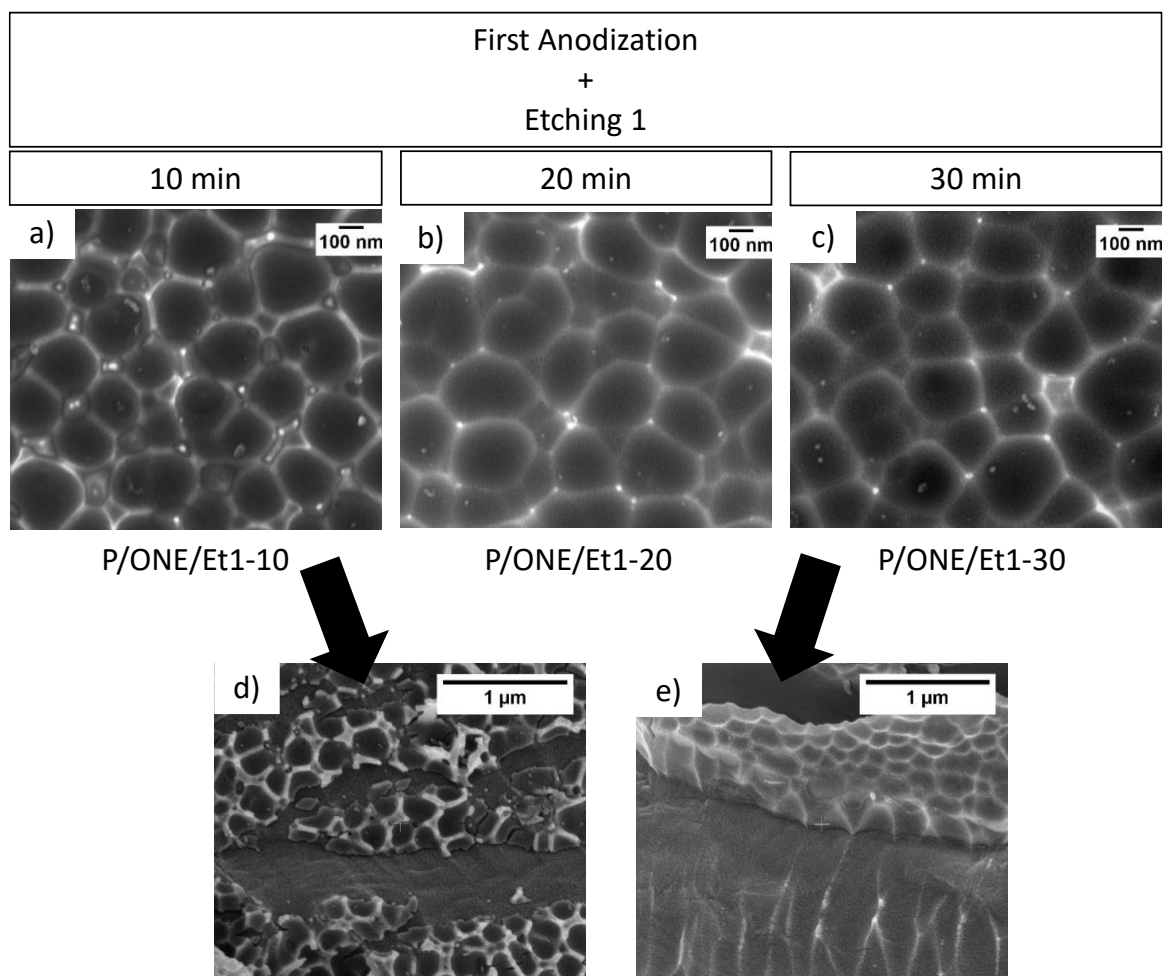
Figure 3.7 SEM morphological characterization of Al surfaces anodized at 100V with 0.5 M H_3PO_4 in 1-step configuration and using a chemical etching in $H_3PO_4/CrO_3/60\,°C$ for a) 10 min, b) 20 min and c) 30 min. Images d) and e) are two sectional views obtained.

chemical dissolution rates of the second-phase precipitates of the Al alloy, that can get trapped in the oxide structure [215, 216]. In fact, the EDS spectra obtained after anodization, which are depicted in Figure 3.5 c) and Figure 3.8 g), showed the Si presence in the anodic layers, when anodizing with H_2SO_4 or H_3PO_4. Moreover, the presence of those intermetallic compounds are also responsible for incorporation of the sulphate (SO_4^{2-}) or phosphate (PO_4^{3-}) anions coming from the electrolyte during the oxide growth. Figure 3.5 b) shows two bright spots/protrusions, featuring the sulphate species incorporation. Together with the EDS analysis that identified S or P elements in the oxide surfaces, XRD analysis (Figure 3.8 h)) performed in H_3PO_4 treated sample (P/TWO/Et1-30/Et2-30), showed the presence of the $AlPO_4$ phase in accordance with results from literature [217].

After the second anodization in H_3PO_4 electrolyte, P/TWO/Et1-30/Et2-0 samples were further chemically etched (Final Etching) for 15 min and 30 min duration in a 0.5 M

a)
P/ONE/Et1-30

2nd anodization		
No Final Etching	Final Etching	
	15 min	30 min

b) P/TWO/Et1-30/Et2-0

c) P/TWO/Et1-30/Et2-15

d) P/TWO/Et1-30/Et2-30

e)

f)

g)

h)
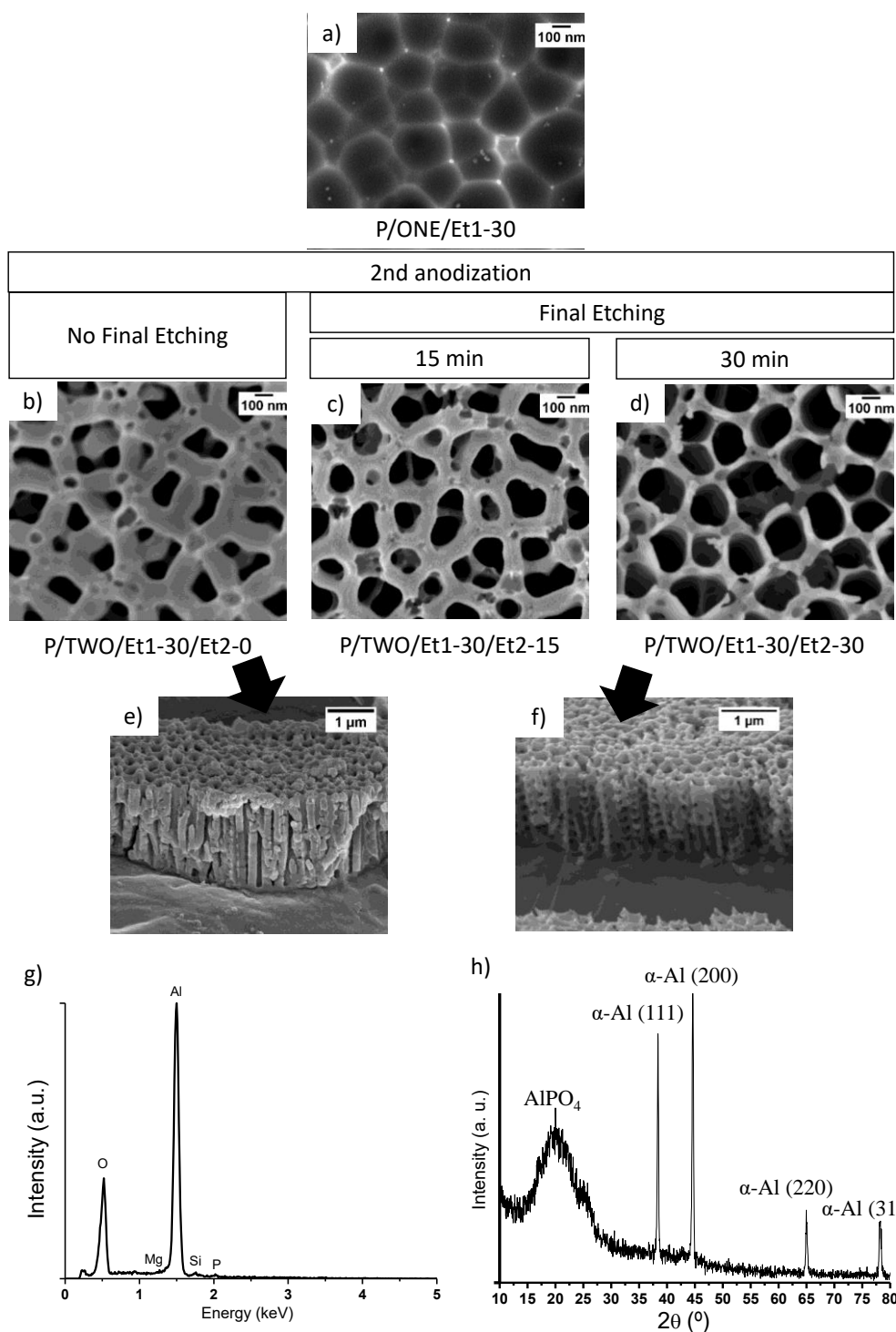
Figure 3.8 SEM images of a) P/ONE/Et1-30 which b) underwent 60 min 2nd anod./final etch. in 0.5 M H_3PO_4 for c) 15 min or d) 30 min. Sectional views were obtained for surfaces e) without and f) with final etching. EDS g) and XRD h) analysis for P/TWO/Et1-30/Et2-30.

H_3PO_4 solution at 30 °C, to promote the pore widening (Figure 3.8 c) and d), respectively). As expected, a progressive pore widening is observed with increasing etching time, reaching average pore size diameters of 250 ± 60 nm. However, the decrease of pore wall thickness (~50 nm) increased the porosity and many pore channels merged with

neighbouring ones showing the well-known bamboo-like structure [218]. Nevertheless, the thickness of the Al anodic oxide layer after 30 min etching was about 2 μm, the same as without any etching (comparing cross-sections of Figure 3.8 e) and f)). In this case, the oxide growth rate is lower when compared to H_2SO_4 one (see Figure A.2 c) in the Appendix regarding the current densities).

In summary, the anodization of an aluminum alloy of the 6000 series showed to be different from the anodization process of pure Al. The presence of precipitates based on the Si and Mg alloying elements, with different oxidation rates comparatively to Al, showed to have a detrimental effect hindering the ordering of the pores and the overall structure, mainly after the two-step anodization [92]. According to the different Al oxide structures developed by the anodization processes, 5 samples with different surface morphologies (pores or concavities of different sizes) were selected for further studies of the wettability behaviour in water and oil (α-bromonaphthalene) (see Figure A.3 in the Appendix for exemplification of *ImageJ* application on pore/dimple size determination). Those samples are: S/0.3/ONE/Et1-90 (Figure 3.4 b)), S/1/TWO/Et1-90/Et2-0 (Figure 3.5 b)), P/ONE/Et1-10 (Figure 3.7 a)), P/TWO/Et1-30/Et2-0 (Figure 3.8 b)) and P/TWO/Et1-30/Et2-30 (Figure 3.8 d)).

3.3.3 The effect of anodization on wettability

Literature studies mainly report on the wettability of water on anodized Al surfaces; this work gives a further insight on the oil repellence level of different structures achieved by Al alloy anodization. As determined above, the as-received Al alloy substrates (NP surface) displayed a hydrophobic and oleophilic behaviour with WCA of 94 ± 4° and OCA of 33 ± 1°, respectively. Similar wettability behaviour was measured for the Al polished surface (P1) (WCA = 91 ± 4° and OCA = 32 ± 6°), this surface behaviour the base condition for this study.

Figure 3.9 plots the static water and oil contact angles for the structures obtained after one-step anodization a) and two-step anodization b). Overall, it is clearly observed that either the roughness or the surface chemistry modification to alumina, by anodization of the Al alloy surface, led to hydrophilic and oleophilic surfaces (WCA and OCA < 90°). The one-step anodization (for both H_2SO_4 and H_3PO_4 electrolytes) followed by oxide removal by chemical etching, allowed to achieve small (sample S/0.3/ONE/Et1-90) and large (sample P/ONE/Et1-10) concavities; the latter topography gave rise to WCA of 93 ± 12° and OCA of 41 ± 2°, providing slightly hydrophobic but still oleophilic character.

EDS analysis (not shown) showed that the oxide removal was not complete; a thin oxide layer was left contaminated by phosphorous coming from the acid etching solution. Since the smaller concavities (size diameter of ~31 nm) gave lower values of static contact angles (45 ± 6° for WCA and 27 ± 4° for OCA) than the larger ones (size diameter of ~223 nm), as they have the same microroughness (Ra values around 0.5 µm, 2D profilometry data), we can conclude that dimple size has a role on wettability.
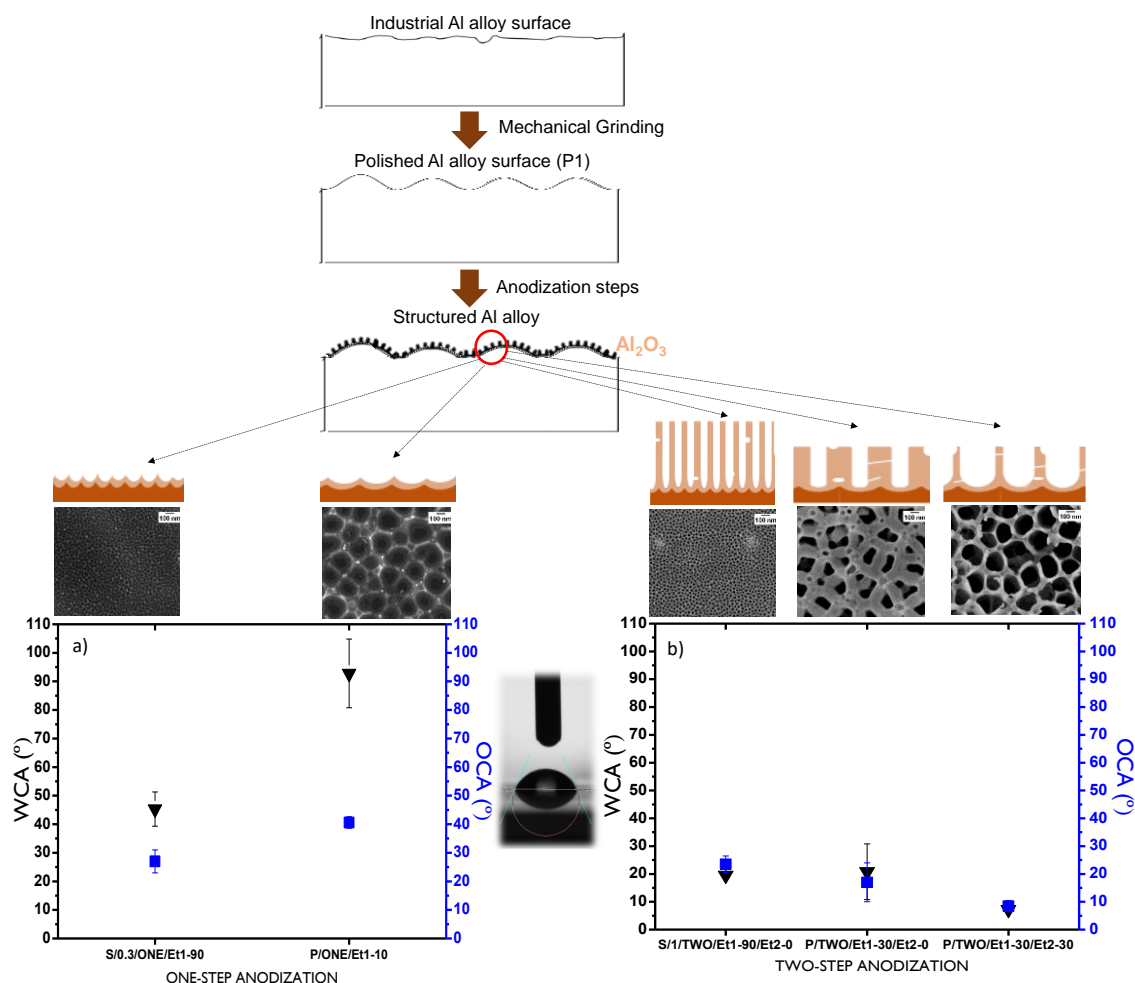
Figure 3.9 WCA and OCA measurements obtained for five different structures produced by Al alloy anodization in a) one-step configuration and in b) two-step configuration. The starting Al alloy surface (P1 treatment) showed WCA of 91 ± 4° and OCA of 32 ± 6°.

In two-step anodization process, thicker porous oxides (microroughness with Ra values of 1.3 µm) were grown on the Al alloy substrates of about 12 µm on S/1/TWO/Et1-90/Et2-0 and 2 µm on both P/TWO/Et1-30/Et2-0 and P/TWO/Et1-30/Et2-30. The increase in porosity mainly led to surfaces with CA < 20°, reaching superhydrophilic and superoleophilic wettability behaviour. The pore widening promoted by 0.5 M H_3PO_4 solution at 30 °C on sample P/TWO/Et1-30/Et2-30, comparing with P/TWO/Et1-30/Et2-0 without etching, did not yield an increase of the WCA as it could be expected from

literature [57] giving, instead, a drop on those values. Despite the deep pores, the small pore size and the thin oxide wall thickness observed for S/1/TWO/Et1-90/Et2-0, a WCA (20 ± 1 °) value below the OCA value (24 ± 3°) was reached. Likewise, the increase on pore openings together with the increase of oxide wall thickness (~ 150 nm) observed for P/TWO/Et1-30/Et2-0 revealed similar contact angle measurements to that of S/1/TWO/Et1-90/Et2-0 with WCA of 21 ± 10° and OCA of 17 ± 7° values.

In wettability mechanisms it is known that the increase in surface roughness enlarges the effective contact area between the liquid and solid. In case that the liquid impregnates the rough surface the so called Wenzel state is applied whereas in case the liquid is suspended on the top of roughness peaks, the Cassie-Baxter state better describes the wettability behaviour. However, the wettability of porous anodic alumina by water is usually explained by a more appropriate model based on an intermediate state between Wenzel and Cassie-Baxter ones [219]. It is a pressure balance model that can predict the penetration of a water droplet into each of the pores, assuming that when the water wets the porous alumina surface, the air inside the pore is not totally expelled out but instead compressed [95]. This way, there was a force balance between the force exerted by the compressed air and the capillary force together with the gravity force (this one caused by the water weight above the air pocket), as Figure 3.10 a) represents.

Then, the capillary force ($\overrightarrow{F_c}$) can be expressed as:

$$F_c = \pi \gamma d \cos\theta, \qquad\qquad\qquad \text{(Equation 3.1)}$$

where γ, d and θ are the water surface tension, the pore diameter and the Young's liquid CA, respectively [220]. Moreover, in that force balance model, the gravity force ($\overrightarrow{w}$) is very small being neglected and, so, the capillary force will be balanced by the air pressure ($\overrightarrow{F_p}$). That air trapped inside the pores is assumed to behave like an ideal gas and, if the size of the pore is much smaller than the size of the liquid droplet, the displacement of the liquid into the pore (h) can be expressed as:

$$h = 4L\gamma\cos\theta / (P_0 d + 4\gamma\cos\theta), \qquad\qquad \text{(Equation. 3.2)}$$

where L and P_0 are the pore depth and atmospheric pressure, respectively. This expression assumes that Young's liquid CA (θ) of flat solid alumina is ~85°, P_0 is 1 atm and γ is 72 mN/m (water) which results that the ratio of liquid that can intrude the hole (h/L) would decrease as the pore diameter (d) increases. For example, for the same pore depth, a pore diameter of around 100 nm gives a h/L ratio of about 0.7, meaning that the surface wetting behaviour is Wenzel state, while for a pore diameter of around 420 nm h/L ratio

is about 0.3 reaching a more Cassie-Baxter state surface behaviour. Certainly, the mentioned capillary-pressure model can also be extrapolated for low surface tension liquids such as bromonaphthalene which γ is equal to 44.5 mN/m.
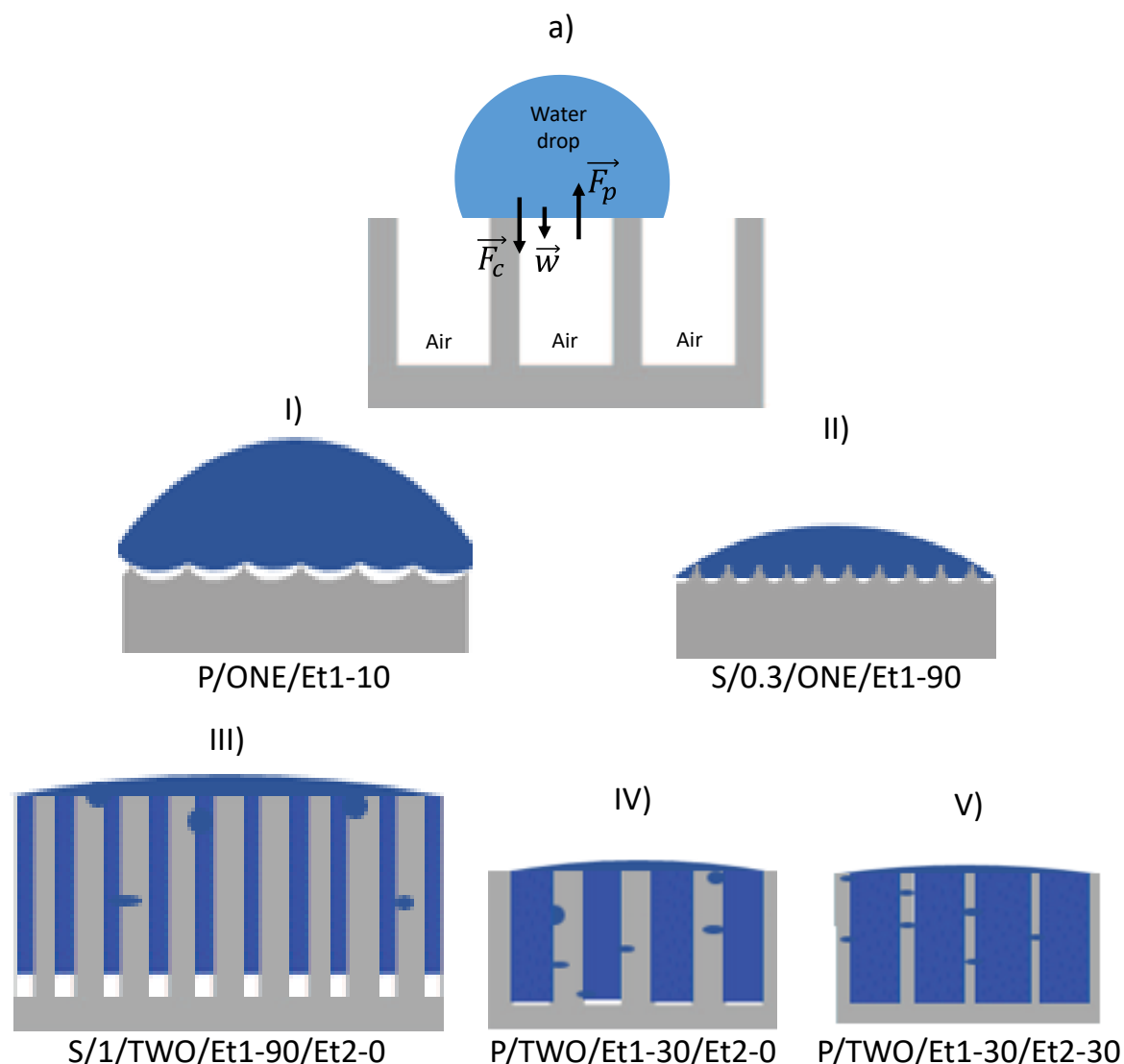
Figure 3.10 Wettability mechanisms in porous structures: a) the schema of the capillary-pressure forces; and the representation of liquid droplet in the developed dimple-shaped structures b) and c), and in porous structures c), d and e).

In our cases, the *h/L* ratios were calculated according to the Equation 3.2 previously mentioned. Table 7 compares the values obtained for the Al oxide surface structures produced in one or two-step anodization.

Even though the one-step anodization gave dimple geometry in the structures, it was also calculated the *h/L* ratio according to the respective dimple size diameter. Related to the one-step anodization, considering 31 nm or 223 nm as the diameters of the dimple geometries, *h/L* ratios of 0.97 and 0.79 were respectively determined. The application of

Equation 3.2 is not completely wrong once the concavities are larger for sample P/ONE/Et1-10 (see representation I of Figure 3.10), although being smaller for sample S/0.3/ONE/Et1-90 (see representation II of Figure 3.10). The highest "diameter" gave the lowest ratio, indicating higher liquid repellence which is in accordance with the CAs measured, although the surface is roughly still inside the Wenzel regime.

Table 7 The h/L ratios obtained for all the anodized samples obtained, which structures are schematically represented as I, II, III, IV and V in Figure 3.10.

	Anodized Sample	d (nm)	L (µm)	h/L	h (µm)	WCA (°)	OCA (°)
Fig. 3.10 I)	P/ONE/Et1-10	223 ± 46	-	0.79	-	93	41
Fig. 3.10 II)	S/0.3/ONE/Et1-90	31 ± 7	-	0.97	-	45	27
Fig. 3.10 III)	S/1/TWO/Et1-90/Et2-0	29 ± 6	12	0.97	11,5	20	24
Fig. 3.10 IV)	P/TWO/Et1-30/Et2-0	205 ± 55	2	0.81	1.6	21	17
Fig. 3.10 V)	P/TWO/Et1-30/Et2-30	250 ± 60	2	0.77	1.5	7	8

Regarding the two-step anodization, theoretically, the increase on pore size diameter would give rise to a decrease on h/L ratio. This trend was verified in our calculations reaching 0.97, 0.81 and 0.77 for S/1/TWO/Et1-90/Et2-0 (pore of 29 nm), P/TWO/Et1-30/Et2-0 (pore of 205 nm) and P/TWO/Et1-30/Et2-30 (pore of 250 nm) samples, respectively. All those ratios would clearly give a Wenzel wettability regime, depicting P/TWO/Et1-30/Et2-30 sample as the less wettable among all three. However, from the CA measurements, P/TWO/Et1-30/Et2-30 sample presented the lowest values showing superhydrophilic and superoleophilic behaviour (see representation V of Figure 3.10). This phenomenon may be in part explained by an overetching of the porous surface that led to a limited pore wall thickness (50 nm), which led to a collapse of the dead-end structure in some areas becoming too thin to support the liquid droplets. This, added to the fact that the transverse pores interconnecting the perpendicular pore channels would increase of liquid-solid contact area, which in turn would increase the capillary forces. That increase would overcome the pressure forces promoted by the air trapped inside the pores, disrupting the capillary-pressure balance assumed for porous structures, and consequently, eliminating the air pocket pressure affect. As a result, that leads to easy water or oil spreading inside the whole structure, thereby strongly decreasing the repellence of the surface. Regarding to samples S/1/TWO/Et1-90/Et2-0 and P/TWO/Et1-30/Et2-0, the oxide walls do not show such a high oxide wall disruption level and the pore sizes (29 nm and 223 nm, respectively) induced h/L ratios in accordance with the Wenzel regime confirmed by the CA values reached. The wettability schema representation of both structures are respectively presented in Figure 3.10 as III and IV.

Another parameter measured was the surface free energy (SFE), which is the energy of a solid surface free to interact with the outside (comparatively to the bulk material) and is usually a key to understand adhesion phenomena of surfaces. In this study, SFE calculation was calculated based on the van Oss approach [221-223], which is reported as being the better direct experimental method for solid surface free energy determination [224]. This model assumes the thermodynamic equilibrium of the solid-liquid-vapour surface tensions, which coexist in the boundary of a liquid droplet in a solid surface. It expresses the surface free energy in terms of the sum of non-polar and polar interactions and in terms of the solid-liquid work of adhesion; combining that result with the Young equation. The final equation contains three unknown parameters which requires the contact angle measurements with three probe liquids, with known surface tensions. Then, Table 8 shows the values calculated for the surface free energy (SFE) in this study which tells that the one-step anodization have lower values than the two-step anodization ones.

Table 8 The surface free energy values determined for the anodized surfaces.

	SFE (mJ/m^2)
P/ONE/Et1-10	-77
S/0.3/ONE/Et1-90	8
S/1/TWO/Et1-90/Et2-0	31
P/TWO/Et1-30/Et2-0	23
P/TWO/Et1-30/Et2-30	31

The disorganized oxide structures of the high-alloyed Al (6016) after anodization, comparatively to the Al alloy 1050 used in other works [57], are due to the alloying elements. In fact, it was figured out that, in our study, the enhanced porosity was due to the presence of intermetallic precipitates (containing Al, Si or Mg), as well as to the incorporation of phosphate anions during anodization, producing $AlPO_4$ species in the oxide layer. Therefore, the wettability results were directly attributed to the low ordering of the pores (high porosity and interconnected pores) and to the anions incorporation in the oxide layer. On the other hand, the increased pore depth (12 µm) achieved with H_2SO_4 electrolyte (sample S/1/TWO/Et1-90/Et2-0) in two-step configuration should be responsible for the high water and oil wettability (Wenzel state). In fact, as the pore depth increases, more difficult is the effective removal of electrolyte after the anodization

treatment; then, the remaining liquid with higher concentration in sulphate anions would induce higher affinity to water.

3.4 Conclusions

In this study, an anodization process was used to promote the surface nanostructuring of an Al alloy of the 6000 series. The alloy was previously microtextured by mechanical polishing. Anodization performed in one-step configuration gave a dimple-shaped surface structure with very thin AAO layers; hydrophilic and oleophilic behaviour was achieved in case of small dimple of about 31 nm whereas slightly hydrophobic and oleophilic character occurred for larger dimples (of about 223 nm). The anodization of polished samples in two-step configuration allowed to achieve porous Al oxide layers. Using H_2SO_4 electrolyte, narrow pores (diameter of about 29 nm) in a thick oxide layer was reached, while using H_3PO_4 electrolyte a higher porosity was achieved with larger pore sizes (~ 250 nm). In last case, the porous structures gave rise to superhydrophilic and superoleophilic wettability behaviours, typical of a Wenzel state.

This study provided a further insight in the role of intermetallic precipitates which greatly influenced the ordering of the oxides grown during the anodization process which in turn have a huge impact in the surface wettability. During anodization, these precipitates, due to their high electrical resistivity, are responsible for a higher heat evolution and, thus, by the local enhanced alumina dissolution. This situation promoted an increased porosity, particularly for the H_3PO_4 case.

The increased solid-liquid contact area, breaks the pressure-balance model leading to an easy liquid penetration inside the structures and a high hydrophilicity and oleophilicity behaviour is reached. It must be noticed that oil wettability of anodized bare Al-alloy surfaces has never been reported so far; the only results in the literature concern low-alloy or unalloyed Al surfaces coated with low energy films.

CHAPTER 4

Development and Optimization of doped WS$_2$-based Coatings deposited by Magnetron Sputtering

This chapter englobes the development and optimization of F/C doped WS$_2$-based coatings deposited by reactive magnetron sputtering method. The coatings were characterized in terms of morphology, structure, chemical analysis, tribological behaviour and wettability character in regard to water and non-polar liquids. The study in this chapter resulted in WS-CF coatings with selected thicknesses to be deposited over selected textured surfaces produced by anodization. This work has been carried out in the University of Coimbra at CEMMPRE research institute and at LED&MAT laboratory in IPN-Coimbra. Moreover, some tribological tests were also carried out in Czech Republic in the Technical University of Prague (CTU).
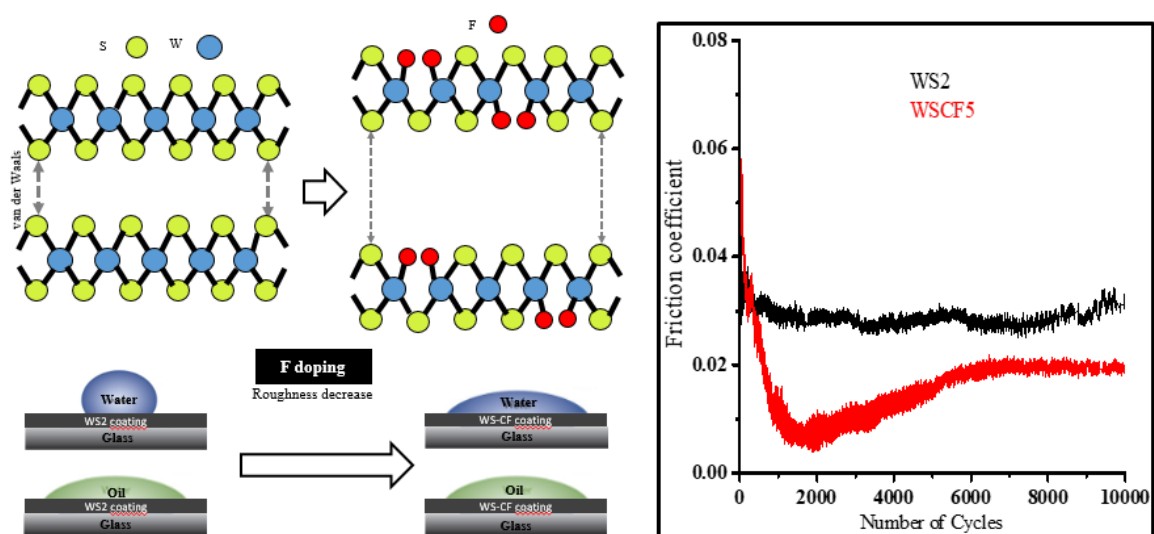
Overview – Part I

One of the main objectives of this study was to deposit WS_2-C based coatings with fluorine incorporation, in order to control the hydro-oleo/phobic-philic characteristics, without compromising the WS_2-C self-lubricating properties and high mechanical strength.

Previous works of the research group reported on the mechanical properties improvement of the WS_2 material by carbon (C) incorporation, as well as their friction performance. Furthermore, a huge amount of works has cited the F-riched polymeric coatings as having a significant role on surface wettability behaviour. Moreover, the F incorporation has been mentioned to also improve the hardness of coatings deposited by magnetron sputtering as well as increase their hydrophobicity.

Then, taking into account all this work background, the second part of this thesis was focused on the development and evaluation of the properties of WS_2 coatings deposited by reactive magnetron sputtering with both fluorine (F) and carbon (C) incorporation. It was used a reactive Ar/CF_4 gas mixture to deposit a set of 6 coatings with different F contents, which had a [1.3-1.9] μm thickness range. In this study, it was verified that the F/C incorporation in the coating did increase the hardness and decrease friction, comparatively to pure WS_2 coating, in room temperature and in high temperature conditions. Further, the F insertion unexpectedly increased the surface energy of the coating, leading to an increased water affinity. Another issue was that after a certain increase of the CF_4 flow rate, the F was not incorporated in the coating anymore. This was related with competitive etching mechanisms happening in the coating growth process, feature widely reported for reactive ion etching (RIE) processes, being not the focus of this study, still not well-understood yet for our deposition system.

The study presented in this next subchapter 4.1 was developed in the University of Coimbra at CEMMPRE research institute and at LED&MAT laboratory in IPN-Coimbra and resulted in a scientific paper already published in the Applied Surface Science journal (IF = 4.3).

4.1 Fluorine-carbon doping of WS-based coatings deposited by reactive magnetron sputtering for low friction purposes

4.1.1 Introduction

The automotive industry is known to have a great impact in the World economy due to the commercialization of a huge amount of diversified electronic systems and mechanical components [225]. Before the assemblage step, many mechanical devices require previous lubrication. The tools, for an efficient and durable lubricants' application should possess a combination of low friction and specific wettability properties. However, the European commission is nowadays more alerting on the use of greases or oils, applying restrictive rules, since most of these lubricants are harmful to the environment and human health [226-228]. Thus, materials and surface engineering is a potential solution for removing or, at least, reducing the lubricants' use by developing functional surfaces through the application of coatings able to provide self-lubricating properties and suitable contact angles in relation to lubricants (oils).

Transition metal dichalcogenides (TMDs) are materials with interesting electronic, optical, mechanical and magnetic characteristics which also triggered intensive research for self-lubricating purposes [128, 229]. Indeed, their anisotropic layered crystal structure allows to reach low friction coefficients mainly in vacuum or in dry air. TMDs' materials consist of a transition metal layer (e.g. Mo, W or Nb) sandwiched between two chalcogen layers (e.g. S, Se or Te), in which the atoms are covalently chemically bonded together while these layers are held together by weak van der Waals interactions [127].

Magnetron sputtering is considered a clean, reproducible and cost-effective method, widely used to deposit TMD coatings [230]. Pure sputtered TMDs exhibit columnar morphology, low hardness (< 1 GPa), with consequent very low load-bearing capacity, and low adhesion to the substrate materials. Their high porosity allows a high reactivity of the coating with oxygen in humid air environments, causing an increased friction and wear which strongly limit their application as self-lubricant only to dry or vacuum atmospheres [143, 145, 231]. Alloying TMDs with selected elements such as, Ti [147] or Cr [146] could improve the mechanical and tribological performances. Another alternative to improve the mechanical performance is to alloy TMD coatings with carbon

or nitrogen. Magnetron-assisted pulsed laser deposition or laser ablation allowed to produce dense self-lubricant W-S-C based coatings, less sensitive to air environment than WS$_2$, combining excellent frictional properties and good tribological performance in vacuum (coefficient of friction (COF) of ~ 0.03) and in humid air (COF of ~ 0.15), when tested against steel balls [232, 233]. Similar TMD-based coatings doped with carbon or nitrogen were deposited by magnetron sputtering [148, 149, 158]. The W-S-C coatings were also tribologically tested against steel balls at 30% of relative humidity (RH), and the COF values decreased down to ~ 0.06 when the load increased from 5 to 47 N [151]. These coatings were also tested at temperatures above 100 °C with COF values below 0.01, and the specific wear rates were almost independent of the temperature up to 400 °C [152]. Apart from the higher thermal stability depicted for the W-S-C system, lower wear volumes were also observed for this system, withstanding higher loads (1000 N) in humid air than other TMDs alloyed with carbon [156, 157]. Therefore, if it would be possible to add the good mechanical and tribological characteristics of the W-S-C coatings with a suitable surface wettability behaviour, the final surface functionality could be improved allowing a more efficient and controlled application of the lubricants and, then, reducing their consumption.

Wettability is a complex surface property which is commonly controlled by the roughness or/and by the chemical composition of the surface [2, 3, 195, 196, 234]. In regard to chemical modification for amphiphobic behaviour, polymeric-based coatings containing F radical [126] or silane (H-Si-H radicals) [235, 236] species are often used. These coatings are able to decrease the surface free energy and, then, induce repellence to particular liquids, although they have intrinsically low mechanical resistance and load-bearing capacity. Then, the purpose of this research was to provide a mechanically strong material with a specific wettability property, through the alloying of W-S-C coatings with fluorine using magnetron sputtering deposition. Fluorine alloying is well-known in many fields for changing specific properties of materials, such as: a) the refractive index for photovoltaic applications [123, 237]; b) the electrical properties to achieve more dielectric or conductive films [124], c) the mechanical properties for achieving ultra-low friction [121, 238] or even, d) the surface properties to avoid coagulation mechanisms in medical devices [125].

The fluorine is reported to deteriorate the hardness and the elastic modulus of the C-F or F-DLC sputtered coatings [115, 118, 239]. In relation to the water contact

angles, the fluorine alloying has shown to increase the coatings' repellence [240, 241], with no report in regard to oil wettability. Other authors sputtered MoS_2 and PTFE (C-F chains) and the produced coatings demonstrated a reduced sensitivity to relative humidity in the tribological assay [242]. Similarly, the tribological behaviour of $WS_2:CF_x$ films deposited by pulsed laser deposition showed less sensitivity to moisture than pure WS_2, at least until 50-60% of RH; these films depicted ultralow friction in dry air (COF $\leq$ 0.01) against stainless steel balls [159]. No results were presented concerning water or oil wettability. The same deposition method was used to deposit $WS_2:CaF_2$ coatings with very good lubrication performances (COF = 0.15) at high temperature (500 °C), with great potential for airspace industry applications [243].

In summary, fluorine doping of TMD coatings for wettability purposes is still not explored. Furthermore, the literature is scarce on the fluorine doping of TMDs-C for improvement of the mechanical properties. Therefore, a study on the F alloying of the W-S-C films for tribological applications at high loads in humid environments with further assessment of the surface coatings' wettability is still missing. In this study, these coatings will be developed to improve the mechanical properties/tribological performance and reduce the surface free energy, in order to validate their applicability on metallic materials for some applications.

4.1.2 Experimental

4.1.2.1 Production of the fluorine-carbon doped W-S coatings

The coatings were deposited by reactive magnetron sputtering on commercial glass, mirror-polished (100) Si, and M2 steel disc substrates. The latter were mechanically polished (RotorPol 21 model by Struers with 25 cm plate diameter) with SiC sandpapers, with increasing grit size, and diamond paste (3 μm). Prior to depositions, all samples were firstly degreased in acetone (15 min) and in ethanol (15 min) in ultrasonic bath and, then, air dried.

A semi-industrial DC closed field unbalanced magnetron sputtering machine (TEER Coating Ltd.) equipped with four cathodes was used for the depositions. The targets (380 x 175 x 10 mm^3) are vertically aligned and oppositely pair-paralleled with a substrate holder placed under rotation (20 rpm) in the centre at 30 cm distance (Figure 4.1). The vacuum chamber (~ 275 dm^3 volume capacity) reached a base vacuum pressure better

than 5 x 10^{-4} Pa by using a primary and diffusion pumping system. Prior to each deposition, the targets were sputter cleaned in an Ar discharge at 0.37 Pa. The opposite WS$_2$ targets were cleaned for 10 min with 1000 W power in each one; then, the shutter was rotated 90° in order to proceed to the metallic Cr target cleaning for 10 min duration at 2000 W, while the substrate holder was kept at 600 V in both cases. Immediately after, and moving the shutter 90° back again, a Cr interlayer of approximately 400 nm thickness was deposited during 10 min in order to improve the coating adhesion. For the WS-CF coatings' deposition, the fluorine-carbon alloying was promoted by using a reactive gaseous atmosphere of Ar + CF$_4$; the flow rates were controlled in order to keep the working pressure at around 0.4 Pa. Table 2 of Chapter 2 of this thesis summarizes the set of six coatings produced (WS2, WS-CF2, WS-CF5. WS-CF7.5, WS-CF10 and WS-CF15), when 1000 W was applied in each WS$_2$ target for 1h deposition time. In these coatings, the CF$_4$ flow rate was increased from 0 to 15 sccm, respectively. Before opening the chamber, the substrates were left in vacuum in order to reach room temperature and, then, industrial N$_2$ gas was blown inside until reaching atmosphere pressure.
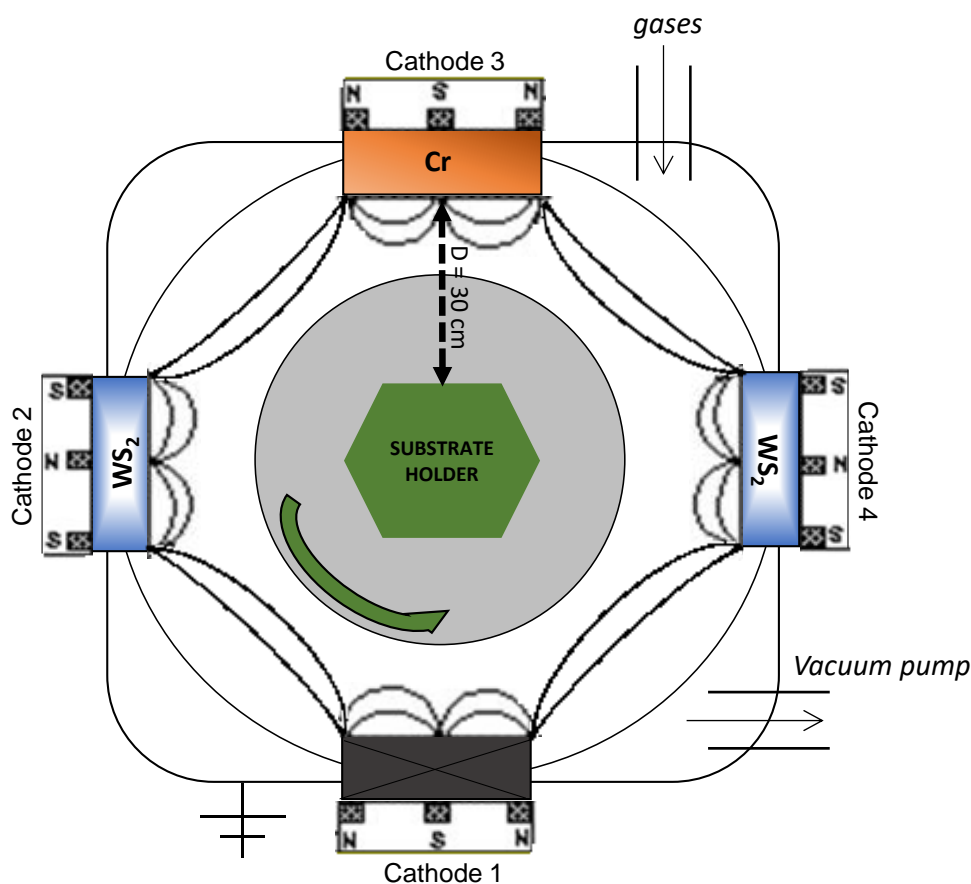
Figure 4.1 Schematic diagram of the interior magnetron sputtering chamber mounted with three targets (two of WS$_2$ and one of metallic Cr) used for the deposition of the fluorine-carbon doped WS-based coatings.

4.1.2.2 The characterization of the coatings

The cross-section/top view morphologies and thickness of the coatings deposited on silicon substrates were observed by scanning electron microscopy (SEM) (ZEISS Merlin – Field Emission Gun, High Resolution with Charge Compensation) operating at 2 (cross-section) or 4 (top view) kV at 7 mm of working distance (WD), in secondary electron mode. For chemical composition, wavelength dispersive spectroscopy (WDS) was used (Oxford Instruments) at 10 kV acceleration voltage and 5 mm WD. The surface coating roughness was measured by a 2D profilometer (Perthometer S4P, Perthen).

X-ray photoelectron spectroscopy (XPS) was performed in an ultrahigh vacuum system at a base pressure of around 10^{-7} Pa using a Kratos AXIS Ultra HAS with VISION software for data acquisition and *CasaXPS* software for data analysis. XPS was carried out with a monochromatic Al Kα X-ray radiation source (hν = 1486.7 eV) with a take-off angle of 45° from the horizontal plane of sample surface, operating at constant power 90 W (15 kV), in FAT mode (Fixed Analyser Transmission), with a pass energy of 40 eV for regions ROI and 80 eV for survey. The acquisition data was performed with a pressure lower than 1×10^{-6} Pa and a charge neutralisation system was also used. Binding energies were calibrated using the oxygen peak O1s (531.0 eV) [172]. Moreover, in order to accurately determine the elemental chemical states, an Ar$^+$ ion etching step of 20 min duration (3 x 3 mm^2 area, 2.2 kV acceleration tension, 70 nA of emission current) was conducted to remove the surface top layers. The crystal structure of the coatings deposited on glass substrates was analysed by X-ray diffraction (XRD) (PANalytical X'Pert Pro MPD system) using Cu Kα radiation (λ = 1.54 Å) (45 kV and 40 mA) in grazing angle (5°) in 10-80° 2θ range.

The adhesion of the coatings was evaluated on steel substrates by *scratch* test (Rockwell indenter) according to ISO EN-1071-3 in progressive load mode (4 – 50 N) at a rate of 100 N/mm, which allowed to calculate the adhesive critical load (L_c) at the time the film starts to fail, exposing the substrate. The critical load values were obtained by analysis of the failure events in the scratch track by optical microscopy provided with an *ImageJ* software.

The hardness (H) and elastic modulus (E) of the coatings were measured by depth-sensing indentation (MicroMaterialsNano Tester) using a Berkovich diamond indenter. The indentations were set with 3 mN maximum load in order to ensure an indentation depth less than 10 % of the coatings' thickness. Sixteen indentation measurements were

recorded on each specimen for accurate determination of both hardness and elastic modulus values. Experiments of the tribological behaviour were carried out with a homemade ball-on-disk tribometer at room temperature (22 °C) with 35-40% of RH. The sliding counterpart was a 100Cr6 steel ball with diameter of 10 mm, the linear speed was 0.1 m/s and the rotational radius was 7.5 mm. The tests were carried out at 20 N normal load (~700 MPa contact pressure), sliding for 10 000 cycles. The coefficient of friction (COF) recorded was the average value of the whole sliding test, unless stated otherwise. The morphology of the wear tracks and the worn scars of the contact surfaces was respectively examined by SEM and optical microscopy (ZEISS) and the depth profile of the wear tracks was evaluated by 2D profilometry. After the tribological test, the chemical composition of the wear tracks was also assessed with energy dispersive spectroscopy (EDS). The specific wear rates of the film and the counterpart ball were determined according to the optimized formulas by ASTM standards for a pin-on-disc test [187, 244]. Then, the 2D depth profiles of the wear tracks were firstly used with the AxioVision software help in order to get an accurate average value of the cross-sectional area of the wear track. The wear volume resulted by multiplying the cross-sectional area of the track by the perimeter of the track, that value which in turn was divided by the load and total sliding distance for the specific wear rate determination. Likewise, the average diameter of the scar (*d*) determined using *ImageJ* software was used for the wear volume calculation of the steel ball according to Equation 2.3 previously expressed in Chapter 2.

Static contact angle (CA) measurements (DataPhysics OCA Analysis system) were carried out on coatings deposited on glass substrates to study the wettability behaviour using the sessile drop method by applying liquid droplets of about 2 µL at room temperature. A minimum number of 10 measurements were carried out on each sample. The liquids used for wettability assessment were ultrapure water and α-bromonaphthalene (non-polar liquid acting as oil) with surface tensions (γ_{LV}) of 72.8 and 44.5 mN/m, respectively. The surface free energy (SFE) of the developed coatings was determined using the OWRK model [182, 183].

4.1.3 Results and Discussion

4.1.3.1 Morphology and Chemical Composition

The top-view and cross-section morphologies of the WS-C/F coatings are presented in Figure 4.2 (a)-(f) as section I and II, respectively. The coatings' surface has a

typical cauliflower morphology for low CF_4 flow rates. For higher flows, the films become denser although fissures could be detected on the surface, particularly for WS-CF10 and WS-CF15 coatings. WS2 and WS-CF2 coatings have high porosity all over the sample; however, quite good compactness was observed in the cross-section of WS-CF5 and WS-CF7.5 coatings. In WS-CF10 coating, fissures are detectable at least until half thickness. For the maximum CF_4 flow rate used in the deposition of WS-CF15 coating, the film porosity largely increased (Figure 4.2 II (f)).

	SEM		III WDS						
	I Top surface	II Cross-section	Chemical Composition (at.%)						
			W	S	C	F	O	S/W	F/C
WS2	(a)	(a)	34.0	52.5	8.0	0	5.5	1.54	-
WS-CF2	(b)	(b)	31.2	45.3	10.7	4.3	8.5	1.45	0.4
WS-CF5	(c)	(c)	27.2	43.7	14.2	9.5	5.4	1.61	0.7
WS-CF7.5	(d)	(d)	24.2	42.2	14.0	7.1	12.5	1.74	0.5
WS-CF10	(e)	(e)	23.0	38.2	15.6	2.2	21.0	1.67	0.1
WS-CF15	(f)	(f)	20.0	33.3	23.5	2.0	21.2	1.66	0.1
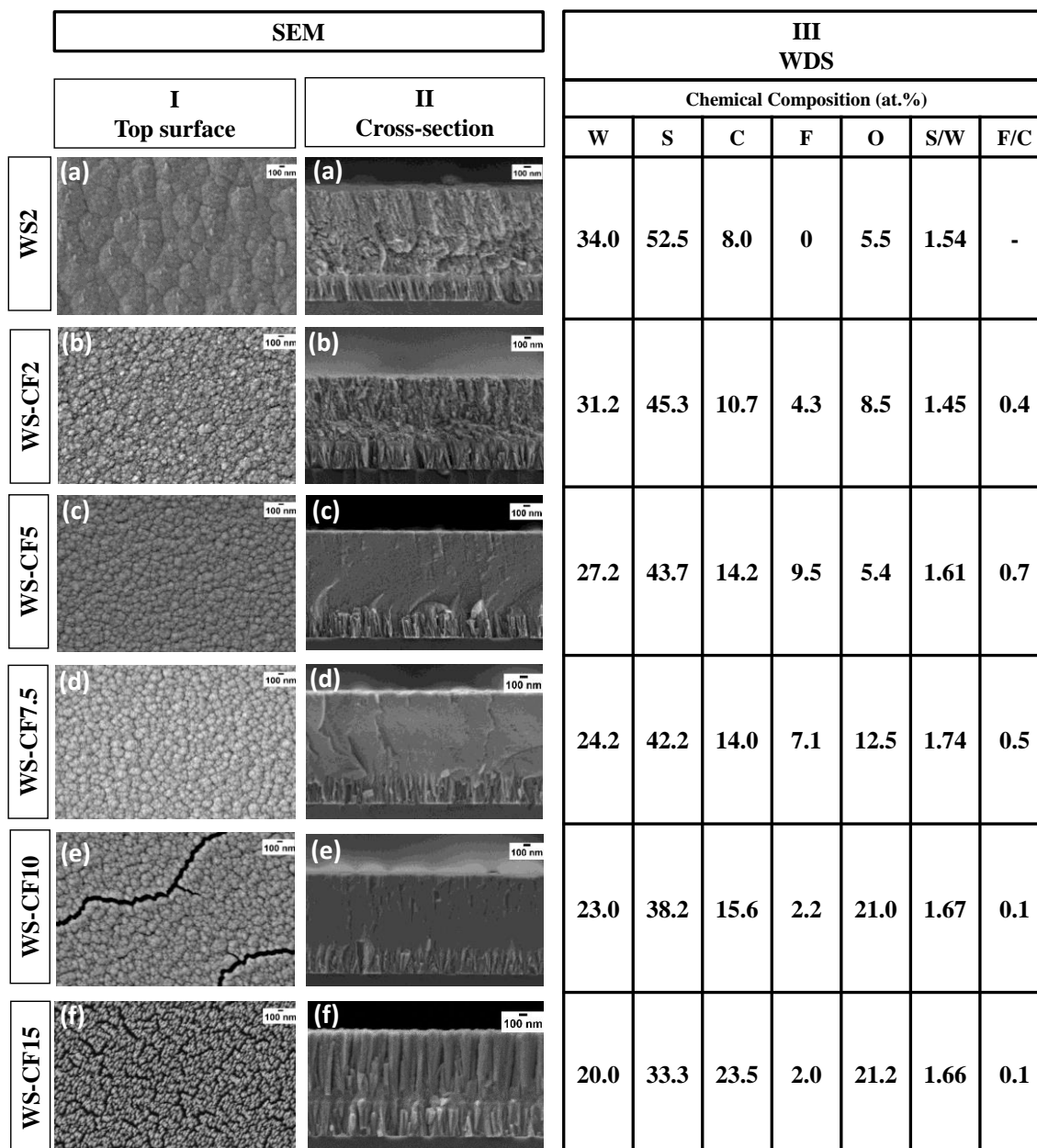
Figure 4.2 SEM characterization of the WS-C/F coatings in regard to TOP-SURFACE (I) and CROSS-SECTION (II) views and the chemical composition obtained by WDS (III).

In regard to the chemical composition, tungsten and sulphur contents decreased with increasing CF_4 flow rate (Figure 4.2, section III); a maximum S/W ratio of 1.74 was reached when depositing with 7.5 sccm CF_4 flow rate. Moreover, the maximum of fluorine insertion in the coatings (9.5 at. %) was achieved with 5 sccm of CF_4 flow rate; for higher values, a decrease in the F content was observed, showing that there was no direct relationship between CF_4 flow rates and F-content in the coatings. Besides, the decrease of the F content corresponded to a significant increase in the oxygen and carbon incorporation in the coatings (WS-CF10 and WS-CF15). These results can be understood on the basis of a CF_4-containing discharge:

(i) Optical emission spectrometry (OES) studies of sputtering mechanisms of PTFE or graphite targets in Ar/CF_4 plasmas showed that CF_3, CF_2, CF and C_2F_2 radicals, CF_4 molecules as well as C_2 and F_2 dimers can mainly be found [118, 245]. For low CF_4 partial pressure, CF and CF_2 radicals are predominant over C_2F_2 radicals and attachment of CF_x species occur over the substrate. On the other hand, for higher CF_4 partial pressures, higher amount of fluorine etchants (in particular C_2F_2 species) are formed promoting a high desorption of CF_x from the growing film which, in extreme conditions, only led to the deposition of graphitic films (C-C chains) [118].

(ii) It is well known that water vapour and carbonaceous species exist in the chamber walls (common vacuum contaminants) when the vacuum system is not able to properly thermally degas it [122]. Then, for high CF_4 partial pressures, C-F species become abundant in the vacuum chamber and can start to interact with the chamber walls, scavenging species such as OH^-, H^+, O^-, O^{2-}, etc…, leading to the formation of HF, CO, CO_2 and COF_2 additional compounds in the discharge, as previously revealed by OES measurements [246-248]. The release of these species into the discharge will surely interfere with the coating growth, i.e. the arrival to the substrate of those additional reactive species will create a complex bonding process, determining the elemental incorporation in the solid coating. An important factor to be considered is the enthalpy of formation ($\Delta_f H°$) of the different gaseous compounds in the plasma, which can determine which should be the species incorporated in the growing film.

The very high enthalpy of formation ($\Delta_f H°$) of different gaseous compounds containing F (e.g. WF_6 = -1721.7 kJ/mole; SF_6 = -1220.5 kJ/mole, CF_4 = -933.6 kJ/mole or HF = -273.3kJ/mole) compared with the energies of the bonds characterizing the solid compounds to be potentially deposited (WO_3 = -842.9 kJ/mole, WS_2 = -202.7 kJ/mole or

WC = -44.4 kJ/mole) will create a competitive bonding process between all the reactive, neutral and excited species arriving to the growing film. Therefore, for high CF_4 partial pressures, the incorporation of O and C in the coatings is predominant over F, which is preferentially removed from the deposition chamber under the form of gases [126, 245]. So, the deposition model can be resumed by the reaction mechanisms schematically represented in Figure 4.3 for (a) low (Deposition Regime) and (b) high (Deposition vs. Etching Regime) CF_4 partial pressure cases, which could explain the coatings chemistry encountered.
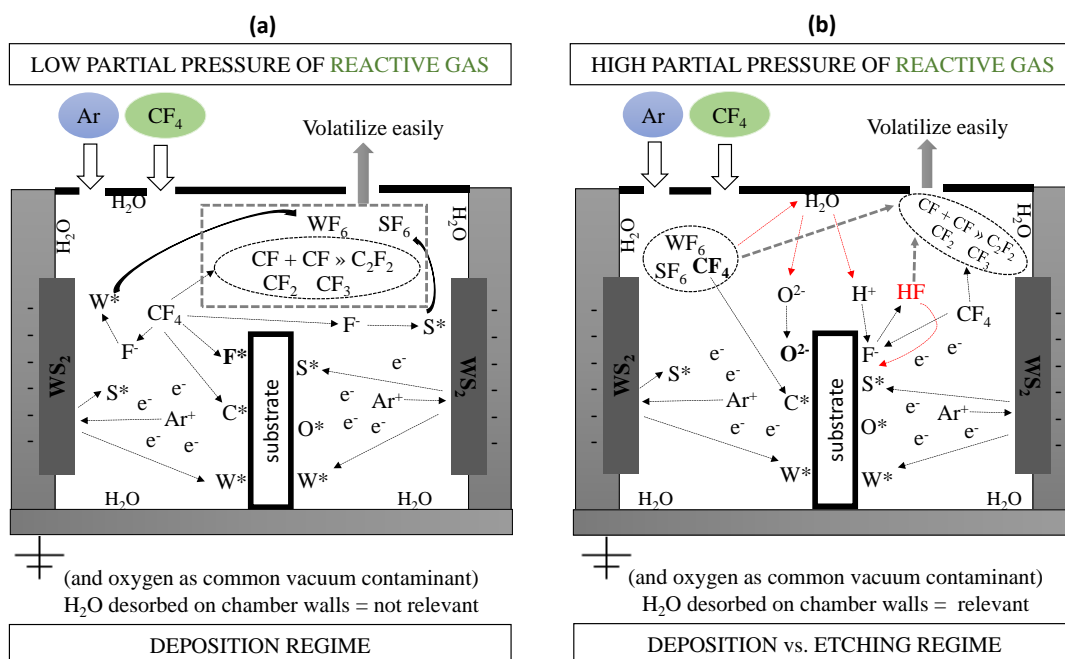
Figure 4.3 Schematic representation of the growth mechanisms in (a) low and (b) high CF_4 flow rate scenarios.

Concerning the deposition rate of the coatings with the CF_4 flow rate increase (graphic profile presented in Figure 4.4), higher value was measured for WS_2 coating (1.61 µm/h) when compared to F-containing coatings, i.e. deposition in a reactive Ar/CF_4 atmosphere led to lower growth rates (1.2-1.3 µm/h) despite the further incorporation of additional elements (F, C, O) in the growing film.

Several factors can influence in different sense the deposition rate presented in Figure 4.4, and, when combined, can justify the small changes observed among the different coatings produced. The points can be as follows:

i) as the SEM cross-sections images show, the incorporation of F/C leads to a significant improvement on the density of the coatings (same mass in a lower volume) which should give rise to a decrease of the deposition rate;

(ii) the F/C incorporation in the growing film should increase the mass of the depositing material and, consequently, the deposition rate;

(iii) the target sputtering rate in a reactive atmosphere containing CF_4 can be lower since, one the one hand, a low number of potential Ar bombarding ions exists inside the chamber (the discharge pressure is kept constant) and, on the other hand, adsorption on the target surface of the reactive species resulting from the CF_4 molecules' decomposition in the discharge which can interfere in the target sputtering process;

(iv) the O resulting from the release of adsorbed species on the chamber walls is one more specie participating in the film growth and, therefore, contributing to the deposition rate;

(v) the attachment of the deposition species in the growing film can be affected by the presence of reactive F-C species, which are able to be bonded to other elements, forming gaseous species, which are easily evacuated from the chamber, leading to a decrease in the deposition rate.
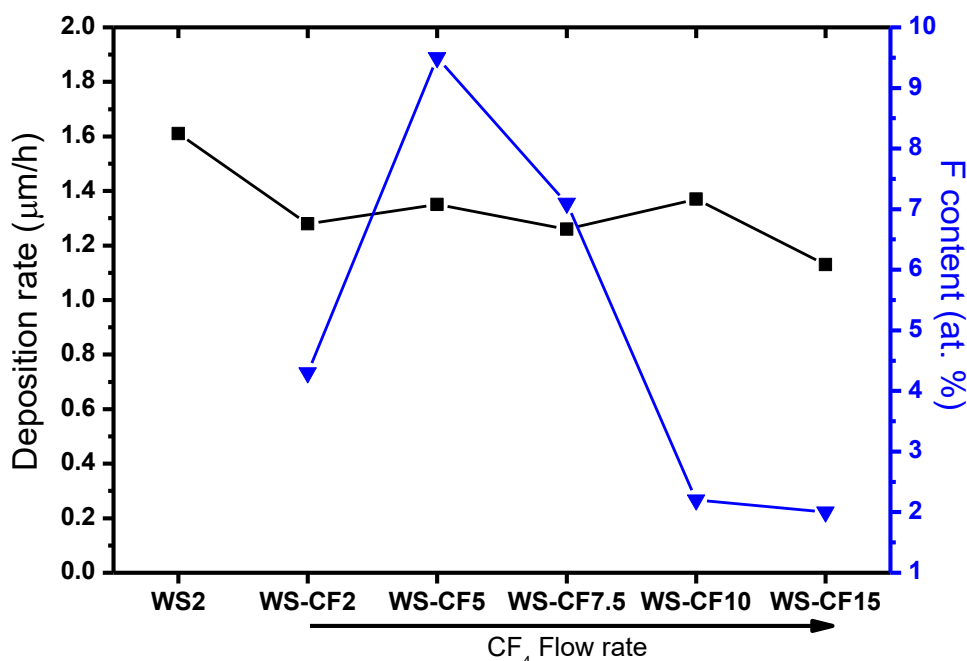
Figure 4.4 Deposition rate and fluorine content obtained by SEM/WDS measurements of the WS-CF coatings as a function of CF_4 flow rate.

Overall, all these factors mentioned above may also justify the slight increase in the deposition rate as well as the fluorine content (9.5 at. %) when the CF_4 flow rate increases from 2 to 5 sccm and they also may explain the lower deposition rate (1.13 µm/h) obtained for the WS-CF15 coating, when using the highest CF_4 flow rate.

XPS was used to investigate the elemental bonding states in the WS-CF coatings in order to understand the fluorine chemical state. Figure 4.5 (a)-(c) show as representative cases, respectively, the W4f, S2p and C1s XPS spectra acquired for WS2 coating without Ar$^+$ ion etching and Figure 4.6 (a)-(d) show as representative cases, respectively, W4f, S2p, C1s and F1s XPS spectra for WS-CF5 coating before and after ion etching.

Without erosion, O1s peaks of both coatings (not shown) show, besides the contribution at 531 eV corresponding to the O-W bonds typical of W^{6+} and W^{4+} states, a broad-peak for higher energies which should be assigned to bonds with other elements of the contamination layer and/or to other more electronegative elements than W, e.g. carbon, fluorine or sulphur. After bombardment cleaning, this peak almost disappeared.
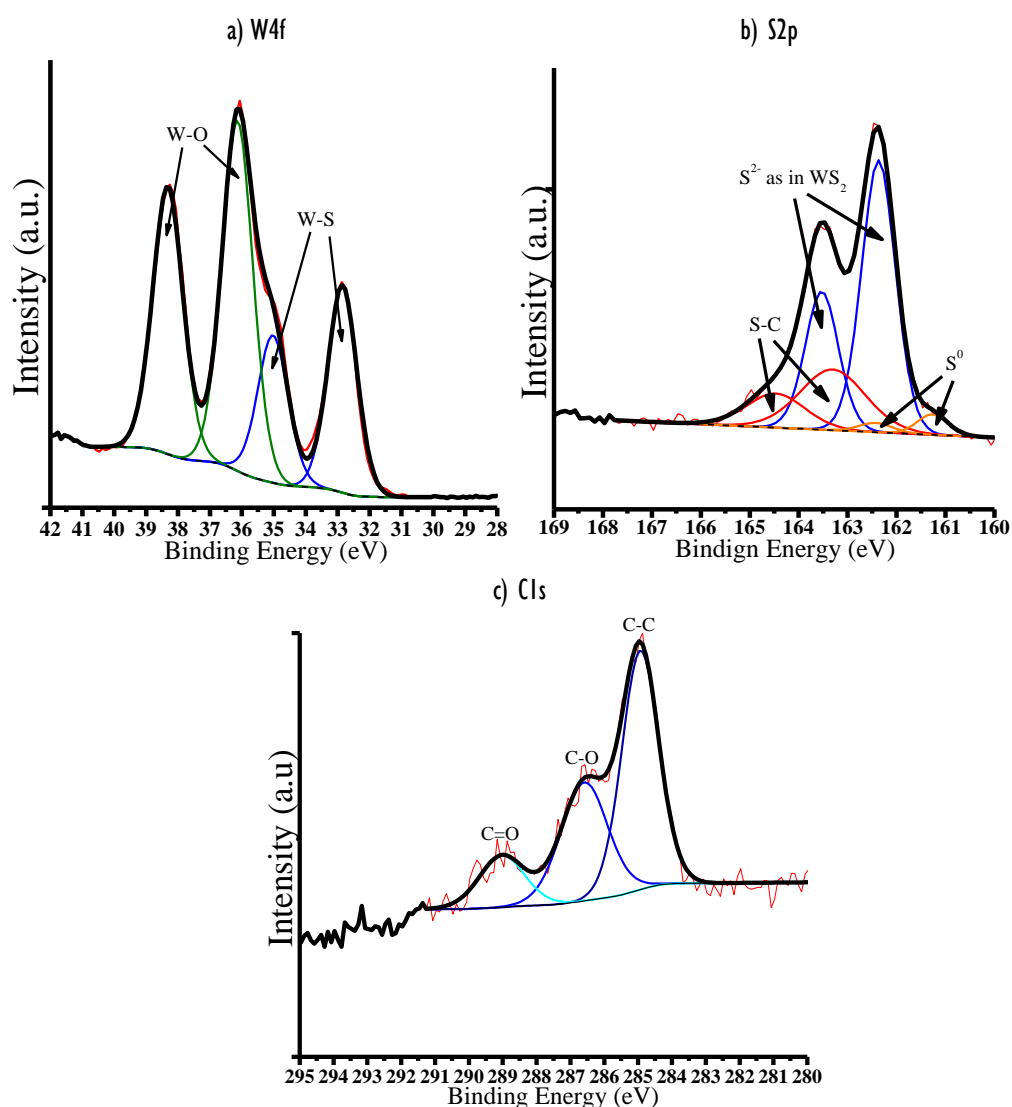
Figure 4.5 XPS analysis of WS2 coating without Ar$^+$ etching represented as (a) W4f, (b) S2p and (c) C1s.

Similar situation occurred with C1s peak. Before surface cleaning, C1s region peaks (Figure 4.5 (c) and Figure 4.6 (c)-i)) were fitted with three components at binding energies (E_b) close to 285.0, 286.7 and 288.8 eV, contributions assigned to C-C, C-O and C=O functional groups, respectively [249]. These peaks, typical of contamination layers, disappeared after Ar^+ bombardment and only a small remaining peak close to 284.0 eV was detected for WS-CF5 case (Figure 4.6 (c)-ii)). This peak can be assigned to the C-W bond as it was found in previous works for W-S-C films [250]. The possible presence of F and O in the WS-CF5 coating (Figure 4.2 – III) can justify the slightly higher Eb values in relation to W-S-C films (in the range 283.0-283.5 eV) [251].

Before contamination cleaning, W4f spectrum of WS2 film can be fitted with four main peaks into two doublets, as represented in Figure 4.5 (a), one assigned to WO_3 contribution at ~36.0-38.0 eV [252] and, the other, at ~33.0–35.0 eV corresponding to the W-S bond [250, 253, 254]. To achieve a good fitting, three doublets are necessary in the WS-CF5 coating, at ~32.3-34.5 eV, ~33.1-35.3 eV and ~36.0-38.2 eV (see Figure 4.6 (a)-i)). These doublets can be assigned to the W-C (in good agreement with the C-W bond detected before in the C1s peak), W-S and W-O bonds, respectively. W-C and W-S bonds are slightly shifted to higher E_b energies, one more time due to the possible incorporation of F and/or O in the phases structurally forming the films. As it will be shown later, the lattice distance of (0001) plans is slightly increased in the F-containing coatings which can be a sign of the presence of F in the WS_2 lattice. This hypothesis is supported by the occurrence of the F-W bond in the F1s peak at 684.6 eV (see Figure 4.6 (d)-i)) [255]. After ion bombardment, the same three W4f doublets, observed before for WS-CF5 coating, are visible (see Figure 4.6 (a)-ii)). No significant differences in the peak positions can be detected.

The W-O contribution strongly decreases and, as it would be expected, was much higher in the WS-CF10 coating (not shown) than in the WS-CF5 coating due to its much higher O content (see Figure 4.2 – III). Furthermore, for WS-CF10 coating, the F-peak almost vanished after erosion in good agreement with the WDS chemical composition already shown in Figure 4.2 III).

The main features in the S2p peaks of WS2 and WS-CF5 coatings before ion cleaning (Figure 4.5 (b)-i) and Figure 4.6 (b)-i)) are in accordance to a previous work [250]. Firstly, the need to introduce a second doublet at high E_b values (163.3-164.5 eV) was suggested to be due to the S-C bond, either from the carbon of contamination (WS2 case)

or incorporated in the coating (WS-CF5 case). Furthermore, another doublet at 161.3-162.4 eV was added to the fitting of WS_2 spectrum also assigned to elemental sulphur (S^0) as a result of mixed-oxygen environments [254, 256].
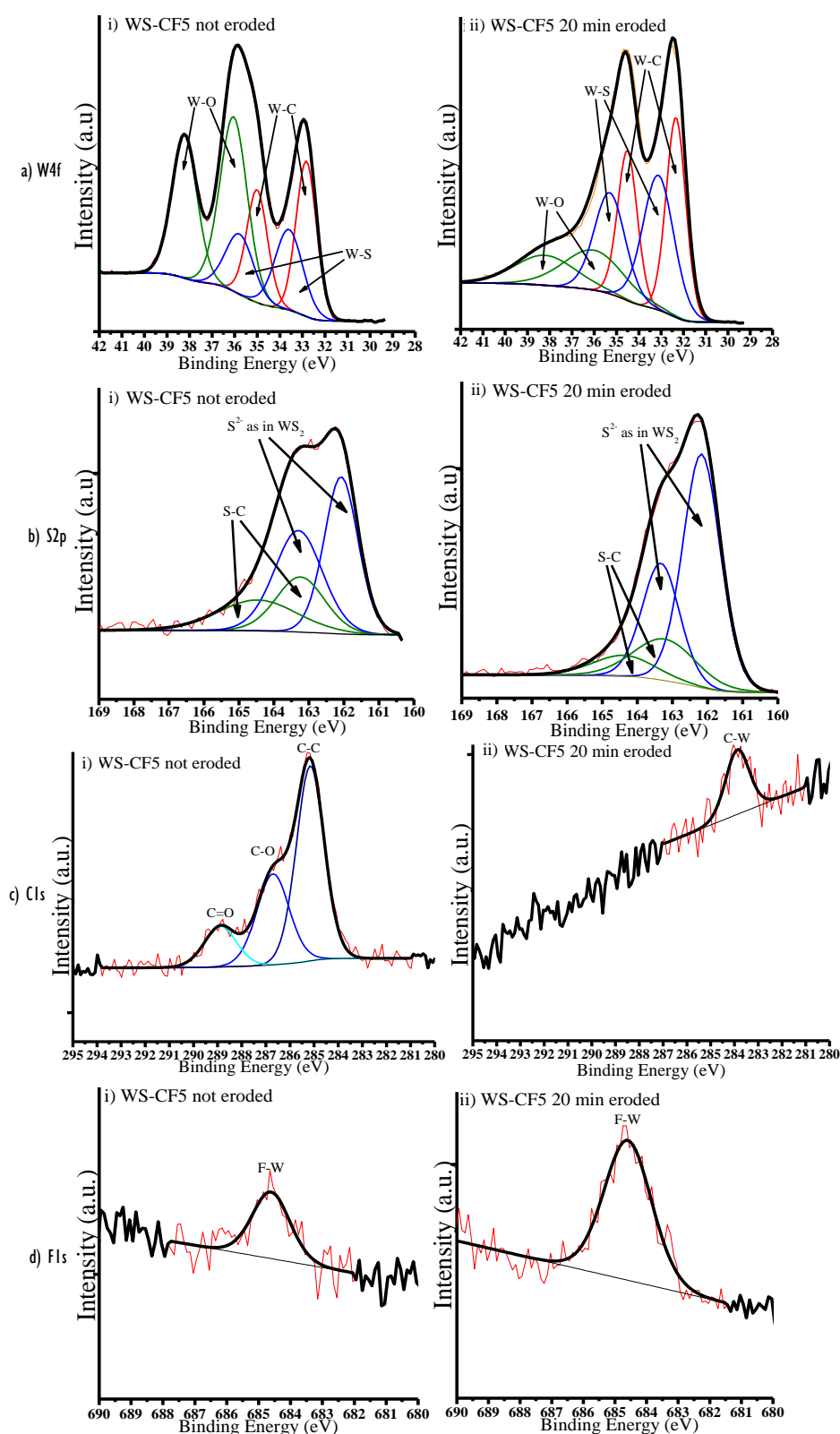
Figure 4.6 XPS analysis of WS-CF5 coating with and without Ar^+ etching represented as (a) W4f, (b) S2p and (c) C1s.

Secondly, the definition of the doublet is lost when C/F is incorporated which was attributed to an evidence of disorder or a multiplicity of chemical states, which both occur when other elements are added to WS_2 coatings. This latter evidence is reinforced when the coatings are ion bombarded for contamination cleaning (Figure 4.6 (b) – ii)). In this case, further disorder takes place and broader peaks are achieved. The main difference between the present work and that previous one is the fact that after ion bombardment there is a slight shift to higher E_b values inversely to what was observed before. The explanation for the shift to lower E_b in our previous works was based on deficiency in sulphur in the WS_2 phase, due to its preferential sputtering during the ion cleaning of the surface. However, in the current study, this preferential sputtering of sulphur will increase the importance of the F/O atoms that can be incorporated in the S-containing phases, moving the S-W peaks to higher E_b energies.

In conclusion, from XPS results it can be suggested that the coatings deposited in CF_4 containing atmospheres will have a phase composition similar to the W-S-C films deposited in previous works, i.e. a WS_2 phase co-existing with another phase, probably amorphous, containing preferentially C and W. In both these phases in the coatings, F and O should be incorporated in these phases as the shifting for higher E_b energies of XPS peaks suggests.

4.1.3.2 Structure analysis

XRD analysis was performed over the 2θ range from 10° to 80° (Figure 4.7). The single W-S coating presents the characteristic peaks of the hexagonal WS_2 structure, in agreement with the ICDD powder diffraction file and literature results [257, 258].

The low intensity of the (002) peak at $2\theta \approx 14$° confirms that low number of basal planes are parallel to the substrate surface. The highest intensity peak was at $2\theta \approx 34$° corresponding to (100) plan. The asymmetry with the long tail for higher angles, due to planes (102) and (103), is a feature of a turbostratic stacking of S-W-S single layers, corresponding to the family of planes (10L) with L = 1, 2, 3. Finally, there are two more peaks at $2\theta \approx 60$° and $2\theta \approx 70$°, which are assigned to the (110) and (108) planes, respectively, typical pattern of sputtered WS_x. Even using the glancing angle mode, in all the three diffraction patterns a small peak occurs at $2\theta \approx 44$°, indexed as the (110) plane from the chromium interlayer.
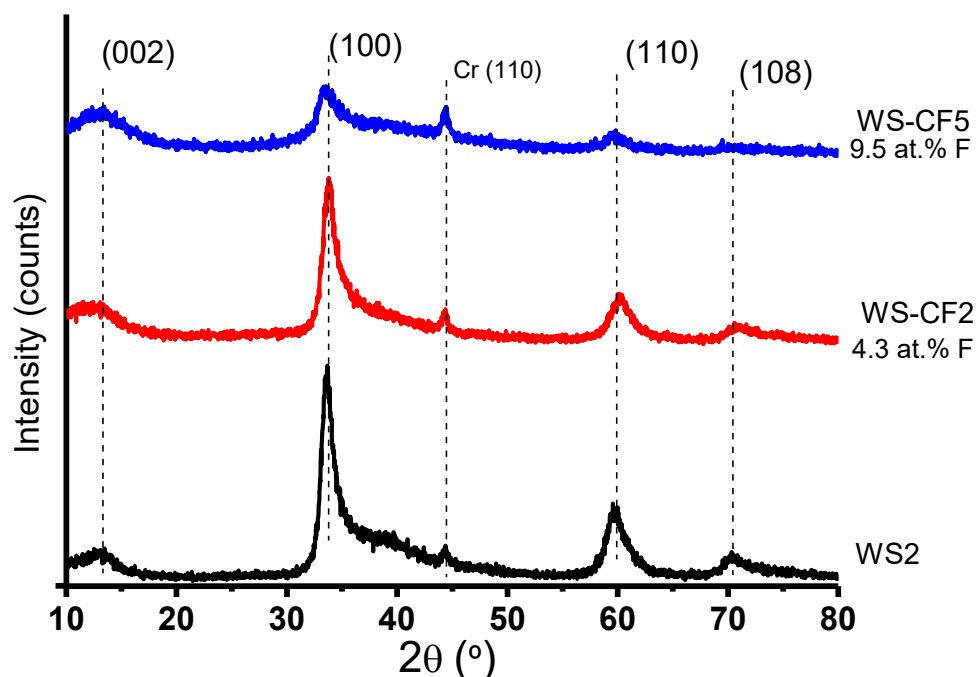
Figure 4.7 XRD diffraction patterns of the WS2, WS-CF2 and WS-CF5 coatings produced in reactive sputtering.

For F-containing coatings, only the ones deposited with 2 and 5 sccm of CF_4 show crystallinity, although broader and less intense peaks are observed in comparison to single W-S films. All the other coatings did not show signs of crystalline peaks suggesting an amorphous character. These structural changes have already been observed for WS-CF coatings deposited by PLD method using both WS_2 and graphite fluoride targets [159]; the authors also reported that the fluorine incorporation caused either an increasing disorder of the WS_2 structure or an expansion of the d-spacing in basal direction. A similar result was also detected in this study with the (002) peak slightly shifted to lower angles in comparison to pure W-S film, supporting our previous conclusion from XPS results, that F should be incorporated in the WS_2 phase. Moreover, since the C-W bond was detected in XPS analysis, the presence of possible WC grains should not be disregarded; however, in this case, they should likely be very small (nanoscale level) and, thus, not detectable by XRD.

4.1.3.3 Mechanical properties

It is commonly reported in the literature that fluorine incorporation in C-based sputtered coatings leads to the deterioration of the mechanical properties [118, 121]. Figure 4.8 presents the values of the hardness (H) of WS-CF sputtered coatings as a

function of the CF_4 flow rate. Pure sputtered WS_2 is very porous: alloying with F/C led to an improvement of the coating density and, consequently, of the hardness (from 0.13 ± 0.01 GPa up to around 3.50-4.00 ± 0.29 GPa), although a decrease was after observed when the F content was vanished.
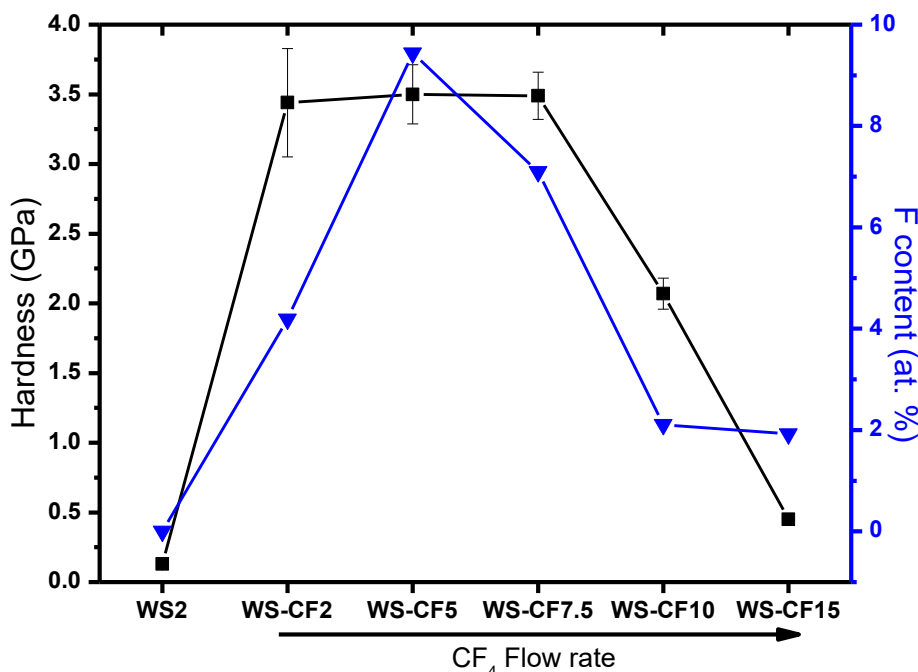
Figure 4.8 The hardness of the WS-C/F coatings plotted as a function of the fluorine content when the CF_4 flow rate was increased from 0 to 15 sccm.

The hardness values can be discussed in the basis of both the chemical composition and the morphology of the films. The strong increase in the hardness of the coatings deposited with lower CF_4 flow rates is due to the synergetic action of the improvement in the density of the films (decrease of the porosity) and the incorporation of C in the coatings. As demonstrated in previous research works [152, 155], these two factors are interconnected and led to the improvement of the mechanical behaviour of the coatings. For the films deposited with the highest CF_4 flow rates, a high number of fissures and a significant increase in the open porosity are observed which, in addition to the very high O content measured, justify the decrease in the hardness. The reduced elastic modulus (E) values follow the same trend as the hardness.

Figure 4.9 shows the scratch tracks performed up to 50 N load and Table 9 presents the adhesion critical loads (L_c) values corresponding to the point where the coating starts to fail in the coating/substrate interface. The first failures occur with the exposure of the coating/substrate interface, being the cohesive critical load not identified.

A similar trend to the hardness could be observed with a first improvement on the adhesion with the addition of F but with a sudden degradation of the L_c values when using higher CF_4 flow rates which, as shown before in Figure 4.2 Section I e), should be related with the existing extensive porosity and cracking occurring in the as-deposited conditions.
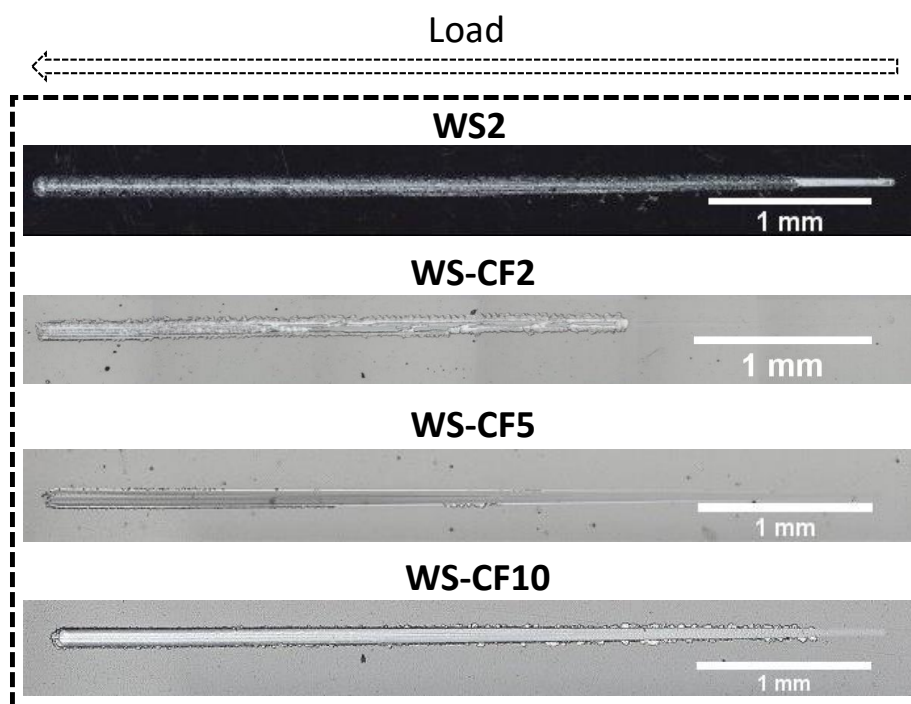
Figure 4.9 The scratch profiles obtained of 4 selected coatings as the indenter load was progressively increased until 50 N.

Table 9 The critical loads (L_c) obtained for four WS-C/F coatings deposited and comparison with their respective fluorine content.

Coating	at. % F	L_c (N)
WS2	0	11.0
WS-CF2	**4.3**	**18.7**
WS-CF5	**9.5**	**16.6**
WS-CF10	2.2	7.8

4.1.3.4 Wettability and preliminary friction/wear properties

The wettability of the coatings to water (WCA) and oil (OCA) is summarized in Figure 4.10. The fluorine insertion did not influence the oil repellence, with all coatings showing an oleophilic character; however, a strong decrease in the water contact angle from 118° (WS2) down to 71° and 40° for WS-CF2 and WS-CF5, respectively, was achieved. Moreover, a slight decrease on the coating roughness was observed as the fluorine was increased, as depicted in Table 10. The surface free energy (SFE), a key

parameter to understand the adhesion phenomena of surfaces, was calculated based on the OWRK approach [29, 190]. As it would be expected for lower roughness values, the SFE results corroborate the values of the contact angles, i. e. to the decrease in the WCA corresponds an increase in the surface free energy. Furthermore, this SFE increase can also be a consequence of the fluorine incorporation in the crystalline structure, favouring the presence of specific crystallographic planes, as shown in other systems, such as the Zr-doping of UO_2 structures [259]. Thus, the surface wettability is influenced by both the chemical nature and the roughness of the surface. Strangely, the fluorine insertion did not lead to enhanced repellence as it would be expected, since surfaces based on fluoralkilsilane radicals are well-known as being hydrophobic.
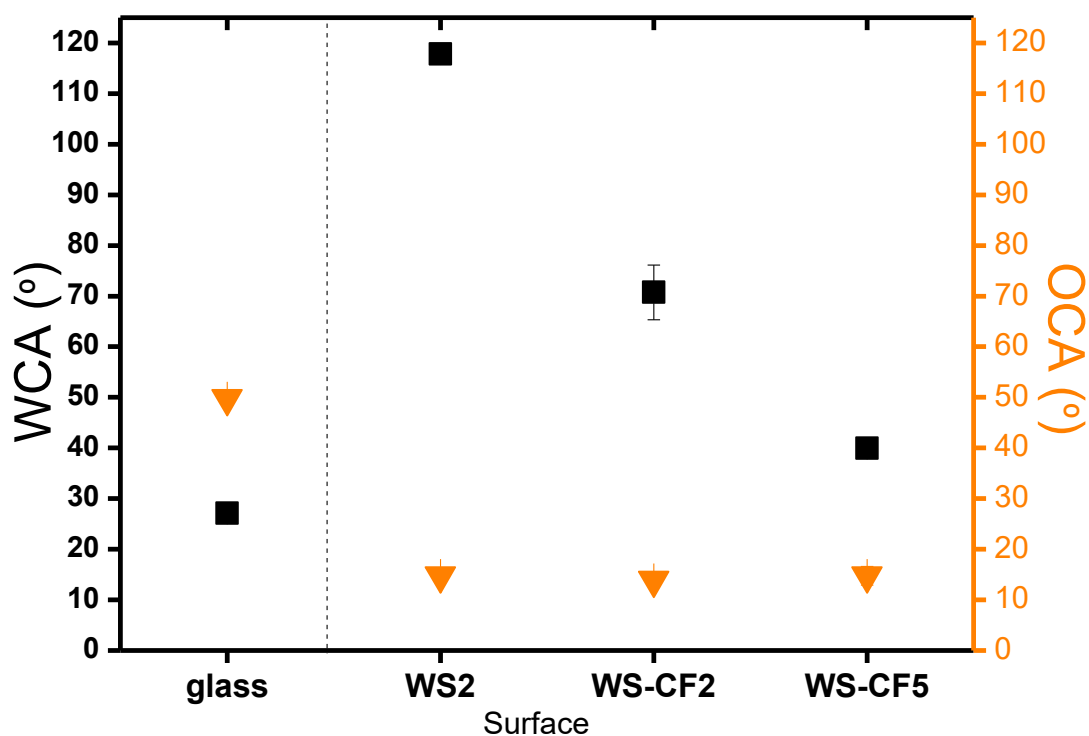
Figure 4.10 Wettability results of WS-C/F coatings: contact angle values measured in regard to water (WCA) and oil (OCA).

Table 10 SFE determination of the WS-C/F coatings according to their roughness and fluorine content.

Coating	F content (at. %)	Roughness (Ra) (μm)	WCA (°)	OCA (°)	SURFACE FREE ENERGY (mJ/m²)
WS2	0	1.15 ± 0.39	117.8 ± 0.5	14.8 ± 0.8	42.7
WS-CF2	4.3	0.10 ± 0.02	70.7 ± 5.4	13.9 ± 1.0	51.3
WS-CF5	9.5	0.08 ± 0.01	40.0 ± 1.9	14.8 ± 1.8	69.1

Figure 4.11 (a) presents the evolution of the friction coefficient during the sliding tests performed in dry condition at room temperature (RT) for the WS2, WS-CF2 and WS-CF5 coatings. In spite of the significant difference in the COF trends, the average of the experimental values of tribological tests are not significantly different, as shown in Table 11. WS2 shows a typical behaviour of these coatings when tested in humidity-containing atmospheres. It follows a COF decrease in the running-in period, corresponding to the alignment of WS_2 basal planes in the sliding contact, afterwards, strong instabilities are then observed related to the destruction and reformation of the low friction tribolayer [148, 154]. The presence of humidity leads to an increase of the interplanar bonding energy, due to the oxidation of the dangling bonds in the S-W-S layers, increasing the friction coefficient. The shearing forces are then able to easily destruct the soft tribolayer, creating abundant wear debris that can adhere to the counterbody. Note that, when flaking from the coating, these wear debris are not oxidized (see zone 4 and 5 in Figure 4.12 (a) - III). Fresh material from the coating can restart the reorientation process in some parts of the wear track which, again, can induce a COF lowering. However, due to the strong detachment of wear debris, the overall wear resistance of the coating is quite low (see Table 11). Zones 2 and 3 in Figure 4.12 (a) - II show a part of the wear track where low O-content, disaggregation and completely worn zones can be identified. The adhered material in the ball (Figure 4.12 (a) - IV) is mainly composed by oxides (Fe and W) although vestiges of W-S material were also detected.
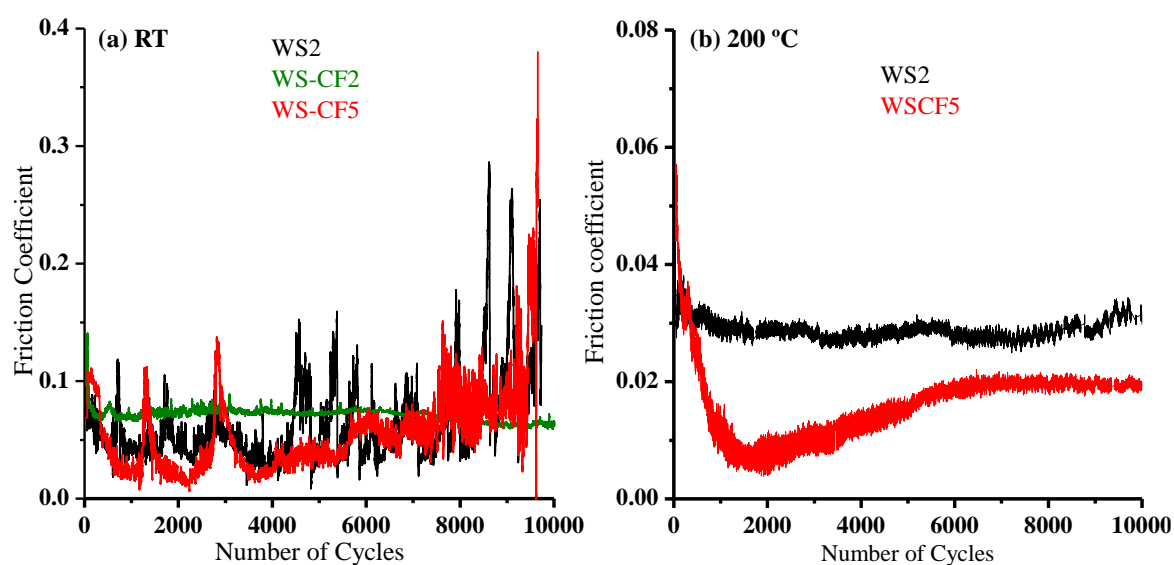
Figure 4.11 Friction curves of the WS-C/F coatings recorded when sliding for 10000 laps against a 100Cr16 steel ball under 20 N load in dry testing at (a) RT and at (b) 200 °C.

Table 11 The friction values and pin/disc specific wear rates determined for the WS-C/F coatings when working at RT and at 200 °C.

		COF			
		5 000 cycles		10 000 cycles	
	at. % F	RT	200 ºC	RT	200 ºC
WS2	0	0.05 ± 0.04	0.030 ± 0.003	0.06 ± 0.06	0.030 ± 0.003
WS-CF2	4.3	0.07 ± 0.02	0.025 ± 0.005	0.07 ± 0.02	0.027 ± 0.005
WS-CF5	9.5	0.04 ± 0.03	0.014 ± 0.008	0.06 ± 0.06	0.016 ± 0.007

		Specific wear rate (mm³/N.m)			
		Pin		Disc	
		RT	200 ºC	RT	200 ºC
WS2	0	$2.0 \times 10^{-7} \pm 2.5 \times 10^{-8}$	$4.6 \times 10^{-9} \pm 2.4 \times 10^{-10}$	$1.1 \times 10^{-5} \pm 5.1 \times 10^{-7}$	$2.2 \times 10^{-6} \pm 5.9 \times 10^{-7}$
WS-CF2	4.3	$1.4 \times 10^{-7} \pm 2.1 \times 10^{-8}$	$1.5 \times 10^{-8} \pm 1.9 \times 10^{-9}$	$1.4 \times 10^{-6} \pm 2.4 \times 10^{-7}$	$2.2 \times 10^{-7} \pm 3.7 \times 10^{-8}$
WS-CF5	9.5	$2.7 \times 10^{-7} \pm 2.4 \times 10^{-8}$	$6.5 \times 10^{-9} \pm 4.0 \times 10^{-10}$	$1.0 \times 10^{-6} \pm 2.4 \times 10^{-7}$	$3.1 \times 10^{-7} \pm 3.5 \times 10^{-8}$

(a) WS2

EDS analysis — Chemical Composition (at. %)

Element	Zone 1	2	3	4	5
W	27	1	6	18	31
S	40	1	8	26	30
C	26	10	9	20	16
O	7	7	44	-	12
Cr	-	59	21	36	11
Fe	-	22	12	-	-
F	N/A				
TOTAL	100				

(b) WS-CF2

EDS analysis — Chemical Composition (at. %)

Element	Zone 6	7	8	9	10	11	12
W	27	18	14	28	17	6	24
S	35	23	18	36	20	8	30
C	26	18	17	24	21	11	22
O	7	6	4	7	13	9	10
Cr	-	30	39	-	22	61	10
Fe	-	-	4	-	4	3	-
F	5	5	4	5	3	2	4
‖F/W‖	0.6	1.2	1.6	0.5	0.9	4.1	0.6
TOTAL	100						

(c) WS-CF5

EDS analysis — Chemical Composition (at. %)

Element	Zone 12	13	14	15
W	23	17	18	15
S	36	19	24	16
C	25	17	21	19
O	6	40	29	38
Cr	-	-	-	-
Fe	-	7	5	9
F	10	0	3	3
‖F/W‖	1.3	0	0.8	1.0
TOTAL	100			

Figure 4.12 SEM characterization and EDS analysis of the wear tracks as well as the optical images of the respective pins for the tribological test conducted at RT of (a) WS2, (b) WS-CF2 and (c) WS-CF5 coatings.

The COF curve of WS-CF2 coating is very regular and smooth along the entire RT test. The friction coefficient is approximately constant and equal to 0.07. This value is

similar to the one measured in our previous works concerning the W-S-C system when the coatings are tested in room temperature conditions. As in those coatings, the films are much denser with much higher hardness than the single W-S. As can be observed in Figure 4.12 (b) - I, the wear track after pin-on-disk testing is rather smooth. In higher magnification (Figure 4.12 (b) - II), zones with different aspect can be detected. However, the chemical composition analyses in most of the zones show that the ratio between the main elements of the coatings are kept approximately constant, which suggests an uniform sliding mechanism all over the contact, justifying the smooth COF curve. The presence of other elements, as Cr or Fe, is due to the lower thickness in those zones, allowing to integrate elements from the interlayer and the substrate. Finally, it is important to remark that the O content is rather low when compared to some areas in the wear track of W-S film (compare e.g points 3 and 8 in Figure 4.12 (a) and (b), respectively).

WS-CF5 coating exhibited quite different behaviour in comparison with the two previous coatings. In the first 4000 cycles the COF behaviour is similar to the single W-S film, i.e. there is a running-in period where the friction goes down to very low values and, suddenly, COF increases abruptly to the original value. This is repeated several times indicating that the formation and destruction of a low friction layer are occurring. However, the lowest COF value achieved is even lower than in W-S suggesting that the formed tribolayer can have different properties. The reduced friction achieved for the W-S-(C) systems has been attributed to the formation of a (0001) well oriented WS_2 tribolayer in the pin-disc sliding interface [154]. F-incorporation in the WS_2 matrix can occur in the S-W-S layers, thus leading to the expansion of the WS_2 network in the basal direction (as it was shown by the shift in the (0002) XRD peak). Similar situation has already been reported for sulphur substitution by oxygen in the MoS_2 matrix [159, 260]. Then, the lamellar distances are likely higher leading to a decrease in the van der Waals bonding between WS_2 sheets reducing the energy for inter and intra-crystalline slippery. This would explain the reduced friction achieved for WS-CF5 coating.

Figure 4.13 shows the Raman analysis of the WS-CF5 wear track with more intense WS_2 peaks than in the as-deposited coatings. It must be pointed out that the as-dep WS-CF5 coating (b)-(1)) presents less free-carbon content than the as-dep WS2 coating (a)-(1)), which is probably related with a less surface contamination due to either a lower surface roughness or the presence of F mentioned to also prevent the coating from oxidizing. WO_xF_y compounds presenting Raman bands in the 700-950 cm^{-1} range are

shown even after the tribological testing of WS-CF5 coating (Figure 4.13 b)-(2)), confirming the possible incorporation of F in the WS_2 lattice. After the tribological tests, the WS_2 contribution is very intense for both coatings (Figure 4.13 a)-(2) and b)-(2)) with sharper peaks (compare e.g. the insets (3) and (4) of Figure 4.13 b)), suggesting indeed an increase of the crystallinity in the contact zone of the sliding contact. Moreover, the F is expected to withdraw more electron density than oxygen attaching to high energy sites in the W_z non-bonding orbital avoiding WS_2 oxidation, leading to easy shear ability of the tribolayer. The reduced COF was not achieved for WS-CF2 coating once less F was incorporated in the WS_2 matrix. Additional tests were conducted on WS-CF5 coating in dry-air conditions, keeping the temperature at 200 °C, in order to evaluate the COF profiles (Figure 4.11 b)). It is easily verified a much lower COF presented by WS-CF5 coating in comparison to WS2 coating, confirming the tribological mechanism suggested above for F alloying.
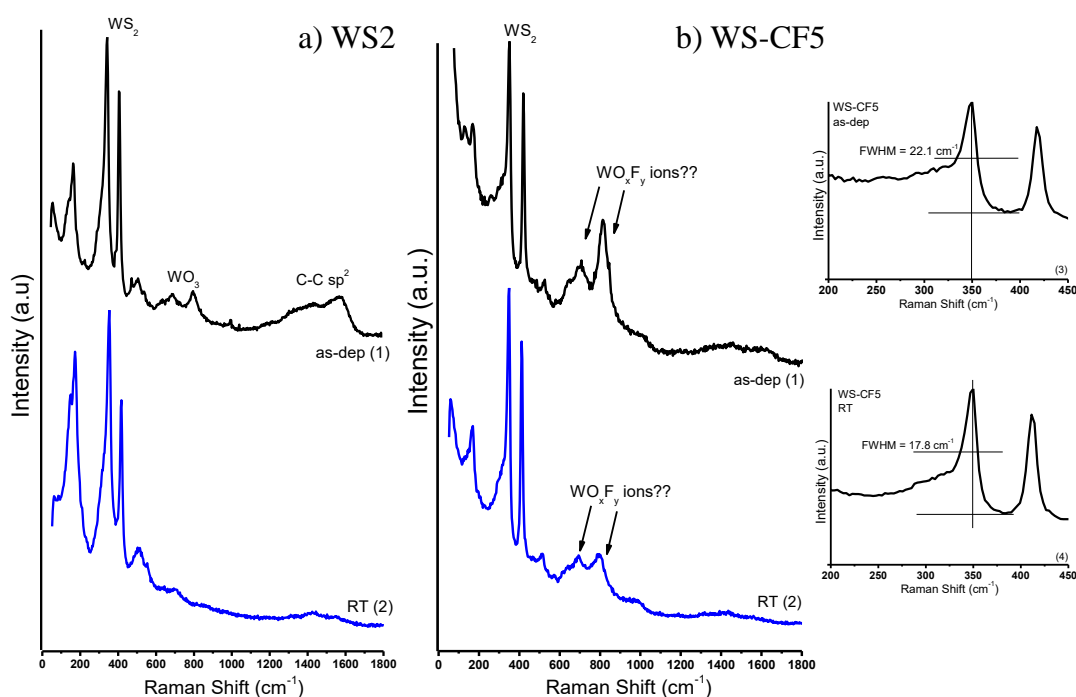
Figure 4.13 Raman spectra of the (a) WS2 and (b) WS-CF5 coatings as-deposited (1) and of their respective worn surfaces after tribological test performed at room temperature (RT) (2).

In a second part of the RT sliding test (from 5000 to 10000 cycles), the reformation of the low friction tribolayer does not seem possible with a consequent strong increase of COF in a very irregular way. A detailed analysis of the WS-CF5 wear track (Figure 4.12 (c) – I and II) allows to show that there are zones with high O content. Moreover, it seems that iron oxides coming from the counterbody (100Cr6 steel ball) are also attached to

wear track (note that Cr is not detected in any point, meaning that the Fe cannot come from the substrate). The progressive attachment of these oxides to the wear track will lead to the increase of the friction coefficient. Note that there are extensive zones of the wear track having chemical composition very close to the original one (compare points 13 and 14 in Figure 4.12 (c)) in terms of W and S elements. In spite of this increase in the COF, the wear resistance of the coating is similar to WS-CF2 sample and much better than single WS. This should be attributed to the higher hardness of this coating when compared to WS.

4.1.4 Conclusions

W-S coatings doped with fluorine and carbon were deposited in an Ar/CF_4 sputtering plasma. The fluorine incorporation in the coatings reached a maximum value of 9.5 at. % for CF_4 flow rate of 5 sccm. For higher flow rate values, fluorine content almost vanished and a significant increase of both oxygen and carbon incorporation was observed. These results show that, until a certain CF_4 threshold value, this gas contributed to the coating growth whereas, for higher flow rates, an etching regime takes place. In the first regime (coating deposition), an improvement of the coatings density was achieved, with the correspondent increase in the hardness (up to ~ 4 GPa), whereas cracking of the film occurred in the second one (etching regime). XPS analysis showed that tungsten was chemically bonded to sulphur and carbon (as W-S and W-C phases), oxygen and fluorine. Relatively to the wettability, the coating surface roughness and chemistry seemed to have great importance on explaining the water/oil repellence degree reached. Then, the fluorine doping led to smoother surfaces and differences in the crystallographic ordering, leading to a more hydrophilic behaviour; meanwhile no difference in the oil repellence was observed.

XRD analysis demonstrated that the fluorine incorporation contributed to the decrease of the WS_2 crystallinity, with a smooth shift of the (002) basal plane position toward lower Bragg angles. Such behaviour suggested that the fluorine insertion on the WS_2 lattice expanded the hexagonal structure leading to the d-spacing increase of adjacent WS_2 sheets, which in turn reduced the van der Waals bonding energy. As a consequence, an easy sliding and, thus, a decrease in the friction was observed in F-containing coatings in relation to WS2. In both room temperature and 200 °C tested in dry conditions (RH of 35%), tribological tests showed that the friction was reduced in the case of F-containing coatings.

This research study provides not only a deep explanation on the chemical nature and sputtering growth process of WS-CF coating system, but also a further insight on the mechanical properties, wettability and tribological performance of F/C reinforced low friction W-S coatings.

4.1.5 Important Remarks of Part 1

From the whole set of developed coatings, they were identified the three most interesting coatings according to their wettability character and friction performance. So, WS2, WS-CF2 and WS-CF5 coatings were selected to pursue in this thesis, which had 0, 4.3 and 9.5 at. % of F contents, respectively. The next step was the optimization of the coating thickness in order to be deposited on the selected anodized Al alloy surfaces to replicate their bottom roughness.

Overview – Part II

The other objective of this study was then to deposit WS-CF coatings over the roughened Al surfaces produced by anodization, which would tune both the friction properties and the wettability behaviour of the bottom anodized surfaces.

In this subsection, it is presented the combination of the WS-CF coatings with the anodic oxides structures to produce the hybrid surfaces. The surface characterization of the first hybrid surfaces created demonstrated the need to optimize coatings with lower thickness than the ones developed in the previous subsection. Besides this, it was verified the low mechanical stability of the porous anodic Al oxides developed by the anodization process, which led those samples to be abandoned. Consequently, the step of coating thickness optimization was followed taking into account the dimple-shaped anodized Al surfaces (SD-Small Dimple and LD-Large Dimple). Thus, this subsection presents the maximum thickness able to replicate the bottom dimple textured Al surfaces.

Note: From now on and for easier understanding, the sample named as S/0.3/ONE/Et1-90 in Chapter 3 will denominated as SD and the sample named as P/ONE/Et1-30 will be identified as LD.

4.2 Deposition of WS-CF coatings over anodized Al surfaces – intermediate study

4.2.1 Thick WS-CF coatings on porous anodized surfaces

WS2, WS-CF2 and WS-CF5 coatings were deposited by magnetron sputtering for 1h, reaching thicknesses of 1.6, 1.3 and 1.4 µm, respectively. They were deposited on different substrates: silicon, polished Al (P1) and on three anodized Al surfaces (LD, S/1/TWO/Et1-90/Et2-0 and P/TWO/Et1-30/Et2-30). As representation, Figure 4.14 shows the top-view morphologies obtained by SEM characterization for all the substrates deposited with the WS-CF2 coating (thickness of 1.3 µm).
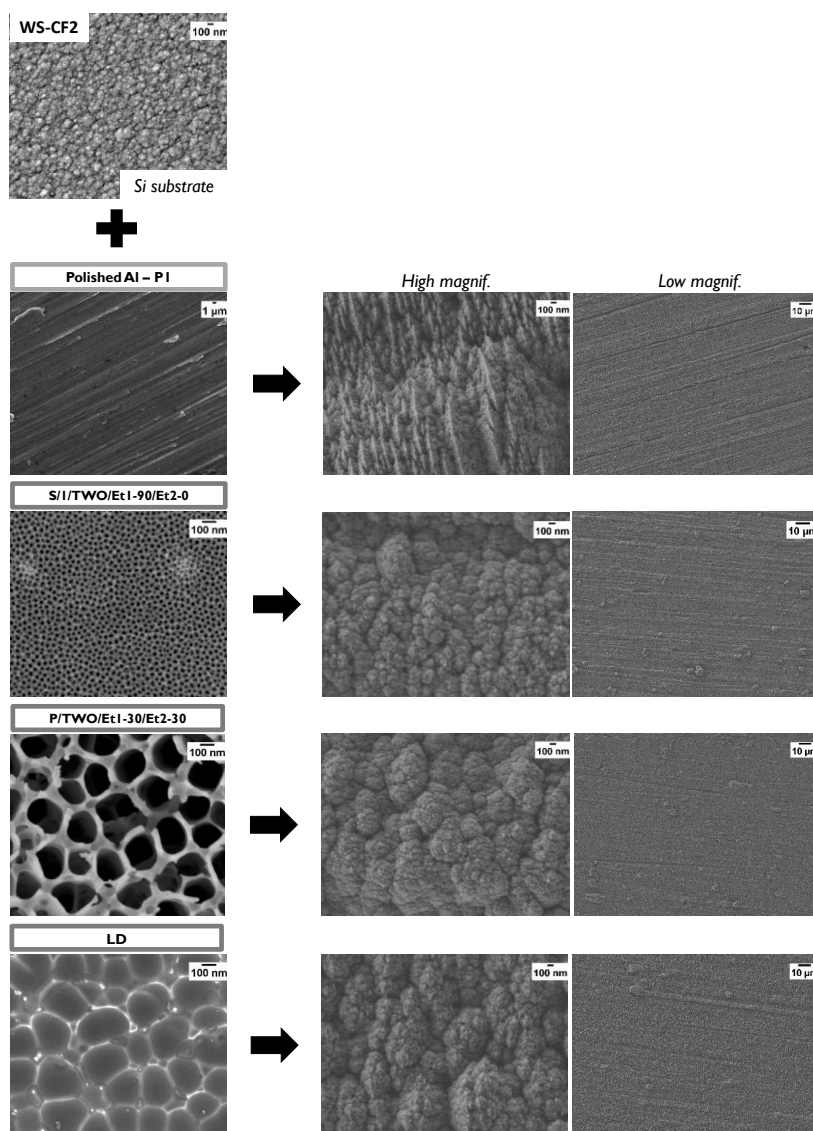
Figure 4.14 SEM images obtained for the hybrid surfaces created when using a thick WS-CF2 coating.

As can be observed, the coating morphology was not greatly affected by the surface texture underneath. This is easily understood by the point that the coating thickness is much higher than the size of the bottom features (e.g for LD case the dimples are have about 200 nm of diameter), which completely masked the nano-scaled surface characteristics.

This part of the study took into account that porous anodic oxide layers of 20 μm thick have been cited to be beneficial for tribological application, in comparison to 60 μm, since they can be used as a reservoir for lubricants, extending the lubrication effect and be more effective in terms of friction [89]. However, the CA measurements obtained for the hybrid surfaces now produced (Figure 4.15 below) revealed that their wettability was not affected by the initial roughened surface, being its hydrophobic-oleophilic behaviour mainly coming from the coating chemistry (WS-CF2). This way, the combination effect of the roughness promoted by anodization with the self-lubricating coatings deposited by magnetron sputtering is somehow lost due to application of excessive thickness of the coating.
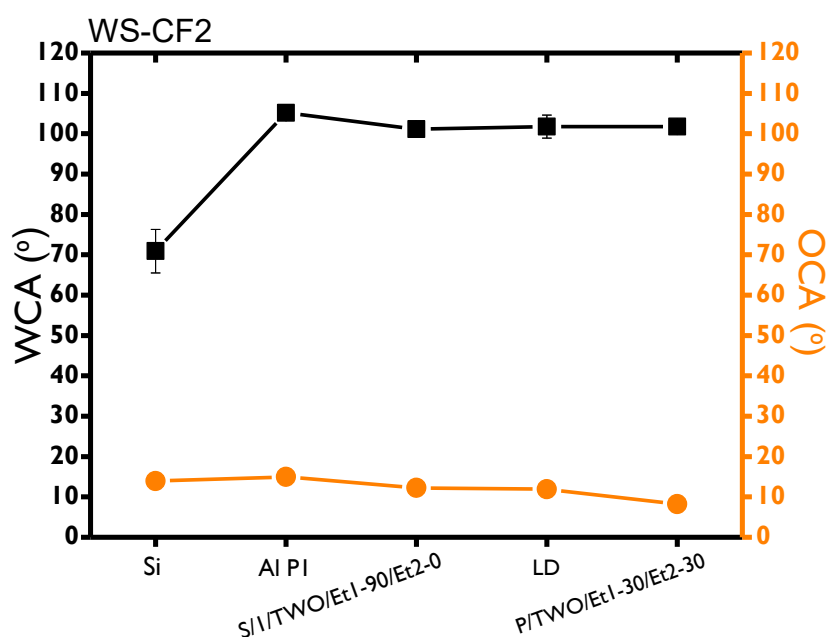
Figure 4.15 CA measurements obtained with water and α-bromonaphthalene on the hybrid surfaces produced in this subsection.

Moreover, it was also mentioned that the strength of the AAO structures increases significantly with the regularity of pore-channel arrangement while the elastic modulus is less sensitive to the regularity [199]. However, SEM images obtained from FIB slicing (Figure 4.16) on the WS-CF5 (1.6 μm) coated P/TWO/Et1-30/Et2-30 anodized

surface (porous-type) (Figure 4.16 (a)) shows that the anodic structure is highly irregular and disrupted. And, it is cited in the literature that thicker oxide structures lead to longer and more open pore structures which are more subjected to major collapse under contact pressures [261]. Thus, it is verified that the porous-type structures developed by anodization are inadequate when high mechanical solicitation is needed.

(b)

(a)

(c)

(d)
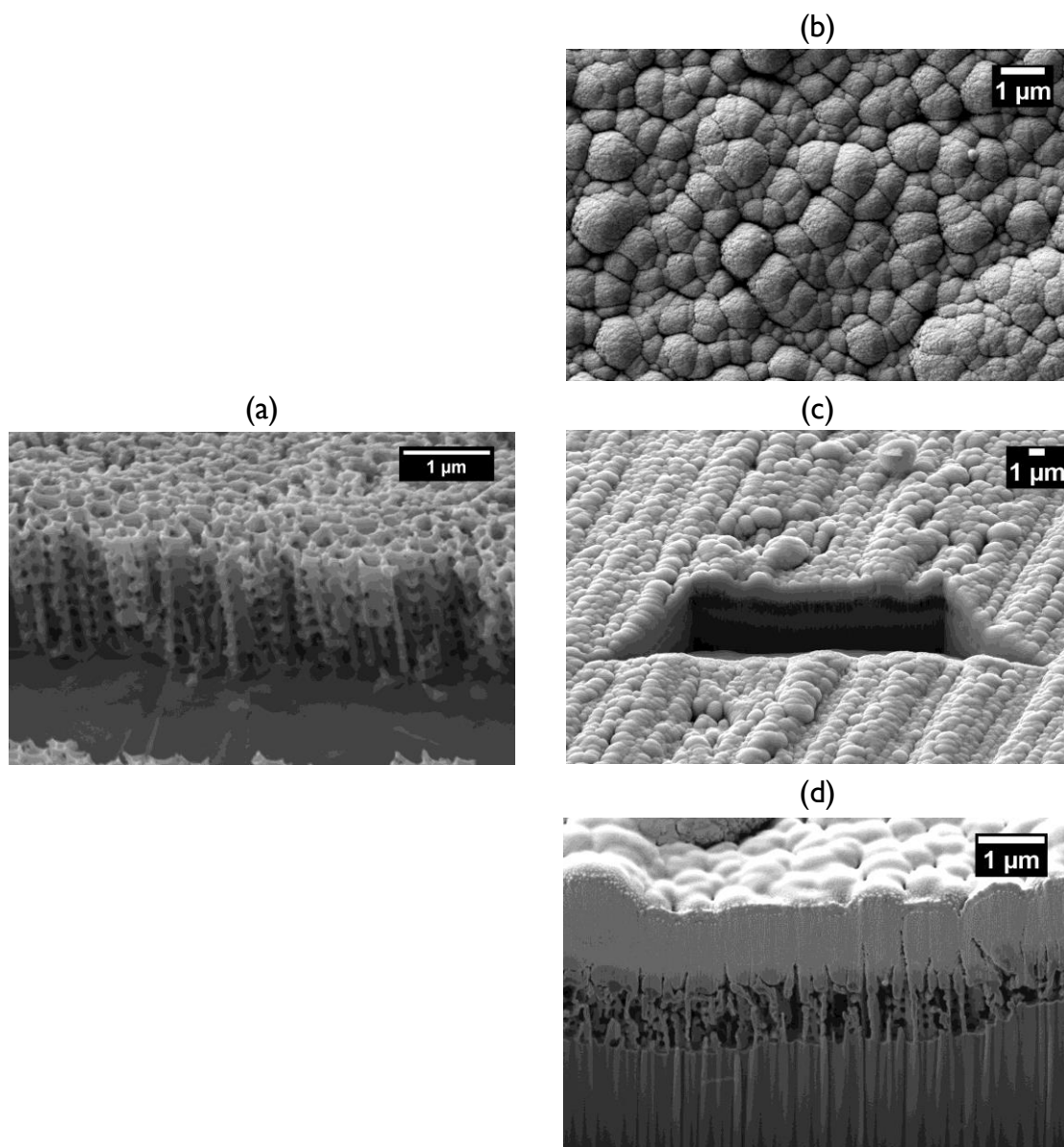
Figure 4.16 SEM images of a porous oxide surface + WS-CF5: (a) cross-section of the oxide surface (5kV), (b) top-view of oxide surface+WS-CF5 (2 kV), (c) zoom-out and (d) zoom-in of the sectional area obtained from FIB milling (15 kV) of the hybrid structure.

This first trial allowed to conclude that a thickness optimization step must be carried out to guarantee that the coating is able to reproduce the bottom Al shape. And consequently, only the two dimple-shaped anodized Al surfaces (one with low diameter

(SD) and other with high diameter (LD)) will be target of that coating thickness optimization.

4.2.2 Thin WS-CF films on dimple-shaped Al surfaces

At this stage, it was scanned over the literature the state of the art about the thickness range of the coatings applied on surfaces with micro-nanoroughness feature. It was found that the thickness of polymeric-based coatings commonly used for surface wettability control were roughly in the ~[50-300] nm range [63, 262]. So, the procedure for the coating thickness optimization took into account to reach the maximum thickness able to reproduce the bottom surface roughness, in order to keep the mechanical strength. For this, WS-CF5 coating was used in the optimization procedure which was carried out taking into account its deposition rate [263], and so, the deposition time was adjusted in order to reach 200, 100, 75 and 50 nm thickness, as Table 12 resumes. The coatings were simultaneously deposited on the small dimple (SD) and large dimple (LD) anodized surfaces, as stated before, without using adhesion interlayer.

Table 12 Summary of the WS-CF5 films deposited by magnetron sputtering with different thicknesses.

Film	Deposition time (min)	Thickness (nm)
WS-CF5	10	200
	5	100
	3.75	75
	2.5	50

It was iteratively used the AFM facility to evaluate and characterize the surface topographies obtained with the different coating thicknesses. The first characterization was followed from the higher to the lower thickness. Figure 4.17 presents the AFM topographical images obtained for the WS-CF5 film deposited over the SD and LD surfaces with 100 and 200 nm thickness, respectively. Firstly, it was confirmed by the profiles extracted from the AFM micrographs (profile 1 and 3) that the SD (a) and LD (c) surfaces had a peak-to-peak distance close to the dimple size diameter (~30 nm for SD and ~200 nm for LD) measured by *ImageJ* on the SEM top-view images in Chapter 3. And, the profiles 2 and 4 in Figure 4.17 easily show that, overall, the film deposition led to the surface smoothening. If profiles 3 and 4 are compared, it is possible to observe that the

thin film (200 nm) was able to follow the bottom dimple-shaped anodized Al surface (LD) with a peak-to-peak profile fairly showing the same discrepancy as it was observed for the
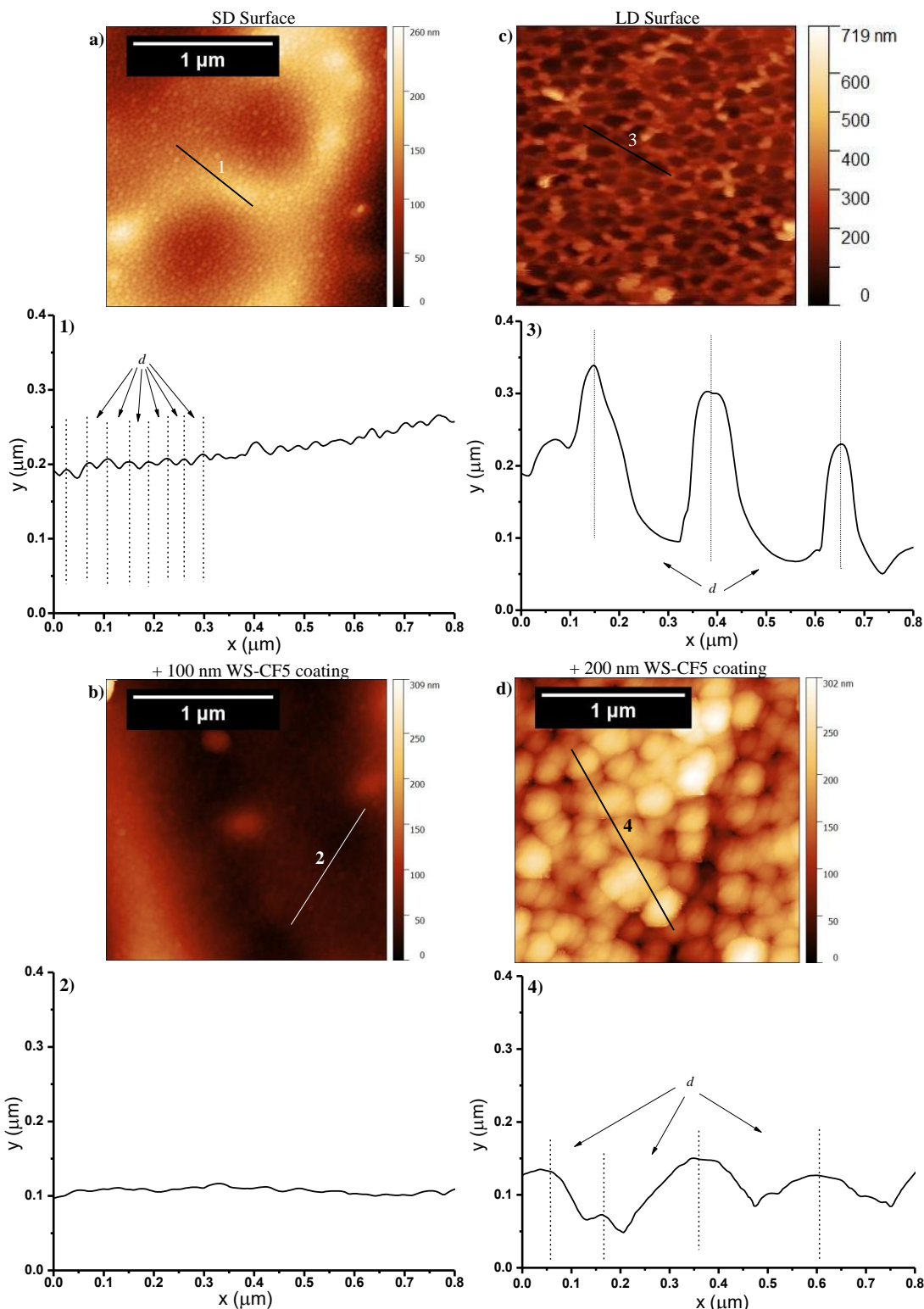
Figure 4.17 Topographic images obtained by AFM for the uncoated a) SD and c) LD surfaces and for the thin WS-CF5 films deposited on the b) SD and d) LD surfaces. Graphic profiles of the all surfaces were recorded for 1 µm length (Profile 1 to Profile 4).

uncoated surface (Figure 4.17 (c)). However, the depth profile demonstrates that the coating makes the peak to valley heights shallower. This smoothening was highly evident for the coated SD surface with 100 nm of thickness of WS-CF5 film, if comparing the profiles 1 and 2 in Figure 4.17. Moreover, the SEM images in Figure 4.18 show that the top-view morphology of the 100 nm WS-CF5 film over the SD texture (a)) was not that different from the one when the same film was deposited over a Si substrate (b)). However, no further characterization was followed on the SD surface for lower thicknesses, once lower film thickness would hinder the mechanical strength of the whole structure, and so, the SD surface will not be considered further on in this thesis.
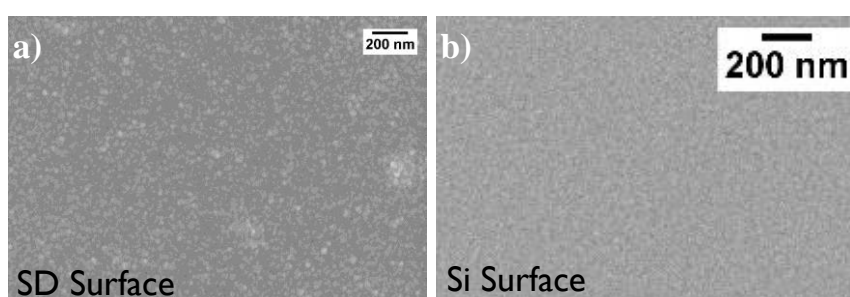
Figure 4.18 SEM top-view morphology of the WS-CF5 film of 100 nm deposited on the a) SD surface and on b) Si substrate.

4.2.3 Important Remarks of Part II

In this subsection, it was demonstrated that the thickness of the developed WS-CF coatings presented in subchapter 4.1 was not suitable to replicate the textured Al alloy surface produced by anodization. Indeed, thicknesses of about ~1.5 μm completely mask the roughness features of the anodized surfaces which are in the nanoscale range (diameters<250 nm). Furthermore, the porous anodic structures produced by anodization revealed to have low robustness and mechanical stability when coated, these brittle structures not suitable for high load solicitation for tribological contacts. Then, only dimple-shaped anodized surfaces (SD and LD) were left to pursue on the study for the coating thickness optimization. This way, the WS-CF5 coating was deposited with different thickness on those surfaces. It was verified that a thickness of ~200 nm was enough to replicate the LD anodized roughness, while lower thickness of 100 nm was hardly able to replicate the bottom roughness of SD surface. This because the thickness of the films was larger than the dimple size (~100 nm over ~30 nm), masking the initial texture. Furthermore, lower coating thicknesses would hinder the mechanical strength of

the whole structure and so, SD surfaces will not be interesting to consider in the next study.

Overview – Part III

Before evaluating the wettability and tribological performance of the coated LD surface (hybrid surface), the thin optimized films (~200 nm thick) must be characterized to ensure if they keep the surface properties encountered for the thicker coatings in subchapter 4.1. It is quite well-known that the final properties of a coating are controlled by its growth, which in turn is governed by the growing time and consequently dependent on thickness. The aim of this study now is to verify if the thin films maintain the interesting properties that these coatings can apport to a base system. For that, new characterization concerning the structural and functional properties was performed to these new "*thin films*".

Then, in order to evaluate the properties of the WS-CF films of ~200 nm thickness, they were deposited on polished steel substrates, which were target of comparison with the characterization results obtained for the thick coatings presented before (results of subchpter 4.1). Then, together with the WS-CF5 coating of 200 nm, which will be designed as WS-CF5_200 in this section, they were adjusted the deposition times to obtain the same thickness for the WS2 and WS-CF2 coatings. Likewise, these two coatings will be denominated as WS2_200 and WS-CF2_200.

This part of the work has been carried out in the University of Coimbra at CEMMPRE research institute and at LED&MAT laboratory in IPN-Coimbra. The tribological tests were conducted in Czech Republic in the Technical University of Prague (CTU). The results of this study have contributed to a scientific paper already accepted for publication to *Surface & Coatings Technology* journal (IF = 3.1), being now under publication process.

4.3. The wettability and tribological behaviour of thin F-doped WS$_2$ films deposited by magnetron sputtering

4.3.1 Introduction

Many industrial sectors need materials with improved performance which commonly impart their surface modification. The surface wettability is usually controlled by modifying the surface roughness and chemistry, creating textured structures and depositing additional films according to the existing features found in nature [7]. These films are often polymeric containing F radical [126] or silane (H-Si-H radicals) species [235, 236], that can lower the surface free energy. However, their polymeric nature gives a low mechanical strength with a deficient impact on the load-bearing capacity. Moreover, the manufacturing methods used to produce those coatings are commonly complex chemical-based routes or expensive procedures [264]. In addition, there are several practical examples where specific wettability behaviour is required in conjunction to good wear resistance, such as the metallic grids used in the oil-water separation processes in the maritime industry for oil capture, where a special surface property (hydrophilic/oleophobic or hydrophobic/oleophilic) is required. This has been a worldwide challenge because of the increasing industrial oily wastewater. Also, the efficiency of lubricative processes for components in the automotive industry, to reach a good lubricant distribution, needs tools with particular surface wettability and high wear resistance. Finally, governmental entities are more and more concerned with the excessive use of lubricants, since most of them are harmful to the environment and cause human risks, a situation which can be attenuated with the use of solid low friction surfaces [226-228].

Anodization process has emerged as a powerful surface modification process to tailor the surface roughness of metals, due to its high reproducibility, reliability, cost-effective feature and easy industrial scalability. However, in some cases, the anodic oxide structures do not gather the desired wettability with a high mechanical resistance [89, 261]. Regarding aluminum alloy anodization, Chapter 3 presents the different developed and optimized surface structures, showing that dimple-shaped morphologies had higher water and oil repellence comparatively to the porous-shaped ones [234]. Furthermore, Chapter 4.1 demonstrated that depositing W-S coatings doped with fluorine (WS-CF) it

was possible to improve the friction performance as well as an enhance water and oil affinity [263]. Therefore, the solution for systems which need both controlled wettability and a high mechanical strength could be the combination of anodized textured metallic surfaces with WS-CF coatings. However, the applied coatings should follow the bottom anodized surface roughness, to keep on the top surface of the coating the desired texture. A literature overview has shown that the thickness of fluorinated-based coatings often applied on rough surfaces to tune the wettability behaviour is in the nanometer-thick range (50-300 nm) [63, 262]. Concerning the WS-CF system, detailed characterization has been carried out on those thick (~2 μm) coatings [263], but their behaviour in the form of thin films was not explored. Then, in a few preliminary studies in Chapter 4.2, it was observed that WS-CF films of ~200 nm thickness were able to follow the bottom dimple-textured aluminum alloy surfaces previously optimized by anodization.

In this subchapter, thin WS-CF coatings are deposited by magnetron sputtering on steel substrates and characterized in terms of morphology/topography, structure, wettability behaviour, and friction performance. Throughout the study, a comparison with the thicker previously optimized coatings is discussed.

4.3.2 Experimental

WS-CF coatings of approximately 200 nm thickness were deposited on glass, silicon and mirror-polished M2 steel disc substrates, using the same magnetron sputtering apparatus (TEER Coating Ltd.) previously used to deposit thicker (1.3-1.5 μm) WS-CF coatings [263]. Two WS_2 targets were used in an Ar/CF_4 reactive mixture at constant total pressure (0.4 Pa), in which the substrate holder was rotating without bias. The depositions were carried out with and without CF_4 flow rates (0, 2 and 5 sccm) in order to reach different C and F contents. According to the deposition rates achieved in Chapter 4.1, the deposition times were adjusted in order to achieve coatings with 200 nm thickness, assigned as WS2_200, WS-CF2_200 and WS-CF5_200, were deposited for 9, 13 and 10 min, respectively.

The cross-section and top-view morphologies of the produced coatings on silicon substrates were observed by scanning electron microscopy (SEM) (ZEISS Merlin – Field Emission Gun, High Resolution with Charge Compensation) operating in secondary electron mode. For chemical composition, wavelength dispersive spectroscopy (WDS) was used (Oxford Instruments) at 10 kV acceleration voltage and 8.5 mm working

distance. The surface coating topography and roughness were characterized using atomic force microscopy (AFM) (Bruker Innova) with a silicon tip of 6 nm nominal radius used in contact mode. Scans of 2 x 2 μm^2 size were acquired at a scanning rate of 1 Hz. Additional image processing was conducted using the *Gwyddion* software. The crystalline structure of the 200 nm thickness coatings on glass substrates was analysed by X-ray diffraction (XRD) (PANalytical X'Pert Pro MPD system) using Cu Kα radiation (λ = 1.54 Å) (45 kV and 40 mA) in grazing angle (2°) in 10-80° 2θ range. Static contact angle (CA) measurements (DataPhysics OCA Analysis system) were carried out on glass substrates to study the coating wettability behaviour using the sessile drop method by applying liquid droplets of about 2 µL at room temperature. A minimum number of 10 measurements were carried out on each sample. The liquids used for wettability assessment were ultrapure water and α-bromonaphthalene. Further, the surface free energy (SFE) was determined by the OWRK model.

The tribological behaviour was carried out in a ball-on-disk tribometer (CSM Instruments) at room temperature (25 °C) with 35-40% of relative humidity (RH), with and without lubrication. The lubricant (PAO-Grade 8, ρ = 0.8 g/cm^3, kinematic viscosities calculated according to ASTM D 445: ν (40 °C) = 48.5 mm^2/s and ν (100 °C) = 7.9 mm^2/s) was used in a hydrodynamic lubrication regime with λ (Tallian parameter) calculated according to the Hamrock-Dowson approach [265]. The tests were performed on the coatings 200 nm thick deposited on polished steel substrates. The sliding counterpart was a 100Cr6 steel ball (H = ~ 5 GPa, R_{qball} = 0.05 ± 0.01 µm) with a diameter of 6 mm, the linear speed was 0.1 m/s, the sliding distance was 50 m and the normal load was 5 N (~700 MPa Hertzian contact pressure). The coefficient of friction (COF) recorded was the average value of the sliding test in the steady-state regime. The morphology of the wear tracks and the worn scars of the contact surfaces were observed by optical microscopy and the depth profile of the wear tracks was evaluated by 3D profilometry (ZYGO). The as-deposited coatings, the wear tracks and worn scars after the tribological tests were also examined with micro-Raman spectroscopy utilizing a green laser (λ = 532 nm) (Horiba Raman system governed by the LabSpec software) and using 99% filtering and 20 min of spectrum acquisition time. The specific wear rates of the film and the counterpart ball were determined according to the procedure mentioned in [263] and by the ASTM standards for pin-on-disc testing.

4.3.3 Results and Discussion

4.3.3.1 Morphology and Roughness

Figure 4.19 presents the top-view (a)-c)) and cross-section (d)-f)) morphologies of the deposited films. As previously observed in Chapter 4.1, with the CF_4 flow rate increase, denser morphologies and smoother surfaces are achieved. Indeed, when compared to the typical porous and columnar morphology of WS_2 film, WS-CF2_200 displays an open morphology only at the external part of the cross-section, whereas WS-CF5_200 film is completely featureless both in section and surface top-view, confirming that no columns are formed at until 200 nm thickness [266]. Topographic analysis performed by AFM (see Figure 4.20) also confirmed the decrease in the roughness with the F incorporation, revealing roughness values (Sa) of 10.7, 2.5 and 0.9 nm for WS2_200 (a), WS-CF2_200 (b) and WS-CF5_200 (c) films, respectively. The chemical composition shown in Table 13 confirms that fluorine is being incorporated in the coating; no significant differences were found in relation to the thicker coatings studied before.
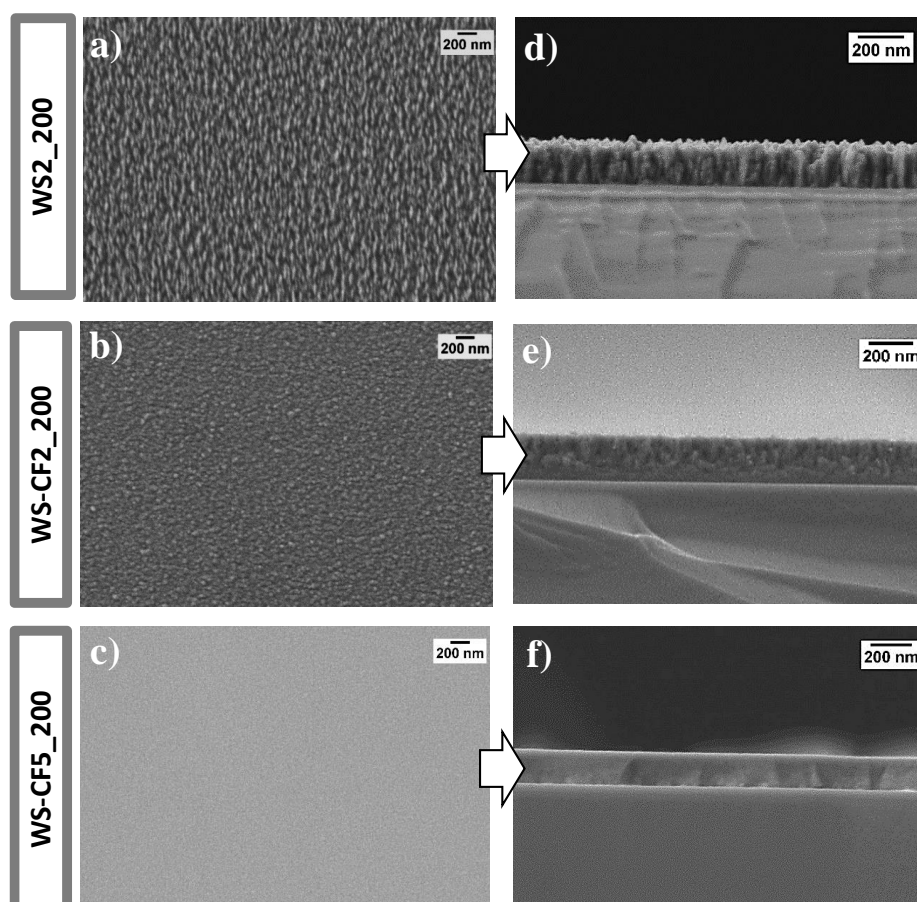
Figure 4.19 Surface morphology of the films with 200 nm thickness for a) WS2, b) WS-CF2 and c) WS-CF5 and their respective d)-f) cross-section.
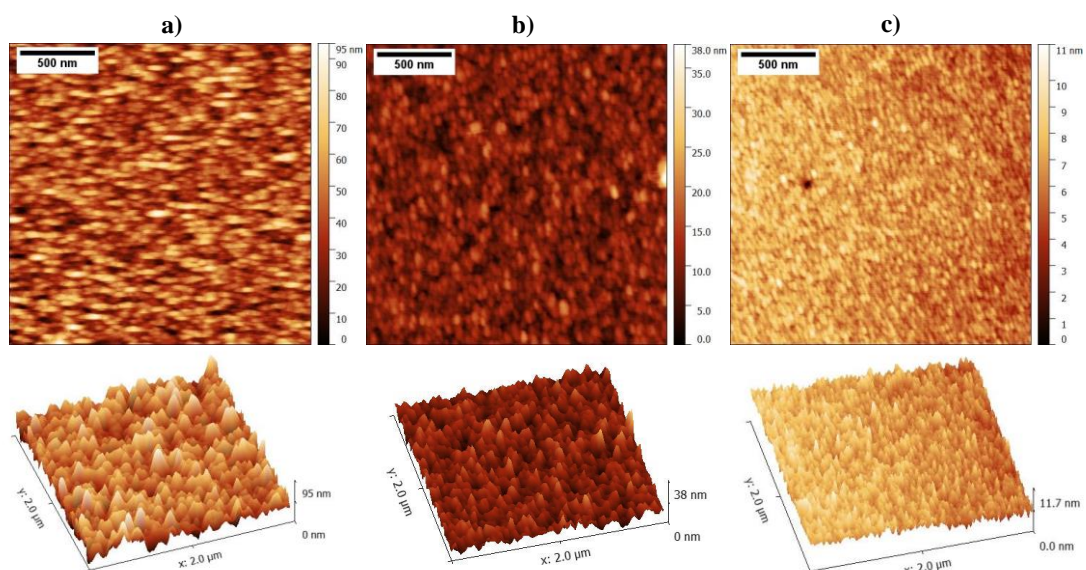
Figure 4.20 Topographic images (2D and 3D) obtained by AFM for a) WS2_200; b) WS-CF2_200 and c) WS-CF5_200 thin coatings deposited on glass substrates (please note the different vertical scales).

Table 13 WDS measurements of the chemical composition of the coatings.

Chemical Composition			
Element	at.%		
	WS2_200	WS-CF2_200	WS-CF5_200
W	36	35	30
S	44	42	42
C	9	10	10
F	-	5	7
O	12	8	12
S/W	1.2	1.2	1.4
F/C	-	0.5	0.7

4.3.3.2 Structure

Figure 4.21 presents the XRD analysis performed over the 2θ range from 10° to 80° on the 200 nm thick coatings. In Figure 4.21 a), WS2_200 coating shows the characteristic peaks of the hexagonal WS$_2$ structure [267]. However, the (002) peak (2θ ≈ 12°) is much more intense for the thin film than for the thick coating deposited before (see Figure 4.21 b)). This could be related to the well-known growth mechanism of sputtered WS$_2$ film, where the initial nucleation results in the structure with basal planes parallel to the substrate [268]. All the other peaks are similar to that of thicker coatings although they are less intense: the peak at 2θ ≈ 34°, corresponding to the (100) plan, is

asymmetric, due to the turbostratic stacking of the S-W-S single layers; there are two other peaks at $2\theta \approx 60°$, assigned to (110) orientation, and at $2\theta \approx 70°$ in the position of (108) orientation, both typical of sputtered WS_x.
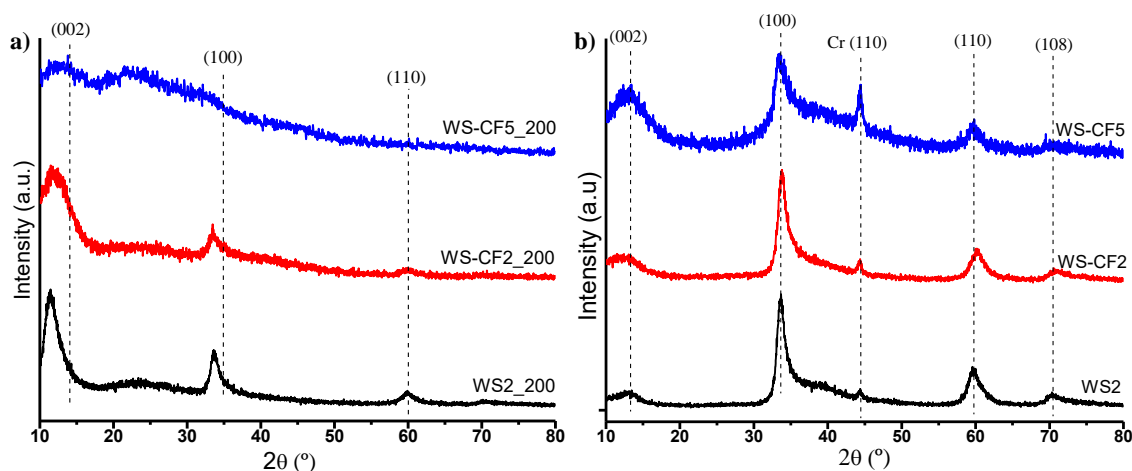
Figure 4.21 XRD diffraction patterns of a) thin WS2, WS-CF2 and WS-CF5 films deposited on glass by reactive sputtering and the b) same coatings with higher thickness (Chaper 4.1).

In case of WS-CF2_200 coatings, broader and less intense peaks in comparison to pure WS_2 are observed, an indication of lower crystallinity. Further increase in F content (WS-CF5_200) led to almost featureless XRD spectrum suggesting an amorphous structure. Thick coatings commonly display more crystalline features since more favourable conditions are reached after the initial growth due to the increase in the temperature promoted by atoms condensation or electron bombardment.

4.3.3.3 Wettability

As observed in Figure 4.20, the F insertion led to coating roughness decrease. Regarding the wettability of the thin films (200 nm), Figure 4.22 shows that, as the fluorine content is increased, lower water contact angles (WCA) and slightly higher oil contact angles (OCA) are achieved. In order to complete the coating wettability evaluation, the surface free energy calculation was also performed for the thin films using the OWRK method (described in Refs [182, 183]), and compared with the values determined before for the thick coatings (Table 14). The method considers the total surface energy as the sum of the dispersive and polar components. The values of the OWRK model show that both thin and thick WS-CF5 coatings have higher surface energy when compared to the non-polar WS_2 coatings. WS2 surface behaves similarly to other TMD materials (e. g., MoS_2) [131, 269], since, as referred to above, it presents dominant dispersion interactions. The basal planes of TMDs are also characterized as being non-polar [269] and they are

predominant in these thin coatings (see XRD results above). Moreover, their open porous surface can enhance an easy aging effect (adsorption of hydrocarbons from ambient air) which reinforces the achieved hydrophobic and oleophilic behaviour. The non-polar behaviour of the oils associated with the non-polar characteristics of WS2 surface contributes to the high oleophilic character of WS2 film (low surface energy and low adhesive interactions with oils). With F incorporation in the WS_2 matrix, the surface becomes more polar with less affinity to the non-polar oil molecules, increasing the oil contact angles.
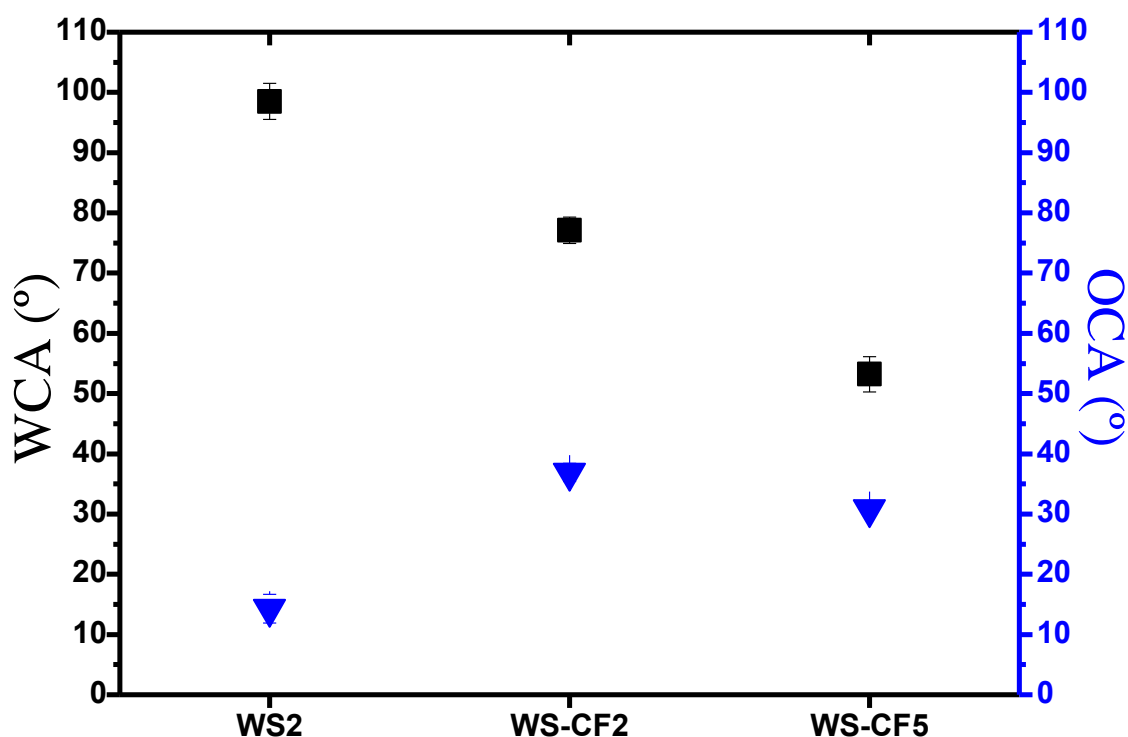
Figure 4.22 Wettability results of the thin WS-CF films (200 nm thickness) deposited on glass substrates: contact angle values measured with pure water (■:WCA) and α-bromonaphthalene (act as an oil) (▼:OCA).

Table 14 Comparison of the polar and dispersive components of surface energy determined for the thin and thick surface coatings using the OWRK model.

Surface Energy	THIN			THICK		
	Polar	Dispersive	TOTAL (mJ/m²)	Polar	Dispersive	TOTAL (mJ/m²)
WS2	0	43.2	43.2	0	42.7	42.7
WS-CF2	5.2	36.3	41.5	8.1	43.2	51.3
WS-CF5	55.4	38.6	94.0	25.9	43.2	69.1

4.3.3.4 Tribological performance

Figure 4.23 shows the comparison of the friction coefficient for the thin (200 nm) WS-CF films tested without lubricant with the respective thicker coatings up to a sliding distance of 50 m. The previous results on thick coatings [263] (sliding distance 450 m) showed that, when tested in these conditions, a continuous formation and destruction of the tribolayer occurred which was evidenced by peaks and valleys in the friction curve during the tribological tests. However, in the valleys (the first one is shown in Figure 4.23 b)), the thick F-doped coating showed lower friction than pure WS2. For the thinner films only short sliding distances were allowed due to wear, being only possible to evaluate the friction behaviour in the initial stage of sliding (50 m) (Figure 4.23 a)).
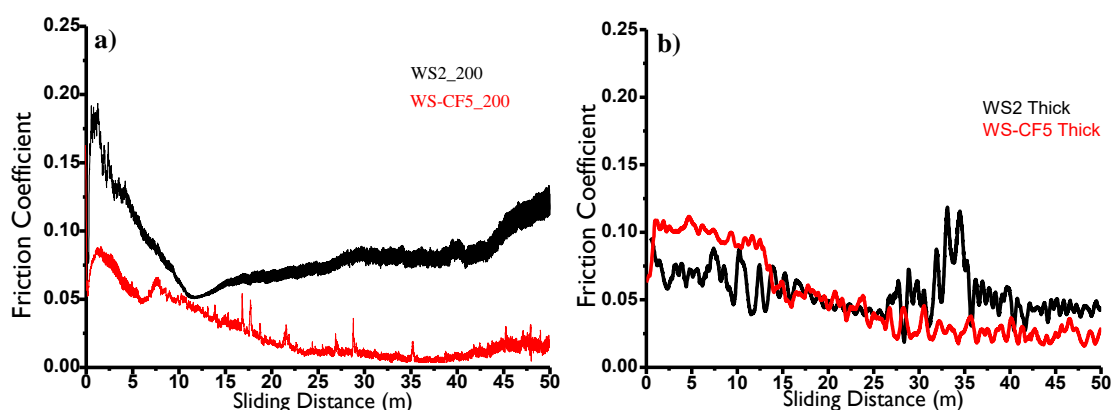
Figure 4.23 Friction curves recorded for the a) thin WS-CF films sliding for 50 m against a 100Cr6 steel ball under 5 N load in dry conditions; b) comparison with the results achieved for thick coatings developed in Chapter 4.1.

However, it seems that the friction evolution for the thin coatings has similar trends as for thicker ones, showing an initial running-in period where the friction drops down to low values (very low in F-doped ones), increasing thereafter. Moreover, once again, the F-doped coating shows lower friction than pure WS_2 over the whole test, for which friction mean value of 0.03 was achieved when calculated from steady-state phase (range 10 - 40 m, see Figure 4.23 and Table 15). This is even a higher reduction than that observed for thicker coatings (compare Figure 4.23 a) and b)). Such friction reduction has been previously justified by the increase in the inter-planar distance between WS_2 layers promoted by F insertion that facilitates the sliding ability of the tribolayer formed [263]. Indeed, the XRD diffractograms obtained before for the thick coatings demonstrated a peak shift to lower angles indicating an increase in the inter-planar distance. Unfortunately,

the low crystallinity of WS-CF5_200 does not allow to confirm this suggestion in the present case.

Table 15 Specific wear rate values determined for the two deposited films tested with and without lubrication. (Lubrication regime with $36 < \lambda < 38$; Rq (WS2_200) = 0.025 ± 0.003 μm; Rq (WS-CF5_200) = 0.018 ± 0.002 μm).

		COF			
		50 m sliding			
	at. % F	RT		LUB	
WS2_200	0	0.07 ± 0.02		0.07 ± 0.01	
WS-CF5_200	7	0.03 ± 0.01		0.07 ± 0.01	
		Specific wear rate (mm³/N.m)			
		Pin	Disc	Pin	Disc
WS2_200	0	$1.1 \times 10^{-9} \pm 2.7 \times 10^{-10}$	$6.7 \times 10^{-6} \pm 7.9 \times 10^{-7}$	$4.5 \times 10^{-8} \pm 2.7 \times 10^{-9}$	$1.9 \times 10^{-6} \pm 1.5 \times 10^{-7}$
WS-CF5_200	7	$3.7 \times 10^{-7} \pm 7.9 \times 10^{-9}$	$1.1 \times 10^{-6} \pm 8.7 \times 10^{-8}$	$6.2 \times 10^{-8} \pm 6.1 \times 10^{-9}$	$4.9 \times 10^{-7} \pm 9.7 \times 10^{-8}$

The images of the ball scars for WS2_200 (a)) and WS-CF5_200 (b)) cases in Figure 4.24 show the higher specific wear rate of the ball in contact with the latter, in spite of its lower friction, as confirmed by the values in Table 15. Inversely, the specific wear rate of this coating is much lower than that of WS2_200. These are expected trends since the hardness of WS-CF5 is much higher [263], resisting more to the wear and inducing higher
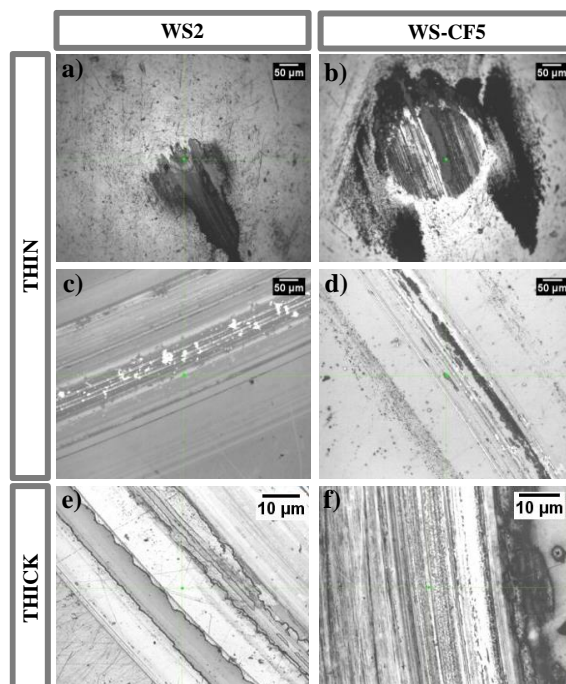
Figure 4.24 Optical images of the a)-b) ball scars and c)-d) wear tracks resulting from the tribological tests performed in dry conditions for the thin films and e)-f) wear tracks of previous developed thick coatings (Chapter 4.1).

wear to the counterbody. Likewise, Figure 4.24 shows the optical images of the wear tracks for WS2 (c) thin and e) thick) and WS-CF5 (d) thin and f) thick). To better understand the wear mechanisms involved, Figure 4.25 shows the Raman analysis for the as-deposited coatings and for their respective wear tracks (a) thick and b) thin) at tribological tests performed in dry conditions. Very low laser power was used to avoid any structural or chemical changes in the material [176]. The Raman analysis detected vestiges of W-S material in the adhered material and in the wear debris found in the ball scar (not shown).
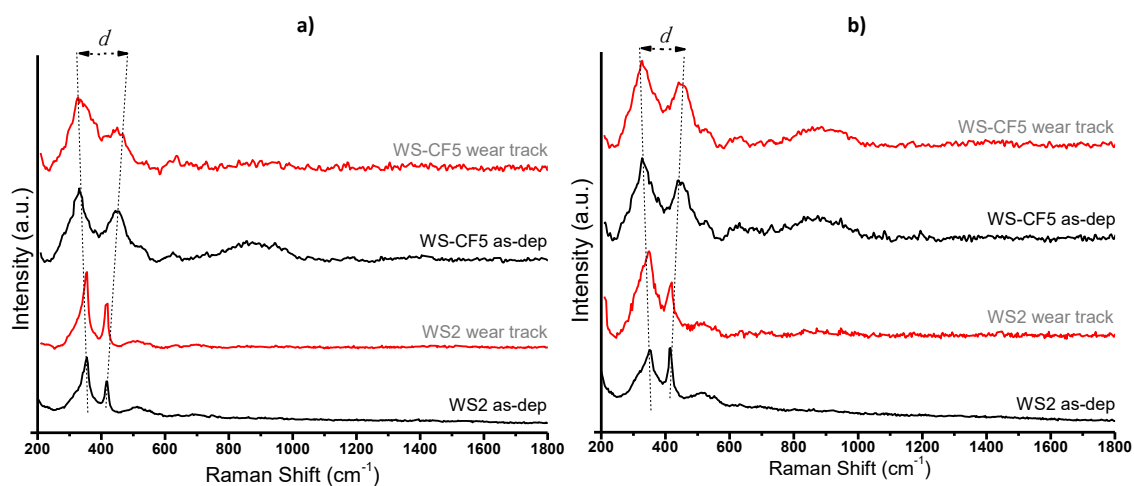
Figure 4.25 Raman spectra of the a) thick and b) thin as-deposited WS-CF coatings and their respective wear track analyses.

The Raman results of the as-deposited thick (a)) and thin (b)) coatings are in accordance with the XRD analysis, showing that the F insertion in both thin and thick coatings causes a loss of the order in relation to the WS_2 crystalline structure. According to the literature, for pure WS_2, two main first-order active Raman modes, with peaks localized at 355 cm^{-1} and 417 cm^{-1}, respectively assigned for the E_{2g}^1 and A_{1g} modes, are observed. However, the peak at 355 cm^{-1} presents high asymmetry, with a broad band superimposed for lower Raman shift values, particularly for the thin WS2_200 film. This can be explained by the second-order Raman peak involving the longitudinal acoustic mode (2LA(M)), which appears at 352 cm^{-1}, this peak having a higher intensity as less S-W-S layers are present [174]. The 2LA(M) peak at 352 cm^{-1} comes usually associated with the first-order vibration mode LA(M) positioned at 176 cm^{-1} also presented for both thin and thick WS2 (not shown). As discussed for similar MoS_2 material, this broad peak (in MoS_2 at 313 cm^{-1}) is characteristic of a highly defected MoS_2, with low purity and amorphous structure [270]. Moreover, as other researchers have shown [271], when an increasing amount of defects is introduced in a Mo-S 2D film, an increase of the intensity

of the 313 cm^{-1} peak occurs revealing the progressive amorphous character of the material. In consequence, overall, for both as-deposited thin and thick fluorine-doped coatings, the peak contributions at 355 and 417 cm^{-1} have their positioning changed (represented as *d* in Figure 4.25), with two broad peaks visible, at ~330 and ~450 cm^{-1} suggesting a much less crystalline character for these coatings, in good agreement with XRD results. Finally, it should be remarked again that thicker coatings seem to be more crystalline than thin ones, since the contribution of the broad 352 cm^{-1} is enhanced in the latter, suggesting a lower order degree.

Regarding the Raman analysis of the wear tracks, both thick and thin WS2 coatings presented a higher intensity of the 355 cm^{-1} peak, meaning a higher amount of WS$_2$ layers presented. Similarly, the wear tracks analysis of F-doped coatings demonstrated that both thick and thin coatings had similar behaviour, but still with the discrepancy (*d*) evident as in the as-deposited case. Notice that the literature reports that the increase of that discrepancy (*d*) between the E_{2g}^1 and A_{1g} peaks means the increase of the number of WS$_2$ layers [272]. Probably, this justifies the ability of basal planes of the WS$_2$ layers to align in the tribolayer on F-doped coating and, thus, decreasing the friction when compared to pure WS2 coating.

Tribological experiments of the thin film were also performed in lubricated conditions with pure PAO-8 oil. Synthetic oils are known as having better stability to oxidation, viscosity, and temperature, providing superior lubrication in air environment or high temperatures and, then, leading to lower steady-state friction. Figure 4.26 a) shows the friction curves for WS2_200 and WS-CF5_200 films during 50 m sliding; both coatings present smooth running-in periods of contact surfaces lubricated with pure PAO. However, it seems that different tribochemical mechanisms are occurring in the contact surfaces during the running-in period. In the first moments of contact, WS-CF5_200 surface shows lower friction value than WS2_200, which can be explained by its lower roughness which in turn reduces the severity of initial asperities contact. Then, the friction for WS2_200 starts to decrease reaching lower values than for WS-CF5_200, until the 20 m sliding distance, due to the progressive smoothening of the surface resulting from the wear. Then, both coatings reached the steady-state friction with very similar COF values close to 0.07, although still lower for WS2_200. The initial interpretation for this friction evolution (from 5 to 20 m sliding) can be based on the surface energy of the

coatings (taking into account the strength of the polar and dispersive interactions) as well as on the characteristics of the oil used in the tribological contact (PAO-8). Indeed, if a
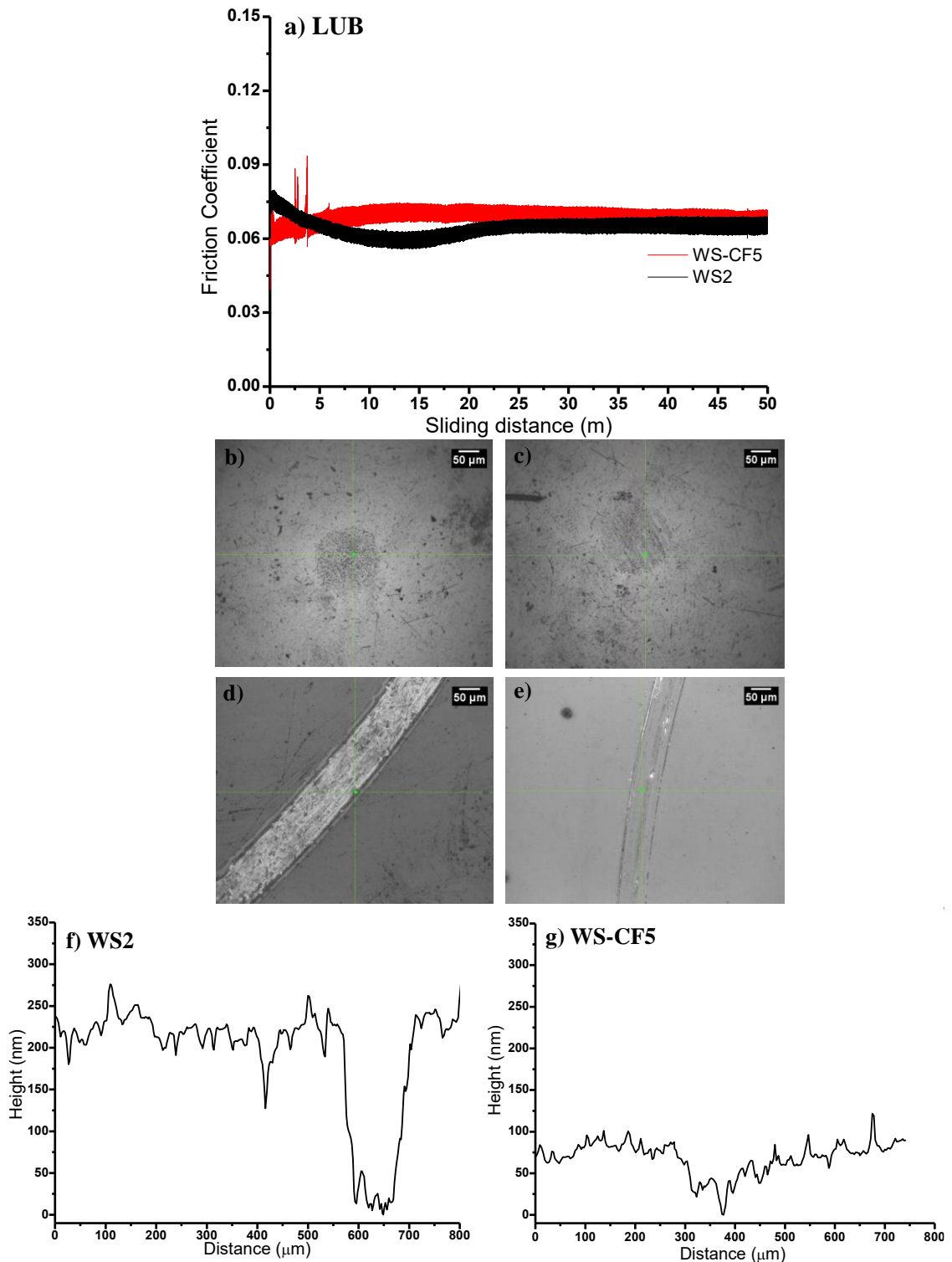
Figure 4.26 Tribological behaviour of the thin films tested in lubricated conditions for 50 m sliding against a 100Cr6 steel ball under 5 N load: a) friction curves, and the optical images of the b)-c) ball scars, d)-e) wear tracks and f)-g) wear track depth profiles, obtained for WS2 and WS-CF5 thin films, respectively.

hydrodynamic lubrication regime is considered, some authors have suggested that the friction is better correlated with the spreading parameter (SP) [182, 190]. SP is related to the adhesion behaviour of liquids to surfaces, with lower values leading to reduced friction. Moreover, non-polar surfaces in contact with non-polar oils give rise to an improvement of the tribological behaviour [273]. Table 16 shows the SP values calculated for WS2_200 and WS-CF5_200 films when these surfaces are in contact with the non-polar PAO-9 oil [190], which has similar characteristics to PAO-8. A SP value of 3 mJ/m^2 for WS2_200 and 21 mJ/m^2 for WS-CF5_200 were calculated. Therefore, the lower SP value for the WS2_200 surface gives rise to a weak interaction with the oil, leading to higher slippery between the contacting surfaces and, thus, to a lower coefficient of friction [274, 275]. On the other hand, the WS-CF5_200 coating is able to create a strong bonding with the non-polar oil (higher SP value), thus, having detrimental effect on the friction justifying the higher COF values observed in Figure 4.26 a).

Table 16 Spreading parameter determined for the thin coatings taking into account PAO-9 characteristics (Similar to PAO-8).

SP – Spreading Parameter[31] (mJ/m²)		γ_S^D - dispersive component of surface energy
$SP = 2 \left[\sqrt{\gamma_S^D \gamma_L^D} + \sqrt{\gamma_S^P \gamma_L^P} - \gamma_L \right]$		γ_L^D - dispersive component of surface tension
		γ_L - total surface tension
WS2	WS-CF5	γ_S^P - polar component of surface energy
3	21	γ_L^P - polar component of surface tension

When the steady state of friction curve is reached in lubricated condition (above 20 m sliding), after a progressive increase of the values for the WS2_200 coating, both coatings show similar trend and COF values. The observation of the wear tracks (Figure 4.26 d) and e)) and the analysis of the depth profiles presented in Figure 4.26 f) and g), show that the WS2_200 coating was completely worn out, leaving the substrate completely uncovered, while WS-CF5_200 coating still remained there. This means that, in WS2_200 case, the 0.07 COF value should be attributed to a steel-oil contact. Steel surfaces are known to have a high surface energy [190] being their global behaviour, from this point of view, closer to WS-CF5_200 than to WS2_200 coating. Although not measured, the literature value for SP of PAO on steel surface (12 mJ/m^2), is much higher than the one for WS2_200 coating, explaining the increase in the COF observed in this sample from 20 m until reaching the steady state, where a total steel-oil contact is expected.

Finally, it should be remarked that the friction coefficient values in the steady-state in lubricated conditions are higher than the ones of the tribological testing without lubrication, in particular for WS-CF5_200 film. This result suggests that the contact dominating the sliding between the two surfaces is different, being in lubricated tests a solid-oil interaction where oil spreading is important, whereas in the solid-solid contact the formation of a F-doped tribolayer determines the value of the COF. Despite the higher friction values attained in lubricated conditions, Table 15 demonstrates that the specific wear rates in both elements of the sliding contact are lower in lubricated than in non-lubricated tests, enhancing the protective role of the oil. As for dry tests referred above, WS-CF5_200 films showed lower specific wear rates than WS2_200 one. Again, this should be mainly due to the higher hardness of WS-CF5, which had also impact on the higher specific wear rate of the counterbody, as observed from Figure 4.26 b) and c).

4.3.4 Conclusions

In this subchapter, WS-CF films of 200 nm thickness were deposited using magnetron sputtering and their wettability behaviour and the tribological performance were evaluated and compared to the same coatings with higher thickness. F insertion led to a more compact morphology of the coating and reduced roughness, which in turn resulted in lower water contact angles. Due to the low thickness of the coatings, XRD confirmed that the initial growth of sputtered WS_2 occurred with the (002) basal planes of the WS_2 crystal structure preferentially orientated parallel to the surface. Contrary to the high oleophilicity achieved for the thick F-doped coatings (OCA = ± 10°), the thin F-doped coatings revealed an increase of their OCA values, this probably due to the (002) preferential orientation that should particularly influence the interaction between the thin F-doped coatings and the oil. Raman analysis demonstrated that F insertion increased the broadening of the main peaks assigned for pure WS_2 in good agreement with the very low crystallinity detected by XRD. Similar Raman results were obtained for the thick coatings.

In non-lubricated conditions, the thin F-doped films showed near-zero friction coefficient values, lower than those measured for WS2_200 sample, in accordance to what has been obtained for thicker coatings. Also, WS-CF5_200 coatings showed lower specific wear rates due to its higher hardness. To understand the potential application for oil-water separation, these thin coatings were tested in lubricated conditions using pure PAO-8 oil. The results showed lower friction coefficient values in the running-in period

for pure WS2_200 in comparison to F-doped ones. This difference could be related to the surface energy of the coatings, as well as with the polar characteristics of the coatings; the values were confirmed by an analysis based on the SP calculation. Despite this, the COF measured in lubricated tests was higher than for non-lubricated ones, particularly for WS-CF5_200 coating, as a consequence of the formation of a tribolayer, responsible for lowering the friction coefficient with no lubrication. However, the specific wear rates achieved in lubricated tests are lower than for non-lubricated ones, benefitting the first from the presence of the oil in the sliding contact.

Although the good tribological performance of thin 200 nm F-doped film was only possible for short running periods, a low mechanical loading expected on the metallic grids for oil-water separation purpose should lead to a suitable life duration. Therefore, in order to further optimize the tribological performance and wettability behaviour, it will be worth to study a hybrid surface modification system consisting of surface roughening by anodization with the application of thin WS_2-F based films. Besides the wettability and friction features, the F-doped coating can also have a high impact either as a catalyst for hydrogen evolution reaction (HER) or for microfluidic applications.

4.3.5 Important Remarks of Part III

This study was important to verify the influence of the thickness on the wettability behaviour and on the tribological performance of WS_2-C coatings doped with fluorine (F), deposited by magnetron sputtering. The morphology of the coatings did not change with the thickness decrease, revealing again an increase on both the compactness and on the smoothening of the coating surface with F increase. Such an evolution led to a more hydrophilic surface character as observed before for thick coatings, despite showing less oleophilic surface behaviour. Due to lower thickness, XRD results confirmed that this type of coatings start growing with an alignment of the (002) planes parallel to the substrate, which changed for randomly oriented crystals with the thickness increase. Overall, F insertion induced a decrease in the crystallinity, which was more evident in the case of thinner coatings. The tribological tests carried out in dry conditions at room temperature showed again lower friction coefficient for F-doped thin coatings (in the overall test, average 0.03). The additional lubricated tribological tests performed with pure PAO oil showed that the thin films presented similar friction coefficients (~0.07) in the steady-state regime. The tribolayer based on oriented W-S layers formed on the wear

track for the F-doped coating can justify the very low friction achieved when testing in non-lubricated conditions.

At this point, two films have been selected (WS2_200 and WS-CF5_200) to be deposited on dimple-shaped anodized Al alloy surfaces (LD). It will be worthy to study the effect of surface roughness promoted by anodization on the friction behaviour of hybrid surfaces created by combination of WS-CF films with anodized surfaces.

CHAPTER 5

Tribological performance of hybrid surfaces: dimple-shaped anodized Al alloy surfaces coated with WS-CF sputtered thin films

In this chapter, selected anodized Al surfaces were coated with the thin WS-CF films deposited by magnetron sputtering. The resultant structures were evaluated in terms of morphology, structure, wettability behaviour and, tribological performance in dry and lubricated conditions. Furthermore, a multisample anodizing system was assembled to reproduce the conditions optimized in the uni-sample system in order to make the sample anodizing a more scalable process. The work has been conducted in the University of Minho (CFUM/UP), in the University of Coimbra at CEMMPRE research institute, at LED&MAT laboratory in IPN-Coimbra and at the CTU-Prague.

Chapter overview

The main goal of this thesis was to create structured surfaces with different wettability behaviour and low friction, which could be applied in different fields. Then, this last chapter addresses the deposition of the thin WS2_200 and WS-CF5_200 films, developed in the previous chapter, on the selected anodized Al surfaces (large dimples – LD), which will create the hybrid surfaces. The first objective was achieved since the coating deposition over the LD surface showed that the hybrid structure continued to reveal dimpled/pore feature. Regardless of its surface wettability was mainly dependent on coating chemistry. The tribological performance was greatly enhanced by coating deposition namely in non-lubricated conditions for the F-doped case. However, in lubricated tests with PAO-8 oil, the hybrid system do not present a good effect on the friction as expected, this mainly correlated with the surface macroroughness and the mechanical properties of the contacts. This meant that, in lubricated testing, the high initial friction behaviour of LD+WS-CF5 case was due to the solid-solid contact properties that were progressively smoothed (this phenomenon was faster for WS2 case) and afterwards the friction was governed by the solid-oil contact of a hydrodynamic lubrication regime.

The results of this study have resulted in a scientific paper submitted for publication to International Journal of Advanced Manufacturing Technology (IF = 2.75).

5.1. Introduction

In our emerging world, the excessive use of plastics and toxic wastes, such as some lubricants, started to be a big concern due to global warming issues. Then, the development of multifunctional materials with advanced performance, which can provide long-term service of devices addressing green production routes, is welcome. For example, transition metal dichalcogenides (TMDs) are well-known materials that received great attention by engineers and R&D people due to their exceptional self-lubricating properties in vacuum and inert environments being able to replace liquid lubricants [276, 277]. Despite their low load-bearing capacity, they appeared as suitable materials for many industrial applications such as aerospace components, engines, MEMs' devices and cutting tools [127, 128, 137]. Particularly, WS_2 presents low friction coefficients and their lubricity can withstand higher temperature working ranges (up to 650°C in air). In order to improve its hardness and the tribological behaviour in humid-containing atmospheres, TMD coatings are often alloyed with other chemical elements (e.g. C, Cr, N) or compounds [152, 232, 278, 279]. Likewise, WS-CF coatings were deposited by magnetron sputtering to enhance the friction performance; the water/oil affinity was also changed as the F content was increased from 0 to 9.5 at. % [263].

From the literature it is known that the increase of the surface roughness can play a role on reducing, not only the friction but also the wear in some specific applications [280-283]. Also for coated samples, their friction and durability can be influenced by the substrate surface roughness underneath. The existence of surface protuberances or texturing enables to store abrasive dusts, allowing to get rid of ploughing effect; furthermore, cavities can also act as reservoirs of lubricant, or wear debris, improving the longevity of the material and avoiding abrasion of the substrate. For rougher surfaces, the effective contact area between surfaces decreases and, thus, the contact pressure in the Hertzian contact increases, as well as the shear stresses between the two sliding surfaces [284]. Alloyed TMD-based materials are able to reach lower friction coefficient with increasing applied loads, oppositely to the Amonton's law [151, 153, 285]. This behaviour has been deeply studied and was justified by the structural changes occurring in the contact. In fact, due to sliding, an alignment of the basal planes in the wear track, parallel to the sliding direction, takes place, condition essential for the self-lubrication behaviour of TMDs. Simultaneously, the formation of a transfer layer in the counterbody, with the basal plans aligned in the sliding direction, can also occur.

In regard to the substrate surface roughness, there are many modification techniques available to control the micro/nano surface roughness of metals. Examples are: mechanical grinding, laser texturing (LT), photolithography and anodization [210, 286-288]. Among them, anodization arises as a powerful method to tailor the surface roughness due to its high reproducibility, reliability, cost-effectiveness and easy industrial scalability; simultaneously, it can also modify the surface chemistry [78]. Aluminum and its alloys have a great potential for replacing heavier materials (steel and copper) due to their low density; moreover, they can be easily recyclable. The anodization process was used to get different topographies and roughness in Al surfaces; then, nanostructuring provided porous-type and dimple-shaped surfaces with different surface energy [234]. Porous-shaped anodized aluminum surfaces have weak mechanical resistance [89, 261]; however, studies on laser texturing of metallic surfaces have reported on the importance of holes or dimples in terms of friction reduction [46, 48].

Rough surfaces combined with self-lubricating coatings can reach better friction and wear behaviours than polished surfaces [289]. Recently, some authors have used laser texturing (LT) on steel substrates providing grooving or dimples (micro-range scale) on surfaces and have coated those surfaces with thick WS_2 coatings produced by EHDA method [288]. Even though LT method can be time-consuming and expensive from the industrial point of view, the results demonstrated that the increase of substrate roughness led to a reduced friction of the WS_2 solid lubricant surface. It should be highlighted that, if the increase of surface roughness is at the nanoscale range, the films have to be thin enough to replicate the surface topography, i.e. with thickness not overcoming the dimension of the topographical features.

In this chapter, dimple-shaped Al alloy surfaces were produced by anodization (Chapter 3) and coated with self-lubricating WS-CF thin films deposited by magnetron sputtering (Chapter 4.3), creating a hybrid structure. The surface modified samples will be evaluated regarding the wettability behaviour and the tribological performance, in view of achieving a functional surface with potential for application in oil industry, microfluidics, printing and more.

5.2 Experimental

5.2.1 Production of the anodized Al surfaces

A commercial 6016 Al alloy sheet of 0.2 cm thick was cut into rectangular plates of 3.5 x 1.5 cm^2. The Al alloy surfaces followed the polishing steps (micro-texturing) and

pre-treatment as described in Chapter 2. However, in order to optimize the process, in this study the anodization was carried out in a multisample system, instead of the unisample configuration as previously used. Then, a maximum of 3 samples could be anodized at once (Figure 5.1).

The selected anodizing conditions have been already optimized (Chapter 3) in order to achieve texturing with dimple-shaped features, reached when using 0.5 M H_3PO_4 at 100 V [234]. Additionally, the anodized surfaces were chemically etched with a phosphoric-chromic acid solution at 30°C for 30 min, and then washed in distilled water for 10 min and dried. In the final, Al oxide dimpled textures with an average diameter of ~220 nm (Large Dimple (LD)) were obtained.
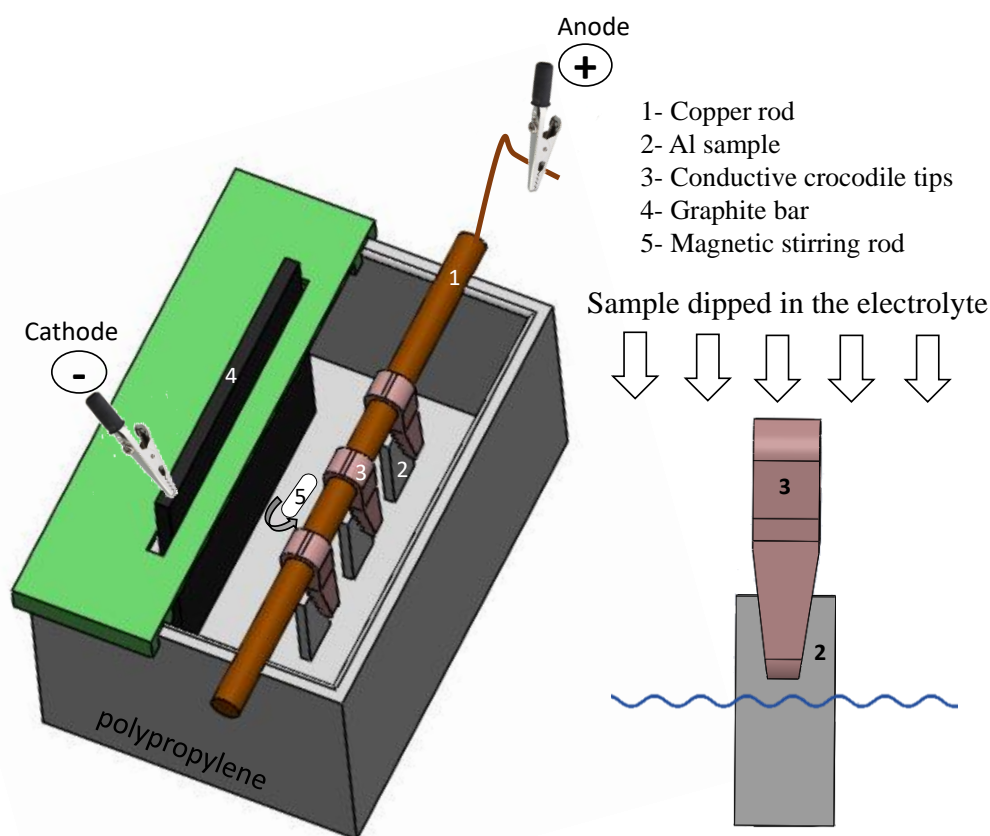
Figure 5.1 Schematic diagram of the multisample anodization cell developed under this thesis to produce the anodized Al alloy surfaces.

5.2.2 Deposition of the WS-CF films on anodized Al surfaces

Thin WS-CF films have been deposited by magnetron sputtering on mirror-polished steel substrates and they were fully characterized (Chapter 4.3) and compared with the results of the thick coatings. Then, WS films with and without F addition of ~200 nm thickness (named as WS2 and WS-CF5) were deposited on the Al anodized surfaces

with large dimples (LD), (Figure 5.2). The same films were also deposited on non-anodized (NA) Al alloy surfaces for comparison purposes.
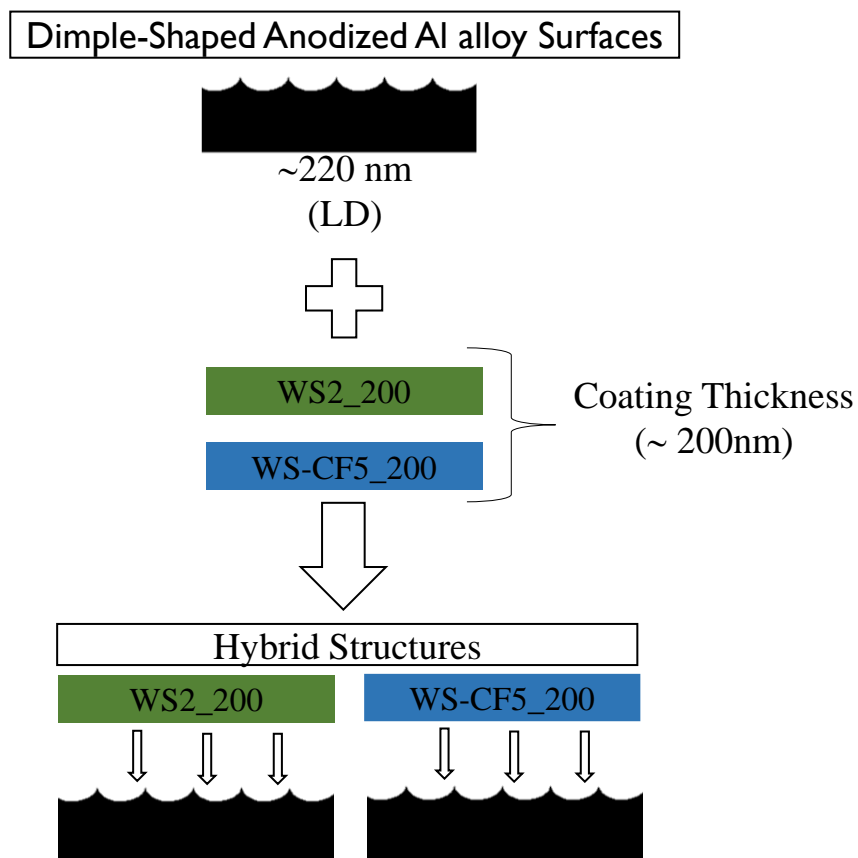
Figure 5.2 Assembly of the hybrid structure: anodized surfaces coated with thin WS-CF films.

5.2.3 Hybrid structure characterization

The top-view morphologies of all the hybrid modified surfaces were observed by SEM, (ZEISS Merlin – Field emission gun, high resolution with charge compensation) operating in secondary electron mode. The topography and roughness of the surfaces were characterized using atomic force microscopy (AFM) (Bruker Innova) with a silicon tip of nominal radius below 8 nm, in tapping-mode. Scans of 2 x 2 μm^2 size were acquired at a scanning rate of 1 Hz. Additional image processing was conducted using the *Gwyddion* software. The structure of the 200 nm thickness films over the dimple-structure was analysed by X-ray diffraction (XRD) (PANalytical X'Pert Pro MPD system) using Cu Kα radiation (λ=1.54 Å) (45 kV and 40 mA) in grazing angle (2°) in 10-80° 2θ range.

The tribological behaviour of the hybrid structures ($R_q \approx 0.5 \pm 0.1$ μm) was carried out in a ball-on-disk tribometer (CSM Instruments) at room temperature (25 °C) with

35-40% of relative humidity in non-lubricated and lubricated conditions; in the latter, PAO-Grade 8 oil ($\rho = 0.8$ g/cm3, ν (40 °C) = 48.5 mm^2/s and ν (100 °C) = 7.9 mm^2/s) was used as lubricant. The Tallian parameter calculated according to the Hamrock-Dowson approach [265], revealed that it was in the 1<λ<5 range, meaning that the tribological testing started in a partial lubrication regime. The sliding counterpart was a 100Cr6 steel ball (H = $\sim$ 5 GPa, R_{qball} = 0.05 ± 0.01 μm) with diameter of 6 mm, the linear speed was 0.1 m/s, the sliding distance was 15 m and the normal load was 5 N ($\sim$700 MPa Hertzian contact pressure). The coefficient of friction (COF) was the average value of the whole sliding test in the steady state. The morphology of the wear tracks and the worn scars of the contact surfaces were observed by optical microscopy and the depth profile of the wear tracks was evaluated by 3D profilometry (ZYGO). Contact angle (CA) measurements were carried with water and α-bromonaphthalene to assess the wettability of the hybrid surfaces, while their surface free energy (SFE) was calculated according to the OWRK method [182, 183].

5.3 Results and Discussion

5.3.1 Morphology, roughness and structure of hybrid structures

The reproducibility of the anodizing conditions in the multi-sample system in comparison to the unisample was evaluated. Figure 5.3 shows the SEM top-view surface morphologies of the anodized Al surfaces obtained in the unisample (a) and multisample (b) anodizing systems. As it can be seen, both treated surfaces presented similar morphology and dimple diameters, confirming the reproducibility of the process.

Figure 5.4 presents the surface morphology of the samples after coating. It is clear that the dimple morphology determined the growth of the WS-based cauliflower-like thin films. For instance, it is reported in [290] that in the deposition of Al and W on porous anodized Al surfaces by magnetron sputtering, using oblique angle deposition (OAD), the *adatoms* were preferably deposited over the hexagonal structure of the substrates (pore walls) and the increase of the deposition time caused the broadening of the grown "islands" and, consequently, caused the narrowing of the pores. Taking into account that thin films tend to mimic the substrate surface roughness, and for the dimples, the material

UNISYSTEM   MULTISYSTEM
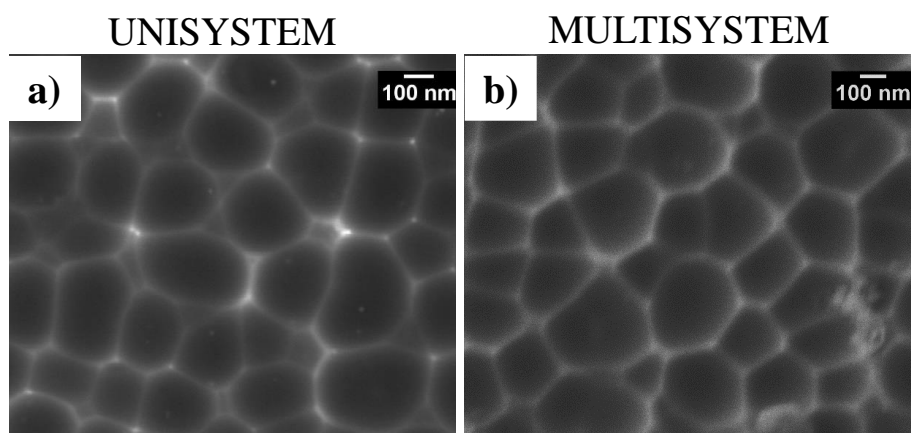
Figure 5.3 Top-view morphologies by SEM for LD anodized surfaces produced in the a) Unisample and b) Multisample anodizing system.
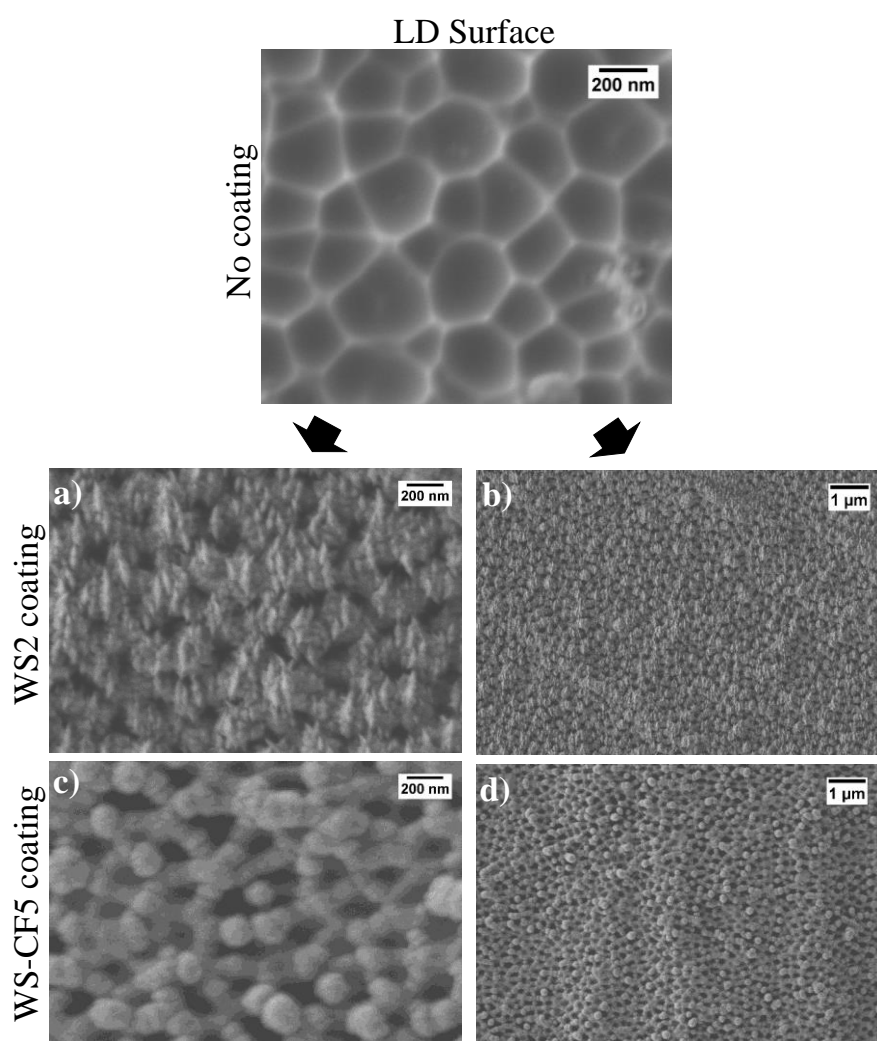
LD Surface

Figure 5.4 SEM morphology of the hybrid surfaces created by combining the thin WS-based films on the LD surface at a), c) high and b)-d) low magnifications.

is preferably deposited on the dimple edges, initially forming "islands" that continue to grow with the deposition time [288]. It was also visible that the columns merging is delayed due to the large dimple size, inhibiting the surface coverage. Then, the *adatoms* can be

deposited in the inner dimple parts; however this zone of the coating cannot grow as much as at the dimple edges, since the depositions were carried out only for short times. Therefore, pores are still presented in the coatings deposited on the LD surface (Figure 5.4 a)-d)), as desired for the hybrid structure. However, the pores are smaller than the original dimple sizes, this being more evident for WS2 coating, as expected, since the F incorporation clearly densifies the coating morphology [263].

From the above mentioned, dimpled morphology of anodized Al substrates can give rise to nanoporous thin films, even without OAD deposition if short deposition times (low thicknesses) are used. Hence, these results show that it is possible to create hybrid structures by combining textured Al surfaces with self-lubricating coatings.

Figure 5.5 shows the XRD patterns of the hybrid surfaces. No significant differences between the structures of WS2 coating deposited on glass or on the LD surfaces are observed. However, changes on the preferential orientation can be remarked.
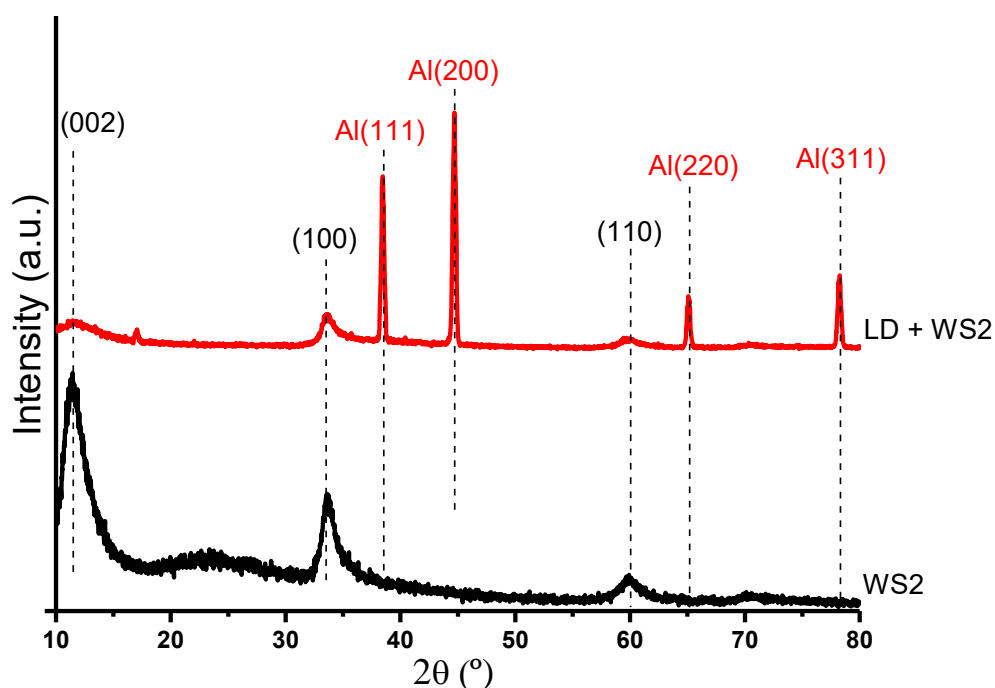
Figure 5.5 The XRD patterns of the thin WS2 coating (200 nm thickness) deposited on glass and on a LD surface.

As previously found [291], the WS2 coating deposited on glass substrate showed a (002) preferential orientation; i.e. WS_2 basal planes are deposited parallel to the substrate. In the case of the films deposited on LD surface only vestiges of the (002) plan could be detected, being the most intense peak occurring at $2\theta \approx 34°$, corresponding to the asymmetric (100) plan typical of WS_2 sputtered coatings. For this example, contributions from the Al-alloy substrate are presented as well. No Al oxide peaks arising from the

anodization process could be detected suggesting that the very thin oxide layer is amorphous. The change in the orientation could be speculated to be related with the difference in the surface free energy (SFE) of the substrates, 63.2 mJ/m^2 and 45.4 mJ/m^2 for the glass and the LD surfaces, respectively. In the initial stage of the film growth, the more non-polar character of LD surface (low surface energy), comparatively to glass, may result in a higher affinity for more polar-like structures, namely the (100) planes of WS$_2$, instead of the interaction with the well-known non-polar (002) basal planes [269], leading to stronger orientation of the crystals following [100] direction.

5.3.2 Wettability of the hybrid structures

Chemical composition and roughness are the main features governing the surface wettability. In regard to roughness, Figure 5.6 presents the topographic profiles obtained by AFM micrographs for the LD anodized Al surfaces before (a)) and after (b)) coating with WS-CF5 film. Profile 1) in Figure 6 demonstrates that the peak-to-peak distance is close to the dimple size diameter statistically measured by *ImageJ* on the SEM top-view images [234]. Indeed, dimpled textures on the Al oxide surface had average *d* diameters
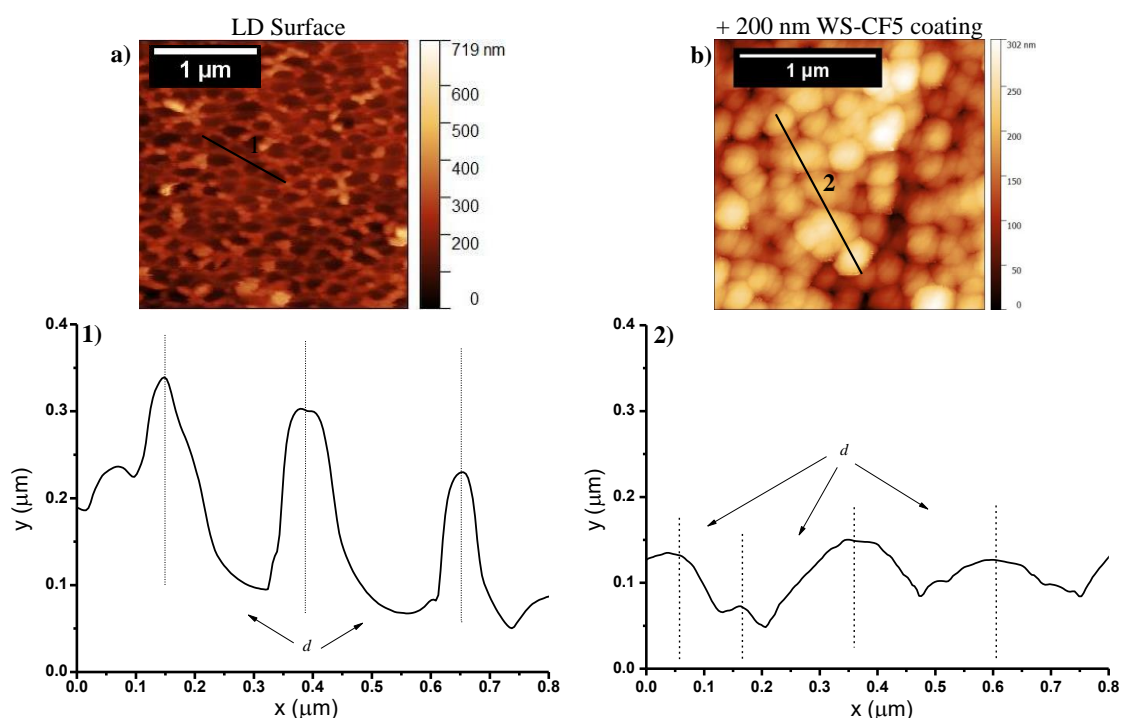
Figure 5.6 Topographic images obtained by AFM for LD surfaces a) not coated and b) coated with thin WS-CF5 coating. Graphic profiles of both surfaces was recorded for 0.8 µm length (Profile 1 and Profile 2). (*From* [291])

of ~253 ± 13 nm (quite well compared with SEM analysis – 223 nm) what is reasonable considering the AFM tip masking in the analysis. On the other hand, profile 2) in Figure

5.6 confirms that the peak-to-valley distance is decreased due to surface smoothening after the coating deposition, as observed above in the SEM morphology. Moreover, the pore size was lower (~183 ± 63 nm) than the original dimple. The roughness increases for the LD surface (Sa = ~96 nm), in relation to the non-anodized surface (NA) (Sa = ~56 nm, AFM picture not shown), suggesting that at nano level the roughness was higher after anodization.

In relation to the wettability, Figure 5.7 a) shows that the anodization process turned the LD surface into the hydrophilic domain in relation to the non-anodized Al surface (LD: WCA = 63 ± 10° and NA: WCA = 91 ± 4°), in contrast with the OCA for which an increase was observed (LD: OCA = 49° ± 2 against NA: OCA = 32° ± 6, see Figure 5.7 b)). The anodized surface presents aluminum oxide which can contribute for the enhanced water affinity. In relation to the OCA value, LD surface showed an increase
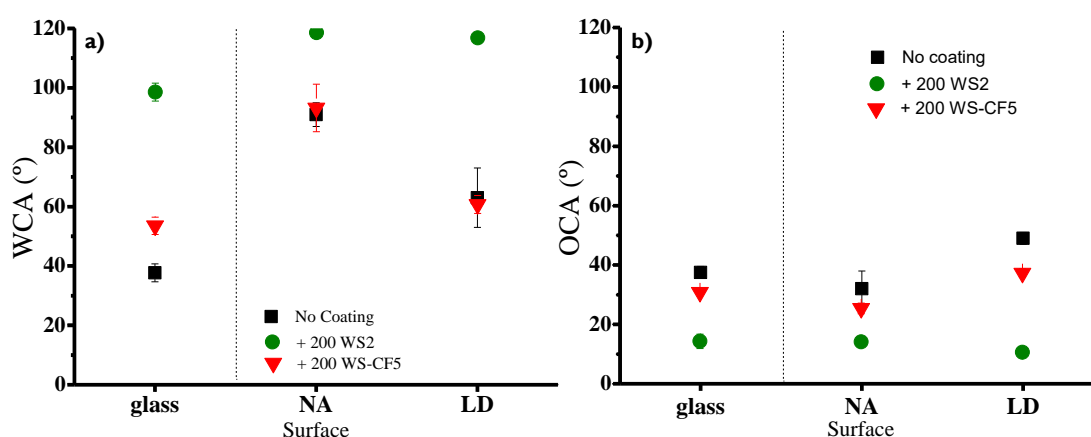
Figure 5.7 Wettability evaluation by contact angle measurements for the hybrid surfaces, showing the a) WCA and b) OCA regarding LD surfaces in comparison to NA surfaces.

of oil repellence comparatively to the non-anodized (NA) surface, showing that the geometrical structure of the dimple-shaped surface (protuberances) can influence the oil interfaces (tends to Cassie-Baxter model of wettability). These wettability results for the multisample anodizing system mostly corroborate the ones previously found for the anodized Al surfaces in the unisample system in Chapter 3 [234].

According to the previous study in Chapter 4.3, when depositing the thin films on glass substrates [291], the F incorporation reduces the film surface roughness leading to a more hydrophilic surface while showing an increase in the oil repellence, comparatively to pure WS_2. That finding had firstly been explained by the increase of the polar component on the F-doped coating which led to higher bonding with water, decreasing

the WCA while conducing to higher OCAs. In relation to the F-doped thin films on LD surface, the measurements recorded at a microscale level demonstrated that the hybrid surface roughness (Ra) was also slightly decreased (LD: ~325 ± 20 nm and LD+WS-CF5: ~300 ± 10 nm, 3D profilometry data), but this verified roughness decrease caused no substantial effect on the WCA and OCA values. Contrary, even the LD+WS2 surface fairly depicted the same roughness as the LD+WS-CF5 hybrid surface, it contributed to increased WCA values (hydrophobic regime) and very low OCA values (oleophilic domain), as Figure 5.7 b) shows. From this CA analysis, it is possible to conclude that the LD+WS-CF5 hybrid surface wettability was mainly ruled by the underneath roughness, having the coating chemistry just a low effect. Oppositely, the wettability of the LD+WS2 surface seemed to be only governed by its coating chemistry. Indeed, the roughness decrease of the LD surface when coated led to just a slight increase of the surface free energy (SFE) values (40-55 mJ/m^2 range), as shown in Table 17.

Table 17 Surface free energy (SFE) values obtained for the hybrid surfaces using the OWRK model.

Surface	SFE (mJ/m^2)
NA	39
LD	45
LD + WS2	46
LD + WS-CF5	50

5.3.3 Tribological behaviour of the hybrid structures

The tribological tests, with and without lubrication (PAO-8 oil), were performed at room temperature at a load of 5 N and sliding speed of 10 cm/s. Only a short number of turns were selected due to the very low coating thickness of the films deposited on the hybrid surfaces. Figure 5.8 shows the friction coefficient without lubrication (a) and b)) and with lubricant (c)). Comparing NA and LD surfaces tested without use of lubricant (Figure 5.8 a)), both showed the same friction behaviour reaching a stable friction coefficient close to 0.6 after the running-in period. As the steel ball is harder (~ 5 GPa) than the aluminum surfaces (~0.5 GPa), severe wear occurs in both cases with the wear tracks showing strong abrasion scratches and plastically deformed wear debris (not shown).
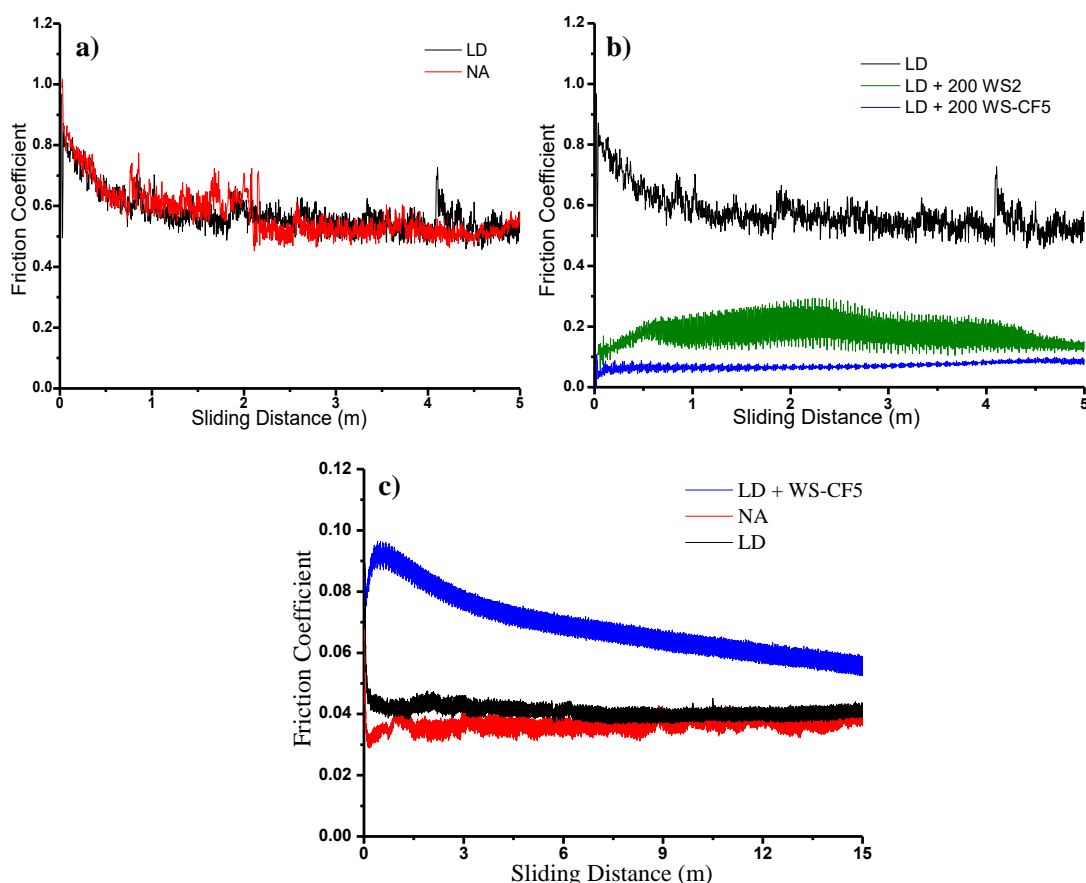
Figure 5.8 Friction curves recorded for the tribological tests performed in a)-b) dry and c) lubricated conditions on the hybrid surfaces created by the deposition of WS-CF-based films on LD anodized surfaces.

Concerning the tribological behaviour of the hybrid surfaces, Figure 5.8 shows that, overall, a friction reduction occurs in non-lubricated tests (b)), whereas an inverse trend is observed in lubricated ones (c)). In dry condition, as found before for other TMD-based coatings as well as for this WS-CF system, the low friction can be explained by the formation of a tribolayer consisting of basal planes of TMD phase well-aligned in the direction of the sliding. The easy intra- and intercrystalline slip, due to the weak van der Waals' forces between the lamellae of S-W-S hexagonal basal planes of WS_2, facilitates the sliding giving rise to low tangential forces and, consequently, to low friction coefficient. The LD surface coated with WS-CF5 film showed again lower friction coefficient than the one coated with WS2 film due to the increase in the interplanar distance promoted by the F incorporation in the WS_2 matrix, which facilitates the sliding ability of the tribolayer [263]. Moreover, the LD+WS2 hybrid surface tested in dry condition revealed to have WS_2 wear debris in the wear track, as well as in the ball, that could keep lower friction than the uncoated one, although showing a similar high degree of plastic deformation. However, the graphic profile of the friction in Figure 5.8 b) shows high instability occurring

during the tribological test suggesting that from the very beginning of the test the coatings were worn out. The low wear resistance made this hybrid surface to not be tested further in lubricated conditions.

Figure 5.8 c) shows different friction behaviours in lubricated regime for the NA/LD surfaces or the LD surface coated with WS-CF5 thin film. When using PAO-8 oil, the LD surface depicted approximately the same COF (~0.04) as the non-textured surface (NA) in the end of the test, inside standard deviation values, although, in the beginning of the test, LD shows higher values than NA. Figure 5.9 a)-b) shows plastically deformed abrasion grooves in the wear track of the LD surface, as well as a few oxidized worn Al particles adhered in the counterbody. NA sample shows similar morphologies excepting the absence of oxidized particles. The surface of the wear track shows that the original scratches, resulting from the polishing of the sample, completely disappear, revealing that the original high roughness was smoothened. Unexpectedly, the LD+WS-CF5 hybrid surface depicted higher friction value in lubricated regime than the uncoated surfaces. The different friction behaviour of these three samples in lubricated condition could be understood based on the spreading parameter (SP) and lubrication regime. SP gives information about the degree of interaction of a surface with a liquid and some authors suggested that as higher is the SP value, the surface has higher interaction with the liquid (e.g. oils) and it leads to a detrimental effect on friction. Table 18 presents the SP values determined for the three surfaces tested in lubricated regime with PAO oil. Although being initially in a boundary/mixed regime contact, due to the low mechanical strength of Al-alloy compared to the steel ball, any solid-solid contact occurring during lubricated test will be immediately plastically deformed, smoothening the surface and reaching the hydrodynamic regime very fast. In this period, LD surface having a higher SP value than NA shows higher friction coefficient. However, as the test is running, wear is occurring, destroying the LD anodized dimples, making both LD and NA surfaces with same chemical composition and morphology, giving rise to similar values of COF. As in case of WS-CF5 film, a different mechanism takes place. As the hardness of this film (H = 3 GPa [263]) is close to the one of the hard steel counterpart, plastic deformation is harder to be achieved with the solid-solid contacts being maintained during the test. Therefore, the COF will be determined by the friction in the solid contacts (see representation of the mechanism in Figure 5.10 a)). With more laps, smoothening of the surface peak asperities starts to occur due to the progressive wear, decreasing the solid-solid contact points (going progressively
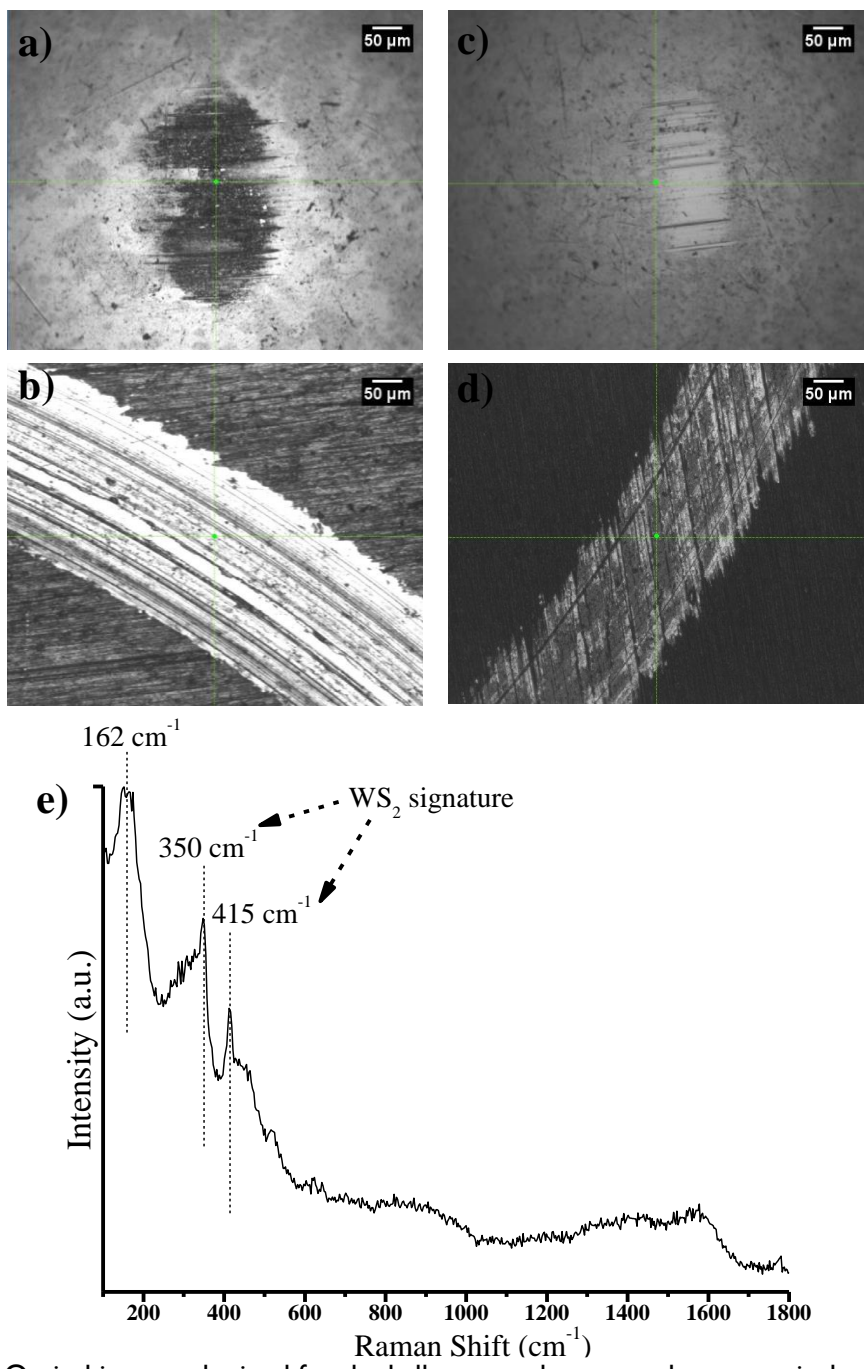
Figure 5.9 Optical images obtained for the ball scars and wear tracks, respectively, when a)-b) LD and c)-d) LD+WS-CF5 surfaces were tested in lubricated condition with PAO. The Raman spectrum of the LD+WS-CF5 wear track is shown in e).

Table 18 Spreading parameter values (mJ/m²) determined for the tested surfaces when interacting with PAO-8 oil.

	SPREADING PARAMETER (SP)
	PAO-8 oil
NA	5
LD	13
LD + WS-CF5	17
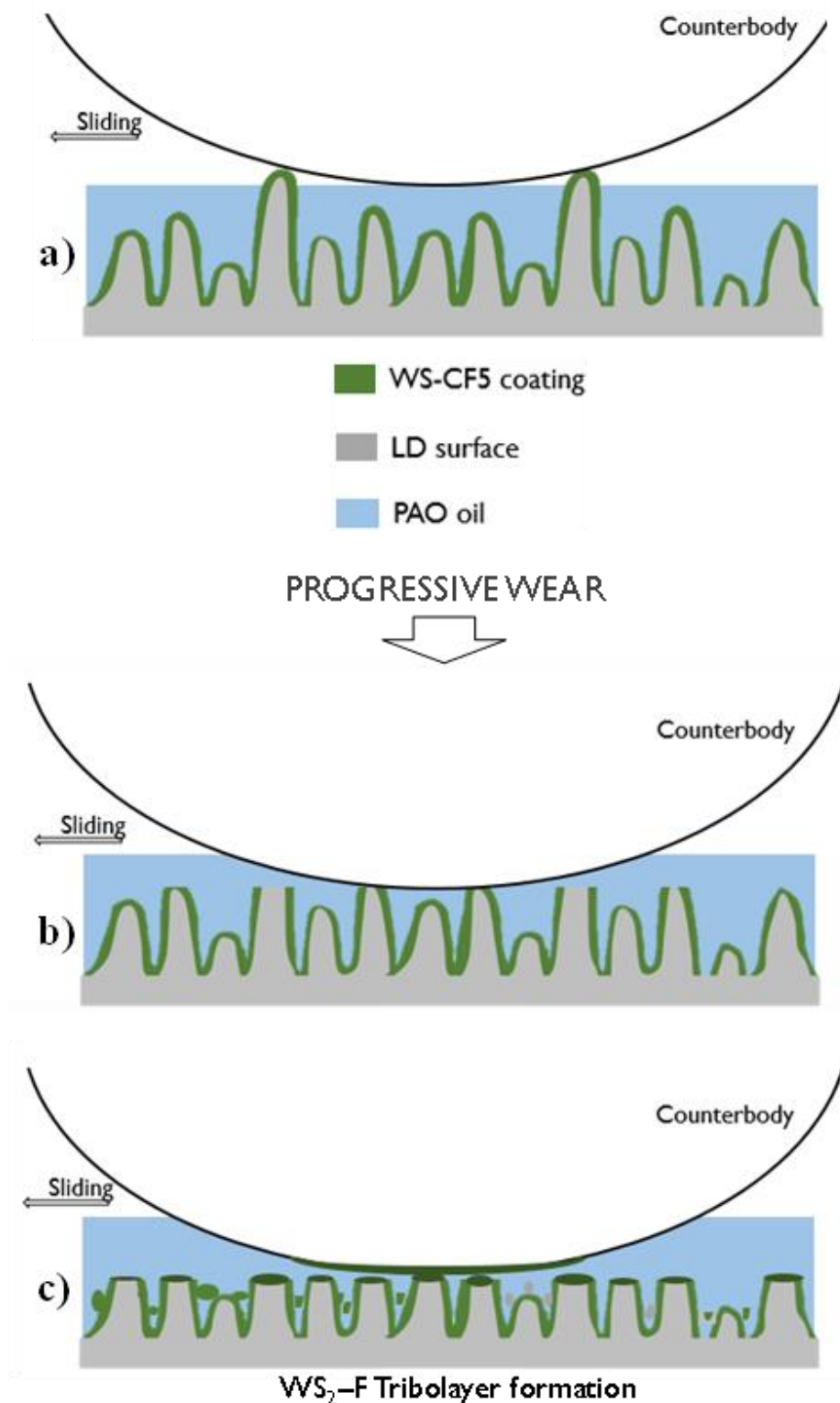
Figure 5.10 Schematic representation of the surface wear progressing in lubricated conditions for the LD+WS-CF5 hybrid surface at a micro-scale level in the a) initial contact; b) after some cycles and c) close to the end of the test.

from the mixed regime to the hydrodynamic one) (see Figure 5.10 b) for representation).

Then, the COF value went progressively down being closer to the one of the uncoated

LD surface in the end of the test. Figure 5.9 c)-d) shows that the counterbody did not present adhered worn material while the wear track still shows the original scratches from the substrate and signs that the coating was not completely worn out. The Raman spectrum in Figure 5.9 e) obtained in the wear track confirms the presence of remaining WS_2.

5.4 Conclusions

Hybrid surfaces consisting of dimple-textured Al alloy surfaces, produced by anodization, and WS-CF films, deposited by magnetron sputtering, were developed. The thin films (~200 nm) deposited onto the anodized surfaces with dimples of similar dimensions end up also with a porous surface but with lower size than the initial dimples. In spite of the increased roughness, the large dimples (LD) on the Al surfaces gave rise to similar friction behaviour as the NA surface either in dry or lubricated conditions.

The smooth LD+WS-CF5 hybrid surface led to both low WCA and OCA values, whereas LD+WS2 shows the highest hydrophobicity and oleophilicity of all the studied surfaces. The deposition of WS-based films on the LD surface (hybrid surface) significantly improved the lubricious performance in dry condition, as expected, especially for the F-alloyed thin film. LD+WS2 showed a very poor wear resistance. However, coated surfaces (LD+WS-CF5) depicted high friction values in lubricated conditions with PAO oil in comparison to bare LD surface. From the tribological point of view, there is a synergetic action of the dimple-shaped anodized surfaces with the thin WS-based films determining the friction performance of the whole hybrid structure, if all lubrication regimes are considered, from dry tests until hydrodynamic conditions. Even though lower COF was reached for the uncoated dimple-shaped surface (LD) than the coated one for the whole tribological test in lubricated regime; the progressive wear of the film on the LD+WS-CF5 hybrid surface can also turn the contact lubricated regime to hydrodynamic and, thus, reduced friction is possible to be achieved.

In conclusion, it was clear that both surface texturing and coating chemistry were particularly important for the wettability and friction behaviours. Taking into account the friction and wettability behaviours, LD+WS2 can be suggested for the separation of oils/water mixtures, due to high hydrophobicity and oleophilicity, whereas LD+WS-CF5 surfaces can be suggested for tribological applications where the different lubrication regimes can take place.

CHAPTER 6

Conclusions and Perspectives

This section summarizes the main conclusions of the thesis, indicating some open window for future improvement in relation to both the anodization step and deposition of WS-CF coatings, in order to reach better functionality of the hybrid structure to broaden its application.

Conclusions and remarks

The anodization of Al alloys revealed to be very challenging on reproducing textures and nanostructures. Overcoming that issue, the anodization in one-step configuration with additional chemical etching for Al oxide removal, allowed for a concave or dimple surface texture. Lower dimple diameter (SD surface $\approx$ 30 nm) was obtained when using H_2SO_4 electrolyte at 15V, and, larger dimple diameter (LD surface $\approx$ 220 nm) was reached with H_3PO_4 as electrolyte operating at 100 V. Additionally, a two-step configuration model was also used with each electrolyte to prepare porous Al oxide structures with different pore diameters and pore channel length. H_2SO_4 allowed for ordered porous oxide layers of 12 µm length and around 30 nm of top pore diameter. Likewise, H_3PO_4 allowed for porous structures (2 µm layer thickness) with around 200 nm or 250 nm of top pore diameter; the latter if an extra final etching was carried out for pore widening. In these thick oxide layers, the EDS analysis and XRD results identified the incorporation of electrolyte anions (SO^{4-} or PO_4^{3-}) in the grown oxide. The wettability evaluation of the three porous oxide topographies obtained in two-step configuration gave both low water and oil contact angles for all those surface textures, attributing them a hydrophilic/oleophilic surface behaviour. This was mainly related with easy liquid penetration in the porous structures, being the interpore walls not able to sustain the liquid droplets. Besides this, the dimple-shaped surfaces produced by anodization gave higher water and oil contact angles, with the larger dimple (LD) (diameter ~220 nm) reaching a hydrophobic behaviour, despite still being in the oleophilic domain.

Moreover, WS-CF coatings with different F contents (0 to 9.5 at. %) were deposited on a reactive magnetron sputtering chamber in an Ar/CF_4 atmosphere. However, after a certain increase of the CF_4 flow rate, the fluorine was not incorporated in the coating anymore, and the coatings started to present high amounts of oxygen and carbon. This was suggested to be related with the competitive growth and etching mechanisms occurring in the growing film surface, due to possible oxygen scavenging from chamber walls what was highly potentiated at higher CF_4 flow rates, as already reported for RIE processes. The morphological characterization allowed to conclude that the F insertion increased the compactness of the coatings as led to the hardness increase (WS-CF5 with 3-4 GPa, comparatively to 0.13 GPa of WS2). The tribological tests performed in dry condition at room temperature retrieved lower friction coefficient for the F-doped

coating. This reduction is more evident when testing at 200 °C (COF value of WS-CF5 was 0.016 against a 100Cr6 ball). XRD data justified this friction performance due to the increase of the interplanar distance promoted by the F insertion in the WS_2 matrix, which facilitated the sliding ability of the formed tribolayer.

Preliminary SEM cross-section images obtained about the morphology of these coatings deposited over porous oxide structures produced by anodization clearly give the information that the coating thickness was excessive, and the dimple-shaped surface feature was also lost. Subsequently, the porous-type hybrid structures were abandoned and a thickness coating optimization was conducted in order to be deposited and to replicate dimple-shaped Al surfaces instead. Further characterization of thin WS-CF films (thickness of 200 nm) confirmed the properties already obtained for the thick coatings in relation to wettability and friction performance, even if a slight increase in the OCA has been verified. Besides this, the XRD characterization showed that due to the low thickness, more (002) basal planes were orientated parallel to the coating surface, these planes cited as having a non-polar character and confirming the typical initial growth for WS_2-based coatings.

Regarding the creation of the hybrid surfaces, the morphological characterization demonstrated that WS-CF films with 100 nm thickness over the small dimples (SD) (diameter ~30 nm) highly masked the bottom roughness and the final roughness was mainly due to the film. Oppositely, the deposition of films with 200 nm thickness over the large dimples (LD) (diameter ~220 nm) showed that the film growth firstly started at the edges of the dimples. Secondly, the continuous film growth led to pore narrowing and consequently, the pores in the top had lower size than the bottom original dimples, as well as lower surface roughness. In addition, it was observed that in case of F-doped hybrid surfaces, the wettability was mainly dependent on the structure roughness while in case of the WS-based hybrid structure, only the coating chemistry ruled it. Afterwards, the friction performance of the coated and non-coated LD surfaces were tested in dry and lubricated conditions with PAO-8 oil. The tests carried out in dry conditions showed that the LD surface coated with thin WS-CF5 film presented a much lower friction coefficient than when coated with WS2 coating (LD+WS-CF5 = 0.07 ± 0.01 and LD+WS2 = 0.19 ± 0.05) in the steady-state interval. However, these COF values reached for the hybrid structures were higher than the ones obtained for these thin coatings deposited over smoothed polished steel substrates (WS-CF5_200 = 0.03 ± 0.01 and WS2_200 = 0.07 ±

0.02). This brings us to conclude on the detrimental effect of the induced roughness promoted by anodization on the tribological behaviour of the hybrid surfaces, contrary to what has been cited in literature. When the tests were followed in lubricated conditions with PAO-8 (non-polar liquid), the coated LD surface depicted higher COF value than the non-coated ones. It is important to note that, the WS2_200 and WS-CF5_200 films deposited on polished steel substrates showed the same friction value (0.07) when tested in lubricated conditions; this result due to a fully lubricated regime and the friction behaviour was highly dependent on the thin film lubricant properties in-between. Later, for the hybrid surfaces tested in lubricated regime, the high roughness of the surfaces and the mechanical properties of contacting surfaces governed the friction behaviour.

Then, the tribological evaluation of the hybrid surfaces tested in lubricated condition demonstrated that there was a synergetic action of the dimple-shaped anodized surfaces (LD) with the thin WS-CF5 films, if all lubrication regimes are considered, from dry tests until hydrodynamic conditions. The lower COF reached for the bare LD surface was due to the low mechanical strength of Al-alloy compared to the steel ball, resulting that any solid-solid contact occurring during lubricated test will be immediately plastically deformed, smoothening the surface and reaching the hydrodynamic regime. In case of LD+WS-CF5 hybrid surface, as the hardness of the WS-CF5 film was close to the one of the hard steel counterpart, plastic deformation is harder to be achieved with the solid-solid contacts being maintained during the test. Consequently, the progressive wear of the film on the LD+WS-CF5 hybrid surface can also turn the contact lubricated regime to hydrodynamic and, thus, reduced friction was possible to be achieved.

In summary, it was possible to combine roughened Al alloy surfaces produced by anodization with WS-CF films deposited by magnetron sputtering, as hybrid structures. The LD+WS2 structure depicted a hydrophobic/oleophilic surface behaviour that can be useful for self-cleaning (outdoors of buildings) and oil-water separation processes (metallic grids). Likewise, the hydrophilic/oleophilic character found for LD+WS-CF5 surface can have a role in printing or microfluidic applications. Moreover, it was possible to conclude that the control of the polar and non-polar character of surfaces (surface energy) was highly demanding to reach the desired liquid affinity as well as the friction performance.

Note that Al anodization process has a limited level of surface texturing, producing only nanoporous structures or dimple-shaped surfaces with limited porous surface arrangements (diameter, pore wall thickness, etc). So, this study opens new possibilities if

other micro/nano textures can be induced, for example using laser texturing. Another open window is to broaden the approach developed in this thesis to other substrate materials, such as steels, broadening its possible industrial applications. It could also be interesting to modify the surface energy of the coatings by using another doping element.

APPENDIX

Appendix
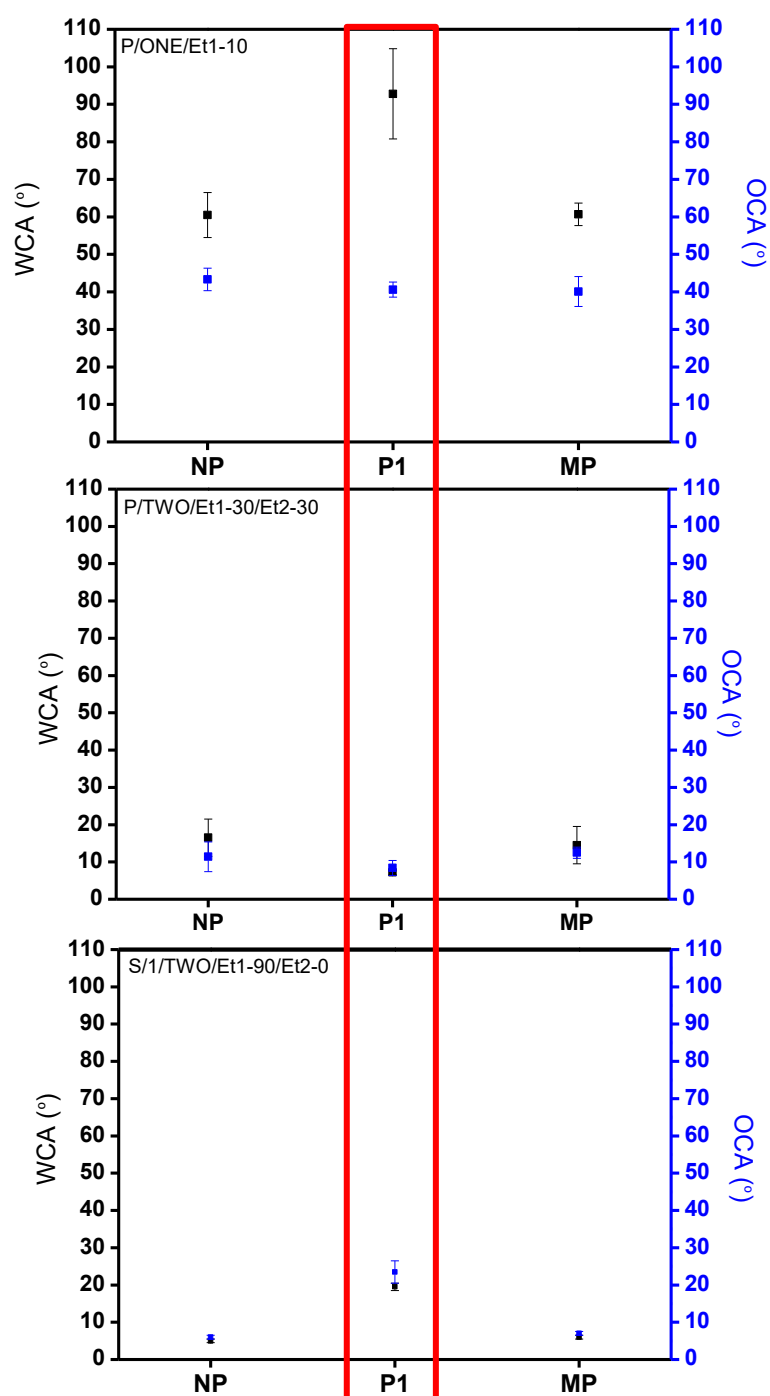
Figure A.1 Water and oil contact angles (WCA and OCA) obtained for 3 different structured Al surfaces obtained by anodization (P/ONE/Et1-10, P/TWO/Et1-30/Et2-30 and S/1/TWO/Et1-90/Et2-0, respectively) on the three types of Al alloy surface finishing (NP, P1 and MP).
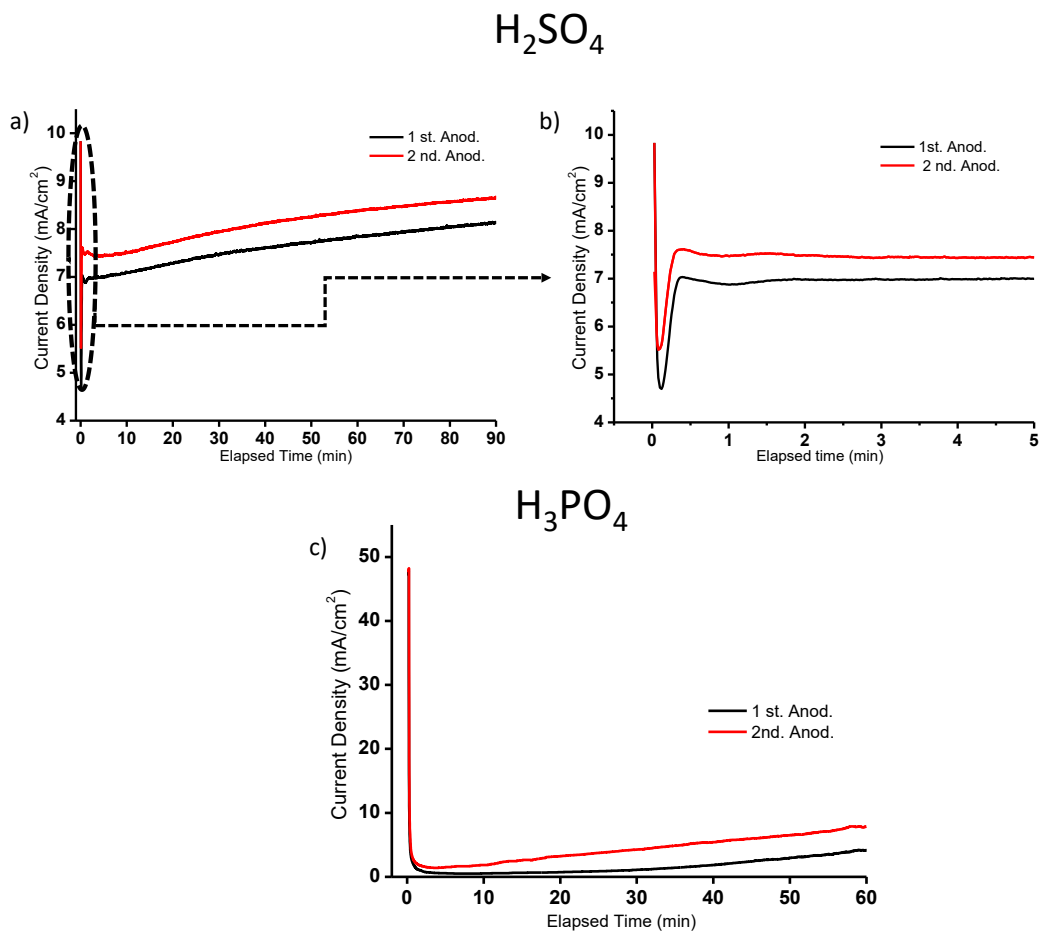
H$_2$SO$_4$

H$_3$PO$_4$

Figure A.2 Typical current density graphs recorded for 1st and 2nd anodization with a), b) 1 M of H2SO4 (15 V) and for c) 0.5 M H3PO4 (100 V) electrolytes.

S/0.3/ONE/Et1-90

S/1/TWO/Et1-90/Et2-0

P/ONE/Et1-10

P/TWO/Et1-30/Et2-0

P/TWO/Et1-30/Et2-30
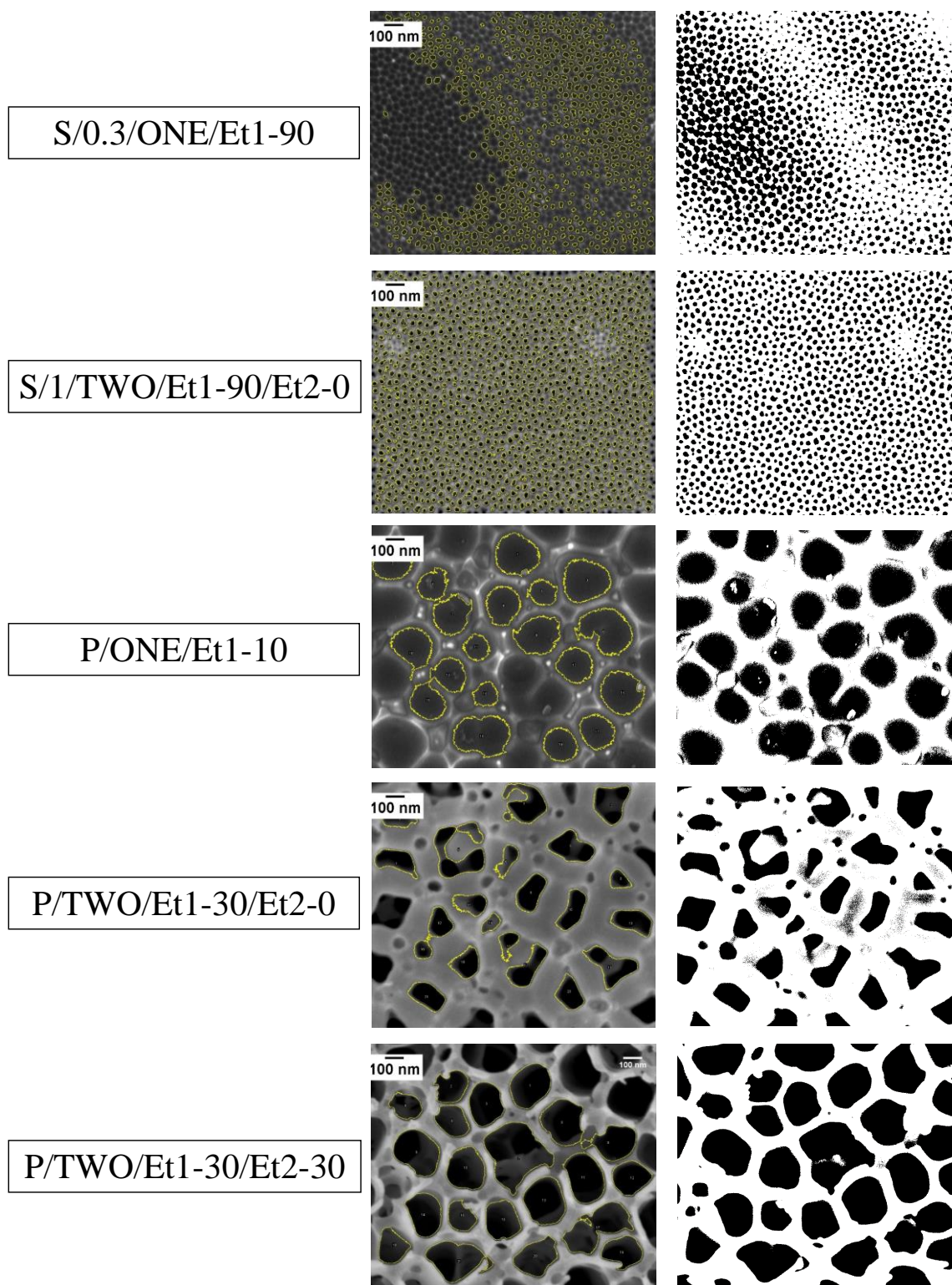
Figure A.3 Exemplification of ImageJ software appliance on the respective SEM images obtained for pore/dimple contour delineation and feature size determination for the 5 Al surface structures obtained by anodization.

REFERENCES

[1]   X. Feng, L. Feng, M. Jin, J. Zhai, L. Jiang and D. Zhu, Reversible Super-hydrophobicity to Super-hydrophilicity Transition of Aligned ZnO Nanorod Films. *Journal of the American Chemical Society*. 126 (2004) 62.

[2]   M. E. Kavousanakis, C. E. Colosqui, I. G. Kevrekidis and A. G. Papathanasiou, Mechanisms of wetting transitions on patterned surfaces: continuum and mesoscopic analysis. *Soft Matter*. 8 (2012) 7928.

[3]   E. S. Savoy and F. A. Escobedo, Molecular Simulations of Wetting of a Rough Surface by an Oily Fluid: Effect of Topology, Chemistry, and Droplet Size on Wetting Transition Rates. *Langmuir*. 28 (2012) 3412.

[4]   S. S. Latthe, A. B. Gurav, C. S. Maruti and R. S. Vhatkar, Recent Progress in Preparation of Superhydrophobic Surfaces: A Review. *Journal of Surface Engineered Materials and Advanced Technology*. 2 (2012)

[5]   X. Liu, Y. Liang, F. Zhou and W. Liu, Extreme wettability and tunable adhesion: biomimicking beyond nature? *Soft Matter*. 8 (2012) 2070.

[6]   T. Darmanin and F. Guittard, Superhydrophobic and superoleophobic properties in nature. *Mater. Today*. 18 (2015) 273.

[7]   R. Hensel, C. Neinhuis and C. Werner, The springtail cuticle as a blueprint for omniphobic surfaces. *Chem Soc Rev*. (2015)

[8]   C. N. W. Barthlott, Purity of the sacred lotus, or escape from contamination in biological surfaces. *Planta*. 202 (1997) 1.

[9]   R. Rakitov and S. N. Gorb, Brochosomal coats turn leafhopper (Insecta, Hemiptera, Cicadellidae) integument to superhydrophobic state. *Proceedings of the Royal Society of London B: Biological Sciences*. 280 (2013)

[10]   R. Helbig, J. Nickerl, C. Neinhuis and C. Werner, Smart Skin Patterns Protect Springtails. *PLoS ONE*. 6 (2011) e25105.

[11]   J. Nickerl, R. Helbig, H.-J. Schulz, C. Werner and C. Neinhuis, Diversity and potential correlations to the function of Collembola cuticle structures. *Zoomorphology*. 132 (2013) 183.

[12]   R. Hensel, R. Helbig, S. Aland, H.-G. Braun, A. Voigt, C. Neinhuis and C. Werner, Wetting Resistance at Its Topographical Limit: The Benefit of Mushroom and Serif T Structures. *Langmuir*. 29 (2013) 1100.

[13]   R. Hensel, A. Finn, R. Helbig, H.-G. Braun, C. Neinhuis, W.-J. Fischer and C. Werner, Biologically Inspired Omniphobic Surfaces by Reverse Imprint Lithography. *Advanced Materials*. 26 (2014) 2029.

[14]   T. Young, An Essay on the Cohesion of Fluids. *Phil. Trans. R. Soc. Lond.* 95 (1805) 65.

[15]   S. Latthe, C. Terashima, K. Nakata and A. Fujishima, Superhydrophobic Surfaces Developed by Mimicking Hierarchical Surface Morphology of Lotus Leaf. *Molecules*. 19 (2014) 4256.

[16]   R. Blossey, Self-cleaning surfaces - virtual realities. *Nat Mater*. 2 (2003) 301.

[17]   R. N. Wenzel, Resistance of solid surfaces to wetting by water. *Ind. Eng. Chem.* 28 (1936) 988.

[18]   R. N. Wenzel, Surface Roughness and Contact Angle. *The Journal of Physical and Colloid Chemistry*. 53 (1949) 1466.

[19]   A. B. Cassie and S. Baxter, Wettability of porous surfaces. *Trans. Faraday Soc.* 40 (1944) 546.

[20]   A. Hongru, L. Xiangqin, S. Shuyan, Z. Ying and L. Tianqing, Measurement of Wenzel roughness factor by laser scanning confocal microscopy. *RSC Adv.* 7 (2017) 7052.

[21]   C. Della Volpe, D. Maniglio, M. Brugnara, S. Siboni and M. Morra, The solid surface free energy calculation: I. In defense of the multicomponent approach. *Journal of Colloid and Interface Science*. 271 (2004) 434.

[22]   S. Siboni, C. Della Volpe, D. Maniglio and M. Brugnara, The solid surface free energy calculation: II. The limits of the Zisman and of the "equation-of-state" approaches. *Journal of Colloid and Interface Science*. 271 (2004) 454.

[23]   M. Żenkiewicz, Methods for the calculation of surface free energy of solids. *Journal of Achievements in Materials and Manufacturing Engineering*. 24 (2007)

[24]   C. J. Van Oss, M. K. Chaudhury and R. J. Good, Interfacial Lifshitz-van der Waals and polar interactions in macroscopic systems. *Chem. Rev.* 88 (1988) 927.

[25]   D. Y. Kwok and A. W. Neumann, Contact angle measurement and contact angle interpretation. *Advances in Colloid and Interface Science*. 81 (1999) 167.

[26]   F. M. Fowkes, ATTRACTIVE FORCES AT INTERFACES. *Ind. Eng. Chem.* 56 (1964) 40.

[27]   F. M. Fowkes, Donor-Acceptor Interactions at Interfaces. *The Journal of Adhesion*. 4 (1972) 155.

[28]   F. M. Fowkes, Calculation of work of adhesion by pair potential suummation. *Journal of Colloid and Interface Science*. 28 (1968) 493.

[29]   D. K. Owens and R. C. Wendt, Estimation of the surface free energy of polymers. *Journal of Applied Polymer Science*. 13 (1969) 1741.

[30]   S. Wu, Polar and Nonpolar Interactions in Adhesion. *The Journal of Adhesion*. 5 (1973) 39.

[31]   P. Ragesh, V. A. Ganesh, S. V. Nair and A. S. Nair, A review on 'self-cleaning and multifunctional materials'. *J. Mater. Chem. A*. 2 (2014) 14773.

[32]   P. S. Brown and B. Bhushan, Bioinspired, roughness-induced, water and oil super-philic and super-phobic coatings prepared by adaptable layer-by-layer technique. *Scientific Reports*. 5 (2015) 14030.

[33]   Z. Yoshimitsu, A. Nakajima, T. Watanabe and K. Hashimoto, Effects of Surface Structure on the Hydrophobicity and Sliding Behavior of Water Droplets. *Langmuir*. 18 (2002) 5818.

[34]   J. Bico, C. Marzolin and D. Quéré, Pearl drops. *EPL (Europhysics Letters)*. 47 (1999) 220.

[35]   M. Miwa, A. Nakajima, A. Fujishima, K. Hashimoto and T. Watanabe, Effects of the Surface Roughness on Sliding Angles of Water Droplets on Superhydrophobic Surfaces. *Langmuir*. 16 (2000) 5754.

[36]   D. Öner and T. J. McCarthy, Ultrahydrophobic Surfaces. Effects of Topography Length Scales on Wettability. *Langmuir*. 16 (2000) 7777.

[37]   G. Goncalves, P. Marques, R. Pinto, T. Trindade and C. Pascoal Neto, Surface modification of cellulosic fibres for multi-purpose TiO2 based nanocomposites. *Composites Science and Technology*. 69 (2009) 1051.

[38]   H. Zhang, Y. Li, Z. Lu, L. Chen, L. Huang and M. Fan, A robust superhydrophobic TiO2 NPs coated cellulose sponge for highly efficient oil-water separation. *Scientific Reports*. 7 (2017) 9428.

[39]   H. Zhou, H. Wang, H. Niu, A. Gestos and T. Lin, Robust, Self-Healing Superamphiphobic Fabrics Prepared by Two-Step Coating of Fluoro-Containing Polymer, Fluoroalkyl Silane, and Modified Silica Nanoparticles. *Advanced Functional Materials*. 23 (2013) 1664.

[40]   C. Petcu, V. Purcar, C.-I. Spătaru, E. Alexandrescu, R. Şomoghi, B. Trică, S. G. Niţu, D. M. Panaitescu, D. Donescu and M.-L. Jecu, The Influence of New Hydrophobic Silica

Nanoparticles on the Surface Properties of the Films Obtained from Bilayer Hybrids. *Nanomaterials (Basel)*. 7 (2017) 47.

[41]   V. A. Ganesh, S. S. Dinachali, A. S. Nair and S. Ramakrishna, Robust Superamphiphobic Film from Electrospun TiO2 Nanostructures. *ACS Appl. Mater. Interfaces*. 5 (2013) 1527.

[42]   W. Choi, A. Tuteja, S. Chhatre, J. M. Mabry, R. E. Cohen and G. H. McKinley, Fabrics with Tunable Oleophobicity. *Advanced Materials*. 21 (2009) 2190.

[43]   S. S. Chhatre, A. Tuteja, W. Choi, A. Revaux, D. Smith, J. M. Mabry, G. H. McKinley and R. E. Cohen, Thermal Annealing Treatment to Achieve Switchable and Reversible Oleophobicity on Fabrics. *Langmuir*. 25 (2009) 13625.

[44]   H. Bellanger, T. Darmanin, E. Taffin de Givenchy and F. Guittard, Influence of intrinsic oleophobicity and surface structuration on the superoleophobic properties of PEDOP films bearing two fluorinated tails. *J. Mater. Chem. A*. 1 (2013) 2896.

[45]   S. Barthwal, Y. S. Kim and S.-H. Lim, Mechanically Robust Superamphiphobic Aluminum Surface with Nanopore-Embedded Microtexture. *Langmuir*. 29 (2013) 11966.

[46]   M. Scaraggi, F. P. Mezzapesa, G. Carbone, A. Ancona, D. Sorgente and P. M. Lugarà, Minimize friction of lubricated laser-microtextured-surfaces by tuning microholes depth. *Tribology International*. 75 (2014) 123.

[47]   A. Dunn, J. V. Carstensen, K. L. Wlodarczyk, E. B. Hansen, J. Gabzdyl, P. M. Harrison, J. D. Shephard and D. P. Hand, Nanosecond laser texturing for high friction applications. *Optics and Lasers in Engineering*. 62 (2014) 9.

[48]   P. W. Shum, Z. F. Zhou and K. Y. Li, To increase the hydrophobicity, non-stickiness and wear resistance of DLC surface by surface texturing using a laser ablation process. *Tribology International*. 78 (2014) 1.

[49]   M. Tang, V. Shim, Z. Y. Pan, Y. S. Choo and M. H. Hong, Laser Ablation of Metal Substrates for Super-hydrophobic Effect. *Journal of Laser Micro/Nanoengineering*. 6 (2011)

[50]   A. Y. Vorobyev and C. Guo, Multifunctional surfaces produced by femtosecond laser pulses. *J. Appl. Phys.* 117 (2015) 033103.

[51]   C. Y. Lin, C. W. Cheng and K. L. Ou, Micro/Nano-Structuring of Medical Stainless Steel using Femtosecond Laser Pulses. *Physics Procedia*. 39 (2012) 661.

[52]   S. Moradi, S. Kamal, P. Englezos and S. G. Hatzikiriakos, Femtosecond laser irradiation of metallic surfaces: effects of laser parameters on superhydrophobicity. *Nanotechnology*. 24 (2013) 415302.

[53]   M. C. Sharp, A. P. Rosowski and P. W. French. *Nanosecond laser texturing of aluminium for control of wettability*. 2015.

[54]   L. Qin, P. Lin, Y. Zhang, G. Dong and Q. Zeng, Influence of surface wettability on the tribological properties of laser textured Co–Cr–Mo alloy in aqueous bovine serum albumin solution. *Appl. Surf. Sci.* 268 (2013) 79.

[55]   D. Wang, X. Wang, X. Liu and F. Zhou, Engineering a Titanium Surface with Controllable Oleophobicity and Switchable Oil Adhesion. *J. Phys. Chem. C.* 114 (2010) 9938.

[56]   S. Barthwal, Y. S. Kim and S.-H. Lim, Fabrication of amphiphobic surface by using titanium anodization for large-area three-dimensional substrates. *Journal of Colloid and Interface Science.* 400 (2013) 123.

[57]   J. G. Buijnsters, R. Zhong, N. Tsyntsaru and J. P. Celis, Surface Wettability of Macroporous Anodized Aluminum Oxide. *ACS Appl. Mater. Interfaces.* 5 (2013) 3224.

[58]   C. W. Extrand and Y. Kumagai, An Experimental Study of Contact Angle Hysteresis. *Journal of Colloid and Interface Science.* 191 (1997) 378.

[59]   Y. C. Jung and B. Bhushan, Wetting Behavior of Water and Oil Droplets in Three-Phase Interfaces for Hydrophobicity/philicity and Oleophobicity/philicity. *Langmuir.* 25 (2009) 14165.

[60]   P. S. Brown, O. D. L. A. Atkinson and J. P. S. Badyal, Ultrafast Oleophobic–Hydrophilic Switching Surfaces for Antifogging, Self-Cleaning, and Oil–Water Separation. *ACS Appl. Mater. Interfaces.* 6 (2014) 7504.

[61]   S. J. Hutton, J. M. Crowther and J. P. S. Badyal, Complexation of Fluorosurfactants to Functionalized Solid Surfaces: Smart Behavior. *Chem Mater.* 12 (2000) 2282.

[62]   J. A. Howarter and J. P. Youngblood, Self-Cleaning and Next Generation Anti-Fog Surfaces and Coatings. *Macromolecular Rapid Communications.* 29 (2008) 455.

[63]   L. Li, Y. Wang, C. Gallaschun, T. Risch and J. Sun, Why can a nanometer-thick polymer coated surface be more wettable to water than to oil? *Journal of Materials Chemistry.* 22 (2012) 16719.

[64]   Q. Wen, J. Di, L. Jiang, J. Yu and R. Xu, Zeolite-coated mesh film for efficient oil-water separation. *Chemical Science.* 4 (2013) 591.

[65]   J. Yang, Z. Zhang, X. Xu, X. Zhu, X. Men and X. Zhou, Superhydrophilic-superoleophobic coatings. *Journal of Materials Chemistry.* 22 (2012) 2834.

[66]   D. Tian, X. Zhang, Y. Tian, Y. Wu, X. Wang, J. Zhai and L. Jiang, Photo-induced water-oil separation based on switchable superhydrophobicity-superhydrophilicity and underwater superoleophobicity of the aligned ZnO nanorod array-coated mesh films. *Journal of Materials Chemistry*. 22 (2012) 19652.

[67]   Z. Cheng, H. Lai, Y. Du, K. Fu, R. Hou, N. Zhang and K. Sun, Underwater Superoleophilic to Superoleophobic Wetting Control on the Nanostructured Copper Substrates. *ACS Appl. Mater. Interfaces*. 5 (2013) 11363.

[68]   Z. Xue, S. Wang, L. Lin, L. Chen, M. Liu, L. Feng and L. Jiang, A Novel Superhydrophilic and Underwater Superoleophobic Hydrogel-Coated Mesh for Oil/Water Separation. *Advanced Materials*. 23 (2011) 4270.

[69]   A. Tuteja, A. K. Kota, G. Kwon and J. M. Mabry, *Superhydrophilic and oleophobic porous materials and methods for making and using the same. 2012: U.S. Patent.*

[70]   X. Zhu, H.-E. Loo and R. Bai, A novel membrane showing both hydrophilic and oleophobic surface properties and its non-fouling performances for potential water treatment applications. *Journal of Membrane Science*. 436 (2013) 47.

[71]   X. Zhu, W. Tu, K.-H. Wee and R. Bai, Effective and low fouling oil/water separation by a novel hollow fiber membrane with both hydrophilic and oleophobic surface properties. *Journal of Membrane Science*. 466 (2014) 36.

[72]   S. Yang, Q. Xia, L. Zhu, J. Xue, Q. Wang and Q.-m. Chen, Research on the icephobic properties of fluoropolymer-based materials. *Appl. Surf. Sci.* 257 (2011) 4956.

[73]   I. A. Ansari, K. G. Watkins, M. C. Sharp, R. A. Hutchinson, R. M. Potts and J. Clowes, Modification of Anodised Aluminium Surfaces Using a Picosecond Fibre Laser for Printing Applications. *Journal of Nanoscience and Nanotechnology*. 12 (2012) 4946.

[74]   K. Hashimoto, H. Irie and A. Fujishima, TiO2 Photocatalysis: A Historical Overview and Future Prospects. *Japanese Journal of Applied Physics*. 44 (2005) 8269.

[75]   K. K. Lee and C. H. Ahn, Superhydrophilic Multilayer Silica Nanoparticle Networks on a Polymer Microchannel Using a Spray Layer-by-Layer Nanoassembly Method. *ACS Appl. Mater. Interfaces*. 5 (2013) 8523.

[76]   W. Zhang, Z. Xi, G. Li, Q. Wang, H. Tang, Y. Liu, Y. Zhao and L. Jiang, Highly Ordered Coaxial Bimodal Nanotube Arrays Prepared by Self-Organizing Anodization on Ti Alloy. *Small*. 5 (2009) 1742.

[77]   A. O. Araoyinbo, A. Rahmat, M. N. Derman and K. R. Ahmad, Room temperature anodization of aluminum and the effect of the electrochemical cell in the formation of porous alumina films from acid and alkaline electrolytes. *Adv. Mat. Lett.* 3 (2012) 273.

[78]   W. Lee and S.-J. Park, Porous Anodic Aluminum Oxide: Anodization and Templated Synthesis of Functional Nanostructures. *Chem. Rev.* 114 (2014) 7487.

[79]   Nanoporous alumina: Fabrication, Structure, Properties and Applications. Springer Series in Materials Science. Vol. 219. D. Losic and A. Santos, eds.: Springer. 361, 2015.

[80]   C. T. Sousa, D. C. Leitao, M. P. Proenca, J. Ventura, A. M. Pereira and J. P. Araujo, Nanoporous alumina as templates for multifunctional applications. *Appl. Phys. Rev.* 1 (2014) 031102.

[81]   D. M. Dotzauer, J. Dai, L. Sun and M. L. Bruening, Catalytic Membranes Prepared Using Layer-by-Layer Adsorption of Polyelectrolyte/Metal Nanoparticle Films in Porous Supports. *Nano Letters.* 6 (2006) 2268.

[82]   O. Sanz, F. J. Echave, J. A. Odriozola and M. Montes, Aluminum Anodization in Oxalic Acid: Controlling the Texture of Al2O3/Al Monoliths for Catalytic Aplications. *Industrial & Engineering Chemistry Research.* 50 (2011) 2117.

[83]   S. Simovic, D. Losic and K. Vasilev, Controlled drug release from porous materials by plasma polymer deposition. *Chem Commun.* 46 (2010) 1317.

[84]   M. Wang, G. Meng, Q. Huang, Q. Xu, Z. Chu and C. Zhu, FITC-modified PPy nanotubes embedded in nanoporous AAO membrane can detect trace PCB20 via fluorescence ratiometric measurement. *Chemical communications (Cambridge, England).* 47 (2011) 3808.

[85]   A. P. Samantilleke, J. O. Carneiro, S. Azevedo, T. Thuy and V. Teixeira, Electrochemical Anodizing, Structural and Mechanical Characterization of Nanoporous Alumina Templates. *J Nano Res-Sw.* 25 (2013) 77.

[86]   A. Mutalib Md Jani, E. J. Anglin, S. J. P. McInnes, D. Losic, J. G. Shapter and N. H. Voelcker, Nanoporous anodic aluminium oxide membranes with layered surface chemistry. *Chem Commun.* (2009) 3062.

[87]   L. Bouchama, N. Azzouz, N. Boukmouche, J. P. Chopart, A. L. Daltin and Y. Bouznit, Enhancing aluminum corrosion resistance by two-step anodizing process. *Surf. Coat. Tech.* 235 (2013) 676.

[88]   C. J. Donahue and J. A. Exline, Anodizing and Coloring Aluminum Alloys. *Journal of Chemical Education*. 91 (2014) 711.

[89]   M. Guezmil, W. Bensalah, A. Khalladi, K. Elleuch, M. D.-P. Wery and H. F. Ayedi. Effect of Test Parameters on the Friction Behaviour of Anodized Aluminium Alloy. *Int Sch Res Notices.* 2014, pp. 9. dx.doi.org/10.1155/2014/795745.

[90]   M. Saeedikhani, M. Javidi and A. Yazdani, Anodizing of 2024-T3 aluminum alloy in sulfuric-boric-phosphoric acids and its corrosion behavior. *T Nonferr Metal Soc.* 23 (2013) 2551.

[91]   L. Zaraska, E. Kurowska, G. Sulka, I. Senyk and M. Jaskula, The effect of anode surface area on nanoporous oxide formation during anodizing of low purity aluminum (AA1050 alloy). *J Solid State Electrochem*. 18 (2014) 361.

[92]   I. Tsangaraki-Kaplanoglou, S. Theohari, T. Dimogerontakis, Y.-M. Wang, H.-H. Kuo and S. Kia, Effect of alloy types on the anodizing process of aluminum. *Surf. Coat. Tech.* 200 (2006) 2634.

[93]   G. Mrówka-Nowotnik, J. Sieniawski and M. Wierzbińska, Analysis of intermetallic particles in AlSi1MgMn aluminium alloy. *Journal of Achievements in Materials and Manufacturing Engineering*. 20 (2007)

[94]   C. Y. Jeong and C. H. Choi, Single-Step Direct Fabrication of Pillar-on-Pore Hybrid Nanostructures in Anodizing Aluminum for Superior Superhydrophobic Efficiency. *ACS Appl. Mater. Interfaces*. 4 (2012) 842.

[95]   C. Ran, G. Ding, W. Liu, Y. Deng and W. Hou, Wetting on Nanoporous Alumina Surface: Transition between Wenzel and Cassie States Controlled by Surface Structure. *Langmuir*. 24 (2008) 9952.

[96]   G. D. Sulka and W. J. Stępniowski, Structural features of self-organized nanopore arrays formed by anodization of aluminum in oxalic acid at relatively high temperatures. *Electrochim. Acta*. 54 (2009) 3683.

[97]   S. Altuntas and F. Buyukserin, Fabrication and characterization of conductive anodic aluminum oxide substrates. *Appl. Surf. Sci.* 318 (2014) 290.

[98]   H. Masuda, F. Hasegwa and S. Ono, Self-Ordering of Cell Arrangement of Anodic Porous Alumina Formed in Sulfuric Acid Solution. *J. Electrochem. Soc.* 144 (1997) L127.

[99]   A. P. Li, F. Muller, A. Birner, K. Nielsch and U. Gosele, Hexagonal pore arrays with a 50-420 nm interpore distance formed by self-organization in anodic alumina. *J. Appl. Phys.* 84 (1998) 6023.

[100] C. H. Voon, M. N. Derman, U. Hashim, K. R. Ahmad and K. L. Foo, Effect of Temperature of Oxalic Acid on the Fabrication of Porous Anodic Alumina from Al-Mn Alloys. *J Nanomater*. (2013)

[101] R. C. Furneaux, W. R. Rigby and A. P. Davidson, The formation of controlled-porosity membranes from anodically oxidized aluminium. *Nature*. 337 (1989) 147.

[102] A. Mozalev, A. Surganov and S. Magaino, Anodic process for forming nanostructured metal-oxide coatings for large-value precise microfilm resistor fabrication. *Electrochim. Acta*. 44 (1999) 3891.

[103] H. Y. Masuda, Haruki; Satoh, Masahiro; Asoh, Hidetaka; Nakao, Masashi; Tamamura, Toshiaki, Highly ordered nanochannel-array architecture in anodic alumina. *Applied Physics Letters*. 71 (1997) 2770.

[104] H. Masuda, K. Yada and A. Osaka, Self-ordering of cell configuration of anodic porous alumina with large-size pores in phosphoric acid solution. *Jpn J Appl Phys 2*. 37 (1998) L1340.

[105] G. Thompson and G. Wood, Anodic films on aluminum. *Treatise on Materials Science and Technology, Vol. 23. Corrosion: Aqueous Processed and Passive Films*. (1983) 205.

[106] S. Mandar, A. Majid Kazemian, S. Akanksha, T. Anju, C. Ram, S. Vasant, P. Deodatta and K. Sulabha, Rapidly switched wettability of titania films deposited by dc magnetron sputtering. *Journal of Physics D: Applied Physics*. 41 (2008) 155308.

[107] D. Lexén, Wettability Gradients Through Chemical Vapor Deposition. Chalmers University of Technology Göteborg, Sweden. p. 36. 2010.

[108] P. Navabpour, D. G. Teer, D. J. Hitt and M. Gilbert, Evaluation of non-stick properties of magnetron-sputtered coatings for moulds used for the processing of polymers. *Surf. Coat. Tech*. 201 (2006) 3802.

[109] Q. Zhao and X. Wang, Heat transfer surfaces coated with fluorinated diamond-like carbon films to minimize scale formation. *Surf. Coat. Tech*. 192 (2005) 77.

[110] M. Ishihara, T. Kosaka, T. Nakamura, K. Tsugawa, M. Hasegawa, F. Kokai and Y. Koga, Antibacterial activity of fluorine incorporated DLC films. *Diam Relat Mater*. 15 (2006) 1011.

[111] M. H. Ahmed and J. A. Byrne, Effect of surface structure and wettability of DLC and N-DLC thin films on adsorption of glycine. *Appl. Surf. Sci*. 258 (2012) 5166.

[112]   S. C. Kwok, J. Wang and P. K. Chu, Surface energy, wettability, and blood compatibility phosphorus doped diamond-like carbon films. *Diam Relat Mater*. 14 (2005) 78.

[113]   L. B. Austin, Evaluation and optimisation of diamond-like carbon for tribological applications. University of Leeds. 2014.

[114]   C. Zhang and M. Fujii, Influence of Wettability and Mechanical Properties on Tribological Performance of DLC Coatings under Water Lubrication. *Journal of Surface Engineered Materials and Advanced Technology*. 5 (2015) 110.

[115]   S. C. Trippe, R. D. Mansano, F. M. Costa and R. F. Silva, Mechanical properties evaluation of fluor-doped diamond-like carbon coatings by nanoindentation. *Thin Solid Films*. 446 (2004) 85.

[116]   R. Mientus and K. Ellmer, Structural, electrical and optical properties of SnO2-x:F-layers deposited by DC-reactive magnetron-sputtering from a metallic target in Ar–O2/CF4 mixtures. *Surf. Coat. Tech.* 98 (1998) 1267.

[117]   H. S. Yoon, K. S. Lee, T. S. Lee, B. Cheong, D. K. Choi, D. H. Kim and W. M. Kim, Properties of fluorine doped ZnO thin films deposited by magnetron sputtering. *Solar Energy Materials and Solar Cells*. 92 (2008) 1366.

[118]   S. Schmidt, G. Greczynski, C. Goyenola, G. K. Gueorguiev, Z. Czigány, J. Jensen, I. G. Ivanov and L. Hultman, CFx thin solid films deposited by high power impulse magnetron sputtering: Synthesis and characterization. *Surf. Coat. Tech.* 206 (2011) 646.

[119]   A. Bendavid, P. J. Martin, L. Randeniya, M. S. Amin and R. Rohanizadeh, The properties of fluorine-containing diamond-like carbon films prepared by pulsed DC plasma-activated chemical vapour deposition. *Diam Relat Mater*. 19 (2010) 1466.

[120]   S. Schmidt, Carbon Nitride and Carbon Fluoride Thin Films Prepared by HiPIMS. Linköpings universitet. p. 82. 2013.

[121]   F. Wang, L. Wang and Q. Xue, Fluorine and sulfur co-doped amorphous carbon films to achieve ultra-low friction under high vacuum. *Carbon*. 96 (2016) 411.

[122]   L. Martinů, H. Biederman and L. Holland, Thin films prepared by sputtering MgF2 in an rf planar magnetron. *Vacuum*. 35 (1985) 531.

[123]   A. Podestà, N. Armani, G. Salviati, N. Romeo, A. Bosio and M. Prato, Influence of the fluorine doping on the optical properties of CdS thin films for photovoltaic applications. *Thin Solid Films*. 511–512 (2006) 448.

[124]   Z. Y. Banyamin, P. J. Kelly, G. West and J. Boardman, Electrical and Optical Properties of Fluorine Doped Tin Oxide Thin Films Prepared by Magnetron Sputtering. *Coatings*. 4 (2014) 732.

[125]   T. Hasebe, S. Yohena, A. Kamijo, Y. Okazaki, A. Hotta, K. Takahashi and T. Suzuki, Fluorine doping into diamond-like carbon coatings inhibits protein adsorption and platelet activation. *Journal of biomedical materials research. Part A*. 83 (2007) 1192.

[126]   V. Satulu, M. Ionita, S. Vizireanu, B. Mitu and G. Dinescu, Plasma Processing with Fluorine Chemistry for Modification of Surfaces Wettability. *Molecules*. 21 (2016) 1711.

[127]   V. Sorkin, H. Pan, H. Shi, S. Y. Quek and Y. W. Zhang, Nanoscale Transition Metal Dichalcogenides: Structures, Properties, and Applications. *Critical Reviews in Solid State and Materials Sciences*. 39 (2014) 319.

[128]   W. Choi, N. Choudhary, G. H. Han, J. Park, D. Akinwande and Y. H. Lee, Recent development of two-dimensional transition metal dichalcogenides and their applications. *Mater. Today*. 20 (2017) 116.

[129]   M. Samadi, N. Sarikhani, M. Zirak, H. Zhang, H.-L. Zhang and A. Z. Moshfegh, Group 6 transition metal dichalcogenide nanomaterials: synthesis, applications and future perspectives. *Nanoscale Horizons*. 3 (2018) 90.

[130]   A. P. S. Gaur, S. Sahoo, M. Ahmadi, S. P. Dash, M. J. F. Guinel and R. S. Katiyar, Surface Energy Engineering for Tunable Wettability through Controlled Synthesis of MoS2. *Nano Letters*. 14 (2014) 4314.

[131]   A. Kozbial, X. Gong, H. Liu and L. Li, Understanding the Intrinsic Water Wettability of Molybdenum Disulfide (MoS2). *Langmuir*. 31 (2015) 8429.

[132]   S. Zhang, X. Zeng, Z. Tang and M. J. Tan, Exploring the antisticking properties of solid lubricant thin films in transfer molding. *International Journal of Modern Physics B*. 16 (2002) 1080.

[133]   P. K. Chow, E. Singh, B. C. Viana, J. Gao, J. Luo, J. Li, Z. Lin, A. L. Elías, Y. Shi, Z. Wang, M. Terrones and N. Koratkar, Wetting of Mono and Few-Layered WS2 and MoS2 Films Supported on Si/SiO2 Substrates. *Acs Nano*. 9 (2015) 3023.

[134]   P. A. Bertrand, Orientation of rf-sputter-deposited MoS2 films. *Journal of Materials Research*. 4 (1989) 180.

[135]   In-situ HRTEMstudyofthereactivecarbidephaseofCo/MoS2 catalyst. Vol. 127. 64, 2012.

[136]   J. Moser and F. Lévy, Random stacking in MoS2−x sputtered thin films. *Thin Solid Films*. 240 (1994) 56.

[137]   Z. Lin, B. R. Carvalho, E. Kahn, R. Lv, R. Rao, H. Terrones, M. A. Pimenta and M. Terrones, Defect engineering of two-dimensional transition metal dichalcogenides. *2D Materials*. 3 (2016) 022002.

[138]   L. Yang, K. Majumdar, H. Liu, Y. Du, H. Wu, M. Hatzistergos, P. Y. Hung, R. Tieckelmann, W. Tsai, C. Hobbs and P. D. Ye, Chloride Molecular Doping Technique on 2D Materials: WS2 and MoS2. *Nano Letters*. 14 (2014) 6275.

[139]   D. Sarkar, X. Xie, J. Kang, H. Zhang, W. Liu, J. Navarrete, M. Moskovits and K. Banerjee, Functionalization of Transition Metal Dichalcogenides with Metallic Nanoparticles: Implications for Doping and Gas-Sensing. *Nano Letters*. 15 (2015) 2852.

[140]   J. Lee, P. Dak, Y. Lee, H. Park, W. Choi, M. A. Alam and S. Kim, Two-dimensional layered MoS2 biosensors enable highly sensitive detection of biomolecules. *Scientific reports*. 4 (2014)

[141]   S. Jiang, R. Cheng, R. Ng, Y. Huang and X. Duan, Highly sensitive detection of mercury(II) ions with few-layer molybdenum disulfide. *Nano Research*. 8 (2015) 257.

[142]   W.-B. Jung, G.-T. Yun, Y. Kim, M. Kim and H.-T. Jung, Relationship between Hydrogen Evolution and Wettability for Multiscale Hierarchical Wrinkles. *ACS Appl. Mater. Interfaces*. 11 (2019) 7546.

[143]   J. Moser, F. Lévy and F. Bussy, Composition and growth mode of MoSx sputtered films. *Journal of Vacuum Science & Technology A*. 12 (1994) 494.

[144]   T. Polcar, M. Evaristo, M. Stueber and A. Cavaleiro, Synthesis and structural properties of Mo–Se–C sputtered coatings. *Surf. Coat. Tech.* 202 (2008) 2418.

[145]   S. V. Prasad, N. T. McDevitt and J. S. Zabinski, Tribology of tungsten disulfide films in humid environments:: The role of a tailored metal-matrix composite substrate. *Wear*. 230 (1999) 24.

[146]   Y. L. Su and W. H. Kao, Tribological behaviour and wear mechanism of MoS2–Cr coatings sliding against various counterbody. *Tribology International*. 36 (2003) 11.

[147]   V. Fox, J. Hampshire and D. Teer, MoS2/metal composite coatings deposited by closed-field unbalanced magnetron sputtering: tribological properties and industrial uses. *Surf. Coat. Tech.* 112 (1999) 118.

[148]   T. Polcar and A. Cavaleiro, Review on self-lubricant transition metal dichalcogenide nanocomposite coatings alloyed with carbon. *Surf. Coat. Tech.* 206 (2011) 686.

[149]   A. Nossa and A. Cavaleiro, Mechanical behaviour of W–S–N and W–S–C sputtered coatings deposited with a Ti interlayer. *Surf. Coat. Tech.* 163–164 (2003) 552.

[150]   A. Nossa and A. Cavaleiro, Chemical and physical characterization of C(N)-doped W–S sputtered films. *Journal of Materials Research.* 19 (2004) 2356.

[151]   T. Polcar, M. Evaristo and A. Cavaleiro, Friction of Self-Lubricating W-S-C Sputtered Coatings Sliding Under Increasing Load. *Plasma Processes and Polymers.* 4 (2007) S541.

[152]   T. Polcar, M. Evaristo and A. Cavaleiro, The tribological behavior of W–S–C films in pin-on-disk testing at elevated temperature. *Vacuum.* 81 (2007) 1439.

[153]   T. Polcar, M. Evaristo and A. Cavaleiro, Self-Lubricating W–S–C Nanocomposite Coatings. *Plasma Processes and Polymers.* 6 (2009) 417.

[154]   J. V. Pimentel, T. Polcar, M. Evaristo and A. Cavaleiro, Examination of the tribolayer formation of a self-lubricant W–S–C sputtered coating. *Tribology International.* 47 (2012) 188.

[155]   J. V. Pimentel, T. Polcar and A. Cavaleiro, Structural, mechanical and tribological properties of Mo–S–C solid lubricant coating. *Surf. Coat. Tech.* 205 (2011) 3274.

[156]   T. Polcar, M. Evaristo, R. Colaço, C. Silviu Sandu and A. Cavaleiro, Nanoscale triboactivity: The response of Mo–Se–C coatings to sliding. *Acta Materialia.* 56 (2008) 5101.

[157]   T. Polcar, M. Evaristo and A. Cavaleiro, Comparative study of the tribological behavior of self-lubricating W–S–C and Mo–Se–C sputtered coatings. *Wear.* 266 (2009) 388.

[158]   F. Gustavsson, S. Jacobson, A. Cavaleiro and T. Polcar, Ultra-low friction W–S–N solid lubricant coating. *Surf. Coat. Tech.* 232 (2013) 541.

[159]   J. S. Zabinski, J. E. Florkey, S. D. Walck, J. E. Bultman and N. T. McDevitt, Friction properties of WS2/graphite fluoride thin films grown by pulsed laser deposition. *Surf. Coat. Tech.* 76 (1995) 400.

[160]   L. Li, Z. Wang, Y. Wang, X. Wang, G. Yang and S. Jiang, Stable all-fiber Er-doped Q-switched laser with a WS2/fluorine mica (FM) saturable absorber. *Laser Physics.* 26 (2016) 105101.

[161]   Y. Wang, S. Liu, X. Hao, J. Zhou, D. Song, D. Wang, L. Hou and F. Gao, Fluorine- and Nitrogen-Codoped MoS2 with a Catalytically Active Basal Plane. *ACS Appl. Mater. Interfaces.* 9 (2017) 27715.

[162]   T.-C. Cheng and C.-C. Chou, The Electrical and Mechanical Properties of Porous Anodic 6061-T6 Aluminum Alloy Oxide Film. *J Nanomater*. 2015 (2015) 5.

[163]   G. D. Sulka and K. G. Parkoła, Temperature influence on well-ordered nanopore structures grown by anodization of aluminium in sulphuric acid. *Electrochim. Acta*. 52 (2007) 1880.

[164]   J. P. O'Sullivan and G. C. Wood, The Morphology and Mechanism of Formation of Porous Anodic Films on Aluminium. *Proc. R. Soc. A*. 317 (1970) 511.

[165]   M. Michalska-Domańska, M. Norek, W. J. Stępniowski and B. Budner, Fabrication of high quality anodic aluminum oxide (AAO) on low purity aluminum—A comparative study with the AAO produced on high purity aluminum. *Electrochim. Acta*. 105 (2013) 424.

[166]   P. Mukhopadhyay. Alloy Designation, Processing, and Use of AA6XXX Series Aluminium Alloys. *ISRN Metallurgy*. 2012, pp. 15. 10.5402/2012/165082.

[167]   D. Lundin, The HiPIMS process. University of Linköping. 2010.

[168]   G. D. Sulka. *Highly Ordered Anodic Porous Alumina Formation by Self-Organized Anodizing*; In *Nanostructured Materials in Electrochemistry*; A. Eftekhari, Ed.; Wiley-VCH Verlag GmbH & Co. KGaA, 2008, Chapter 1, pp. 1.

[169]   C. Cushman, S. Chatterjee, G. H. Major, N. Smith, A. Roberts and M. Linford, Trends in Advanced XPS Instrumentation. 1. Overview of the Technique, Automation, High Sensitivity, Imaging, Snapshot Spectroscopy, Gas Cluster Ion Beams, and Multiple Analytical Techniques on the Instrument. *Vacuum Technology & Coating*. (2016)

[170]   Y. Koçak, Y. Akaltun and E. Gür, Magnetron sputtered WS2; optical and structural analysis. *Journal of Physics: Conference Series*. 707 (2016) 012028.

[171]   J. Sundberg, R. Lindblad, M. Gorgoi, H. Rensmo, U. Jansson and A. Lindblad, Understanding the effects of sputter damage in W–S thin films by HAXPES. *Appl. Surf. Sci.* 305 (2014) 203.

[172]   Handbook of X-ray Photoelectron Spectrosocpy. Perkin-Elmer Corp, 1992.

[173]   Available from: https://wiki.anton-paar.com/en/x-ray-diffraction-xrd/.

[174]   A. Berkdemir, H. R. Gutiérrez, A. R. Botello-Méndez, N. Perea-López, A. L. Elías, C.-I. Chia, B. Wang, V. H. Crespi, F. López-Urías, J.-C. Charlier, H. Terrones and M. Terrones, Identification of individual and few layers of WS2 using Raman Spectroscopy. *Scientific Reports*. 3 (2013) 1755.

[175]   E. Serpini, Friction mechanisms of MoS2 surfaces with different crystallographic order. Universitá degli studi di Modena e Reggio Emilia. p. 143. 2017.

[176]   B. C. Windom, W. G. Sawyer and D. W. Hahn, A Raman Spectroscopic Study of MoS2 and MoO3: Applications to Tribological Systems. *Tribology Letters*. 42 (2011) 301.

[177]   Atomic force microscopy method development for surface energy analysis. University of Kentucky. p. 366. 2011.

[178]   Y. Wei, Z. Dong and C. Wu, Methods for simultaneously obtaining surface elasticity image and ccurate height image using contact mode AFM. *IEEE Transactions on Nanotechnology*. (2011)

[179]   I. Carvalho, M. Henriques and S. Carvalho, New strategies to fight bacterial adhesion. Microbial pathogens and strategies for combating them: science, technology and education. *FORMATEX*. (2013) 170.

[180]   C. J. V. OSS and R. F. Giese, The hydrophilicity and hydrophobicity of clay minerals. *Clays Clay Miner*. 43 (1995) 474.

[181]   C. J. V. Oss, M. K. Chaudhury and R. J. Good, Interfacial Lifshitz-van der Waals and polar interactions in macroscopic systems. *Chem. Rev.* 88 (1988) 927.

[182]   M. Kalin and M. Polajnar, The correlation between the surface energy, the contact angle and the spreading parameter, and their relevance for the wetting behaviour of DLC with lubricating oils. *Tribology International*. 66 (2013) 225.

[183]   M. Kalin and M. Polajnar, The wetting of steel, DLC coatings, ceramics and polymers with oils and water: The importance and correlations of surface energy, surface tension, contact angle and spreading. *Appl. Surf. Sci.* 293 (2014) 97.

[184]   M. Yordanov, Investigation of the Correlation Between Internal Stresses and Adhesion of Magnetron Deposited crn Coatings for Different Bias Voltage. *Indian Journal of Applied Research*. 4 (2014) 556.

[185]   F. Gustavsson, Trioactive component coatings: Tribological Testing and Microanalysis of Low-Friction Tribofilms. Uppsala University. p. 100.

[186]   J. E. Shigley. *Mechanical Engineering Design*; Ed.; McGraw Hill, 1986, Chapter 2, pp. 78.

[187]   *"Standard test method for linearly reciprocating ball-on-flat sliding wear", Norma ASTM*. in *G 133-02*. 2002.

[188]   J. V. B. Pimentel, Adaptive self-lubricating low-friction coatings. Technical University in Prague. 2013.

[189]   *"Standard test method for wear testing with a pin-on-disk apparatus", Norma ASTM*. in *G 99-95*. 1995.

[190]   M. P. M. Kalin, The effect of wetting and surface energy on the friction and slip in oil-lubricated contacts. *Tribol Lett.* 52 (2013) 185.

[191]   E. A. Starke and J. T. Staley, Application of modern aluminum alloys to aircraft. *Prog. Aerosp. Sci.* 32 (1996) 131.

[192]   T. Darmanin and F. Guittard, Recent advances in the potential applications of bioinspired superhydrophobic materials. *J. Mater. Chem. A.* 2 (2014) 16319.

[193]   A. V. Rao, S. S. Latthe, S. A. Mahadik and C. Kappenstein, Mechanically stable and corrosion resistant superhydrophobic sol–gel coatings on copper substrate. *Appl. Surf. Sci.* 257 (2011) 5772.

[194]   A. Tuteja, W. Choi, M. Ma, J. M. Mabry, S. A. Mazzella, G. C. Rutledge, G. H. McKinley and R. E. Cohen. Designing superoleophobic surfaces. *Science.* 2007, 318, 1618.

[195]   D. Quéré, Wetting and Roughness. *Annu. Rev. Mater. Res.* 38 (2008) 71.

[196]   S. Nishimoto and B. Bhushan, Bioinspired self-cleaning surfaces with superhydrophobicity, superoleophobicity, and superhydrophilicity. *RSC Adv.* 3 (2013) 671.

[197]   M. H. Kwon, H. S. Shin and C. N. Chu, Fabrication of a super-hydrophobic surface on metal using laser ablation and electrodeposition. *Appl. Surf. Sci.* 288 (2014) 222.

[198]   D. V. Ta, A. Dunn, T. J. Wasley, R. W. Kay, J. Stringer, P. J. Smith, C. Connaughton and J. D. Shephard, Nanosecond laser textured superhydrophobic metallic surfaces and their chemical sensing applications. *Appl. Surf. Sci.* 357, Part A (2015) 248.

[199]   K. Y. Ng and A. H. Ngan, Effects of pore-channel ordering on the mechanical properties of anodic aluminum oxide nano-honeycombs. *Scr. Mater.* 66 (2012) 439.

[200]   Y. Lin, Q. Lin, X. Liu, Y. Gao, J. He, W. Wang and Z. Fan, A Highly Controllable Electrochemical Anodization Process to Fabricate Porous Anodic Aluminum Oxide Membranes. *Nanoscale Res. Lett.* 10 (2015) 495.

[201]   J. W. Diggle, T. C. Downie and C. Goulding, Anodic oxide films on aluminum. *Chem Rev.* 69 (1969) 365.

[202]   F. Keller, M. S. Hunter and D. L. Robinson, Structural Features of Oxide Coatings on Aluminum. *J. Electrochem. Soc.* 100 (1953) 411.

[203]   G. E. Thompson, Porous anodic alumina: fabrication, characterization and applications. *Thin Solid Films.* 297 (1997) 192.

[204]   P. Erdogan, B. Yuksel and Y. Birol, Effect of chemical etching on the morphology of anodic aluminum oxides in the two-step anodization process. *Appl. Surf. Sci.* 258 (2012) 4544.

[205]   J. M. Montero-Moreno, M. Sarret and C. Müller, Influence of the aluminum surface on the final results of a two-step anodizing. *Surf. Coat. Tech.* 201 (2007) 6352.

[206]   A. P. Li, F. Muller, A. Birner, K. Nielsch and U. Gosele, Hexagonal pore arrays with a 50–420 nm interpore distance formed by self-organization in anodic alumina. *J. Appl. Phys.* 84 (1998) 6023.

[207]   K. Nakayama, E. Tsuji, Y. Aoki and H. Habazaki, Fabrication of superoleophobic hierarchical surfaces for low-surface-tension liquids. *RSC Adv.* 4 (2014) 30927.

[208]   K. Nakayama, E. Tsuji, Y. Aoki, S.-G. Park and H. Habazaki, Control of Surface Wettability of Aluminum Mesh with Hierarchical Surface Morphology by Monolayer Coating: From Superoleophobic to Superhydrophilic. *J. Phys. Chem. C.* 120 (2016) 15684.

[209]   T. Fujii, H. Sato, E. Tsuji, Y. Aoki and H. Habazaki, Important Role of Nanopore Morphology in Superoleophobic Hierarchical Surfaces. *J. Phys. Chem. C.* 116 (2012) 23308.

[210]   S. Ji, P. A. Ramadhianti, T. B. Nguyen, W. D. Kim and H. Lim, Simple fabrication approach for superhydrophobic and superoleophobic Al surface. *Microelectron. Eng.* 111 (2013) 404.

[211]   K. S. Choudhari, P. Sudheendra and N. K. Udayashankar, Fabrication and high-temperature structural characterization study of porous anodic alumina membranes. *J. Porous Mater.* 19 (2012) 1053.

[212]   M. Michalska-Domanska, M. Norek, W. J. Stepniowski and B. Budner, Fabrication of high quality anodic aluminum oxide (AAO) on low purity aluminum-A comparative study with the AAO produced on high purity aluminum. *Electrochim. Acta.* 105 (2013) 424.

[213]   Z. Ling and Y. Li. *Mechanisms of Nanoporous Alumina Formation and Self-organized Growth*; In *Nanoporous Alumina: Fabrication, Structure, Properties and Applications*; D. Losic and A. Santos, Ed.; Springer Series in Materials Science, 2015, 219, Chapter 1, pp. 20.

[214]   K. Byeol and L. J. Seok, Effect of Aluminum Purity on the Pore Formation of Porous Anodic Alumina. *Bull. Korean Chem. Soc.* 35 (2014) 349.

[215]   L. E. Fratila-Apachitei, F. D. Tichelaar, G. E. Thompson, H. Terryn, P. Skeldon, J. Duszczyk and L. Katgerman, A transmission electron microscopy study of hard anodic oxide layers on AlSi(Cu) alloys. *Electrochim. Acta.* 49 (2004) 3169.

[216]   L. Zaraska, E. Wierzbicka, E. Kurowska-Tabor and G. D. Sulka. *Synthesis of Nanoporous Anodic Alumina by Anodic Oxidation of low Purity Aluminum substrates*; In *Nanporous Alumina: Fabrication, Structure, properties and Applications*; D. Losic and A. Santos, Ed.; Springer Series in Materials Science, 219, 2015, 219, Chapter 3, pp. 61.

[217] T. Masuda, H. Asoh, S. Haraguchi and S. Ono, Fabrication and Characterization of Single Phase α-Alumina Membranes with Tunable Pore Diameters. *Materials*. 8 (2015) 1350.

[218] S. P. Albu, D. Kim and P. Schmuki, Growth of aligned TiO2 bamboo-type nanotubes and highly ordered nanolace. *Angew. Chem. Int. Ed.: Electroch. Nanotech.* 47 (2008) 1916

[219] Y. Rahmawan, M.-W. Moon, K.-S. Kim, K.-R. Lee and K.-Y. Suh, Wrinkled, Dual-Scale Structures of Diamond-Like Carbon (DLC) for Superhydrophobicity. *Langmuir*. 26 (2010) 484.

[220] A. W. Adamson and A. P. Gast. *Physical Chemistry of Surfaces 6th Ed.*; Ed.; John Wiley & Sons: New York, 1997, Chapter II, Section 4., pp.

[221] C. V. Oss, R. Good and M. Chaudhury, The role of van der Waals forces and hydrogen bonds in "hydrophobic interactions" between biopolymers and low energy surfaces. *Journal of Colloid and Interface Science*. 111 (1986) 378.

[222] C. J. v. Oss, R. J. Good and M. K. Chaudhury, Additive and nonadditive surface tension components and the interpretation of contact angles. *Langmuir*. 4 (1988) 884.

[223] C. J. v. Oss, Acid-base interfacial interactions in aqueous media. *Colloids Surfaces A.* 78 (1993) 1.

[224] E. Chibowski, K. Terpilowski and L. Holysz. *Effect of relative humidity on contact angle and its hysteresis on phospholipid DPPC bilayer deposited on glass*; In *Advances in Contact angle, Wettability and Adhesion*; K. L. Mittal, Ed.; Scrivener, 2013, 19, pp. 334.

[225] L. M. Clements and K. M. Kockelman, Economic Effects of Automated Vehicles. *96th Annual Meeting of the Transportation Research Board*. (2017) 19.

[226] Atiel, *REACH and its impact on base oils and lubricants markets*. in 97. 2010, LUBE Magazine: The European Lubricants Industry Magazine: *ICIS World Base Oils & Lubricants Conference*. p. 21.

[227] E. Commision, *Directive 2010/75/EU of the European Parliament and of the Council of 24 November 2010 on industrial emissions (integrated pollution prevention and control)* 2010. p. 17.

[228] E. Commission, Revision of European Ecolabel Criteria for Lubricants. *JRC Rechnical Reports*. (2016) 213.

[229]   X. Zhang, H. Xu, J. Wang, X. Ye, W. Lei, M. Xue, H. Tang and C. Li, Synthesis of Ultrathin WS2 Nanosheets and Their Tribological Properties as Lubricant Additives. *Nanoscale Res. Lett.* 11 (2016) 442.

[230]   *Chapter 9. Lubrication by molybdenum disulphide alone*; In *Tribology Series*; A. R. Lansdown, Ed.; Elsevier, 1999129.

[231]   J. M. Martin, C. Donnet, T. Le Mogne and T. Epicier, Superlubricity of molybdenum disulphide. *Physical review. B, Condensed matter.* 48 (1993) 10583.

[232]   A. A. Voevodin and J. S. Zabinski, Supertough wear-resistant coatings with 'chameleon' surface adaptation. *Thin Solid Films.* 370 (2000) 223.

[233]   A. A. Voevodin and J. S. Zabinski, Nanocomposite and nanostructured tribological materials for space applications. *Composites Science and Technology.* 65 (2005) 741.

[234]   S. P. Rodrigues, C. F. A. Alves, A. Cavaleiro and S. Carvalho, Water and oil wettability of anodized 6016 aluminum alloy surface. *Appl. Surf. Sci.* 422 (2017) 430.

[235]   J.-D. Brassard, D. K. Sarkar and J. Perron, Fluorine Based Superhydrophobic Coatings. *Applied Sciences.* 2 (2012) 453.

[236]   K. Liu and L. Jiang, Metallic surfaces with special wettability. *Nanoscale.* 3 (2011) 825.

[237]   M. J. O'Keefe and J. M. Rigsbee, Reactive sputter deposition of crystalline Cr/C/F thin films. *Materials Letters.* 18 (1994) 251.

[238]   J. Fontaine, J. L. Loubet, T. L. Mogne and A. Grill, Superlow Friction of Diamond-Like Carbon Films: A Relation to Viscoplastic Properties. *Tribology Letters.* 17 (2004) 709.

[239]   G. Tang, X. Ma, M. Sun and X. Li, Mechanical characterization of ultra-thin fluorocarbon films deposited by R.F. magnetron sputtering. *Carbon.* 43 (2005) 345.

[240]   S. Schmidt, C. Goyenola, G. K. Gueorguiev, J. Jensen, G. Greczynski, I. G. Ivanov, Z. Czigány and L. Hultman, Reactive high power impulse magnetron sputtering of CFx thin films in mixed Ar/CF4 and Ar/C4F8 discharges. *Thin Solid Films.* 542 (2013) 21.

[241]   T. Kimura, R. Nishimura, K. Azuma, S. Nakao, T. Sonoda, T. Kusumori and K. Ozaki, Surface treatment of diamond-like carbon films by reactive Ar/CF4 high-power pulsed magnetron sputtering plasmas. *Nuclear Instruments and Methods in Physics Research Section B: Beam Interactions with Materials and Atoms.* 365, Part A (2015) 155.

[242]   P. Niederhäuser, H. E. Hintermann and M. Maillat, Moisture-resistant MoS2-based composite lubricant films. *Thin Solid Films.* 108 (1983) 209.

[243]   P. J. John, S. V. Prasad, A. A. Voevodin and J. S. Zabinski, Calcium sulfate as a high temperature solid lubricant. *Wear*. 219 (1998) 155.

[244]   *"Standard test method for wear testing with a pin-on-disk apparatus"*, *Norma ASTM*. in *Norma ASTM*. 1995. p. G 99.

[245]   H. W. Lehmann, K. Frick, R. Widmer, J. L. Vossen and E. James, Reactive sputtering of PTFE films in argon-CF4 mixtures. *Thin Solid Films*. 52 (1978) 231.

[246]   G. S. Oehrlein and J. L. Lindstöm, Competitive reactions of fluorine and oxygen with W, WSi2, and Si surfaces in reactive ion etching using CF4/O2. *Journal of Vacuum Science & Technology A: Vacuum, Surfaces, and Films*. 7 (1989) 1035.

[247]   C. C. Tang and D. W. Hess, Tungsten Etching in CF 4 and SF 6 Discharges. *J. Electrochem. Soc.* 131 (1984) 115.

[248]   G. Turban, J. F. Coulon and N. Mutsukura, A mechanistic study of SF6 reactive ion etching of tungsten. *Thin Solid Films*. 176 (1989) 289.

[249]   A. Felten, C. Bittencourt, J. J. Pireaux, G. Van Lier and J. C. Charlier, Radio-frequency plasma functionalization of carbon nanotubes surface O2, NH3, and CF4 treatments. *J. Appl. Phys.* 98 (2005) 074308.

[250]   A. Nossa and A. Cavaleiro, Chemical and physical characterization of C(N)-doped W–S sputtered films. *Journal of Materials Research*. 19(8) (2004) 2356.

[251]   M. C. Peignon, C. Cardinaud and G. Turban, Etching processes of tungsten in SF6-O2 radio-frequency plasmas. *J. Appl. Phys.* 70 (1991) 3314.

[252]   M. C. Peignon, C. Cardinaud and G. Turban, A Kinetic Study of Reactive Ion Etching of Tungsten in SF 6 / O 2 RF Plasmas. *J. Electrochem. Soc.* 140 (1993) 505.

[253]   *National Institute of Standards and Technology (NIST)*. Available from: https://srdata.nist.gov/xps/main_search_menu.aspx.

[254]   J. Zekonyte and T. Polcar, Friction Force Microscopy Analysis of Self-Adaptive W–S–C Coatings: Nanoscale Friction and Wear. *ACS Appl. Mater. Interfaces*. 7 (2015) 21056.

[255]   T. D. Bestwick and G. S. Oehrlein, Tungsten etching mechanisms in CF4/O2 reactive ion etching plasmas. *J. Appl. Phys.* 66 (1989) 5034.

[256]   I. Martin-Litas, P. Vinatier, A. Levasseur, J. C. Dupin, D. Gonbeau and F. Weill, Characterisation of r.f. sputtered tungsten disulfide and oxysulfide thin films. *Thin Solid Films*. 416 (2002) 1.

[257]   M. Regula, C. Ballif, J. H. Moser and F. Lévy, Structural, chemical, and electrical characterisation of reactively sputtered WSx thin films. *Thin Solid Films*. 280 (1996) 67.

[258]   International Centre for Diffraction Data (ICCD), Pensylvania. *ficha 00-002-0131*.

[259]   H. Xiao, C. Long, H. Chen, X. Tian, T. Wei, Y. Zhao and W. Gao, Effects of Zr doping on the surface energy and surface structure of UO2: Atomistic simulations. *Appl. Surf. Sci.* 351 (2015) 517.

[260]   P. D. Fleischauer, J. R. Lince, P. A. Bertrand and R. Bauer, Electronic structure and lubrication properties of molybdenum disulfide: a qualitative molecular orbital approach. *Langmuir*. 5 (1989) 1009.

[261]   T. Aerts, T. Dimogerontakis, I. De Graeve, J. Fransaer and H. Terryn, Influence of the anodizing temperature on the porosity and the mechanical properties of the porous anodic oxide film. *Surf. Coat. Tech.* 201 (2007) 7310.

[262]   X. Zhou, D. Xu, G. Yang, Q. Zhang, J. Shen, J. Lu and K. Zhang, Highly Exothermic and Superhydrophobic Mg/Fluorocarbon Core/Shell Nanoenergetic Arrays. *ACS Appl. Mater. Interfaces*. 6 (2014) 10497.

[263]   S. P. Rodrigues, M. Evaristo, S. Carvalho and A. Cavaleiro, Fluorine-carbon doping of WS-based coatings deposited by reactive magnetron sputtering for low friction purposes. *Appl. Surf. Sci.* 445 (2018) 575.

[264]   K. Paso, T. Kompalla, N. Aske, H. P. R⊘nningsen, G. Øye and J. Sjöblom, Novel Surfaces with Applicability for Preventing Wax Deposition: A Review. *Journal of Dispersion Science and Technology*. 30 (2009) 757.

[265]   R. G. S. Hsu. *Boundary lubrication and boundary lubricating films*; In *Modern Tribology Handbook* B. Bhushan, Ed.; CRC Press LLC, 2001, 12, pp. 455.

[266]   T. Spalvins, A review of recent advances in solid film lubrication. *Journal of Vacuum Science & Technology A: Vacuum, Surfaces and Films*. 5 (1998) 212.

[267]   W. J. Schutte, J. L. De Boer and F. Jellinek, Crystal structures of tungsten disulfide and diselenide. *Journal of Solid State Chemistry*. 70 (1987) 207.

[268]   V. Weiß, S. Seeger, K. Ellmer and R. Mientus, Reactive magnetron sputtering of tungsten disulfide (WS2−x) films: Influence of deposition parameters on texture, microstructure, and stoichiometry. *J. Appl. Phys.* 101 (2007) 103502.

[269]   A. Govind Rajan, V. Sresht, A. A. H. Pádua, M. S. Strano and D. Blankschtein, Dominance of Dispersion Interactions and Entropy over Electrostatics in Determining the Wettability and Friction of Two-Dimensional MoS2 Surfaces. *Acs Nano*. 10 (2016) 9145.

[270]   A. Jagminas, G. Niaura, R. Žalnėravičius, R. Trusovas, G. Račiukaitis and V. Jasulaitiene, Laser Light Induced Transformation of Molybdenum Disulphide-Based Nanoplatelet Arrays. *Scientific Reports*. 6 (2016) 37514.

[271]   S. Mignuzzi, A. J. Pollard, N. Bonini, B. Brennan, I. S. Gilmore, M. A. Pimenta, D. Richards and D. Roy, Effect of disorder on Raman scattering of single-layer $\mathrm{Mo}{\mathrm{S}}_{2}$. *Physical Review B*. 91 (2015) 195411.

[272]   X. Zhang, X.-F. Qiao, W. Shi, J.-B. Wu, D.-S. Jiang and P.-H. Tan, Phonon and Raman scattering of two-dimensional transition metal dichalcogenides from monolayer, multilayer to bulk material. *Chemical Society Reviews*. 44 (2015) 2757.

[273]   M. Kalin, I. Velkavrh, J. Vižintin and L. Ožbolt, Review of boundary lubrication mechanisms of DLC coatings used in mechanical applications. *Meccanica*. 43 (2008) 623.

[274]   M. Kalin, I. Velkavrh and J. Vižintin, The Stribeck curve and lubrication design for non-fully wetted surfaces. *Wear*. 267 (2009) 1232.

[275]   J. H. Choo, H. A. Spikes, M. Ratoi, R. Glovnea and A. Forrest, Friction reduction in low-load hydrodynamic lubrication with a hydrophobic surface. *Tribology International*. 40 (2007) 154.

[276]   S. R. Cohen, L. Rapoport, E. A. Ponomarev, H. Cohen, T. Tsirlina, R. Tenne and C. Lévy-Clément, The tribological behavior of type II textured MX2 (M=Mo, W; X=S, Se) films. *Thin Solid Films*. 324 (1998) 190.

[277]   T. Polcar and A. Cavaleiro, Self-adaptive low friction coatings based on transition metal dichalcogenides. *Thin Solid Films*. 519 (2011) 4037.

[278]   J. V. Pimentel, M. Danek, T. Polcar and A. Cavaleiro, Effect of rough surface patterning on the tribology of W–S–C–Cr self-lubricant coatings. *Tribology International*. 69 (2014) 77.

[279]   S. V. Prasad, N. T. McDevitt and J. S. Zabinski, Tribology of tungsten disulfide–nanocrystalline zinc oxide adaptive lubricant films from ambient to 500°C. *Wear*. 237 (2000) 186.

[280]   Y. Xing, J. Deng, Y. Zhou and S. Li, Fabrication and tribological properties of Al2O3/TiC ceramic with nano-textures and WS2/Zr soft-coatings. *Surf. Coat. Tech.* 258 (2014) 699.

[281]   X. Song, J. Z. Huang, S. Oh, A. Danno and S. Castagne, Development of a form rolling micro surface texturing system for friction reduction application in the shaft

component. *Proceedings of the Institution of Mechanical Engineers, Part C: Journal of Mechanical Engineering Science*. 231 (2016) 4263.

[282] J. Han, J. Sun, S. Xu, D. Song, Y. Han, H. Zhu and L. Fang, Tuning the Friction of Silicon Surfaces Using Nanopatterns at the Nanoscale. *Coatings*. 8 (2018)

[283] E. W. Roberts, B. J. Williams and J. A. Ogilvy, The effect of substrate surface roughness on the friction and wear of sputtered MoS2films. *Journal of Physics D: Applied Physics*. 25 (1992) A65.

[284] A. C. Smith, The Interfacial Shear Strength of Molybdenum Disulfide and Graphite Films. *A S L E Transactions*. 25 (1982) 349.

[285] B. N. J. Persson, I. M. Sivebaek, V. N. Samoilov, K. Zhao, A. I. Volokitin and Z. Zhang, On the origin of Amonton's friction law. *Journal of Physics: Condensed Matter*. 20 (2008) 395006.

[286] T. D. Ling, P. Liu, S. Xiong, D. Grzina, J. Cao, Q. J. Wang, Z. C. Xia and R. Talwar, Surface Texturing of Drill Bits for Adhesion Reduction and Tool Life Enhancement. *Tribology Letters*. 52 (2013) 113.

[287] T. Obikawa, A. Kamio, H. Takaoka and A. Osada, Micro-texture at the coated tool face for high performance cutting. *International Journal of Machine Tools and Manufacture*. 51 (2011) 966.

[288] R. J. Santos, A. Chuvilin, E. Modin, S. P. Rodrigues, S. Carvalho and M. T. Vieira, Nanoporous thin films obtained by oblique angle deposition of aluminum on porous surfaces. *Surf. Coat. Tech*. 347 (2018) 350.

[289] E. W. Roberts and W. B. Price, In-Vacuo, Tribological Properties of "High-Rate" Sputtered MoS2 Applied to Metal and Ceramic Substrates. *MRS Proceedings*. 140 (2011) 251.

[290] G. K. Kannarpady, K. R. Khedir, H. Ishihara, J. Woo, O. D. Oshin, S. Trigwell, C. Ryerson and A. S. Biris, Controlled Growth of Self-Organized Hexagonal Arrays of Metallic Nanorods Using Template-Assisted Glancing Angle Deposition for Superhydrophobic Applications. *ACS Appl. Mater. Interfaces*. 3 (2011) 2332.

[291] S. P. Rodrigues, T. Polcar, S. Carvalho and A. Cavaleiro, The wettability and tribological behaviour of thin F-doped WS2 films deposited by magnetron sputtering. *Surf. Coat. Tech. 378* (2019) 125033.